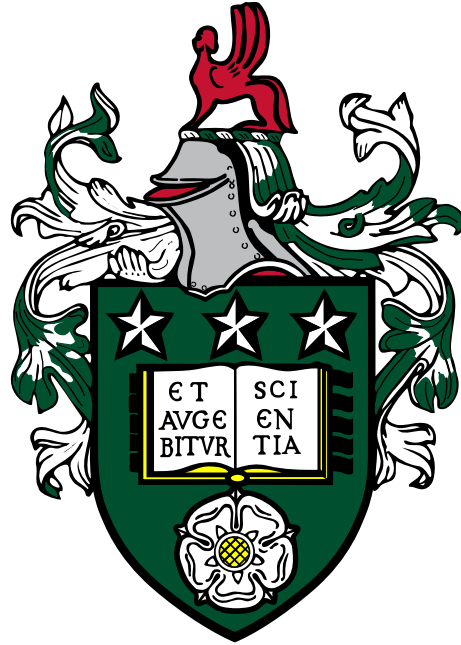


**Developing and Evaluating FlexiLayer Fabrication Technique
for Thin Planar Soft Pneumatic Robot with Experimental
Demonstration**



Majed Melibary

Submitted in accordance with the requirements for the degree
of Doctor of Philosophy

The University of Leeds
School of Mechanical Engineering

Thursday 15th May, 2025

To my beloved parents, always on my mind

Intellectual Property and Publication Statements

The candidate confirms that the work submitted is his own and that appropriate credit has been given where reference has been made to the work of others. This copy has been supplied on the understanding that it is copyright material and that no quotation from the thesis may be published without proper acknowledgement.

© 2025 The University of Leeds and Majed Melibary

Acknowledgements

I would like to start by thanking my two supervisors, Dr. Ali Alazmani and Prof. Peter Culmer. They have been a great support and invaluable mentors during my doctoral journey. I am especially grateful to Dr. Ali Alazmani for his support during the difficult time of my dear mother's passing. I also extend my gratitude to Ahmet Colakoglu for his development of the pneumatic control box used for the characterisation in my doctorate and to Sina Najjari for his developing the control motion box used in the coating technique. I also express my gratitude to Dr. Ahmad Serjouei for his advice on numerical simulation.

I am deeply grateful to my mother and father, who were physically absent but emotionally present with me throughout these years and were my greatest support. Their constant prayers for me before their passing have had a profound impact on me to this day. I also want to thank my two sisters, Aziza Melibary and Nuha Melibary, for their presence in my life, their continuous support and their unwavering encouragement, which helped me reach this point. In addition, I would like to express my gratitude to my father-in-law, who has also supported me throughout this journey and was truly present along the way. I would also like to add that my friend Mohammed Holdar has been with me throughout this period. Since we are in the same field, talking to him about my research and my challenges was beneficial and supportive. He was a great motivator and helped me get started in the lab. Finally, I extend my heartfelt thanks to my wife, Sara Allaf, who has always been by my side throughout my PhD journey and was a key factor in successfully achieving this milestone. Thank you all.

I also acknowledge the financial support provided by the Ministry of Education, Kingdom of Saudi Arabia, through a full scholarship for my PhD. I acknowledge the use of Artificial Intelligence (AI) tools, specifically Copilot (Microsoft, <https://m365.cloud.microsoft/chat>) and Claude (Anthropic, <https://www.anthropic.com/claude>) to assist with proofreading and refining the writing style of this document.

Abstract

This thesis introduces FlexiLayer, a new fabrication technique for pneumatic thin planar soft actuators (PneuThin) that combines doctor blade coating and laser cutting. This method allows for precise control over layer thickness, cavity geometry, and material integration through a layer-by-layer construction process. The initial analysis of the finite element method (FEM) verified the conceptual design and identified key design parameters that affect actuator performance. The fabrication process achieved precise control of the thickness of the layer (coefficient of variation $<4\%$) and precise cavity alignment (<1 mm deviation) using vacuum-assisted positioning.

Eight PneuThin configurations with varying three cavity shapes (rectangular, oval, triangular), cavity widths (5, 10 and 15 mm), and thickness distributions (0, 200 and 400 μm) were experimentally validated. The rectangular cavity design with a thickness difference of 400 μm achieved the highest bending ($245 \pm 33^\circ$ at 5 psi) and the force output (265.6 ± 13.3 mN at 6.5 psi). Adding strain-limiting fabric layers improved control precision but reduced maximum bending by $\approx 63\%$. However, the configuration with strain limiting layers achieves an approximately $\approx 5\%$ increase in force at 7 psi compared to the configuration without these layers at 6.5 psi. Two case studies demonstrated the applicability of the FlexiLayer method to robotic applications; a soft gripper capable of handling objects of 5-194 g and a quadrupedal robot achieving controlled locomotion at 1.7 ± 0.2 mm/s.

The refined FEM analysis, which incorporates experimentally characterised material properties, showed a strong correlation with the measured performance ($R^2 > 0.96$ for force prediction), establishing FEM as a reliable tool in the design process. The FlexiLayer technique overcomes limitations of traditional fabrication methods by offering improved precision, design flexibility, and material compatibility, while remaining simple and scalable. This research advances soft robotics fabrication by providing an approach to creating functional thin-planar soft robots with customisable properties.

Contents

Intellectual Property and Publication Statements	iii
Acknowledgements	iv
Abstract	v
List of Abbreviations	ix
List of Figures	x
List of Tables	xiii
1 Introduction	1
1.1 Introduction	1
1.2 Research Aim and Objectives	2
1.2.1 Aim	2
1.2.2 Objectives	2
1.3 Contributions of this Research	3
1.4 Structure of the Thesis	4
2 Literature Review	7
2.1 Introduction	7
2.2 Soft Pneumatic Actuators	9
2.2.1 Principles of Pneumatic Soft Actuator Operation	9
2.2.2 Bending Pneumatic Actuators	10
2.2.3 Properties and Characteristics of Elastomers	12
2.2.4 Testing of Bending Pneumatic Actuators	14
2.2.5 Applications	16
2.3 Fabrication Techniques for Soft Pneumatic Actuators	18
2.3.1 Moulding and Casting Methods	19
2.3.2 3D Printing Approaches	21
2.3.3 Planar Fabrication Methods	23
2.4 Summary of the Current State of the Art	28
3 FlexiLayer Concept and Preliminary FEM	30
3.1 Introduction	30
3.2 FlexiLayer Concept and Soft Material Selection	31
3.2.1 Concept	31
3.2.2 Soft Material Selection for FlexiLayer	32
3.3 Actuator Design and Geometry Parameters Definitions	34
3.4 FEM Modelling	36
3.4.1 Qualitative Bending Response Assessment	36

3.4.2	Quantitative Performance Analysis	37
3.4.3	Modelling Method	38
3.5	Results	40
3.5.1	Qualitative Behaviour Analysis	40
3.5.2	Quantitative Performance Analysis	45
3.6	Discussion	49
3.7	Chapter Summary	51
4	Development of the FlexiLayer Protocol	53
4.1	Introduction	53
4.2	Development of Laboratory Blade Coating Machine	54
4.2.1	Design and Construction	54
4.2.2	Operating Principles and Control	55
4.3	FlexiLayer Fabrication Protocol	56
4.3.1	Process Overview	56
4.4	Characterisation of the Process Parameters	58
4.4.1	Method 1: Layer Thickness Control	58
4.4.2	Method 2: Alignment Between Layers	64
4.4.3	Method 3: Laser Cutting	66
4.4.4	Method 4: Investigation of Channel Layout Effects on PneuThin inflation	68
4.4.5	Method 5: Integration of Sacrificial Skeleton Features for Complex Cavity Shape Alignment	70
4.4.6	Method 6: Layer Bonding Strength Characterisation	70
4.5	Results	72
4.5.1	Results from Layer Thickness Control and Characterisation	72
4.5.2	Results from PVA Mask Layer Alignment Analysis	78
4.5.3	Results from Laser Cutting Test	78
4.5.4	Results from Channel Layout Study	79
4.5.5	Results from Sacrificial Skeleton Testing	81
4.5.6	Results from Layer Bonding Analysis	81
4.6	Discussion	83
4.7	Chapter Summary	85
5	Characterisation and Case Studies of PneuThin	87
5.1	Introduction	87
5.2	PneuThin Characterisation Methods	88
5.2.1	Actuator Design Configurations	88
5.2.2	Bending Angle Measurement	88
5.2.3	Blocked-Force Measurement	91
5.3	PneuThin Characterisation Results	94
5.3.1	Bending Angle Characterisation	94
5.3.2	Blocked-Force	97
5.4	Case Studies	100
5.4.1	Case Study 1: Soft Gripper	101
5.4.2	Case Study 2: Soft Quadrupedal Robot Locomotion	102
5.5	Discussion	104
5.6	Chapter Summary	106

6	Developing of FEM as a Design Tool for PneuThin	108
6.1	Introduction	108
6.2	Methods	109
6.2.1	Material Characterisation for Modelling	109
6.2.2	Finite Element Model Development	111
6.3	Results	113
6.3.1	Experimental Stress-Strain and Model Fitting	113
6.3.2	Assessment of FEM Predictions for Bending response	113
6.3.3	Assessment of FEM Blocked-Force Predictions	120
6.4	Discussion	121
6.5	Chapter Summary	124
7	Discussion, Future Work and Conclusion	125
7.1	Overall Discussion	125
7.2	Future Research Directions for FlexiLayer Fabrication	129
7.3	Conclusion	131
	Bibliography	133
A	Appendix 1	155
B	Appendix 1	157
C	Appendix 1	159

List of Abbreviations

FEM	Finite Element Method
PneuThin	Pneumatic Thin Planar Soft Actuator
LBCM	Laboratory Blade Coating Machine
DFT	Dry Film Thickness
GH	Gap Height
PVA	Polyvinyl alcohol
2D	Two-dimensional
SL	strain-limiting
IPA	Isopropyl alcohol
CV	Coefficient of variation
MEMS	Micro-electro-mechanical systems
FDM	Fused Deposition Modelling
AM	Additive Manufacturing
DLP	Digital Light Processing
SLA	Stereolithography
DIW	Direct Ink Writing
3D	Three-Dimensional
UV	Ultraviolet
TPU	Thermoplastic Polyurethane

List of Figures

1.1	FlexiLayer fabrication technique: from concept to experimental validation	6
2.1	Schematic illustration of the working principle of a planar pneumatic soft actuator.	10
2.2	Comparison of three approaches to creating anisotropic bending in soft pneumatic actuators	11
2.3	Timeline of soft pneumatic actuator applications (1990-2022).	17
2.4	Comparison of soft pneumatic actuator fabrication techniques.	20
3.1	Schematic representation of the FlexiLayer fabrication concept	32
3.2	PneuThin design structure and parameters	35
3.3	Curvature analysis of PneuThin ($L_r = 0.38$, $C_W = 4$ mm)	37
3.4	FEM simulations diagram for PneuThin soft actuators	38
3.5	FEM model development	40
3.6	Relationship between L_r and curvature (κ) for different C_W	41
3.7	FEM simulation results showing deformed shapes for different geometric configurations of PneuThin.	42
3.8	Comparison of deformation patterns for oval and rectangular cavities of PneuThin actuator.	43
3.9	Mesh analysis of PneuThin with triangular cavity configuration.	44
3.10	Different mesh densities examined for PneuThin	46
3.11	Stress distribution comparison for oval cavity configurations	47
3.12	Performance analysis of PneuThin under 6 psi pressure load	48
4.1	Components of the Laboratory Blade Coating Machine	55
4.2	Phase one of the FlexiLayer fabrication protocol showing the sequential processing steps.	57
4.3	Precision alignment system showing the steps for vacuum-assisted PVA mask positioning.	58
4.4	Phase two of the FlexiLayer fabrication protocol	59
4.5	Schematic illustration of the four stages developed for layer thickness characterisation	61
4.6	Protocol for mapping thickness uniformity of fabricated soft layers.	63
4.7	Experimental setup and measurement methodology for Polyvinyl alcohol (PVA) mask alignment	65
4.8	Template design and experimental setup for laser cutting characterisation	67
4.9	PneuThin design characterisation and fabrication analysis	69
4.10	Design Schematic of Sacrificial Skeleton Features for Pneumatic Thin Planar Soft Actuator (PneuThin) Fabrication	71
4.11	T-peel test configuration	72
4.12	Relationship between Gap Height (GH) and Dry Film Thickness (DFT) for silicone layers coated on steel substrates.	73

4.13	Thickness mapping profiles for key GH, a) 200 μm , b) 400 μm , c) 600 μm and d) 800 μm	74
4.14	Thickness distribution maps showing the DFT measurements of the SL2 coated onto a previously cured silicone substrate.	76
4.15	Analysis of layer thickness variation.	77
4.16	Thickness distribution analysis of silicone layers: PVA-coated and strain-limiting embedded configurations	77
4.17	Comparison of alignment methods and quantitative analysis.	79
4.18	Laser cut path alignment analysis for PneuThin fabrication.	80
4.19	Laser cut quality analysis for 1 mm thick Elastosil M4601	80
4.20	T-peel test analysis at different semi-cure times	82
5.1	Actuator design configurations	89
5.2	Characterisation of PneuThin bending behaviour	91
5.3	Experimental setup and force measurement characterisation of PneuThin	93
5.4	Effect of Thickness Distribution on Bending Angle.	94
5.5	Effect of Cavity Shape on Bending Actuation.	95
5.6	Influence of Cavity Width on Bending Actuation in PneuThin.	96
5.7	Impact of Strain-Limiting Layer on Bending Actuation.	97
5.8	Peak force output versus actuation pressure for actuators with varied thickness distributions (R10-d0, R10-d200, R10-d400).	98
5.9	Peak force output versus actuation pressure for actuators with oval (O10-d400), rectangular (R10-d400), and triangular (T10-d400) cavity shapes.	99
5.10	Peak force output versus actuation pressure for actuators with 5 mm (R5-d400), 10 mm (R10-d400), and 15 mm (R15-d400) cavity widths.	99
5.11	Force output versus actuation pressure for actuators with strain limiting layer (R10-d400-sl), and without strain limiting layer (R10-d400) configurations.	100
5.12	Demonstration of the FlexiLayer-fabricated soft gripper's capability	101
5.13	Sequential actuation of a quadrupedal soft robot showing undulating locomotion.	103
6.1	Methodology flowchart for Finite Element Method (FEM) assessment of PneuThin	110
6.2	Experimental workflow for material model development and FEM validation	111
6.3	FEM workflow and results for PneuThin simulation.	112
6.4	Material characterization results for PneuThin configurations	113
6.5	FEM vs. experimental bending angles for PneuThin actuators	114
6.6	Inflation sequence of the R10-d400 actuator from 0.5 to 3 psi through experimental images, FEM simulations, and profile plots	115
6.7	deformation sequence of the R10-d400 actuator from 3.5 to 5 psi through experimental images, FEM simulations, and profile plots	116
6.8	Deformation sequence of the R10-d400-SL actuator from 0.5 to 4 psi through experimental images, FEM simulations, and profile plots	118
6.9	Deformation sequence of the R10-d400-SL actuator from 4.5 to 5.5 psi through experimental images, FEM simulations, and profile plots	119
6.10	Comparison between experimental measurements and FEM predictions of force output	120
A.1	Deformation patterns of PneuThin with oval cavity at smaller cavity widths	156
B.1	Thickness mapping profiles for key GH, a) 100 μm , b) 300 μm , c) 500 μm and d) 700 μm	158

C.1	Schematic of the custom-designed pneumatic control box	160
C.2	Technical drawing of the quadrupedal soft robot showing key dimensions . .	160
C.3	2D layout of the quadrupedal soft robot showing integrated chambers . . .	160
C.4	Bending angle response of PneuThin design R5-d400 (5 mm cavity width) .	161
C.5	Bending angle response of PneuThin design R10-d400 (10 mm cavity width)	161
C.6	Bending angle response of PneuThin design R15-d400 (15 mm cavity width)	162
C.7	Bending angle response of PneuThin design O10-d400 (10 mm cavity width)	162
C.8	Bending angle response of PneuThin design T10-d400 (10 mm cavity width)	163
C.9	Bending angle response of PneuThin design R10-d200 (10 mm cavity width)	163
C.10	Bending angle response of PneuThin design R10-d0 (10 mm cavity width) .	164
C.11	Bending angle response of PneuThin design R10-d400-sl (10 mm cavity width)	164

List of Tables

3.1	Processing parameters of common elastomer silicone rubbers used in soft robotics	33
3.2	Material properties of ELASTOSIL® M 4601 A/B (AG, 2024)	34
3.3	Design constraints for PneuThin bending actuator simulation model	35
3.4	Geometric Parameters for Cavity Shape Investigation	37
3.5	Yeoh hyperelastic material parameters for ELASTOSIL® M 4601	39
3.6	Mesh sensitivity analysis results for rectangular cavity configuration ($W = 5$ mm, $L_r = 0.38$, $C_W = 4$ mm, $P = 6$ psi)	45
3.7	Stress and displacement results for different cavity configurations ($L_r = 0.38$)	47
3.8	Curvature measurements for different cavity configurations	49
4.1	Experimental parameters used for fabricating silicone layers using LBCM .	61
4.2	Experimental thickness characterisation of four fabrication stages	62
4.3	Parameter Testing Coverage for Laser Cutting Optimization	68
4.4	DFT measurements for different GH values of layer formation on steel substrate. Values represent mean thickness with standard deviation (n=60 per sample). CV: Coefficient of Variation (%).	74
4.5	Statistical analysis of dry film thickness measurements for second silicone layer (SL2)	75
4.6	Effective laser cutting parameters for 1 mm thick Elastosil M4601	81
4.7	Summary of failure characteristics and bond strengths across semi-cure times	82
4.8	T-peel test results for fully cured specimens at 75 °C for 15 minutes	83
4.9	T-peel test results for semi-cured specimens (7 minutes at 75°C)	83
5.1	Threshold activation pressures for mitigating strain softening in different actuator configurations	90
5.2	Operating parameters for quadrupedal robot locomotion	102
6.1	Material properties and FEM parameters for R10-d400 and R10-d400-sl configurations	112
6.2	Experimental vs. FEM Predicted Forces for PneuThin configurations	121

Chapter 1

Introduction

1.1 Introduction

Soft robot technologies have emerged as a transformative solution to the limitations of traditional rigid robotic systems, particularly in terms of safety and adaptability (Laschi et al., 2016; Yang et al., 2018). These technologies leverage the inherent softness and compliance of materials to create devices that can interact with humans safely and adapt to complex environments. Soft robotics applications include wearable exosuits (Zhu et al., 2022a), assistive devices (Kulasekera et al., 2021), artificial organs (Cohrs et al., 2017), surgical tools (Cianchetti et al., 2013), diagnostic devices (Pittiglio et al., 2022), and human-robot collaboration systems (Sun et al., 2022).

Central to these applications are soft actuators, which generate motion through elongation (De Pascali et al., 2022), bending (Polygerinos et al., 2015), or twisting (Choi et al., 2020). Among these, pneumatic bending actuators, also known as Elastic Inflatable Actuators, are particularly significant due to their ability to produce complex movements by inflating a cavity surrounded by anisotropic elastic material (Suzumori et al., 1997). However, existing fabrication techniques for these actuators, such as moulding and 3D printing, present several challenges. Moulding involves multiple steps and often results in limited design flexibility and repeatability (Wei and Ghosh, 2022). Three-Dimensional (3D) printing, while enabling rapid prototyping, is constrained by high costs and limited material options, particularly for soft materials (Lalegani Dezaki and Bodaghi, 2023). These limitations hinder the scalability and broader application of soft pneumatic actuators.

This research addresses these challenges through the development of FlexiLayer, a hierarchical lamination technique that combines doctor blade coating for precise layer deposition with laser cutting for accurate patterning. The term 'FlexiLayer' reflects the

technique's ability to create flexible, multilayered structures with controlled thickness distributions and integrated functionalities. To validate this fabrication approach, the research introduces a class of PneuThin with a characteristic of bending motion, demonstrating the precision and versatility of the FlexiLayer technique. The name 'PneuThin' reflects two key characteristics: pneumatic actuation and thin planar geometry (≈ 1 mm thick). The FlexiLayer technique, through its combination of precise layer control and design flexibility, enables better replication of biological motion (e.g. bending) patterns while maintaining manufacturing simplicity. This advancement in fabrication methodology aims to accelerate the development of novel soft robotic applications in research communities.

1.2 Research Aim and Objectives

1.2.1 Aim

The primary aim of this research is to address the limitations of current fabrication methods for thin planar soft robots, particularly in terms of precision, scalability, and design flexibility. To overcome these challenges, this work proposes and validates FlexiLayer, a novel layer-by-layer fabrication technique for soft pneumatic actuators. The method is demonstrated through the development of PneuThin, which demonstrates precise layer control, cavity definition, and adaptability to various designs and functionalities.

1.2.2 Objectives

To achieve this aim, the following objectives will be pursued:

1. Conduct preliminary FEM analysis to verify feasibility of the conceptual design of pneumatic thin 'PneuThin' soft actuators and identify critical geometric parameters affecting their bending performance. The investigation examines the influence of the thickness distribution of the layer, the dimensions of the cavity, and the shape of the cavity on the deformation patterns of bending through systematic numerical simulation-based studies. This foundational analysis establishes essential design parameters for the development of precise fabrication protocols.
2. Develop a systematic fabrication protocol combining doctor blade coating and laser cutting techniques to create PneuThin actuators. The investigation establishes precise control over the layer thickness through a methodical analysis of the Gap Height (GH) parameters and Dry Film Thickness (DFT) relationships. The protocol implements

vacuum-assisted alignment methods to achieve consistent layer positioning with submillimeter precision. The study verifies laser cut path accuracy against intended design specifications and determines effective cutting parameters to ensure clean patterning in silicone elastomer structures. The development includes verification of critical processing steps, including semi-curing duration for optimal layer bonding and channel layout effects on air transfer capability in zero-volume chambers.

3. Validate the versatility of the FlexiLayer technique by fabricating and characterising eight PneuThin design configurations with varying cavity shapes (rectangular, triangular, and oval), cavity widths, and thickness distributions, demonstrating precise control over bending behaviour through off-centre chamber placement.
4. Present two case studies that demonstrate the capabilities of FlexiLayer-fabricated PneuThin actuators:
 - (a) Fabricating a multi-gait soft robot and documenting its locomotion capabilities.
 - (b) Creating a soft gripper using actuators made with the FlexiLayer technique and evaluating its performance in handling objects of different weights and geometries.
5. Verify the effectiveness of FEM as a design tool for PneuThin actuators through systematic numerical simulation-experimental comparison investigation. The study develops hyperelastic material models using experimental material property data of doctor blade-coated elastomers to accurately simulate actuator bending deformation. The investigation examines two representative designs: an unconstrained configuration (R10-d400) and a constrained configuration (R10-d400-sl). The analysis quantifies FEM model accuracy in predicting critical performance metrics, specifically bending deformation profiles under incremental pressure loading and force output capability. This verification establishes FEM as a reliable tool for optimising PneuThin designs prior to fabrication.

1.3 Contributions of this Research

This research makes the following key contributions to the field of soft robotics:

1. **Development of the FlexiLayer fabrication technique:** This new technique simplifies the fabrication of thin planar soft pneumatic actuators, offering enhanced precision, versatility and accessibility compared to conventional methods.

2. **Design and development of PneuThin:** A class of bending actuators that demonstrates precise control over key design parameters, including cavity shape, cavity width and thickness distributions, enabling customised bending characteristics through the FlexiLayer technique.
3. **Establishment of a characterisation methodology:** The research establishes an approach to characterising the performance of FlexiLayer-fabricated PneuThin actuators, including experimental protocols and analysis methods.
4. **Validation through case studies:** The development of a multi-gait soft robot and a soft gripper demonstrates the capabilities of FlexiLayer-fabricated PneuThin actuators in creating functional soft planar robot.
5. **Advancement of soft robotics fabrication:** Research contributes to the advancement of soft robotics fabrication by providing a simple, cost-effective, and versatile method to create thin planar soft robotic structures, validated through PneuThin bending actuators, with potential for broader applications and material compatibility.
6. **Scientific publication plan** Two draft manuscripts are under internal review for scientific publication. These publications aim to increase the use of FlexiLayer in the field of soft robotics.

1.4 Structure of the Thesis

This thesis presents research on the FlexiLayer fabrication technique. Fig. 1.1 outlines the logical progression of chapters with a graphical abstract showing the key technical developments and experimental demonstrations within each chapter. The remaining chapters are organised as follows:

- **Chapter 1: Introduction** establishes the context and significance of soft robotics, identifies the limitations of current fabrication techniques, and presents the research aims and objectives for developing the FlexiLayer fabrication technique.
- **Chapter 2: Literature Review** examines soft robotics, soft pneumatic actuators, and existing fabrication techniques, highlighting the limitations that motivate this research.
- **Chapter 3: FlexiLayer Concept and Preliminary FEM** for PneuThin bending actuators presents computational analysis to validate the fabrication concept and identify critical design parameters influencing actuator behaviour.

- **Chapter 4: Development of the FlexiLayer Protocol** details the development and characterisation of the fabrication process, establishing precise control over layer thickness, alignment, and bonding.
- **Chapter 5: Characterisation and Case Studies of PneuThin** demonstrate the capability of the fabrication technique through the evaluation of eight configurations of pneumatic thin soft actuator, including the demonstration of two case studies; multi-gait robot and soft gripper.
- **Chapter 6: Developing of FEM as a Design Tool for PneuThin** evaluates the efficacy of FEM through a detailed comparison of computational predictions with experimental results for two specific actuator cases: unconstrained and constrained (fabric-reinforced) configurations. The analysis examines bending profiles under incremental pressure loading and blocked force generation, establishing FEM's utility for the initial design optimisation of similar PneuThin configurations.
- **Chapter 7: Discussion, Conclusions and Future Work** summarises key findings, discusses implications, and outlines future research directions.

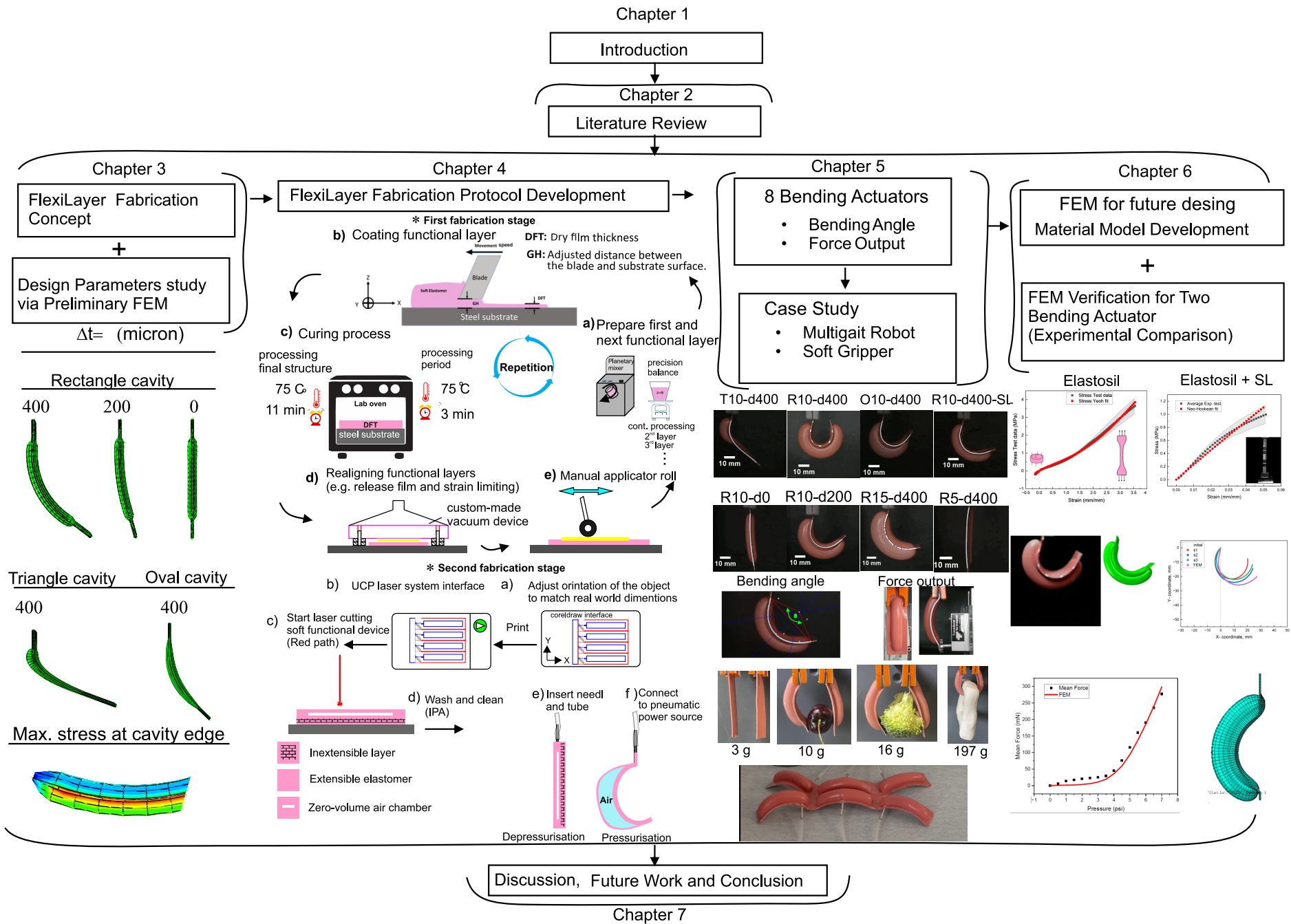


Figure 1.1: FlexiLayer fabrication technique: from concept to experimental validation

Chapter 2

Literature Review

Chapter 2 examines the current state of soft robotics fabrication, with particular focus on pneumatic actuators and their manufacturing methods. The review progresses through four key areas: (1) the fundamental principles and significance of soft robotics, (2) the working mechanisms and characteristics of pneumatic soft actuators, (3) current fabrication techniques and their limitations, and (4) the emerging opportunities in planar fabrication approaches. This review sets the stage for the development of the new fabrication method introduced in this study.

2.1 Introduction

Soft Robotics

Robotic systems have shown explosive growth in the industrial sector (Delgado et al., 2019). These systems are typically implemented as rigid-bodied robots (Rus and Tolley, 2015). Conventional rigid robots can potentially harm human operators or bystanders during close interaction (Rukhlenko et al., 2020) due to their fabrication from hard materials such as metal (Shepherd et al., 2011). Furthermore, rigid robots often have limited flexibility (Rus and Tolley, 2015). For example, mobile robots built with hard materials can become unstable in difficult terrain (Shepherd et al., 2011).

The potential risks and limitations of rigid robots can be alleviated by using soft robots, which are made primarily of soft materials (Hao et al., 2022). This improves safety in human-robot interactions (Rukhlenko et al., 2020). From an application perspective, soft robots can address many challenges, such as wearable soft robots for rehabilitation (Lee et al., 2017; Liu et al., 2020), and can be used in medical operations, including minimally invasive surgical tools, transplant surgeries (Watanabe et al., 2007), and handling delicate

objects (Suzumori et al., 1991a).

Soft Materials

Soft materials are the key to creating soft robot bodies (Rus and Tolley, 2015). The degree of softness of these bodies is defined by moduli of the materials (predominantly elastomeric polymer) used in the manufacture of these robots (Shepherd et al., 2011). The modulus of a material is a quantitative measure of its stiffness, which describes the resistance of the material to elastic deformation under applied stress. Specifically, Young's modulus defines the relationship between stress and strain in the linear elastic region of a material (Chubb et al., 2019). In the context of soft robotics, Majidi (2013) and Rus and Tolley (2015) both suggested that soft materials have moduli in the range of soft biological materials. Biological materials such as skin or muscle tissue have moduli in the range of 10^4 to 10^9 Pa (Rus and Tolley, 2015). Materials with a modulus in this range exhibit characteristics of high deformability, stretchability, and safe human-robot interaction (Tawk and Alici, 2020a; Whitesides, 2018). In addition to modulus, Shore hardness scales are commonly used to quantify the softness of elastomeric materials in soft robotics, where lower Shore values indicate softer materials that are more easily deformed under pressure (Limited, 2022).

The question of what is meant by softness in soft robotics has been explored in works by Chubb et al. (2019) and Kastor et al. (2017). In particular, Chubb et al. (2019) examined the ambiguity of using the term softness in the literature whether it refers to the compliance of the material, the compliance of the robot's structure, or simply a way to distinguish it from conventional rigid robots. Chubb et al. (2019) emphasised that softness has been viewed as the opposite of hardness (resistance to local permanent deformation), and compliance as the opposite of stiffness (resistance to elastic deformation) (Chubb et al., 2019). However, in soft robotics, softness often refers to how much a robot or material can deform, either due to the material itself or the design of the structure (Chubb et al., 2019). In line with this, Kastor et al. (2017) also pointed out that a material can be called soft if it bends more than the environment it touches. This means that softness is not just about the type of material, but about how it behaves during use (Kastor et al., 2017).

The soft robot made of compliant materials allows safer interaction with humans and simplifies tasks such as grasping delicate objects without damaging them (Rus and Tolley, 2015). To achieve completely soft robots, soft materials should be integrated into every component of the robotic system, including structures, sensors, power sources, and

actuators (Elango and Faudzi, 2015).

Soft Actuators

Soft actuators are essential components of soft robotics (Tang et al., 2022), allowing robots to generate movement and perform tasks (Gorissen et al., 2017). Several actuation methods exist for soft actuators, including pneumatic (Feng et al., 2021), electrical (Gu et al., 2017), and thermal (Jin et al., 2018). Among these, pneumatic soft actuators are gaining attention in soft robotics due to their low cost, simplicity, and long life (Amiri Moghadam et al., 2018). The following section emphasises the review of pneumatic soft actuators, focussing specifically on their design, applications, and fabrication.

2.2 Soft Pneumatic Actuators

Pneumatic soft actuators have shown advantages of high flexibility, high force output, easy fabrication, and control (Luo et al., 2021; Connolly et al., 2015). This type of actuators is known by different names in the literature, such as 'soft fluidic actuator' (Xavier et al., 2020) and 'flexible fluidic balloon actuator' (B.Gorissen et al., 2011). Additional, Pneumatic actuation of elastic inflatable actuators is developed for soft robots (Wehner et al., 2014; Gorissen et al., 2017; Lee et al., 2017) enables applications including rehabilitation (Liu et al., 2020) such as soft wearable assistive gloves (Feng et al., 2021), transplant surgery (Watanabe et al., 2007) and handling delicate objects (Suzumori et al., 1991a). This actuator is driven by a pressurised fluid, such as gas or liquid, for actuation (Hu et al., 2018). In addition, biocompatible fluid is suitable for pressurising these actuators in medical applications without disrupting their working principles (Gorissen et al., 2017).

2.2.1 Principles of Pneumatic Soft Actuator Operation

The principle workings of these types of actuators are very simple. Soft pneumatic actuators are designed mainly with rubber structures. This substantial rubber structure includes one or more chambers that are also built in the rubber structure, see Fig. 2.1. This internal chamber when subjected to a pneumatic pressure load causes the rubber structure to deform elastically. This elastic deformation works as an actuator (Suzumori et al., 2007). This simple principle enables one of the most critical movements in soft robotics (e.g., bending motion) (Suzumori et al., 1997).

2.2.2 Bending Pneumatic Actuators

Bending motion of the inflatable elastic actuator can be achieved using the anisotropy elasticity (Suzumori et al., 1997). This anisotropic behaviour can be achieved through an asymmetric axial cross section such as multimaterial (Shepherd et al., 2011; Suzumori et al., 1991b), corrugated membrane (Mosadegh et al., 2014), or eccentric void asymmetry (Gorissen et al., 2011) of the elastic inflatable actuator design (Suzumori et al., 1997; Xavier et al., 2020). Fig. 2.2 illustrates these three primary approaches to achieving asymmetry in bending pneumatic actuators. Each approach creates anisotropic properties through different structural configurations: (a) eccentric void placement shifts the air channel off-centre within a homogeneous material; (b) multimaterial integration combines layers with different elastic properties; and (c) corrugated membrane design incorporates structured chambers to control deformation pathways. The longitudinal and axial cross-sections reveal how each design directs the pneumatic force into controlled bending motion. For example, Suzumori et al. (1991b) have developed bending microactuator based on the multimaterial concept using fibre-reinforced silicone rubber. Mosadegh et al. (2014) have used the concept of corrugated membrane to maximise bending performance by designing multiple air chambers. Gorissen et al. (2011) have proposed bending pneumatic balloon actuator by bonding two layers with an eccentric void placement.

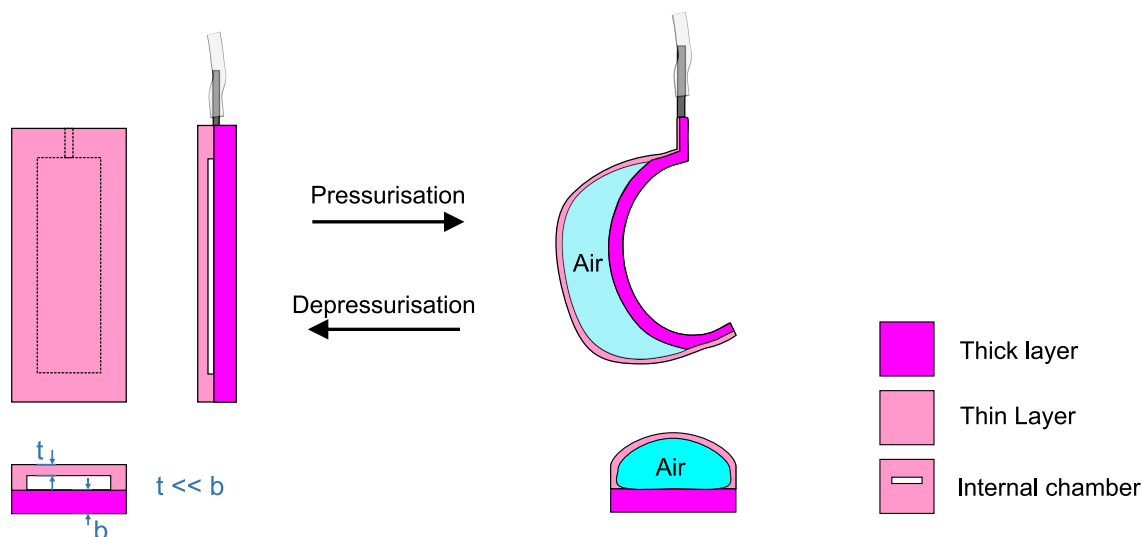


Figure 2.1: Schematic illustration of the working principle of a planar pneumatic soft actuator.

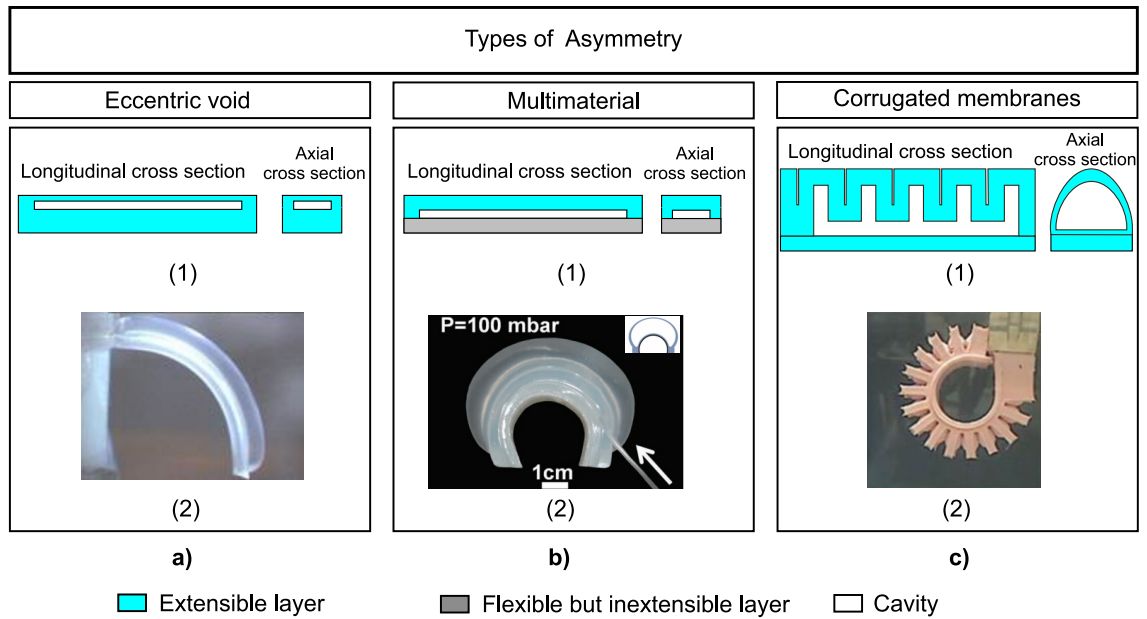


Figure 2.2: Comparison of three approaches to creating anisotropic bending in soft pneumatic actuators: (a) eccentric void asymmetry, (b) multimaterial integration, and (c) corrugated membrane design. Each column shows the structural configuration through longitudinal and axial cross-sections (1) with corresponding physical implementations (2). a) (2) Pneumatic Balloon Actuator. Reproduced with permission (Konishi, 2015). Copyright 2015, IEEE. b) (2) Paper–elastomer composite soft actuator. Reproduced with permission (Martinez et al., 2012). Copyright 2012, John Wiley and Sons. c) (2) Pneu-Net bending actuator. Reproduced with permission (Mosadegh et al., 2014). Copyright 2014, John Wiley and Sons.

Bending Based on Eccentric Void Asymmetry

In particular, Fig. 2.2a shows a cross section of eccentric void asymmetry to achieve the bending motion. The eccentric void means that the inner channel is not centrally embedded within the actuator structure (Gorissen et al., 2017). The inner channel of the pneumatic soft actuator is made up of two thin films (Jeong and Konishi, 2006; Konishi et al., 2001), see the cross section in Fig. 2.2a (1). Generally, the main configuration involves two monolithic rectangular layers of elastomer combined using a thermal curing process, creating different layer thicknesses above and below the inner channel. To realise the bending motion mode, anisotropic properties in the soft material are necessary. This anisotropy can be achieved through the structural design of the soft actuator cross section (Suzumori et al., 1997). Typically, if the inner channel is placed off-centre in the cross section of the actuator, a different layer thickness is obtained. As a result, variations in bending stiffness are achieved, leading to differential strain between the upper and lower layers that envelope the channel, which subsequently causes the actuator to bend when pressurised (Gorissen et al., 2011; Xavier et al., 2020; Shepherd et al., 2011); (see

Fig. 2.2a(1,2).

As mentioned above, this actuator structure is mainly made up of two flexible layers; see Fig. 2.2a. The top layer is a thin silicone-based layer, which can be referred to as a membrane, while the lower layer is a thick silicone-based layer. Both layers are bonded together along their surrounding edges; thus, the inner cavity is formed. The cavity is initiated by inserting a mask layer such as release film, release spray, or wax between the main two layers; see Fig. 2.2a. This concept is known as a zero-volume air chamber and was proposed by (Park et al., 2014a; Wirekoh and Park, 2017). The role of the cavity is to provide room for compressed air and its volume increases when the pressure load is active. This step is called soft actuator inflation (Gorissen et al., 2011).

2.2.3 Properties and Characteristics of Elastomers

Many soft robots and actuators are designed using materials such as hydrogels, electroactive polymers (for example, dielectric elastomer actuators) and elastomers (McCracken et al., 2020). The selection of these materials for use in soft robotic and actuator design is largely influenced by the type of actuation mechanism used to generate motion in the device (Miriyeve et al., 2017). For example, Shintake et al. (2015) demonstrated a variable stiffness actuator based on a dielectric elastomer actuator integrated with a low melting point alloy, achieving an electrically driven gripper capable of lifting 11 grams (Shintake et al., 2015). More recently, Kozuki et al. (2024) developed a hybrid soft actuator that combines a temperature-responsive hydrogel adhered to a 3D soft grid skeleton, resulting in a system capable of bending and cyclically responding to thermal stimuli (Kozuki et al., 2024). However, elastomers such as silicone rubber are widely used in the fabrication of pneumatic actuators (Xavier et al., 2022). This section, therefore, focusses specifically on the properties and behaviour of elastomeric materials used in soft pneumatic actuators.

The geometry and properties of the constituent materials significantly influence the behaviour and motion of soft pneumatic devices (Ranzani et al., 2018). In soft robotics applications, silicone rubbers are widely used in soft robotics due to their ability to withstand large strains, along with their biocompatibility, low cost, ease of processing, robustness and the ability to match the softness of human and natural environments (Marechal et al., 2021; Ranzani et al., 2018). These products include the Ecoflex series (Smooth-On, Inc.), the Dragon Skin series, the Elastosil 4601M and the Smooth-Sil series (Xavier et al., 2020). These soft materials have low elastic moduli, ranging from 10^4 to 10^9 Pa (Rus and Tolley, 2015), allowing significant stroke in elastic inflatable actuators

(Gorissen et al., 2017). The mechanical properties of these hyperelastic materials depend on several factors, including the curing temperature and the mixture ratio between the elastomer and the curing agent (Xavier et al., 2020; Marechal et al., 2021; Case et al., 2015). Moreover, Case et al. (2015) investigated how the non-linear behaviour of these materials varies with the loading rate and the variations in the production process (Case et al., 2015).

Case et al. (2015) and Liao et al. (2021) discussed how these elastomeric materials demonstrate the Mullins effect¹ or stress softening. This occurs when materials are subjected to initial strain, resulting in irreversible changes in their properties (Case et al., 2015). First reported by Mullins (1969), this effect is characterised by a reduction in stiffness after the first loading cycle. Diani et al. (2009) reviewed various physical interpretations of this effect. They associated it with microstructural changes in the material, such as polymer chain slippage, network rearrangement, filler-cluster rupture, and molecular disentanglement. These irreversible changes typically occur during the initial strain and result in a softer response in subsequent cycles. To minimise the influence of this effect, some studies have employed pre-conditioning procedures before material or actuator testing. For example, Moseley et al. (2016) and Wehner et al. (2016) applied approximately ten pre-cycles above the activation threshold to ensure consistent performance and reproducible bending behaviour.

Further, Case et al. (2015) highlighted that this effect appears most prominently in the middle of the elastic regime (Case et al., 2015). This is consistent with Russo et al. (2017), who observed less pressure required in cyclical testing than in initial inflation cycles (Russo et al., 2017). However, subsequent testing reveals that no significant property changes occur after the first ten loading cycles (Case et al., 2015) and that hysteresis remains minimal. Furthermore, stress softening demonstrates temporary rather than permanent characteristics, with these elastomers showing a stress recovery behaviour over time (Liao et al., 2021). These material behaviours demonstrate the complication of working with hyperelastic materials in soft pneumatic actuators. It is crucial to understand these properties, particularly the stress-softening behaviour and production-dependent variations, to develop reliable fabrication techniques and increase the repeatability of actuator performance.

¹The Mullins effect refers to a characteristic stress softening phenomenon occurring when an elastomer undergoes its first loading-unloading cycle. During subsequent loading cycles, the stress level in a given stretch decreases compared to the initial loading path (Liao et al., 2021).

2.2.4 Testing of Bending Pneumatic Actuators

The characteristic response to bending motion in balloon-type actuators can be controlled by varying the shapes of the air chamber, the variation in the thickness or different elastic modulus of the layers surrounding the cavity, and the overall geometry of the actuator (Sinatra et al., 2018). The primary metrics used to evaluate the effect of these variations on the bending behaviour of soft pneumatic actuators are the bending angle and force output. The bending angle is how much an actuator bends when a force or pressure is applied to its internal chamber or cavity (van Vlerken et al., 2023). This metric (e.g., bending angle) was measured in the literature through empirical testing using physical prototypes (Libby et al., 2022), analytical modelling using mathematical equations (Shapiro et al., 2011; Gorissen et al., 2011), and numerical simulation through finite element analysis (Xavier et al., 2020).

The beam deflection model used to describe the bending deformation in pneumatic soft actuators (Gorissen et al., 2017). This model was used with the assumption that the elastic modulus remains constant during inflation and cross section shape does not change along the actuator (Gorissen et al., 2017; Shapiro et al., 2011). Alici et al. (2018) applied this model to predict bending angles in pneu-net actuators (Alici et al., 2018). However, this model achieved accurate results only under low pressure conditions and small deformations (Alici et al., 2018; Gorissen et al., 2017). Inadequacy of the model to predict accurate behaviour of the soft actuator in large bending deformation due to two key factors. First, soft materials in which these actuators are made exhibit complex non-linear stress-strain relationships, therefore the elastic modulus varies with the applied force (Moseley et al., 2016). Second, large deformations create geometric nonlinearity effects. These effects make this model only valid for small strain and simple configuration design (Gorissen et al., 2017; Moseley et al., 2016). Furthermore, Gorissen et al. (2017) emphasises that assumptions of constant Young's modulus and linear elasticity lead to a major source of errors in the prediction of actuator behaviour (Gorissen et al., 2017).

Numerical modelling, particularly the FEM, addresses the limitations of analytical modelling in soft robotics (Gorissen et al., 2017). In particular, it facilitates handling material nonlinearities and the large deformations that occur in soft fluidic actuators during actuation (Xavier et al., 2020). This modelling approach helps visualise maximum stress distributions and understand local strain effects on actuator performance during pressurisation (Polygerinos et al., 2015). Consequently, a rapid and efficient design process can be achieved while reducing development costs (Xavier et al., 2020; Tawk and Alici,

2020a). A critical aspect of accurate FEM prediction is the use of a hyperelastic material model, which enables the accurate capture of the large strain range exhibited in rubber-like materials for soft robotics (Marechal et al., 2021; Gorissen et al., 2017; Xavier et al., 2020; Moseley et al., 2016). The accuracy of the model can be improved by obtaining appropriate hyperelastic material constants through uniaxial testing, ensuring that samples are prepared based on fabrication processing variables (Marechal et al., 2021; Gorissen et al., 2017). This is essential due to batch-to-batch variations (Case et al., 2015) and material processing factors, such as the curing agent and the curing temperature (Johnston et al., 2014; Khanafer et al., 2009), which affect the material's properties and, consequently, its stress-strain response. Furthermore, Xavier et al. (2020) noted that uniaxial tensile testing is sufficient for certain models. The Yeoh model accurately describes elastic behaviour in a wide range of strains greater than 400% and predicts stress-stretch behaviour in various deformation modes using uniaxial data (Libby et al., 2022). However, caution is needed when using the Ogden model with limited data, such as only uniaxial tension (Xavier et al., 2020). These constants alone may not fully represent actual actuation behaviour due to complex loading conditions, manufacturing variations (Dezaki et al., 2022b), experimental measurement errors (Hu et al., 2018), and material property inconsistencies during operation (Xavier et al., 2020; Libby et al., 2022). As noted in Marechal et al. (2021), it was emphasised that the subsequent stress-strain curves of soft materials are more significant for soft devices than the initial ones, particularly when the device undergoes cyclic actuation (Marechal et al., 2021; Libby et al., 2022).

To validate these computational predictions, fabrication and experimental characterisation is performed (Xavier et al., 2020). An empirical approach to characterising the performance of the bending actuator involves two key metrics as previously mentioned; bending angle and force output (Shintake et al., 2017). The bending angle is measured by testing the actuator in a cantilever beam configuration, where one end remains fixed while the other end moves freely. This setup enables the capture of deformation profiles at specific pressures through image analysis (Polygerinos et al., 2015). Various methods have been used in the literature to measure the bending angle of actuators. Rehman et al. (2017) and Rehman et al. (2016) calculated the bending angle of a circular pillow actuator design using a trigonometric approach (Rehman et al., 2017; Rehman et al., 2016). This was based on a right-angled triangle formed during deformation. Similarly, Shapiro et al. (2011) employed the Taubin algorithm developed by Chernov (Chernov, 2025) to fit a circle that passes through the side of the actuator (Shapiro et al., 2011). This enabled the

quantification of the bending curvature at various air pressures for an elastic tube actuator with an asymmetric cross section (Shapiro et al., 2011). Auysakul et al. (2020) determined the coordinates of three points on the actuator side to quantify the centre of curvature and the circular chord, using this information to measure the bending angle Auysakul et al. (2020). Both Shapiro et al. (2011) and Auysakul et al. (2020) assumed that the actuator bends along a true arc. Thomson and Motani (2021) measured claw curvature to assess whether its functions, such as locomotion and gripping, could be inferred confidently from its morphology (Thomson and Motani, 2021). The bending angle was determined using the Feduccia (1993) method, applied to photographs of claw specimens, with post-processing performed in a programming environment software (MATLAB 2018Ra, MathWorks Inc.). (Thomson and Motani, 2021). This method provides a potential approach to characterising the bending behaviour of soft pneumatic actuators. In addition, the characterisation of force output involves constraining the actuator's deflection and measuring the resultant force (Wehner et al., 2016), by placing a force sensor in front of the actuator's tip, providing quantitative data under different pressure conditions (Shintake et al., 2017). In addition, a custom clamp may be required to ensure that the tip actuator is in contact with the load cell during the testing (Moseley et al., 2016).

2.2.5 Applications

Pneumatic soft actuators have been developed for various applications. Fig. 2.3 illustrates the evolution of soft pneumatic actuator applications from 1990 to 2022. The timeline presents a progressive diversification across three domains: gripping mechanisms, locomotion systems, and medical devices. The development trajectory in Fig. 2.3 reflects how improvements in materials and manufacturing methods directly enabled more complex functional capabilities. For example, soft pneumatic actuators based on the concept of Pneu-nets (Mosadegh et al., 2014) can generate significant bending motion. This soft pneumatic actuator based on Pneu-nets offers a high potential for medical applications, particularly for rehabilitation (Ge et al., 2020). For example, Ge et al. (2020) designed soft fabric-based pneumatic actuators for hand rehabilitation, and their clinical evaluation results demonstrate the feasibility of this design in assisting hand motion and grasping tasks. Moreover, bending pneumatic soft actuator has the potential to allow challenging surgery. For example, Suzumori et al. (1997) explored a pneumatic micro-actuator for applications such as disposable micro-manipulators for medical purposes. In addition, Watanabe et al. (2007) developed a novel surgical tool for transplant surgery, with a

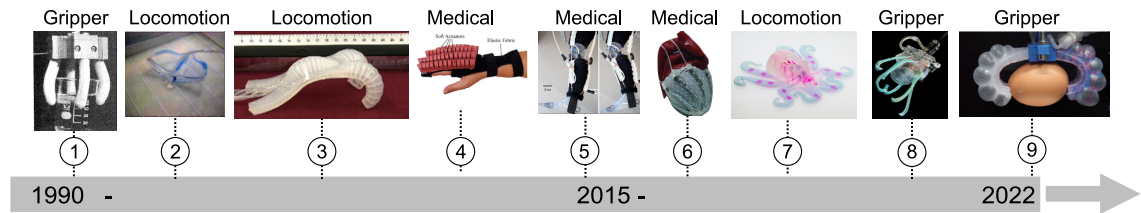


Figure 2.3: Timeline of soft pneumatic actuator applications (1990-2022). The progression demonstrates diversification across three decades, spanning medical devices, gripping mechanisms, and biomimetic locomotion systems. (1) Multi-fingered robot hand. Reproduced with permission (Suzumori et al., 1991c). Copyright 1991, IEEE. (2) Soft manta swimming robot. Reproduced with permission (Suzumori et al., 2007). Copyright 2007, IEEE. (3) Multigait soft robot. Reproduced with permission (Tolley et al., 2014). Copyright 2011, Mary Ann Liebert. (4) Soft pneumatic glove. Reproduced with permission (Polygerinos et al., 2013). Copyright 2013, IEEE. (5) Soft wearable robotic device. Reproduced with permission (Park et al., 2014a). Copyright 2014, IEEE. (6) Soft robot heart assist device. Reproduced with permission (Roche et al., 2017). Copyright 2017, AAAS. (7) Fully soft ‘octobot’ robot. Reproduced with permission (Wehner et al., 2016). Copyright 2016, Springer Nature. (8) Ultragentle soft gripper. Reproduced with permission (Sinatra et al., 2019). Copyright 2019, AAAS. (9) Recycled soft gripper. Reproduced with permission (Partridge et al., 2022). Copyright 2022, IEEE.

working principle based on a bending pneumatic soft actuator. Furthermore, the possibility of using the tool in vivo was experimentally verified (Watanabe et al., 2007).

From a commercial and industrial perspective, a few companies have successfully translated this technology into products. For example, *Schmalz Group* offers soft grippers under the *mGrip* product line for hygienic and adaptive gripping in food handling and packaging (Schmalz UK Inc). Additionally, *Festo* provides soft grippers designed for applications where safe human-machine contact is essential, such as the *Bionic Handling Assistant* (Festo Ltd). However, real-world adoption of soft robotics remains largely limited to soft grippers. The fabrication of soft actuators is often complex and time-consuming. Combined with the lack of standardised manufacturing processes and the challenges of multimaterial integration with existing fabrication methods, these are key factors that hinder widespread commercialisation and technological advancement in soft robotics (Schmitt et al., 2018). Thus, simplifying the fabrication process is essential for scaling up production and enabling the transition of soft robotic technologies from research settings to real-world applications (Amiri Moghadam et al., 2018). This underscores the significance of the present research and motivates the following section. The next section evaluates existing fabrication techniques, identifies their limitations, and establishes the aim of this research to support the broader adoption of soft pneumatic actuator devices.

2.3 Fabrication Techniques for Soft Pneumatic Actuators

Despite recent efforts to integrate soft mechanisms into real-world applications, new fabrication methods and tools are still needed to harness the full potential of soft robots in domains such as medicine, wearables and space exploration (Yin et al., 2024; Zhang et al., 2022; Stella and Hughes, 2023). According to De Greef et al. (2009), both surgeons and engineers emphasise the need for soft surgical robots that overcome the limitations of conventional rigid tools. Although current soft robot fabrication methods form the foundation for soft robot development, they remain insufficient for rapid design iteration and scalable production (Zhang et al., 2022). Existing techniques are often complex, time-consuming and labour intensive, which hinders their widespread adoption (Yap et al., 2020).

The choice of fabrication technique significantly influences the mechanical performance, structural precision, and functional integration of soft pneumatic actuators (Ranzani et al., 2018). Moulding and casting remain widely used because of their accessibility and compatibility with soft elastomers, but are inherently limited by their time-consuming multistep nature. For example, Marchese et al. (2015a) presented a pleated-channel actuator using a lost wax casting process to enable seamless, complex internal geometries. Although this approach allows robust delamination under high pressures and allows arbitrary channel shapes, it involves an eight-step procedure, making the fabrication process labour intensive and complex (Marchese et al., 2015a). Moreover, any design modification requires the fabrication of a new mould, which restricts rapid prototyping and slows the exploration of the actuator design space.

On the other hand, 3D printing offers greater speed and geometric freedom, making it well-suited for rapid prototyping and accelerating design optimisation. For example, Ge et al. (2018) a micro soft pneumatic gripper with a wall thickness of 0.2 mm and 0.4 mm wide square air channels, which was printed in less than 30 minutes using a Digital Light Processing (DLP) 3D printer, highlighting the speed and precision achievable with 3D printing technology (Ge et al., 2018; Zolfagharian et al., 2020). However, current printable soft materials exhibit lower strain capabilities compared to moulded silicone rubbers, thus restricting their use in high-strain applications where large deformations are critical (Petersen and Shepherd, 2019). Although Manns et al. (2018) demonstrated a PneuNet actuator fabricated using PolyJet technology to fabricate actuators with silicone-like materials that matched the performance characteristics of actuators developed by Polygerinos et al. (2013), the printed actuators still present limitations. From the author's

point of view, 3D printed actuators exhibit shortcomings in durability and efficiency. A primary issue is the incomplete dissolution of the support material, which adds weight, reduces flexibility, and impairs functionality. Such constraints limit the wider adoption and design flexibility needed for more advanced actuator geometries. Therefore, the following subsections examine three primary fabrication strategies: moulding and casting, 3D printing, and planar fabrication, to identify limitations, discuss recent advances, and highlight gaps that motivate the need for alternative methods such as the FlexiLayer approach introduced in this thesis.

Fig. 2.4 compares three primary fabrication approaches for soft pneumatic actuators: moulding, 3D printing, and planar methods. Each technique follows distinct process flows with unique advantages and limitations. The moulding techniques (a) involve the design and fabrication of moulds, the assembly of multipart components, the pouring of liquid elastomers, and the post-processing steps. 3D printing approaches (b) enable direct fabrication from digital designs using methods such as Fused Deposition Modelling (FDM) and Stereolithography (SLA), followed by support removal. Planar fabrication methods (c) use a layer-by-layer approach with patterned and unpatterned materials, precise alignment and bonding, and final definition through laser cutting. These different manufacturing methods directly affect the shapes that can be made, the materials that can be used, and the soft actuators work.

2.3.1 Moulding and Casting Methods

Moulding techniques represent a fundamental approach to the fabrication of soft pneumatic bending actuators (Luo et al., 2021). This fabrication technique evolved to address various challenges in soft actuator fabrication. Initial developments focused on basic casting methods. This involves pouring elastomer materials into prepared moulds and allowing them to cure into the desired shape. Early developments focused on fibre-reinforced bending actuator designs that required complex manufacturing steps to integrate reinforcement materials (Suzumori et al., 1991b; Suzumori et al., 1991c; Suzumori et al., 1992).

The concept of elastic anisotropy enabled precise control of bending motion through simpler manufacturing methods. Suzumori et al. (1997) demonstrated that basic extrusion moulding could create effective actuators without fibre reinforcement. The design used an asymmetric cross section to generate directional bending while preventing unwanted radial expansion. This approach simplified manufacturing by controlling bending motion through geometric design instead of complex material layering.

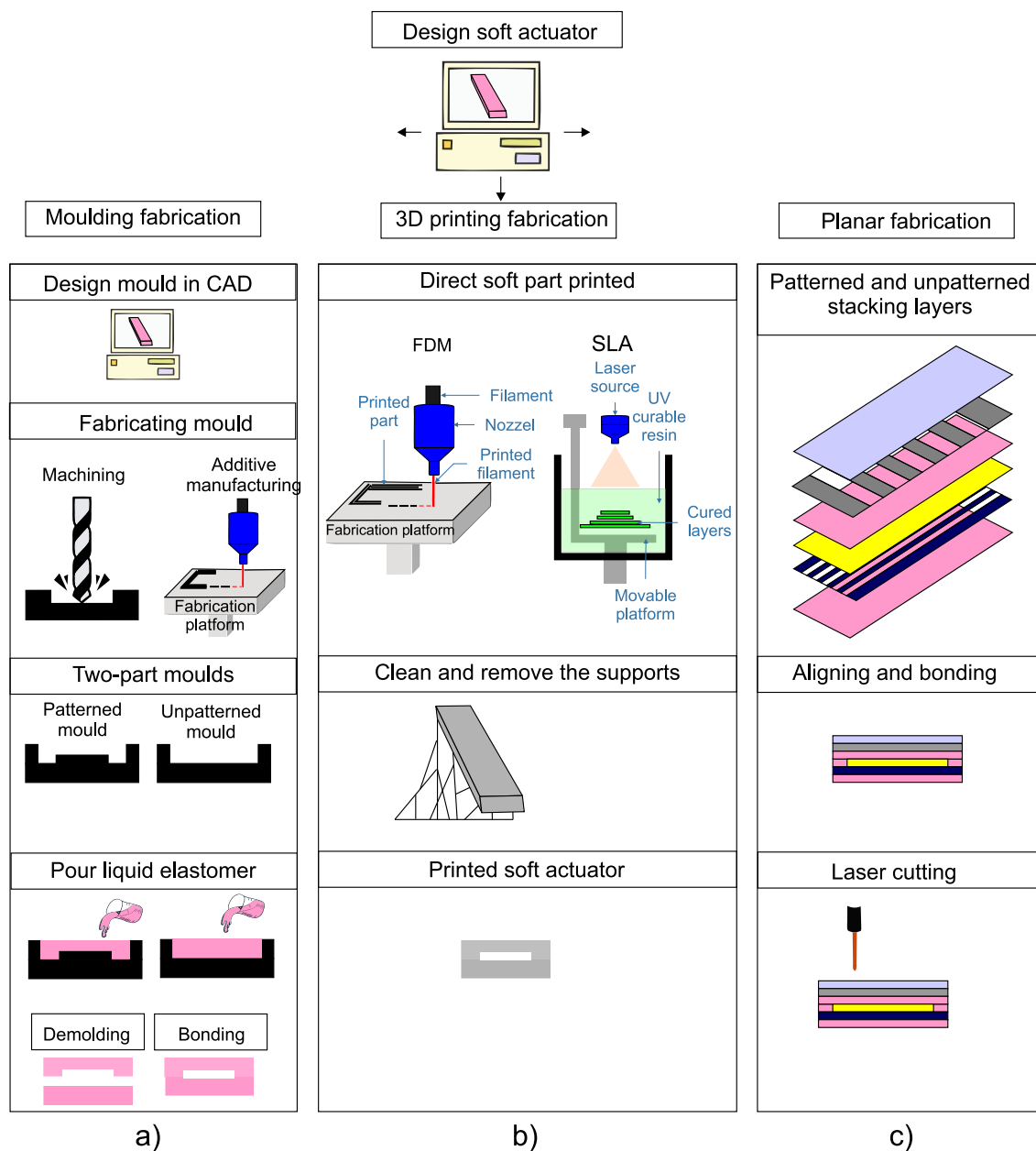


Figure 2.4: Comparison of soft pneumatic actuator fabrication techniques. (a) Moulding process involving mould design, fabrication, assembly, elastomer pouring and post-processing. (b) 3D printing approaches including FDM and SLA with support removal. (c) Planar fabrication method featuring layer stacking, alignment, bonding and laser cutting.

Building on these early advances, researchers explored microscale fabrication for greater precision and miniaturisation. Wakimoto et al. (2009) achieved bidirectional bending motion in rubber structures with a 1 mm radius using micro-casting processes. This approach addressed the complexity in the fabrication of fibre-reinforced actuators proposed by Suzumori et al. (1991b).

To further enhance miniaturisation, Micro-electro-mechanical systems (MEMS) technology was adopted. For example, Jeong et al. (2005) demonstrated PDMS-based microfingers

that achieved bending angles of 20-80 degrees at a pressure of 50 kPa. However, delamination occurred at higher pressures (100 kPa), indicating limitations in the material bond interface. Wakimoto et al. (2009) addressed this using plasma oxidation and excimer light treatment to enhance adhesion between layers. Despite this, plasma oxidation of PDMS films with large bonding area and multiple layers is considered a difficult task (Unger et al., 2000), attributed to the difficulty in achieving a reliable transfer method and efficient handling time to realise a strong bonding process (Konishi et al., 2006).

However, this issue was improved using the soft lithography manufacturing process to overcome the weak interface bonding strength between PDMS layers. For example Konishi et al. (2006) develop pneumatic micro hand-based PDMS. As the strength of the interface, using this approach, equals the strength of the bulk elastomer (Unger et al., 2000).

Despite advances in moulding techniques, significant limitations persist in the fabrication of pneumatic soft actuators and robots. The process is time-consuming, involves multiple steps of casting and assembly, and is challenging for complex structures (Luo et al., 2021). These constraints have driven the exploration of alternative methods, such as 3D printing technology.

2.3.2 3D Printing Approaches

3D printing technology has transformed the fabrication of soft robots by accelerating production times, enhancing precision, and ensuring manufacturing consistency (Gonzalez et al., 2022). This advancement enables the creation of more sophisticated pneumatic actuators with improved bending capabilities (Ang and Yeow, 2017). The evolution of Additive Manufacturing (AM) methods has expanded the available fabrication approaches to include FDM (Herianto et al., 2019), polyjet printing (Dämmer et al., 2019), and DLP (Zhang et al., 2021). Additional techniques such as immersion-based SLA (Xavier et al., 2021), Direct Ink Writing (DIW) (Wang et al., 2022a), and inkjet-based printing (You et al., 2024) have further diversified the manufacturing options. These developments have broadened the applications of soft robotic devices while simplifying customisation and production processes (Xin et al., 2023).

Current 3D printable materials for soft actuators primarily include thermoplastic polymers and Ultraviolet (UV)-curable polymers (Xin et al., 2023). SLA and DLP methods utilise UV light or lasers to solidify photocurable resins (Xin et al., 2023), though these UV-curable elastomers exhibit significant limitations compared to silicone rubbers, with a maximum elongation at break of only 170-220% (Patel et al., 2017). For example,

Xavier et al. (2021) demonstrated direct 3D printing of an omnidirectional soft pneumatic actuator using SLA printing technology with elastic resin (Formlabs, USA), offering strain breaking of 100% (uncured) or 160% (post-cured) (Xavier et al., 2021). In addition, Zhang et al. (2019) demonstrated a 3D-printed miniature pneumatic actuator using DLP printing technology with TangoPlus (a commercial UV-curable elastomer), achieving 140% strain breaking (Zhang et al., 2019). Furthermore, Peele et al. (2015), using the same printing technology, enabled a 3D-printed soft pneumatic actuator with multiple degrees of freedom using a commercial photocurable elastomer (Spot-E resin) that achieved only 40% strain breaking (Peele et al., 2015).

While FDM with Thermoplastic Polyurethane (TPU) filaments enables the production of finger-inspired soft grippers, conventional FDM demonstrates marginal compatibility with soft materials (Georgopoulou et al., 2021). For example, Xavier et al. (2021) used FDM printing technology to print an omnidirectional soft actuator using commercial NinjaFlex filament, which can achieve strain break up to 660%. However, careful control of the printing parameters is required with FDM to avoid air gaps between the printed layers (Xavier et al., 2021). Moreover, a novel UV-curable elastomer system developed by Patel et al. (2017) demonstrated remarkable stretchability up to 1100% elongation before failure (Patel et al., 2017). Although this value is competitive with that of the most stretchable silicone rubbers, it is inherently tied to custom formulations and specific DLP printing conditions, limiting reproducibility and accessibility for broader adoption in soft robotics. Consequently, moulded silicone rubbers such as Elastosil M4601 remain preferable for applications requiring reliable high stretchability and ease of processing. The aforementioned 3D printing technologies highlight significant limitations in material performance. As Petersen and Shepherd (2019) point out, despite technological advances in 3D printing, substantial limitations persist in the manufacturing of soft actuators, as most printable materials remain too brittle and unsuitable for high-stretch applications compared to moulded rubbers (Petersen and Shepherd, 2019).

Soft pneumatic actuators manufactured with direct 3D printing technology require careful consideration of printing parameters, such as layer height, infill density, and printing speed (Gonzalez et al., 2022). Yap et al. (2020), reviewed how various 3D printing methods were used for soft robots, including extrusion-based, direct printing, photopolymer resin-based, polymer powder-based printing, and multimaterial strategies (Yap et al., 2020). For example, Gonzalez et al. (2022) used FDM to 3D print a bellow pneumatic actuator with a sine wave-like shape, obtaining bending deformation behaviour (Gonzalez et al.,

2022). Keong and Hua (2018) utilised FDM with Ninjaflex filament (shore hardness 85 A) to create a robotic gripper with four bending actuators capable of holding an object weighing approximately 1 kg at 175 kPa (Keong and Hua, 2018). However, AL-Hasni and Santori (2020) noted that FDM has a significant drawback due to the inherent porosity of printed structures, increasing the likelihood of leaks in pneumatically driven soft actuators (AL-Hasni and Santori, 2020). Multiple multimaterials can be printed; for example Herianto et al. (2024) employed a multimaterial approach using eFlex and elastic filaments, stopping the printing process to change materials (Herianto et al., 2024). However, the author reported that this interruption creates challenges as inspection reveals small gaps between the bottom and upper layers (Herianto et al., 2024), and Yin et al. (2018) complements this observation claiming that the interruption of the process results in weak interfacial bonds between different materials (Yin et al., 2018).

Although revolutionary in 3D printed soft actuators, they face some performance limitations (Xin et al., 2023). The layer-by-layer deposition process creates anisotropic mechanical properties that affect actuator behaviour (Blanco et al., 2024). For example, evidence indicates that both print orientation and layer count significantly impact mechanical performance under external loads (Gonzalez et al., 2022). Studies by Gonzalez et al. (2019) demonstrated this effect, showing that samples printed parallel to the load direction (0° angle) achieve a strain at break of 9.31 mm/mm, while those printed perpendicularly (90° angle) reach only 5.11 mm/mm. Moreover, most commercially available 3D printing materials show insufficient stability when subjected to temperature fluctuations, leading to creep under load and decreased device repeatability (Xin et al., 2023). This contrasts with traditional moulded elastomers (for example, silicone rubber), which maintain elastic properties in environments down to -60 degrees Celsius (Shit and Shah, 2013; Sinatra et al., 2019).

2.3.3 Planar Fabrication Methods

Planar fabrication methods refer to a class of manufacturing techniques where soft robot devices or soft actuators are constructed in a flat, layer-by-layer manner on a two-dimensional substrate, enabling precise alignment (Ranzani et al., 2018), scalable production (Ou et al., 2016), and integration of multiple functional layers (Luo et al., 2021). While moulding is a common fabrication technique for pneumatic soft actuators (Marchese et al., 2015b), the entire production process for soft robots is time intensive due to the numerous steps involved (e.g. casting, degassing, addition of fibre / fabric, demoulding and bonding

parts) (Amiri Moghadam et al., 2018). Although 3D printing technology allows for the direct fabrication of soft actuators with complex chamber geometry, its application is limited by the need for specialised materials and high costs (Luo et al., 2021).

Recent evidence suggests that two-dimensional planar fabrication processes have emerged as an alternative manufacturing method (Park et al., 2014b). This method allows for both compact 2D configuration design and simplified manufacturing steps (Wirekoh and Park, 2017). Layer-by-layer methods, employed by numerous researchers, have their origins in early techniques to create inflatable structures using inextensible materials such as thermoplastic film (You et al., 2024). For example, Ou et al. (2016) proposed a planar fabrication with the introduction of *aeroMorph*-based heat sealing method. In this research work, the heat sealing method uses TPU to create an inflatable structure (Ou et al., 2016), similar to the planar design concept of Peano fluidic actuators (Sanan et al., 2014; Veale et al., 2016). Furthermore, the Ou et al. (2016) approach can control bending behaviours in inextensible materials such as paper, plastics, and fabrics. Although the material library for this method is still somewhat limited, Ou et al. (2016) believes that it has great potential to be incorporated into roll-to-roll manufacturing² (Ou et al., 2016). Amiri Moghadam et al. (2018) introduced a thin soft actuator using TPU film, demonstrating a soft gripper and a device that mimics swimming motion. Through this method, thin actuators can be designed arbitrarily in 2D, fabricated with cutting and welding in a single step, using laser cutting machine without requiring complex moulds or assembly steps. With this rapid fabrication technique Amiri Moghadam et al. (2018) has successfully achieved various motions (e.g., bending, rotary, and linear) actuators (Amiri Moghadam et al., 2018).

Inspired by the concept of layer-by-layer assembly, Luo et al. (2021) have used a laser cutting and manual stacking process, facilitating the fabrication of soft pneumatic actuators with various actuation modes, such as bending, contraction, elongation, and twisting (Luo et al., 2021). The design of these actuators is composed of various materials, including low stretchable layers (e.g., double-coated adhesive tape) and non-stretchable (e.g., strain-limiting layers). Luo et al. (2021) demonstrated that the selective placement of these materials enables diverse actuation modes. Recently, You et al. (2024) have introduced a rapid and monolithic method to manufacture a multilayer pouch motor using inkjet and heat press. Inkjet-printed masking layers were used to facilitate selective bonding between

²Roll-to-Roll (R2R) technique adapts the film forming method (e.g., doctor blade coating) for high-volume production. It uses a flexible substrate, such as a large sheet, which is unwound from the roll to be coated or printed. This approach enables rapid and economical manufacturing (Krebs, 2009; Goodship et al., 2016).

plastic layers (e.g., low-density polyethylene film), resulting in the successful demonstration of pouch robots with independent multidegree-of-freedom actuators (You et al., 2024).

The materials used in the fabrication mentioned above are limited to flexible-inextensible materials with inherent low extension (You et al., 2024), and limited to commercially available sheets (Petersen and Shepherd, 2019). For example, Amiri Moghadam et al. (2018) obtained a maximum strain of 30%. As You et al. (2024) pointed out, the inextensible film used in the study had poor elastic performance. This is significantly lower than the strain exhibited by silicone elastomers used in soft pneumatic actuators, such as the Smooth-On Ecoflex series (Marechal et al., 2021). Furthermore, You et al. (2024) found a hysteresis of 35% in their pouch bending actuator, which is significantly higher than that of silicone-based bending actuators You et al. (2024). The current fabrication methods reported by You et al. (2024), Amiri Moghadam et al. (2018), and Luo et al. (2021) have a central limitation of low force output due to the constraints (small strain level) of the materials used. This limitation restricts the application of soft robots (Russo et al., 2017).

Therefore, it is suggested to explore new fabrication methods that combine soft materials and inextensible materials to obtain effective force output (Russo et al., 2017). In line with this exploration, Allen and Swensen (2019) developed a soft pneumatic actuator using a layering fabrication method. The authors used fibre and polyester mesh fabric to bidirectionally constrain the expansion, achieving bending motion with a total thickness of 3.5-4.5 mm across the build layers. The authors identified two main limitations of this fabrication method. First, layer thickness could not be precisely controlled because measurements were possible only after complete curing. Second, the actuator experienced delamination between layers due to the excessive spread of the release mould, creating chambers that extended to the edge and resulted in air leakage during actuation (Allen and Swensen, 2019). Despite these limitations, Allen and Swensen (2019) demonstrated that their approach allowed batch fabrication of soft pneumatic actuators in large sheets. However, their method has required a new 3D printed mould for each change in soft actuator geometry design, which has limited manufacturing flexibility (Allen and Swensen, 2019).

Park et al. (2014b) introduced contraction soft artificial muscles using simple manufacturing steps through a 2D configuration design concept. A significant contribution of this work was the proposal of a zero-volume air chamber less than 0.1 mm, created via two different fabrication processes involving both negative and positive masks. In the first process, similar to that of (Allen and Swensen, 2019), a release mould was sprayed to

form the chamber. In the second process, a mask film was used to create a thin adhesive layer via spin coating, which assisted in bonding the two cured parts. Although Park et al. (2014b) demonstrated serial and parallel configurations of multiple muscle cells to obtain a high output force, the geometry of the actuator was still restricted to the dimensions of the actuator mould. This limitation hindered flexible exploration of the design space. (Wirekoh and Park, 2017) pointed out that a prominent failure mode at the edge of the cavity of the actuator of the developed flat soft pneumatic actuator demonstrated by Park et al. (2014b) was due to the stress concentration at the edge of the chamber during inflation. Consequently, Wirekoh and Park (2017) proposed a new fabrication method using a water-soluble mask (Paper Solvy, Sulky) as a release film, which allows the building of layers on the uncured layer (for example, Dragon Skin 10, Smooth-On). This type of mask film allowed for the creation of a customised and controlled chamber geometry after curing the assembled parts.

An alternative approach proposed by (Tinsley and Harris, 2020) is based on a layered fabrication method using a maskless concept to create a bending pneumatic actuator. The author successfully demonstrated the selective creation of bonding areas between two different types of material; extensible (e.g., Ecoflex 00-50) and inextensible (e.g., polyethylene terephthalate (PET)). This was achieved through plasma laser treatment, which selectively modified the surface chemistry of the two materials. However, Tinsley and Harris (2020) claimed that unequal inflation behaviour occurred in the large actuator fabricated due to variations in the bonding approach and the large dimensions of the actuator ($2 \times 60 \times 150$ mm thickness \times width \times length respectively). Existing fabrication methods still lack consistency and reliability in the production of soft robots, due to intensive manual steps during manufacturing and the skilled personnel required to produce these functional devices. Failure of the elastomer substrate suggested a high bond between layers. Furthermore, they pointed out that the use of this method resulted in an uneven width (19.8-20.4 mm) of the chamber along its length due to variations in the bond area and may produce undesirable deformation behaviour (Tinsley and Harris, 2020).

Similarly, Ranzani et al. (2018) and Wehner et al. (2016) showed the significant capability of using the layer-by-layer approach to fabricate soft robot devices. For example, Wehner et al. (2016) introduced an embedded 3D printing technique to fabricate a fully soft robot (“Octobot”), embedding fugitive and catalytic inks into an uncured matrix to create internal pneumatic networks. The final form of this method achieved complex architectures, but it depends on precisely tuned ink rheology, embedded print resolution,

and thermal evacuation steps (Wehner et al., 2016). These requirements significantly limit material compatibility and scalability, as the matrix must be soft and self-healing, and the fugitive inks must match the matrix's thermal and chemical behaviour. Furthermore, Ranzani et al. (2018) presented a multilayer soft lithography approach to fabricate a 12-layer spider-like soft robot. The method involved creating patterned silicon wafers, laser micromachining, and oxygen plasma surface modification to achieve bonding between layers (Ranzani et al., 2018). This method is effective in constructing hierarchical designs, but the technique required manual alignment at each stacking step and relied heavily on clean-room level processes and equipment. The use of oxygen plasma bonding introduced strict time constraints and equipment requirements, making the process labour intensive and difficult to scale (Konishi et al., 2005; Unger et al., 2000).

In support of this method, Sinatra et al. (2018) produced a soft nanofibre on a small scale using a layering approach. Interestingly, they mentioned using film applicator to deposit a controlled film thickness in microns (e.g., 300 microns). In addition, Sinatra et al. (2019) scaled the size of this actuator concept to be implemented as a soft gripper used in the marine environment to generate a very low contact force with jellyfish. However, the fabricated soft bending actuator by Sinatra et al. (2019) method retained dependence on mould-based features. The role of using a film applicator was to produce an uncured thin film that bonds to already patterned, cured parts (Sinatra et al., 2019). As a result, the potential to exploit film applicators for scalable or planar fabrication remained limited. In contrast, the FlexiLayer method introduced in this research integrates doctor blade coating (e.g., film applicator) and mask-layer patterning to enable batch fabrication. This method supports the simultaneous fabrication of multiple actuators, demonstrating scalability not shown in previous work. Furthermore, Atalay et al. (2017) demonstrated the fabrication of soft sensor-based fabric. This work highlighted the ability to fabricate a batch of sensors with the assistance of a film applicator while customising the shapes using laser cutting, but did not address the limitations related to alignment or layer integration for actuation applications (Atalay et al., 2017).

The research work of Atalay et al. (2017) and Sinatra et al. (2019) demonstrates the potential of combining film application and laser cutting techniques for soft robot fabrication. This combination offers promising capabilities for achieving precise layer control and geometric definition in planar soft robotic structures. The integration of these established manufacturing processes suggests opportunities for developing precise approaches to fabricating thin, planar soft pneumatic actuators. The planar fabrication

methods discussed above demonstrate promising approaches for creating thin, flexible soft robots. However, these planar methods demonstrate potential for building thin, flexible actuators, but they face several limitations: (1) dependence on precise manual alignment between layers, (2) reliance on surface modification steps such as oxygen plasma treatment, (3) limited compatibility with high-performance elastomers, and (4) process complexity and high operator dependency. These factors constrain reproducibility, design flexibility, and accessibility for broader adoption. In addition, the reliance on manual manufacturing steps and the requirement for skilled personnel result in inconsistent and unreliable production processes (Fras and Althoefer, 2019). These limitations, combined with restricted material options and force output capabilities, highlight the need for more robust and accessible fabrication techniques that can expand the practical applications of soft robots.

To address these limitations, this thesis introduces the FlexiLayer fabrication technique. This method combines micrometer-controlled doctor blade coating for uniform silicone deposition with laser-cut dissolvable masks (e.g., Super Solvy) to define cavity shapes. The masks are integrated directly into the fabrication stack, eliminating the need to align separate pre-patterned moulds. Silicone layers bond naturally during partial curing or through controlled curing sequences, avoiding plasma treatment or manual alignment of patterned parts. This reduces fabrication complexity, improves reproducibility, and broadens material compatibility. As such, FlexiLayer provides a scalable and accessible approach for fabricating planar soft actuators with customisable mechanical properties and geometries.

2.4 Summary of the Current State of the Art

The review reveals three key fabrication approaches for soft pneumatic actuators: traditional moulding, 3D printing, and emerging planar techniques. Although moulding methods offer superior material properties and reliability, they involve time-intensive multistep processes that limit design flexibility and scalability. 3D printing technologies enable rapid prototyping and complex geometries but face significant limitations in material selection, with most printable materials exhibiting insufficient elasticity compared to silicone rubbers. Planar fabrication techniques represent a promising direction offering potential advantages in manufacturing simplicity and design flexibility. However, current planar methods predominantly use inextensible materials with limited strain capabilities (typically less than 30%), significantly constraining actuator performance. Although some researchers have demonstrated successful integration of soft materials in planar fabrication, challenges

remain in achieving precise layer thickness control and consistent alignment between layers. The review identifies several critical gaps in current fabrication approaches:

1. The need for precise control over layer thickness in multi-layer soft structures.
2. Challenges in achieving reliable alignment and bonding between layers.
3. Limited material options that combine high elasticity with manufacturing compatibility.
4. Lack of repeatable manufacturing processes that can consistently produce thin planar soft actuators at scale.

These findings suggest an opportunity to develop new fabrication techniques that combine the material advantages of silicone elastomers with the manufacturing efficiency of planar approaches. Such techniques should focus on achieving precise dimensional control while maintaining process simplicity and reliability.

Chapter 3

FlexiLayer Concept and Preliminary FEM

3.1 Introduction

Chapter 3 describes the FlexiLayer fabrication concept, a novel layer-by-layer approach to create PneuThin soft actuators, and evaluates its feasibility using FEM simulation. The investigation follows two main methods. First, a qualitative analysis examines the fundamental relationships between geometric parameters and bending deformation. This includes studying various cavity shapes (rectangular, oval, and triangular) and their impact on actuator performance. Second, a quantitative analysis evaluates stress distribution patterns and bending deformation to identify critical process and geometry parameters that require precise control during PneuThin fabrication.

Primary Objectives

The primary objectives of this chapter are:

1. Confirm the feasibility of creating bending actuators using the layer-by-layer FlexiLayer approach.
2. Determine key geometric and process parameters that influence actuator performance and require precise control during fabrication.

The chapter begins by introducing the FlexiLayer fabrication concept and its key principles. Then, it outlines the soft material requirements for this approach and presents the selection process for an appropriate silicone elastomer. The actuator design is then

described before the FEM modelling and results. The findings of this analysis guide the development of specific fabrication methods detailed in Chapter 4.

3.2 FlexiLayer Concept and Soft Material Selection

3.2.1 Concept

This research presents the original development of a novel fabrication protocol, termed FlexiLayer, described in Chapter 4. FlexiLayer method introduces a versatile and scalable approach for creating pneumatic thin soft robotic devices by constructing two-dimensional elastomer layers that are precisely patterned, coated, aligned, and bonded to form the final structure. This planar fabrication strategy offers simplified alignment, faster prototyping, and is particularly suited for soft actuators with compact or low-profile geometries. Fig. 3.1 illustrates the FlexiLayer concept; layer-by-layer material stacking on a substrate, where each layer serves a distinct function. Key functional layers, such as actuation, sensing, and stiffness elements, are highlighted. This simple yet effective fabrication method yields complex, multifunctional devices. To enable this, this research uses three key characteristics of the FlexiLayer; (1) precise deposition of thin elastomer layers using doctor blade coating¹ for controlled thickness; (2) selective alignment of functional layers within the elastomer layers; and (3) laser cutting to release the final functional soft robot structure. This research focusses specifically on the actuation and stiffness elements of the FlexiLayer technique as an initial step in validating the effectiveness of this proposed fabrication method. To demonstrate the feasibility of this approach, a pneumatic thin soft actuator 'PneuThin' was designed. The PneuThin actuators developed in this research are characterised by; (1) thin films of silicone elastomer that comprise the main structure body; (2) zero-volume air chambers with cavity thicknesses of sub-0.1 mm (Park et al., 2014a); (3) a 2D planar configuration for compact design and integration of multifunctional layers (Wirekoh and Park, 2017); (4) integration of strain limiting layers when necessary, improving bending control and force output (Galloway et al., 2013); and (5) simple, safe, and low-cost pneumatic actuation (Zhang et al., 2023).

Although the concept of zero-volume air chambers was previously introduced by Park et al. (2014a), their fabrication method relied on silicone moulding and spin coating, combined with manual masking and multistep layer lamination of cured layers. These steps require multiple curing or bonding phases and increase fabrication time, which limits scalability

¹Doctor blade coating is a deposition technique in which a thin, uniform layer of liquid material is spread onto a substrate using a blade (Goodship et al., 2016)

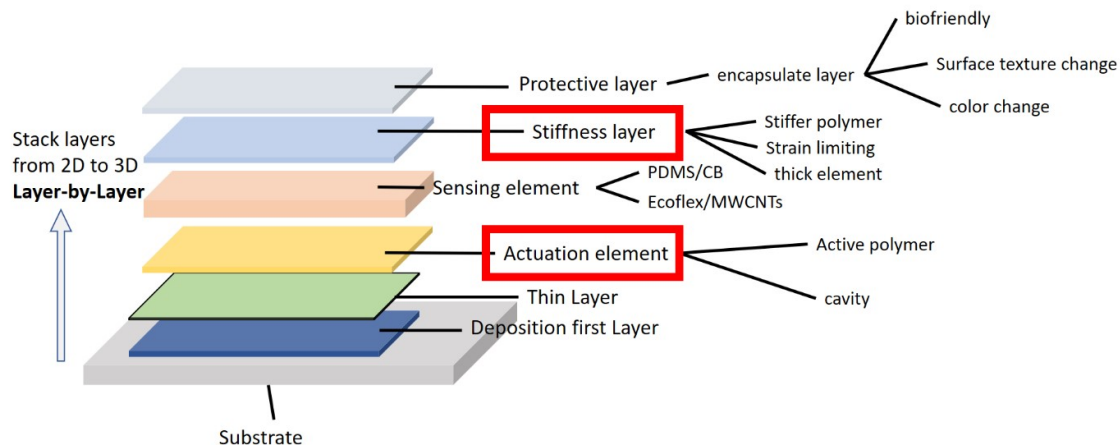


Figure 3.1: Schematic representation of the FlexiLayer fabrication concept, showing the layer-by-layer stacking process. This research focuses specifically on the actuation element and stiffness layer (highlighted in red boxes) for developing PneuThin.

and reproducibility, and increases operator dependency. In contrast, the FlexiLayer method eliminates the need for physical moulds by using laser-cut dissolvable mask layers placed directly onto uncured or partially cured elastomer films. This enables cavity formation without the need for alignment between separately patterned parts. Furthermore, the use of a micrometer-controlled doctor blade provides consistent film thickness and the entire fabrication process supports batch production with minimal equipment, as demonstrated in Chapter 4 and validated in Chapter 5. These factors distinguish FlexiLayer as a simpler, scalable, and accessible alternative to existing layer-by-layer fabrication techniques.

3.2.2 Soft Material Selection for FlexiLayer

The development of the FlexiLayer fabrication method requires careful selection of soft materials to ensure compatibility with the layer-by-layer process and achieve reliable fabrication results. As described in Section 3.2.1, FlexiLayer involves the precise deposition of thin elastomer layers using Doctor blade coating to create multilayered structures with various functional components. To achieve this, the selected material must meet specific requirements, mainly related to viscosity and pot life². Viscosity plays a crucial role in the Doctor Blade coating technique, influencing the quality and reproducibility of each deposited layer. An optimal viscosity range (1,000-10,000 mPa.s) ensures uniform layer formation and thickness control, fundamental to achieve consistent mechanical properties in the final soft robotic device (Goodship et al., 2016). The pot life, on the other hand,

²Pot life is the time before a material's viscosity doubles, after which processing becomes difficult (Gubbels, 2024).

Table 3.1: Processing parameters of common elastomer silicone rubbers used in soft robotics

Material	Viscosity (mPa.s)	Pot Life (min)	Reference
ELASTOSIL® M 4601 A/B	10,000	90	[(AG, 2024)]
Ecoflex™ 00-10	14,000	30	[(Smooth-On Inc., 2024b)]
Ecoflex™ 00-30	3,000	45	[(Smooth-On Inc., 2024c)]
Ecoflex™ 00-50	8,000	18	[(Smooth-On Inc., 2024d)]
Mold Star™ 30	12,500	45	[(Smooth-On Inc., 2024e)]
Dragon Skin™ 30	20,000	45	[(Smooth-On Inc., 2024a)]

is vital for the layer-by-layer stacking process. A longer pot life allows sufficient working time between successive layers, enabling proper manipulation and positioning before curing. This is essential for complex planar structures that require multiple processing steps during fabrication. Table 3.1 compares popular elastomer silicone rubbers commonly used in soft robotics, highlighting their processing parameters. These materials represent potential candidates for FlexiLayer fabrication, each offering different processing characteristics that could influence the fabrication outcome. Based on these requirements, the ideal material should possess a viscosity within the optimal range for Doctor Blade coating (1,000-10,000 mPa.s), a pot life of at least 90 minutes to allow for complex layer-by-layer processing, and mechanical properties suitable for soft robotic applications, including adequate tensile strength, elongation at break, and hardness.

ELASTOSIL® M 4601 A/B was selected as the primary material to validate the FlexiLayer fabrication concept due to its excellent combination of processing and mechanical properties. Its viscosity of 10,000 mPa.s falls within the optimal range for Doctor Blade coating, ensuring reproducible film production and uniform layer thickness. In addition, its 90-minute pot life provides ample working time for reliable layer-by-layer processing, crucial for complex planar soft robotic structures. Furthermore, its mechanical properties, including a tensile strength of 6.5 N mm^{-2} , elongation at break 700%, and Shore A hardness of 28, make it a suitable choice for soft robotic applications (Wacker Chemie AG, 2024). ELASTOSIL® M 4601 A/B cures at room temperature in 12 hours; see Table 3.2. Importantly, its curing behaviour can be accelerated through heat application, offering flexibility in processing parameters while maintaining the integrity of the material (Hu et al., 2018). With ELASTOSIL® M 4601 A/B selected as the validation material, Section 3.3 presents the actuator design and geometric parameters that form the basis for the preliminary FEM modelling.

Table 3.2: Material properties of ELASTOSIL® M 4601 A/B (AG, 2024)

Property	Value	Unit
Density	1.13	g/cm^3
Mix Ratio A:B	9:1	by weight
Tensile Strength	6.5	N/mm^2
Elongation at Break	700	%
Shore A Hardness	28	-
Viscosity (after mixing)	10,000	mPa.s
Pot Life	90	min
Curing Time (at 23 °C)	12	hours

3.3 Actuator Design and Geometry Parameters Definitions

The PneuThin bending actuator design consists of a three-layer structure as shown in Fig. 3.2a. Two layers of elastomers with different thicknesses surround an internal cavity, similar to the configuration initially reported in (Fujiwara et al., 2009; Jeong and Konishi, 2006; Kusuda et al., 2007). This cavity forms from a mask layer placed between the elastomer layers. The design creates an eccentric void structure that generates directional bending when pressurised (Gorissen et al., 2017). During inflation, air enters through the inlet and fills the internal chamber. The asymmetric structure produces a differential strain (Suzumori et al., 1997). The thinner top layer deforms more than the thicker bottom layer. This creates a controlled bending motion without additional strain-limiting elements Fig. 3.2b. The PneuThin bending actuator has a total thickness (L_t) of 1 mm, with overall dimensions of 50 mm in length (L_o) and 5 mm in width (W). Its bending performance depends on key parameters; the width of the cavity (C_W) is the maximum lateral size of the internal chamber, the length of the cavity (C_L) is its longitudinal size, and the thickness ratio of the layer (L_r) is the ratio of thin to thick layers Fig. 3.2b. The applied pressure (P) acts as the pneumatic input for actuation, thus defining the level of deformation and bending. Table 3.3 summarises these dimensional parameters. Understanding how geometry parameters affect actuator performance helps regulate the bending response and reduce fabrication defects. This insight will guide the development of the FlexiLayer process in Chapter 4. The next section uses FEM modelling to examine the effect of these parameters.

Table 3.3: Design constraints for PneuThin bending actuator simulation model

Parameter	Value	Description
Dimensional Constraints		
Total Length (L_o)	50 mm	Overall actuator length
Cavity Length (C_L)	35 mm	Internal chamber length
Actuator Width (W)	5 mm	Total actuator width
Thickness Constraints		
Total Thickness (L_t)	1 mm	Overall thickness
Mask Layer	0.01 mm	Constant cavity height
Layer Sum ($l_1 + l_2$)	0.9 mm	Combined elastomer layers
Simulation Conditions		
Pressure Load	6 psi	Fixed operating pressure
Material	ELASTOSIL® M 4601 A/B	Selected elastomer
Material Model	Yeoh hyperelastic	Constitutive model

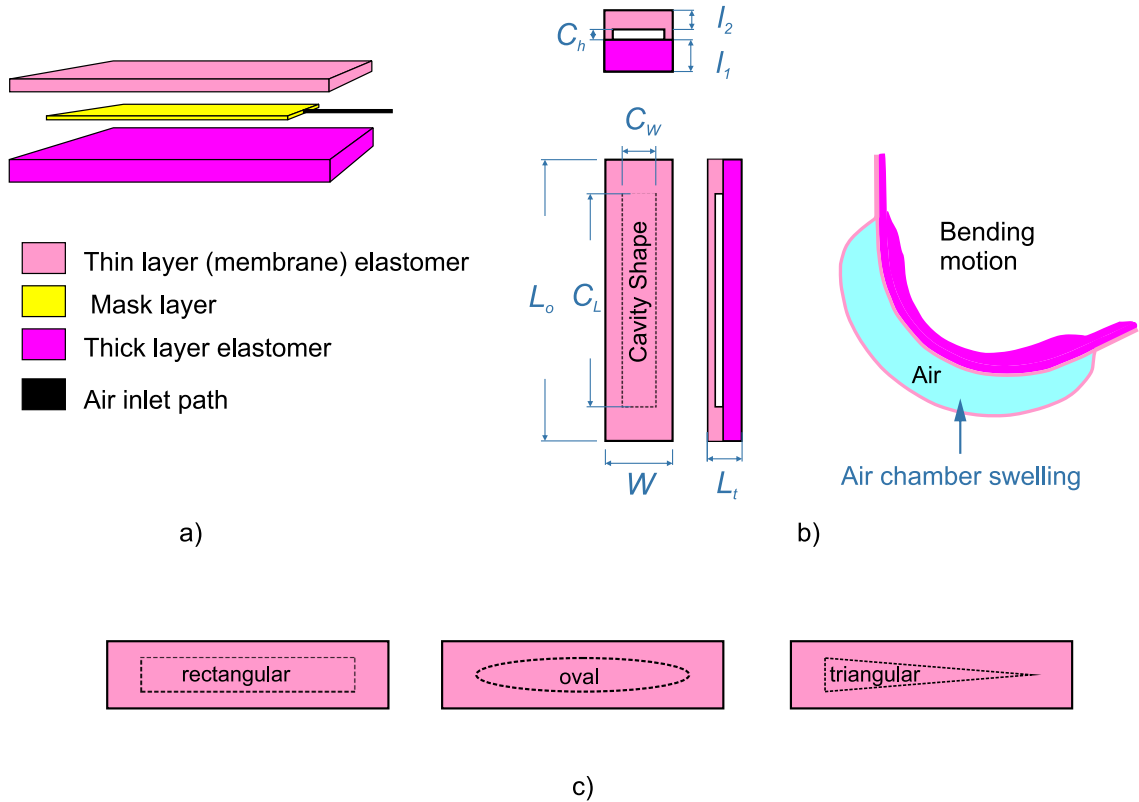


Figure 3.2: PneuThin design structure and parameters. (a) Schematic view showing the three-layer construction: thin elastomer membrane (top, pink), sacrificial mask layer (middle, yellow), and thick elastomer layer (bottom, magenta) with air inlet. (b) Geometric parameters of the PneuThin: cavity width (C_W), cavity length (C_L), total actuator length (L_o), width (W), thickness (L_t), and layer thicknesses (l_1 , l_2) with cavity height (C_h). The asymmetric layer configuration produces directional bending during inflation, as illustrated on the right. (c) Three cavity shape variants tested: rectangular (uniform width), oval (curved profile), and triangular (tapered width), each producing different bending deformation outcomes.

3.4 FEM Modelling

The investigation of the performance of PneuThin was carried out using qualitative and quantitative methods. The qualitative study initially examined the effect of geometric parameters on bending performance by investigating a rectangular cavity, which led to the exploration of other cavities such as oval and triangular Fig. 3.2c. The quantitative study assessed the stress distribution at the edges of the rectangular and oval cavities and measured the bending ability using curvature calculations.

3.4.1 Qualitative Bending Response Assessment

The bending response of PneuThin was examined through three cavities (rectangular, oval, and triangular) by systematically varying the thickness ratio ($L_r = \frac{t_2}{t_1}$) and the width of the cavity (C_w). This approach revealed fundamental relationships between geometry and deformation patterns. For rectangular cavities, a matrix study investigated 20 configurations combining five thickness ratios ($L_r = 1.0, 0.64, 0.38, 0.20,$ and 0.125) with four cavity widths ($C_w = 4, 3, 2,$ and 1 mm). The qualitative bending response results, presented in Section 3.5.1 and Fig. 3.7, demonstrated that configurations with $L_r = 0.38$ and 0.20 exhibited substantial and stable bending deformations. In contrast, lower thickness ratios (e.g., $L_r = 0.125$) showed extreme bending deformation associated with numerical convergence challenges, while higher thickness ratios (e.g., $L_r = 1.0$ and 0.64) exhibited minimal bending deformation. Therefore, $L_r = 0.38$ and 0.20 were selected for further examination with oval and triangular cavity shapes to systematically study the impact of cavity geometry on the bending deformation response. For oval cavities, eight configurations combined two thickness ratios ($L_r = 0.38$ and 0.20) with four cavity widths ($C_w = 1 - 4$ mm). For triangular cavities, only one configuration ($L_r = 0.38, C_w = 4$ mm) was examined due to computational convergence problems with ($L_r = 0.20$).

Despite its limited scope, this study offered crucial insights into the impact of cavity geometry on stress distribution and the pattern of bending deformation. The geometry parameters study are summarised in Table 3.4. Throughout all configurations, variables such as L_o (50 mm), W (5 mm), L_t (1 mm), and C_L (35 mm) remained fixed, facilitating a direct comparison. A pressure load of 6 psi was applied in all simulations to isolate the effects of geometric variations on deformation patterns; see Table 3.3.

Table 3.4: Geometric Parameters for Cavity Shape Investigation

Cavity Shape	Thickness Ratio (L_r)	Cavity Width (C_w , mm)	Number of Configurations
Rectangular	1.0, 0.64, 0.38, 0.20, 0.125	4, 3, 2, 1	20
Oval	0.38, 0.20	4, 3, 2, 1	8
Triangular	0.38	4	1

3.4.2 Quantitative Performance Analysis

A mesh sensitivity study preceded this analysis to ensure the reliability of the result (Pu et al., 2024). Four mesh densities were tested: coarse (102 elements), normal (336 elements), fine (1862 elements), and very fine (5852 elements). This test verified that the fine mesh density provided an optimal balance between accuracy and computational efficiency. The quantitative performance of PneuThin designs with different cavity shapes was examined by stress distribution and bending characteristics. Based on qualitative findings in which profound deformation of the bending was predicted, a thickness ratio (L_r) of 0.38 was selected to compare the rectangular and oval cavity configurations. The analysis focused on C_W (3 mm and 4 mm) under 6 psi pressure load. Key metrics included the von Mises stress distribution and maximum displacement. The performance of the bending actuator was quantified by measuring the curvature in multiple geometric configurations. The study examined two thickness ratios ($L_r = 0.38$ and 0.20) and C_W ranging from 1 to 4 mm for rectangular and oval shapes. A comparison was made between two techniques used to calculate the curvature; the Taubin method (Chernov, 2025; Taubin, 1991) and the three-point method (Auysakul et al., 2020). The initial verification used a rectangular

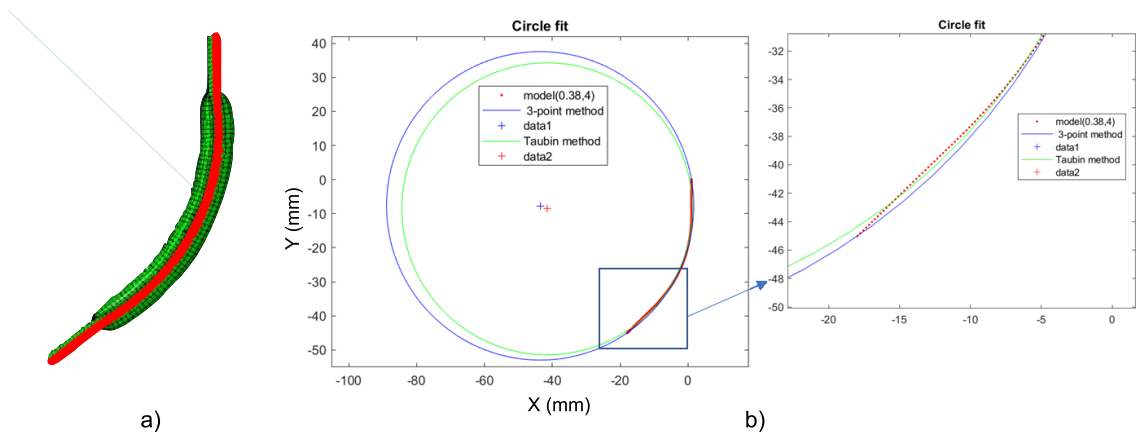


Figure 3.3: Curvature analysis of PneuThin ($L_r = 0.38$, $C_W = 4$ mm). (a) FEM model with extracted edge coordinates (red line) showing 150 sampling points (e.g., nodes), with coordinate system origin (0,0) at the proximal tip. (b) Quantitative comparison of curvature calculation methods showing circle fitting implementations (Taubin and three-point methods), with magnified view demonstrating computational convergence between approaches.

cavity configuration ($L_r = 0.38$, $C_W = 4$ mm).

The process of calculating the curvature was started by extracting the edge coordinates from the actuator side using results from the FEM software (ABAQUS 2022), as demonstrated in Fig. 3.3a. These coordinates, denoted as (X,Y), outlined the path of the deformed actuator line. Both circle fitting methods showed similar performance in approximating the curved profile of the actuator, as shown in Fig. 3.3b. The Taubin method was selected for all subsequent analyses due to its greater stability and computational efficiency. This method was implemented in MATLAB (MathWorks, R2021a, UK) using the code adapted from Chernov (2025). This method similar to the previous research by Shapiro et al. (2011).

3.4.3 Modelling Method

According to the simulation design methodology described in Sections 3.4.1 and 3.4.2, an initial FEM analysis (ABAQUS 2022) was used to understand how variations in geometry parameters would affect the bending performance of PneuThin. The FEM was chosen due to its ability to handle material and geometric nonlinearity during bending motion in a soft actuator (Tawk and Alici, 2020a). In addition, it has proven the capability to model hyperelastic materials and capture large deformation problems in soft actuators (Hu et al., 2018). The software also provides post-processing tools for analysing stress distributions and deformation patterns (Xavier et al., 2020). The modelling process integrated several key modules to investigate the qualitative and quantitative aspects of PneuThin performance as illustrated in Fig. 3.4.

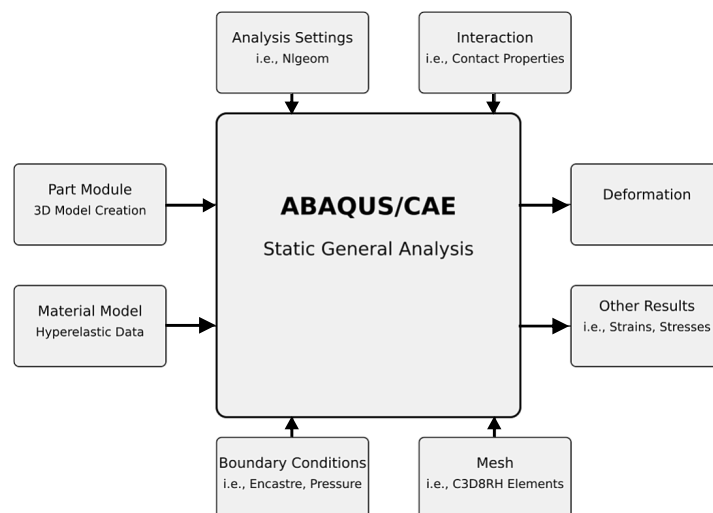


Figure 3.4: FEM simulations diagram for PneuThin soft actuators

Table 3.5: Yeoh hyperelastic material parameters for ELASTOSIL® M 4601

Parameter	Value	Unit
C_{01}	0.11	MPa
C_{02}	0.02	MPa
C_{03}	0	MPa

The PneuThin was modelled as a three-layer structure: two elastomer layers (L_1 and L_2) separated by cavity geometry, as shown in Fig. 3.5(a). The layers were assembled using face-to-face constraints and merged into a single part for the application of boundary conditions. This approach to FEM modelling is similar to the methodology employed in previous studies (Mosadegh et al., 2014; Polygerinos et al., 2013). Following the actuator design concept established in Section 3.3, this construction implements the eccentric void configuration to achieve controlled bending deformation through structural asymmetry (Gorissen et al., 2017). The Yeoh (1993b) hyperelastic material model was used to describe the behaviour of the selected silicone (ELASTOSIL® M 4601) (Polygerinos et al., 2015). The third-order strain energy density function of the Yeoh model is given by:

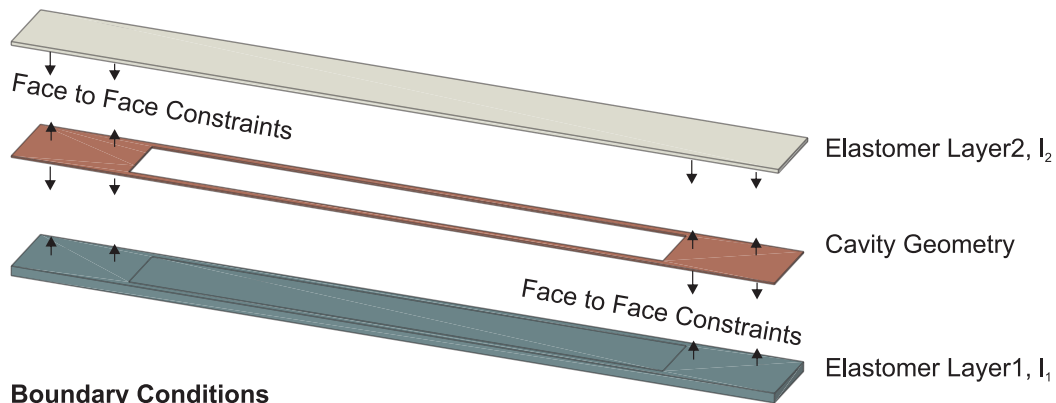
$$U = \sum_{i=1}^3 C_i (I_1 - 3)^i \quad (3.1)$$

where U represents the strain energy density, C_i are material constants, and I_1 is the first strain invariant. The material parameters for ELASTOSIL® M 4601 are summarised in Table 3.5, where the values of C_i were adopted from (Polygerinos et al., 2013; Mosadegh et al., 2014). The actuator was modelled as a cantilever beam configuration, with one end fixed while the opposite end remained free to move during actuation. A uniform pressure load of 6 psi was applied to all surfaces of the internal cavity, as illustrated in Fig. 3.5(b). For this preliminary analysis, gravitational effects were neglected, and large deformation analysis (NLGEOM³) was allowed to account for the significant geometric changes during actuation. The model used C3D20RH⁴ is particularly suitable to model incompressible hyperelastic materials (Moseley et al., 2016), hexahedral elements throughout the actuator body (Fig. 3.5(c)). For qualitative analysis (Section 3.4.1), a global element size of approximately 0.7 mm (fine mesh) was used. The edge nodes were specifically highlighted, as shown in Fig. 3.5(c), to extract the x-y coordinates of the actuator profile, which were subsequently used for the calculation of the curvature following the method described in Section 3.4.2

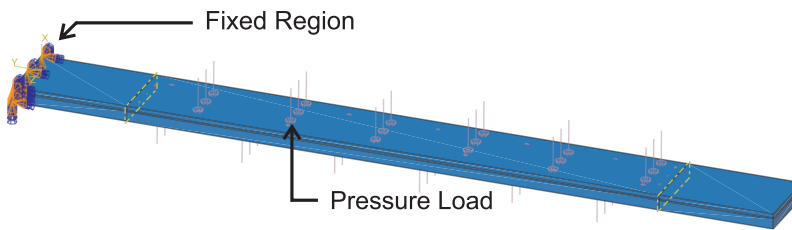
³NLGEOM is an ABAQUS parameter that accounts for geometric nonlinearity in the analysis.

⁴C3D20RH refers to a 20-node quadratic brick element with reduced integration and hybrid formulation.

a) 3D Model Creation



b) Boundary Conditions



c) Mesh Element Type

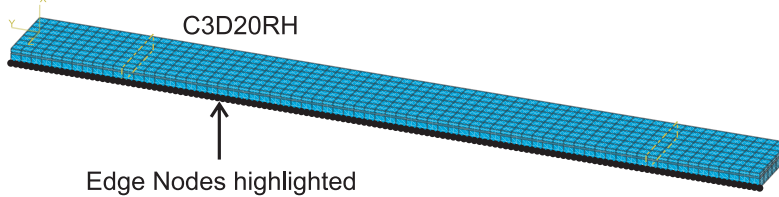


Figure 3.5: FEM model development: (a) 3D model construction showing layer assembly and face-to-face constraints, (b) boundary conditions and pressure load application, and (c) mesh configuration using C3D20RH elements with highlighted edge nodes.

3.5 Results

3.5.1 Qualitative Behaviour Analysis

a) Rectangular Cavity Investigation

The response to bending deformation of PneuThin with varying geometric parameters is shown in Fig. 3.7 and further quantified in Fig. 3.6. The PneuThin simulation indicates that there is no bending in all C_W for a symmetric L_r of 1, see Figs. 3.6 and 3.7. As L_r decreased, the bending deformation increased, with a larger $C_W = 4$ mm and 3 mm, producing a pronounced bending deformation. For example, a maximum curvature of 0.160 mm^{-1} was achieved with the combination of $L_r = 0.125$ and $C_W = 4$ mm, demonstrating that thinner upper layers produce significant bending deformation. It can be observed that at $L_r = 0.63$, the change in curvature in different C_W remains negligible, confirming the qualitative observations in Fig. 3.7. Moderate sensitivity emerges at $L_r = 0.38$, where the

curvature begins to differentiate between C_W . This sensitivity intensifies dramatically at $L_r = 0.2$ and 0.125 , where changes in C_W produce substantial differences in curvature, see Fig. 3.6. This indicates that both the thickness ratio and C_W significantly influence the actuator's deformation behaviour.

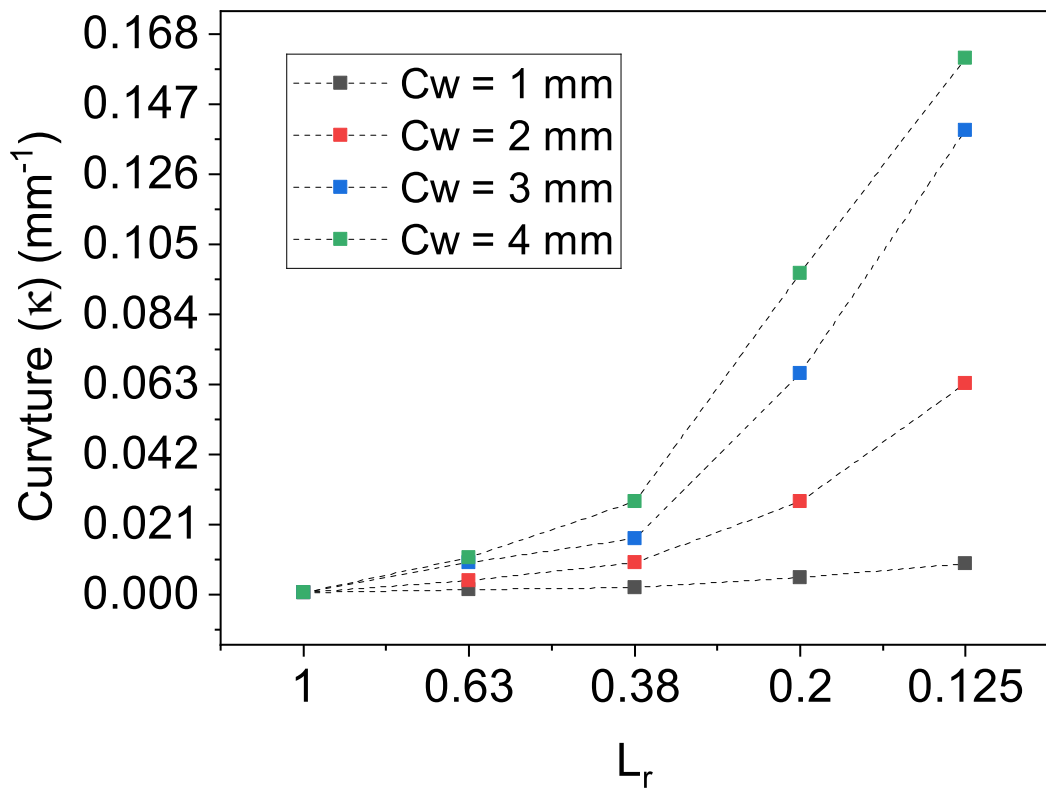


Figure 3.6: Relationship between L_r and curvature (κ) for different C_W for rectangular cavity configurations in PneuThin. Each data point represents FEM simulation results at 6 psi pressure load.

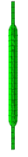
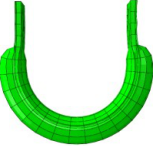
Actuator's design parameters	$C_w = 4 \text{ mm}$	$C_w = 3 \text{ mm}$	$C_w = 2 \text{ mm}$	$C_w = 1 \text{ mm}$
$L_r = 1$ $l_1 = 0.45 \text{ mm}$ $l_2 = 0.45 \text{ mm}$				
$L_r = 0.63$ $l_1 = 0.55 \text{ mm}$ $l_2 = 0.35 \text{ mm}$				
$L_r = 0.38$ $l_1 = 0.65 \text{ mm}$ $l_2 = 0.25 \text{ mm}$				
$L_r = 0.20$ $l_1 = 0.75 \text{ mm}$ $l_2 = 0.15 \text{ mm}$				
$L_r = 0.125$ $l_1 = 0.80 \text{ mm}$ $l_2 = 0.10 \text{ mm}$				

Figure 3.7: FEM simulation results showing deformation patterns for different geometric configurations of PneuThin. The matrix presents combinations of five (L_r) and four (C_w), all simulated under 6 psi pressure load.

b) Oval Cavity Investigation

Fig. 3.8 shows the result of the PneuThin simulation with oval cavity at L_r (0.38 and 0.20). The deformation patterns show that the configurations with $L_r = 0.20$ produced a larger deformation of the bending compared to $L_r = 0.38$, as illustrated in Fig. 3.8a. Variations in C_W demonstrated a moderate influence on the bending behaviour, as observed in configurations with $C_W = 4$ mm and $C_W = 3$ mm. Configurations with smaller $C_W = 2$ mm, 1 mm exhibited minimal bending deformation for both thickness ratios (see Appendix A Fig. A.1). The direct comparison between oval and rectangular cavities, presented in Fig. 3.8b, shows similar deformation trends for both cavities. This indicates that the layer thickness ratio has a more dominant effect on the bending behaviour than on the C_W in both cavity configurations.

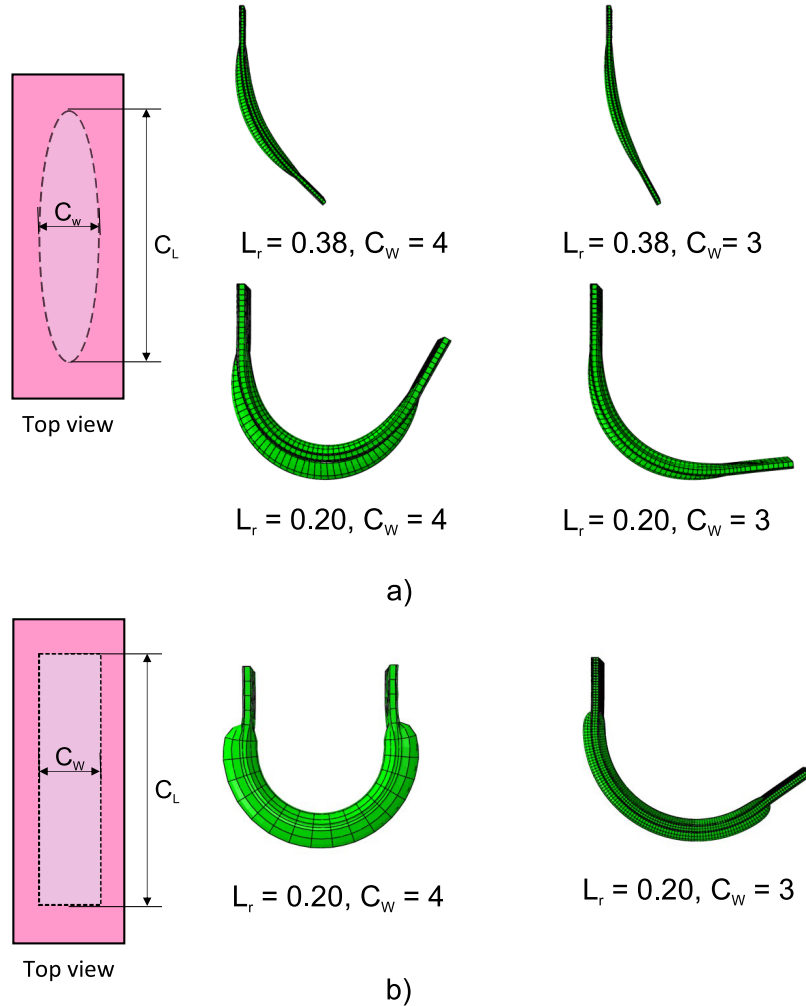


Figure 3.8: Comparison of deformation patterns for oval and rectangular cavities under pneumatic actuation. (a) The top view shows oval cavity geometry (left) with parameters C_W and C_L , alongside four deformation profiles at different L_r and C_W . (b) The top view shows rectangular cavity geometry (left) with corresponding deformation profiles at $L_r = 0.20$ with (C_W) of 4 mm and 3 mm.

c) Triangular Cavity Investigation

Fig. 3.9a shows the simulation of PneuThin with triangular cavity configuration. The FEM simulation revealed a distinct joint-like bending deformation pattern, different from the uniform bending observed in rectangular and oval configurations (see Fig. 3.8b). The simulation achieved 77% of the applied pressure load (6 psi) before converging. Multiple mesh refinements were attempted using both structure and sweep mesh techniques with mesh sizes ranging from 1.7 to 0.27 mm (Fig. 3.9b), but similar convergence limitations were encountered. This indicates that triangular cavity geometry introduces significant computational challenges due to high localised deformations.

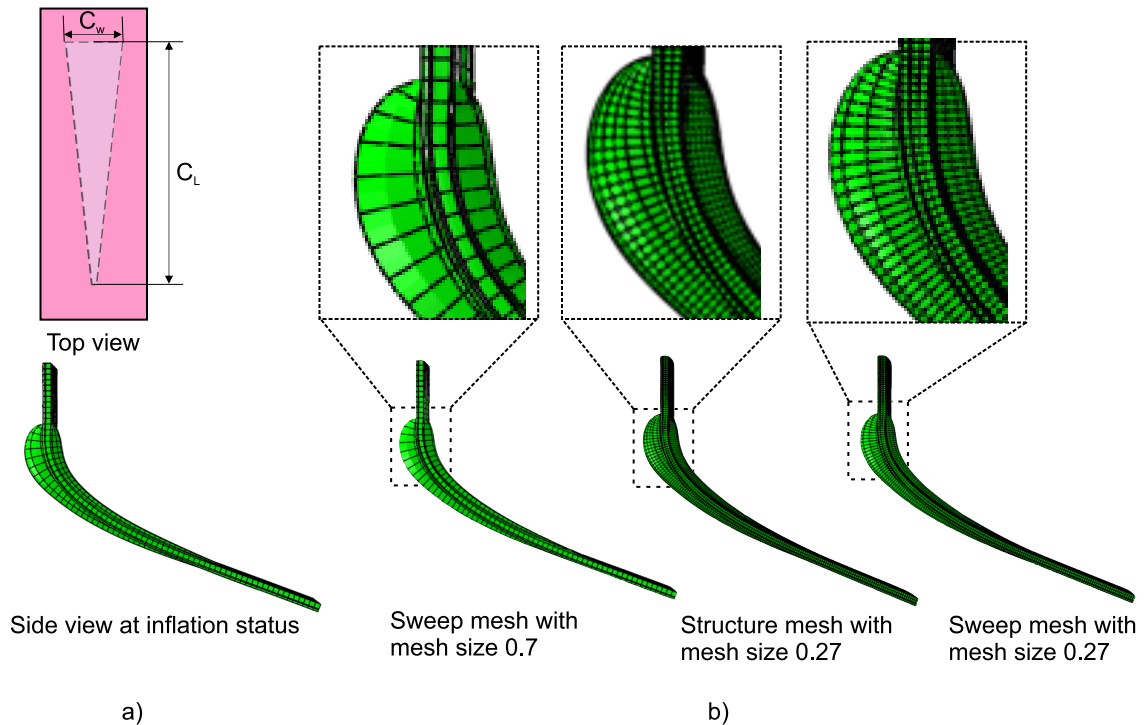


Figure 3.9: Mesh analysis of PneuThin with triangular cavity configuration. (a) Design schematic showing cavity geometry (C_W , C_L) in top view and resultant deformation in side view under pressure load. (b) Mesh refinement comparison demonstrating deformation patterns across three configurations: sweep mesh (0.7 mm), structure mesh (0.27 mm), and sweep mesh (0.27 mm), with magnified sections showing mesh detail.

Table 3.6: Mesh sensitivity analysis results for rectangular cavity configuration ($W = 5$ mm, $L_r = 0.38$, $C_W = 4$ mm, $P = 6$ psi)

Mesh Density	Tip Displacement (mm)	Max. Stress (MPa)	Relative CPU Time
Coarse (102)	7.9	1.99	0.15
Normal (336)	22.5	1.61	0.30
Fine (1862)	21.7	1.05	2.7
Very fine (5852)	21.06	1.07	11.8

3.5.2 Quantitative Performance Analysis

Mesh Sensitivity Study

A mesh sensitivity study was conducted using four different mesh densities: coarse (102 elements), normal (336 elements), fine (1862 elements) and very fine (5852 elements), as shown in Fig. 3.10a. The analysis examined three key parameters: deformation profile, tip displacement, and Von Mises stress concentrations along the circumference of the cavity (Fig. 3.10b). The von Mises stress is a metric that represents a uniaxial equivalent of a multiaxial stress state within the elastomeric material of the actuator, developed due to bending and internal cavity expansion upon pressurisation. It is commonly used to predict the onset of material yielding under multiaxial loading conditions (Bower, 2009).

As shown in Table 3.6, the tip displacement increased significantly from 7.9 mm with coarse mesh to approximately 21-22 mm with finer meshes. The maximum stress at the adhesion line decreased from 1.99 MPa (coarse mesh) to approximately 1.05 MPa (fine mesh) as the mesh density increased. However, this improvement in accuracy came with increased computational cost, with the relative CPU time increasing from 0.15 to 11.8 for the very fine mesh. The deformation profiles converged for normal, fine and very fine meshes Fig. 3.10c (left). Maximum stress concentrations were observed along the edges of the cavity Fig. 3.10c (right). The normalised results (Fig. 3.10d) show convergence in the fine mesh density (1862 elements) for both the tip displacement and the maximum stress values.

Stress and Displacement Analysis

Stress and displacement analysis was performed using fine mesh for rectangular and oval cavities with $L_r = 0.38$ and C_W of 3 mm and 4 mm. The results are summarised in Table 3.7. The oval cavity with $C_W = 4$ mm showed the highest stress concentration (2.61 MPa) localised in the middle region (Fig. 3.11a). Reducing the width of the cavity to 3 mm decreased the maximum stress to 1.30 MPa, with the stress distributed more uniformly throughout the length of the cavity (Fig. 3.11b). Rectangular cavities exhibited lower stress values of 1.05 MPa and 0.75 MPa for 4 mm and 3 mm widths, respectively,

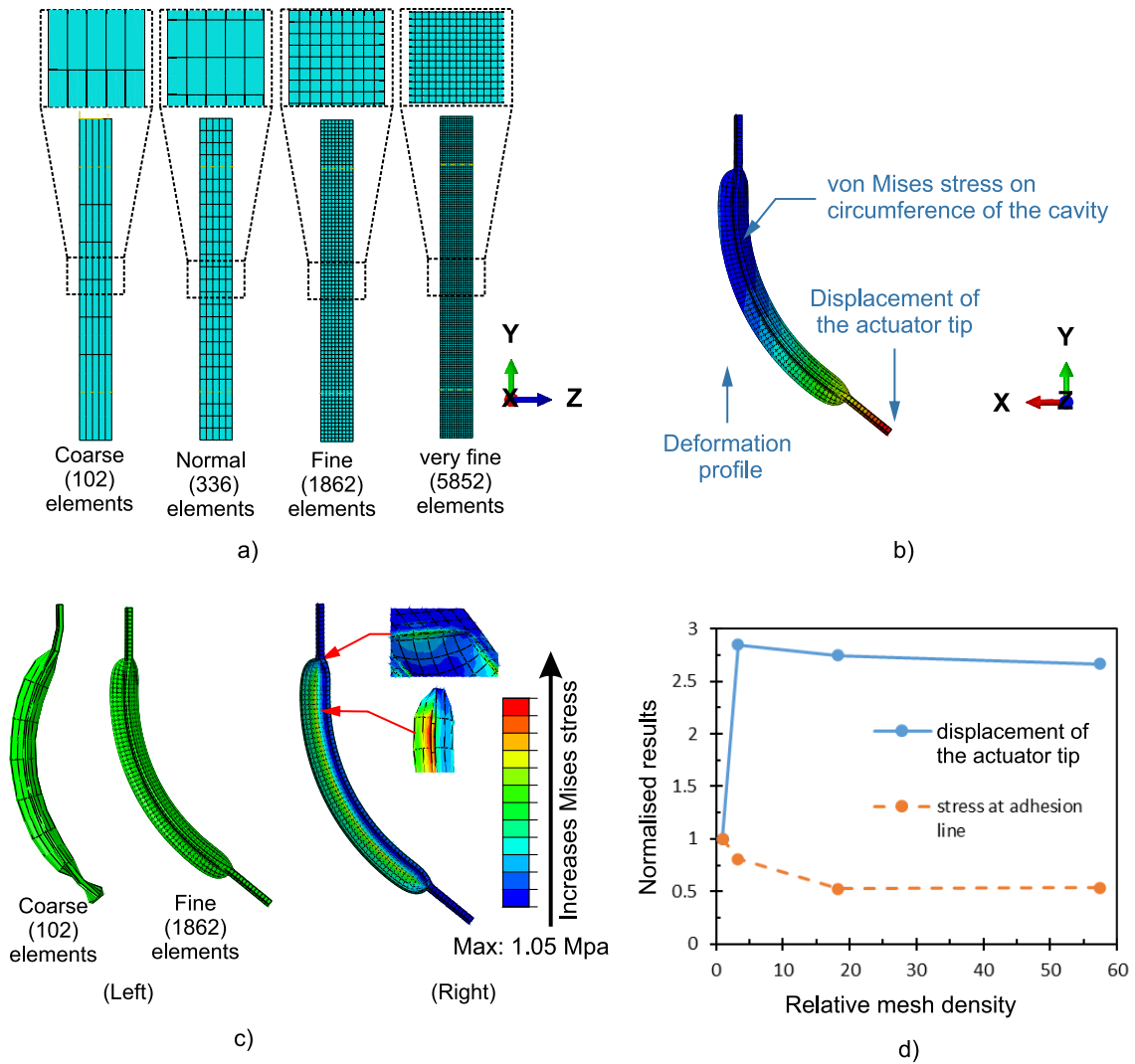


Figure 3.10: Mesh sensitivity analysis of PneuThin ($W = 5$ mm, $L_o = 50$ mm, $C_W = 4$ mm). (a) Progressive mesh refinement showing element density variations, with magnified sections illustrating mesh detail. (b) Key measurement parameters: deformation profile, tip displacement, and circumferential von Mises stress. (c) Qualitative comparison of deformation between coarse and fine meshes densities at 6 psi pressure load (left) and Von Mises stress contour (right), where the von Mises stress represents an equivalent uniaxial stress used to identify regions of high multiaxial stress concentration. Magnified views highlight the regions of maximum stress concentration where delamination or material failure is likely to initiate. (d) Mesh convergence plot showing normalised tip displacement and stress along adhesion lines against relative mesh density.

with stress concentrated along the edges of the cavity. This indicates that the shape of the cavity significantly influences both the magnitude and the distribution pattern of internal stresses. In terms of displacement, the rectangular cavity with $C_W = 4$ mm exhibited the highest tip displacement of 21.7 mm, while the oval cavity with $C_W = 3$ mm showed the lowest displacement of 12.3 mm, demonstrating a direct correlation between cavity width and deformation response. Although the oval cavity exhibits significantly higher stress than the rectangular cavity, 2.5 times higher for $C_W = 4$ mm and 1.73 times higher

Table 3.7: Stress and displacement results for different cavity configurations ($L_r = 0.38$)

Configuration	Max. Stress (MPa)	Tip Displacement (mm)	Stress Location
Rectangle, $C_W = 4$ mm	1.05	21.7	Cavity edge
Rectangle, $C_W = 3$ mm	0.75	13.6	Cavity edge
Oval, $C_W = 4$ mm	2.61	19.7	Middle region
Oval, $C_W = 3$ mm	1.30	12.3	Along cavity length

for $C_W = 3$ mm—the difference in tip displacement between the two shapes is relatively small, with rectangular cavities showing only 10.2% and 9.5% higher displacement for $C_W = 4$ mm and $C_W = 3$ mm, respectively, as shown in Table 3.7. This indicates that while the shape of the cavity strongly affects the stress distribution, its influence on overall deformation remains minimal. However, the increased stress concentration in oval cavities suggests a potential reduction in actuator lifetime due to higher localised material fatigue over repeated cycles.

Bending Ability Characterisation

Fig. 3.12a-d depict the coordinates (X,Y) that mapped the actuator profile at the applied pressure load (6 psi) for rectangular and oval cavities with varying widths ($C_W = 1-4$ mm) and thickness ratios ($L_r = 0.38, 0.20$). The measured curvature for all configurations is summarised in Table 3.8 and Fig. 3.12e. For rectangular cavities with a thickness ratio (L_r) of 0.20, the curvature increased from 0.0051 to 0.0963 mm^{-1} as C_W expanded from 1 mm to 4 mm. For a thickness ratio of $L_r = 0.38$, a modest increase in curvature was observed, ranging from 0.0021 to 0.028 mm^{-1} . The oval cavity configurations exhibited consistent trends, where $L_r = 0.20$ resulted in curvatures ranging from 0.0042 to 0.086

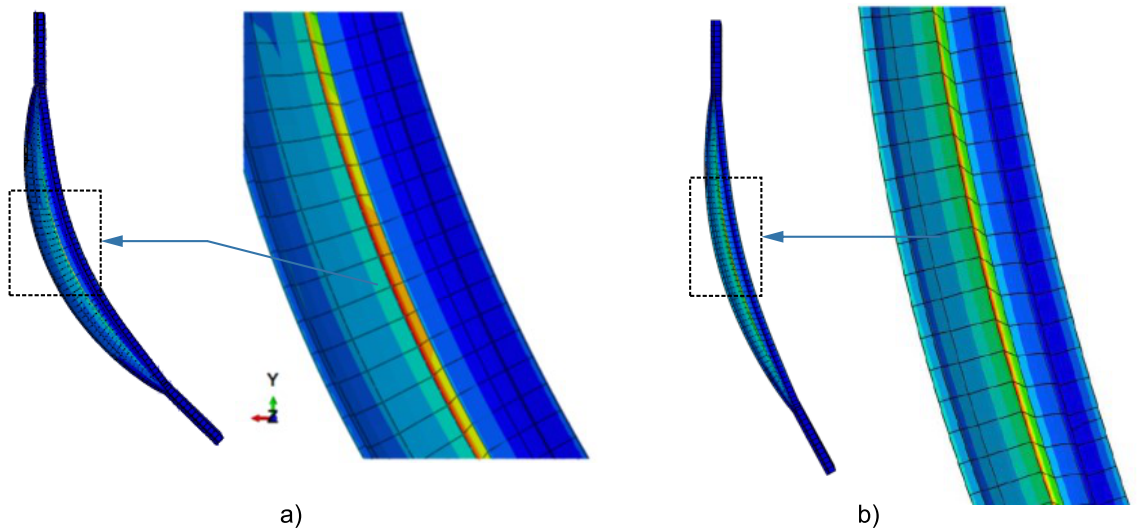


Figure 3.11: Stress distribution comparison for oval cavity configurations, (a) concentrated stress in middle region for $C_W = 4$ mm and (b) distributed stress pattern for $C_W = 3$ mm.

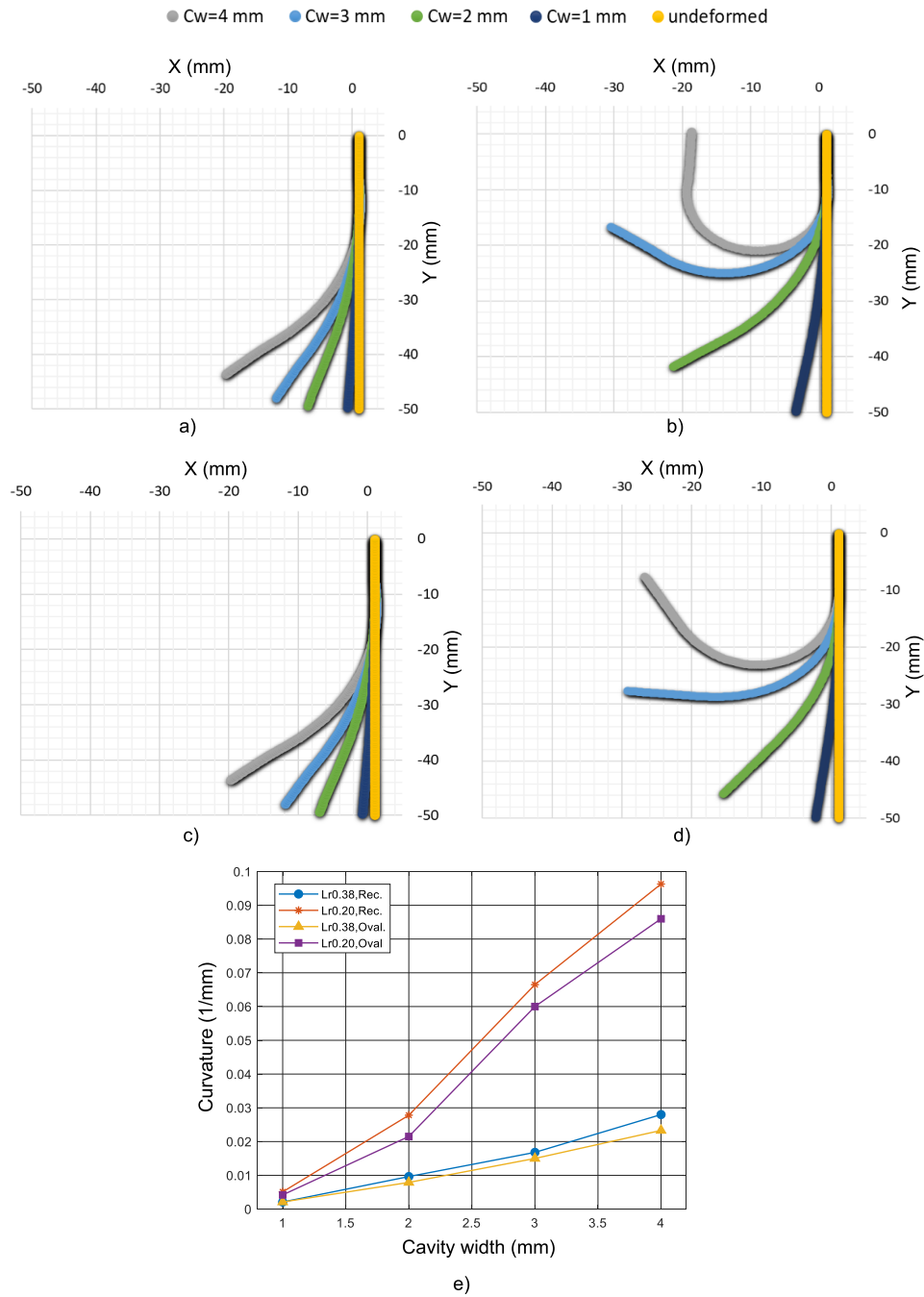


Figure 3.12: Performance analysis of PneuThin under 6 psi pressure load. (a-d) Deformation profiles comparing ($C_W = 1-4$ mm) against undeformed state, with consistent coordinate system origin at proximal tip. (e) Curvature response to C_W variations for rectangular cavities ($L_r = 0.38, 0.20$) and oval cavities ($L_r = 0.38, 0.20$), showing geometric influence on deformation behaviour.

mm^{-1} , compared to $L_r = 0.38$, which produced curvatures ranging from 0.0021 to 0.0233 mm^{-1} . This indicates that both the C_W and the thickness ratio significantly influence the bending behaviour, with lower thickness ratios and wider cavities producing larger curvatures.

Table 3.8: Curvature measurements for different cavity configurations

Configuration	Model (L_r, C_W)	Radius (mm)	Curvature
Rectangle	(0.38, 4)	35.73	0.028
	(0.38, 3)	59.39	0.0168
	(0.38, 2)	103.85	0.0096
	(0.38, 1)	486.50	0.0021
	(0.20, 4)	10.38	0.0963
	(0.20, 3)	15.05	0.0665
	(0.20, 2)	35.99	0.0278
	(0.20, 1)	196.82	0.0051
Oval	(0.38, 4)	42.89	0.0233
	(0.38, 3)	66.89	0.0150
	(0.38, 2)	125.87	0.0079
	(0.38, 1)	469.59	0.0021
	(0.20, 4)	11.63	0.0860
	(0.20, 3)	16.68	0.0600
	(0.20, 2)	46.42	0.0215
	(0.20, 1)	238.89	0.0042

3.6 Discussion

The preliminary analysis (FEM) reveals that the thickness ratio functions as the primary factor influencing the bending behaviour of PneuThin see Fig. 3.6. This finding aligns with the research of Hu et al. (2018) on PneuNet actuators, where the width of the wall and the thickness of the bottom layer critically affected the performance of the actuator. Similarly, Gorissen et al. (2011) and Sinatra et al. (2018) demonstrated how variations in membrane and beam thickness significantly impact the bending behaviour of pneumatic balloon microactuators. This consistency among different actuator types emphasises the fundamental importance of structural asymmetry in achieving controlled bending motion (Gorissen et al., 2017). The quantitative relationship between the thickness ratio and curvature, illustrated in Fig. 3.6, confirms this effect. In addition, there is an exponential growth trend in curvature as the thickness ratio decreases, with this effect becoming pronounced at cavity widths of 3 mm and 4 mm; see Fig. 3.6. This nonlinear relationship establishes the thickness ratio as a critical design parameter that requires precise control during fabrication. Consequently, precise control over layer thickness during fabrication becomes essential, leading to the development of methodologies in Chapter 4 that characterise the correlation between doctor blade gap height settings and final dry layer thickness, allowing reliable coating with high repeatability. From a fabrication perspective, very small thickness ratios ($L_r = 0.125$) present practical challenges despite producing the largest curvature values. Extremely thin membrane layers become susceptible to

excessive strain during inflation, increasing the risk of bursting or uneven expansion. This manufacturing constraint suggests that moderate thickness ratios ($L_r = 0.38$ and 0.63) offer a practical balance between fabrication reliability and bending performance. These intermediate values provide substantial curvature while maintaining sufficient mechanical integrity to withstand pneumatic pressurisation. The selection of appropriate L_r values must therefore consider this trade-off between theoretical performance and practical fabrication limitations.

The preliminary FEM simulation was guided by initial testing of cavity shapes and layer configurations. Konishi et al. (2006) reported layer delamination at the edges of the cavity in their experimental work (Konishi et al., 2006). Unger et al. (2000) highlighted that the construction of multiple layers for active devices makes layer adhesion a critical practical concern (Unger et al., 2000). This observation led us to examine stress distributions through FEM, which revealed high stress concentrations at the interface between layers of Elastosil M4601. Wirekoh and Park (2017) identified similar bonding strength limitations in PDMS actuators (Wirekoh and Park, 2017). These combined experimental and computational findings were used to directly influence the development of the fabrication protocol in Chapter 4. The bond strength between layers was established as a critical parameter and methods were developed to control it through semi-curing times and T-peel testing, as detailed in Section 4.4.6.

Physical testing combined with FEM analysis confirms the viability of the FlexiLayer technique. Ranzani et al. (2018) examined different cavity shapes and reported joint-like bending in triangular cavities. The FEM predictions matched these experimental results. Fujiwara et al. (2009) demonstrated continuous bending profiles in rectangular cavities, which simulation models also accurately predicted. This consistent agreement between FEM predictions and published experimental data shows that the FlexiLayer approach can produce reliable soft actuators. This agreement between FEM predictions and experimental data validates the modelling approach for evaluating the PneuThin design concept.

The refinement mesh is important to ensure the accuracy of the mesh density (Pu et al., 2024). In addition, the analysis demonstrates that increasing the density of the mesh minimally affects the predicted bending behaviour in the PneuThin models Fig. 3.9b. This observation is consistent with findings from Tawk and Alici (2020b) and Rad et al. (2022), who determined that finer meshes do not necessarily improve accuracy in the modelling of soft materials. Quantitative results show clear convergence patterns: tip displacement values remain consistent between normal (22.5 mm) and fine meshes (21.7 mm), with

minimal change in very fine mesh (21.06 mm). While the very fine mesh (5852 elements) increases the processing time by 11.8 times compared to the coarse mesh, it only improves accuracy by 3% over the fine mesh (1862 elements). These findings suggest that the normal to fine mesh density provides an optimal balance between the reliability of the result and the computational efficiency.

The effectiveness of FEM implementation remains limited by its reliance on literature-based material constants for ELASTOSIL® M 4601. Although this approach functions adequately, it may not fully capture how the FlexiLayer fabrication process affects the mechanical properties of the material. Incorporating direct measurements (e.g., stress-strain curve) from doctor-blade-coated samples would enhance the accuracy of the material model. Despite these limitations, the current FEM implementation achieves three significant outcomes; it validates the feasibility of the FlexiLayer concept to produce functional actuators, it identifies critical geometric parameters that control actuator performance, and it demonstrates good agreement with experimental results from Chapter 5 by accurately predicting the evolution of deformation patterns across variations in cavity geometry and L_r .

The analysis reveals that the layer thickness ratio L_r predominantly determines the behaviour of bending, while the geometry of the chamber dictates the distribution of stress and the deformation patterns. This understanding enables the development of FEM into a reliable design tool in Chapter 6 through the incorporation of material properties measured directly from the FlexiLayer fabrication process. The subsequent validation of model predictions against experimental data from two prototype PneuThin designs in Chapter 5 establishes a systematic approach to refine the PneuThin design and enhance its performance.

3.7 Chapter Summary

This chapter established the foundation for the development of the FlexiLayer fabrication technique through FEM simulations. The preliminary investigation began with a qualitative assessment of the deformation behaviour in three cavity shapes, including rectangular, oval, and triangular configurations. The results indicated that rectangular and oval cavities enable continuous bending deformation. The triangular cavity investigation revealed distinct joint-like bending deformation but showed excessive radial expansion in its wider base region, leading to computational convergence limitations. Subsequent quantitative analysis focused on rectangular and oval cavities, with stress analysis revealing stress concentrations

at the layer interfaces. The measured curvature demonstrating the significant influence of C_W and L_r on the bending performance. These insights from FEM guided the identification of critical parameters in the development of the fabrication process.

The FEM analysis identified key parameters that require characterisation; these are experimentally investigated and verified during the development of the fabrication protocol presented in Chapter 4. First, the relationship between doctor blade gap height and dry film thickness must be characterised across different substrates to achieve target layer thicknesses with high repeatability. This characterisation ensures precise control over the silicone layer thickness, which is crucial to realise the actuator's structural design and desired bending deformation. This characterisation is presented in Chapter 4. Second, developing a reliable method for cavity alignment is essential. Because the FlexiLayer method uses a planar configuration and zero-volume air chambers, precise placement of the mask layer (e.g. PVA) between elastomer layers is necessary to achieve consistent cavity geometry. To support this, a vacuum-assisted alignment system was developed -detailed in Chapter 4- to improve positioning accuracy and repeatability. Third, verification of laser cutting alignment is required. This process ensures that laser-cut profiles accurately reflect the intended design, preserving precise relationships between cavity edges and actuator boundaries. Proper alignment prevents irregular deformation during actuation and contributes to consistent performance across fabricated samples. Fourth, the air channel layout must be characterised to ensure effective pressure transfer from the inlet to the cavity. Unlike traditional 3D chambers, the planar 2D design used in PneuThin actuators presents unique challenges for airflow distribution. Finally, the stress analysis revealed the need to characterise interlayer bonding through T-peel testing at different semi-cure times to prevent delamination during actuation. These fabrication requirements establish the framework for the verification process of these key parameters in Chapter 4, where each parameter will undergo thorough investigation. A fabrication protocol will be developed through systematic testing, and its effectiveness will be evaluated using quantitative performance metrics.

Chapter 4

Development of the FlexiLayer Protocol

4.1 Introduction

Chapter 4 presents the development and testing of the FlexiLayer fabrication technique for PneuThin. The FEM analysis in Chapter 3 demonstrated that bending performance is highly sensitive to layer thickness ratios, establishing the need for precise thickness control during fabrication. The aim is to develop a reliable fabrication protocol that enables accurate control of the layer thickness and cavity shape in pneumatic thin planar soft robots.

Primary Objectives

This chapter addresses two key objectives to establish a reliable manufacturing process:

1. Develop and verify fabrication process steps for PneuThin with precise layer thickness control
2. Establish experimental protocols for reliable layer deposition, mask alignment, and laser cutting.

The chapter introduces a method using a Laboratory Blade Coating Machine (LBCM) capable of producing uniform silicone layers with controlled thickness. This equipment enables accurate silicone deposition while achieving the thickness ratios identified by FEM analysis. A complete fabrication protocol that integrates layer deposition, alignment, and laser cutting is present. The experimental investigation examines layer thickness consistency in different substrate materials, mask layer alignment accuracy, laser cut alignment and

process parameters, air channel layout configurations, and layer bonding strength to establish reliable manufacturing parameters.

4.2 Development of Laboratory Blade Coating Machine

4.2.1 Design and Construction

The development of the LBCM¹ addresses the need for precise control of the thickness of the layer in the FlexiLayer fabrication process. Fig. 4.1(a,b) shows the integrated system, which combines a casting knife film applicator with an automated linear motion system. The structure uses aluminium strut profiles (Bosch Rexroth, UK) to ensure stability during operation. The design enables film production up to 150 mm wide across a 300 mm coating length, providing sufficient area to fabricate multiple actuators in a batch. A casting knife film applicator (Model 3580/5, Elcometer, UK) with extended sides to contain the coating during application. Additionally, its integrated with two micrometric screws enables vertical distance control from 0 to 6000 μm in 10 μm increments (3580/5, 2025), meeting the layer thickness requirements (100 - 1000 μm) identified in Chapter 3.

The coating substrate comprises a cold-rolled steel sheet (410 mm \times 250 mm \times 3 mm). Steel was selected for its magnetic properties, enabling thickness measurements using magnetic coating gauges (Elcometer 456 Ferrous, Model S, UK) and facilitating alignment through magnetic pins (N42 Neodymium rod magnet, FIRST4MAGNETS, UK). The 3 mm thickness represents a careful balance between structural requirements and practical constraints. While thicker steel could potentially offer better flatness, the substrate requires manual transfer between the coating platform, curing oven, and laser cutting table. A thicker plate would increase handling difficulty and safety risks during transfers. Additionally, the laser cutting table imposes specific weight limitations. The substrate's flatness limitations are mitigated by using the first silicone layer as a levelling layer, providing a uniform surface for subsequent layer deposition, as demonstrated in Section 4.5.

¹The Laboratory Blade Coating Machine (LBCM) was developed through a collaboration with the Healthcare Mechatronics Research Group at the University of Leeds. The mechanical design and CAD modelling of the LBCM frame were undertaken by Shengbo Sun, a bachelor's student. Shengbo also laser cut acrylic sheet components and assembled the structural frame based on agreed design specifications. The motion control system, including the integration of electronic hardware and software development for the motion control box, was designed and implemented by Sina Najjari, a Ph.D. student. His work involved circuit design, electronic wiring, and programming the microcontroller to enable user-controlled movement of the blade. These contributions supported the broader development of the LBCM platform used in this research for achieving controlled and repeatable silicone layer deposition.

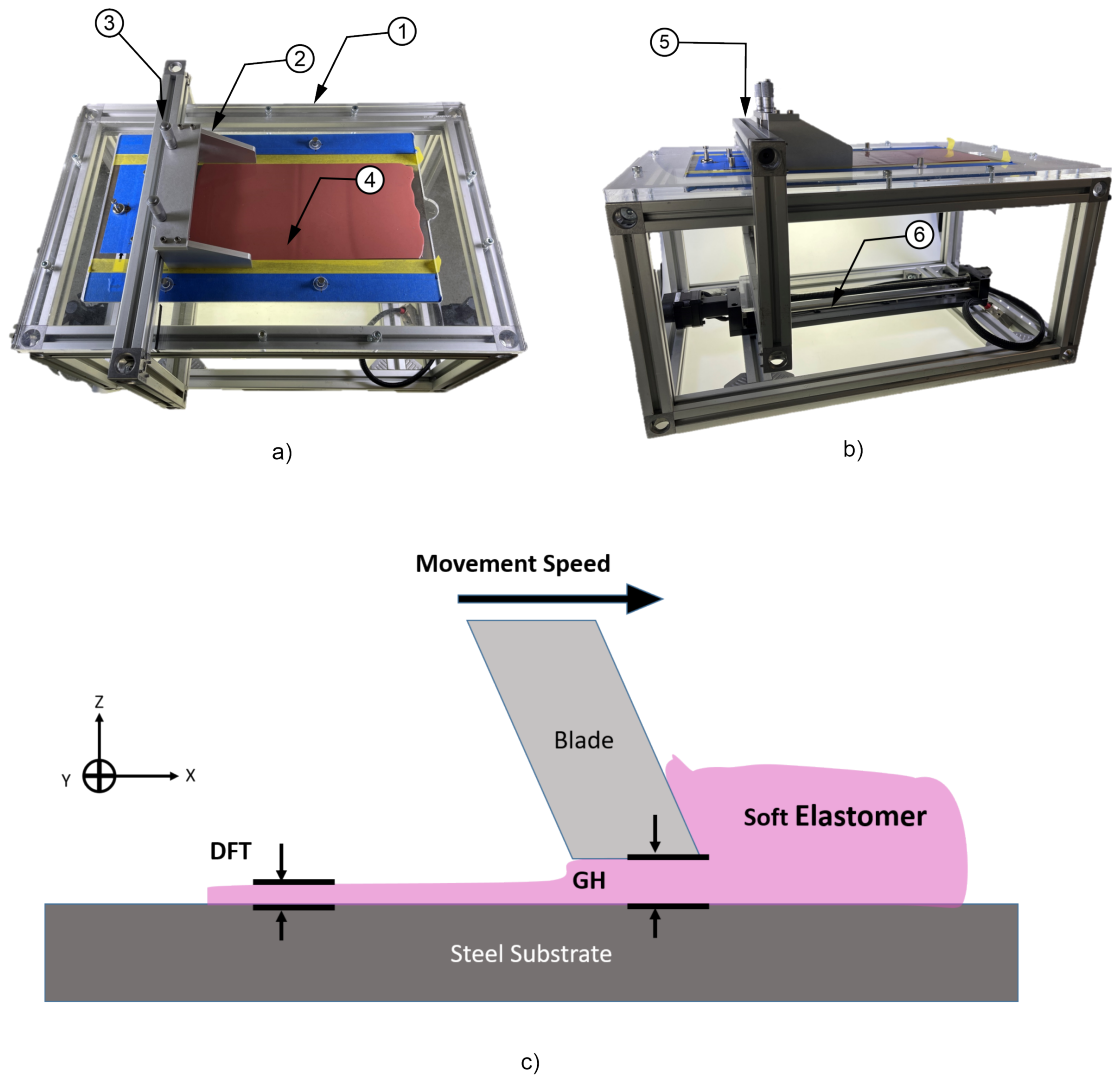


Figure 4.1: Components of the LBCM and operating principle: (a) Top view showing: (1) Rexroth aluminium strut profile structure; (2) Casting knife film applicator; (3) Micrometric screws for blade height adjustment; (4) Cold-rolled steel substrate coated with silicone elastomer; (b) Side view highlighting: (5) Rectangular aluminium frame for linear motion; (6) Linear stage (LC-300) with stepper motor (NEMA 17); (c) Schematic of blade coating process illustrating key parameters: GH represents the adjusted distance between blade and substrate surface, while DFT indicates the final thickness after curing. The blade moves at a controlled speed across the substrate to create uniform layer thickness. A coordinate system (X,Y,Z) is shown for reference.

4.2.2 Operating Principles and Control

The principle of blade coating operation appears in Fig. 4.1(c), where the GH between the blade and substrate determines the coating thickness, while the DFT represents the final cured layer thickness. Controlled coating speed is crucial for achieving uniform layer thickness. A linear stage (LC-300, Newmark Systems) driven by a stepper motor (NEMA 17) enables precise speed control between 1 - 12 mm/s in 1 mm/s increments. The motion control box features a user-friendly interface with LCD display for real-time

parameter monitoring, offering three motion modes: homing for initialisation, absolute for fixed-distance movements, and relative for incremental adjustments. This automated control ensures consistent coating speed and uniform layer deposition.

4.3 FlexiLayer Fabrication Protocol

This sections detail the specific fabrication protocols developed using LBCM, focussing on the PneuThin design structure using Elastosil M4601 silicone material. This material was selected for its 90 minute pot life, allowing sufficient working time for layer-by-layer processing, and its suitable viscosity characteristics for blade coating (see Section 3.2.2).

4.3.1 Process Overview

The FlexiLayer fabrication protocol enables the creation of PneuThin through a combination of precise layer stacking deposition and alignment, controlled curing, and laser cutting processes. The protocol consists of two primary phases. The first phase (Fig. 4.2) begins with material preparation, where ELASTOSIL M 4601 A/B is mixed in a 9:1 ratio in a planetary mixer to eliminate air bubbles. The knife film applicator maintains a uniform layer thickness through precise GH control between the blade and the steel substrate. During the layer-by-layer stacking process, each newly deposited layer undergoes a 3 minute partial cure at 75 °C to achieve optimal surface tackiness for enhanced interlayer bonding (see details in Section 4.5.6). After completion of the full layer stack construction, the entire structure undergoes an 11-minute cure at 75 °C to ensure complete cross-linking of the elastomer. For enhanced mechanical properties, the integration of a strain-limiting (SL) layer² becomes possible between elastomer layers during the stacking process.

The alignment accuracy of the layer significantly influences the final actuator performance (Ranzani et al., 2018; Wehner et al., 2016). The protocol employs a custom vacuum handling system (Fig. 4.3) to ensure precise positioning of the PVA³ mask layer (see details Section 4.5.2). This system incorporates a grid pattern comprising 10 mm × 10 mm unit cells, with each cell containing 36 precisely positioned holes of 0.25 mm diameter. A red grid marking on the vacuum chuck surface facilitates consistent operator alignment. The system utilises magnetic pins for additional guidance, while flat washers regulate vacuum

²Soft'n Sheer non-woven stabiliser (Sulky of America, Inc.) was employed as the strain-limiting layer in this research to enhance the actuator's bending performance. This material was chosen for its lightweight and flexible properties, good porosity for silicone penetration and excellent adhesion to the silicone elastomer.

³Throughout this research, Super Solvy water-soluble stabiliser (Sulky of America, Inc.) was used as the sacrificial layer to create zero-volume air chambers in the soft pneumatic actuators. This material was selected for its complete solubility in water and minimal residue after dissolution

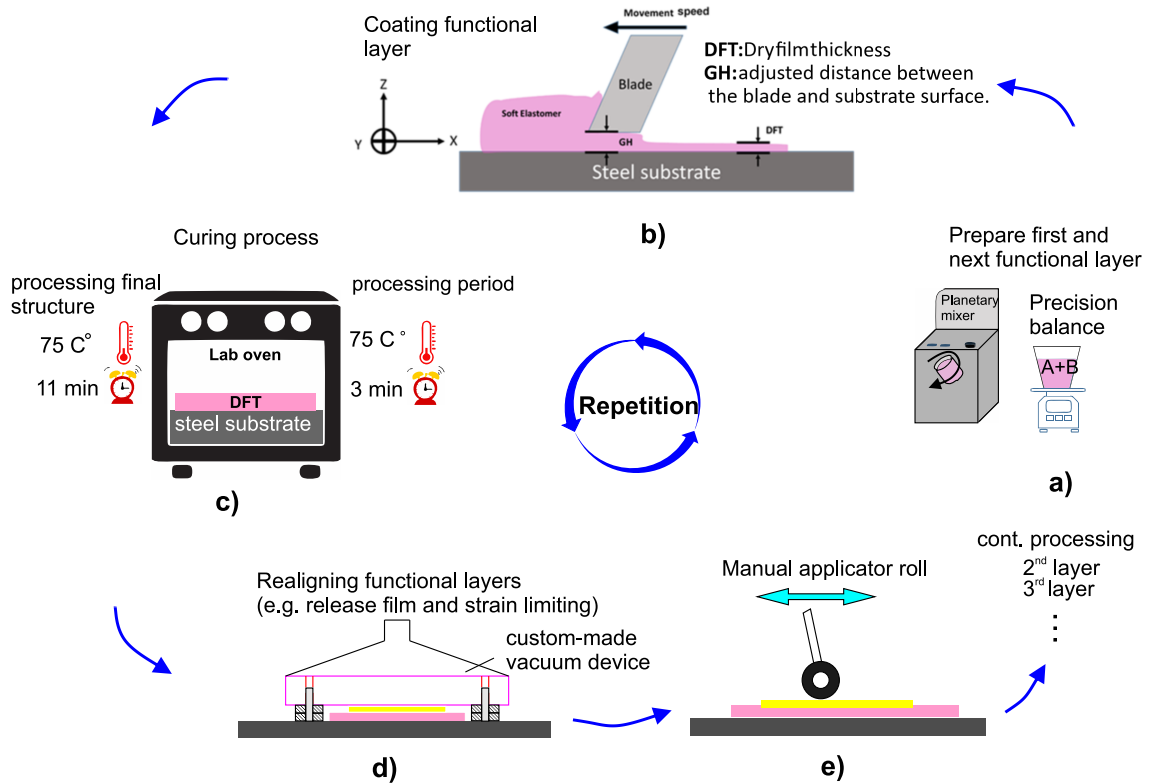


Figure 4.2: Phase one of the FlexiLayer fabrication protocol showing the sequential processing steps: (a) Material preparation step comprising measurement of components using precision balance, followed by mixing and degassing utilising a planetary mixer. (b) Blade coating step illustrating the key processing parameters: GH controls the distance between blade and substrate surface, whilst DFT represents the final cured layer thickness. (c) Thermal curing process at 75°C with two distinct stages: partial curing (3 minutes) during layer-by-layer processing to maintain surface tackiness, followed by complete curing (11 minutes) after final layer deposition. (d) Layer alignment step employing custom-designed vacuum device for precise positioning of PVA release film, whilst strain-limiting materials are manually aligned. (e) Manual pressure application step using roller applicator to ensure uniform contact between layers, enabling continuation to subsequent layer processing.

levels to enable gentle handling of delicate materials.

The second phase (Fig. 4.4) transforms the layered structure into a functional actuator through laser cutting processing. This transformation involves transferring the Two-dimensional (2D) vector design (*CorelDRAW 2021*) to the laser cutter (Universal Laser System, VLS3.50/60DT) with precise coordinate compensation (see details in Fig. 4.18). The protocol employs effective laser parameters of (25 - 40)% power and 5% speed for the final cutting of the actuator profile (see details in Section 4.5.3). The process ends with the injection of water and the withdrawal via syringe to dissolve the PVA mask (Fig. 4.4d), followed by the integration of metal needles and air tubes using Sil-poxy adhesive (Smooth-On, Inc.) for pneumatic connectivity.

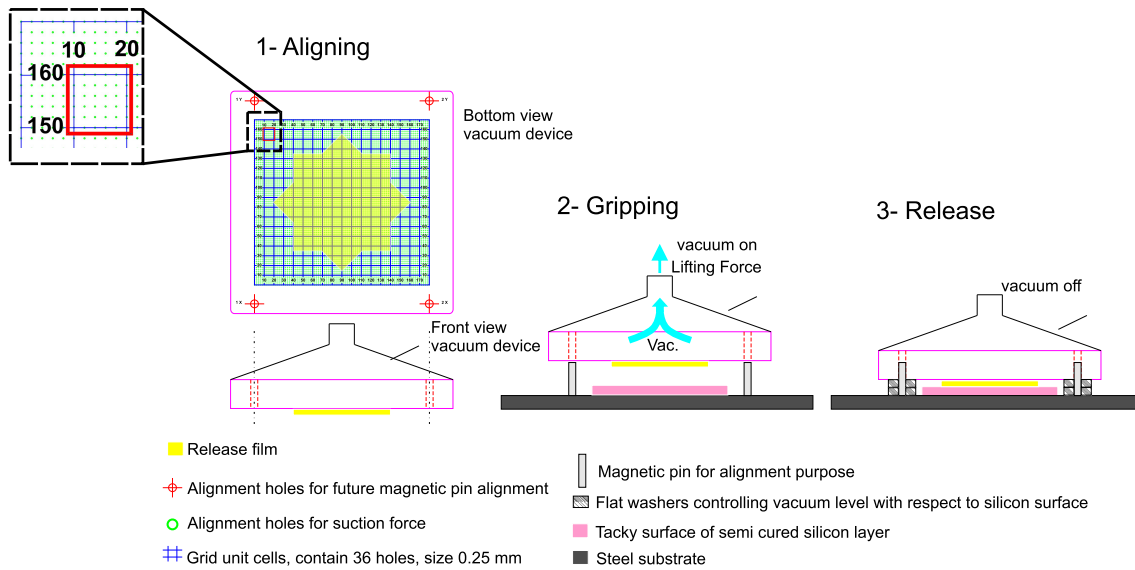


Figure 4.3: Precision alignment system showing the steps for vacuum-assisted PVA mask positioning: (1) Alignment step depicting the vacuum chuck design with a grid pattern (10 mm × 10 mm unit cells) containing 36 precisely placed holes (0.25 mm diameter) and strategic positioning of magnetic alignment pins. The bottom and front views illustrate the chuck geometry and placement of alignment features. (2) Gripping step demonstrating active vacuum engagement for controlled lifting of the PVA mask layer. Flat washers regulate the vacuum force relative to the silicone surface. (3) Release step showing controlled placement onto the steel substrate through vacuum deactivation. The integrated system combines alignment holes for both vacuum suction and magnetic pin guidance to achieve precise mask positioning.

This protocol offers three key advantages. First, the layer-by-layer approach facilitates the straightforward integration of various materials and functional elements. Second, the vacuum handling system achieves consistent alignment with sub-millimetre precision. Third, the standardised steps and controlled parameters enable scalability for mass production of customised soft robots. The subsequent sections present detailed characterisation of critical process parameters, including layer thickness control, alignment precision, and preliminary laser cutting exploration.

4.4 Characterisation of the Process Parameters

4.4.1 Method 1: Layer Thickness Control

Controlling the thickness of the layer is fundamental to fabricate reliable soft pneumatic actuators. As demonstrated in the FEM analysis of Chapter 3, the bending behaviour of these actuators is highly dependent on the thickness ratio between layers (Section 3.5.1). Moreover, understanding thickness formation on different surfaces is crucial because the results of doctor blade coating vary according to the properties of the substrate material

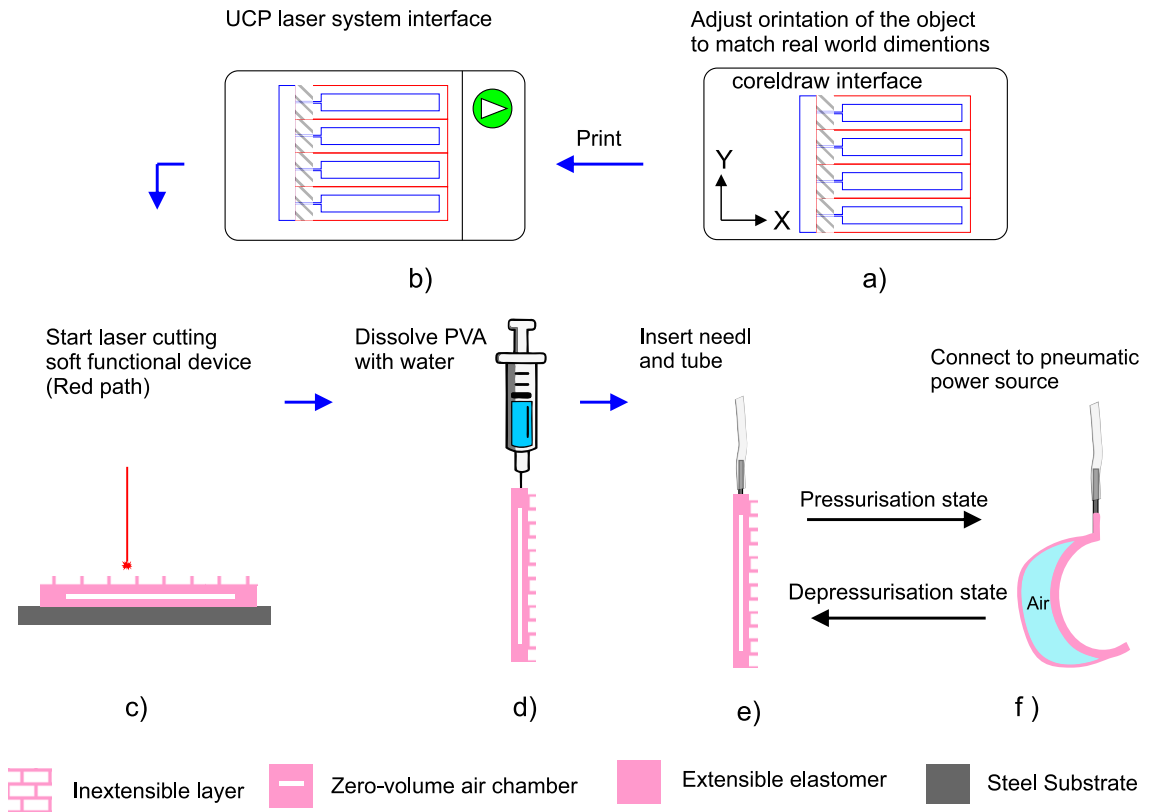


Figure 4.4: Phase two of the FlexiLayer fabrication protocol illustrating the laser cutting and assembly sequence: (a) Design preparation in 2D vector graphics software (CorelDraw 2021, Corel Corporation, Canada) with coordinate system alignment for dimensional accuracy. (b) Transfer to laser system control interface (Universal Control Panel VLS3.50/60DT, Universal Laser Systems, UK) for cutting parameter adjustment. (c) Execution of laser cutting process following predefined paths (shown in red) to create the soft functional device, with material composition indicated (extensible elastomer, inextensible layer, and zero-volume air chamber). (d) Application of water using a syringe to dissolve the PVA mask and create the internal cavity. (e) Integration of needle and tubing for pneumatic connection, showing the actuator in its depressurised state. (f) Final assembly step connecting to pneumatic power source, demonstrating cavity expansion between depressurised and pressurised states.

(Howard et al., 2019). To address this, a standardised silicone layer preparation protocol was developed to ensure reproducibility and control over the fabrication parameters. Following the preparation of silicone layer samples, a four-stage of thickness layer characterisation was implemented to systematically investigate thickness formation at different stages of the FlexiLayer process. This multi-stage was necessary to capture the variations introduced by different fabrication conditions, such as substrate type, intermediate layers, and composite material integration.

Preparation of Silicone Layer Samples

The fabrication of uniform silicone layers follows a protocol developed to ensure reproducibility and precision. The process consists of two main phases: preliminary preparation steps and layer fabrication process.

(a) Preliminary Preparation Steps:

Before each silicone layer is fabricated, three essential preparation steps are performed.

Step 1: Surface Preparation: The steel substrate and casting knife applicator are cleaned using Isopropyl alcohol (IPA) spray followed by compressed air to remove dust and contaminants. **Step 2: Parameter Setting:** The GH of the casting knife is adjusted using integrated micrometric screws. The motion controller is programmed with predefined coating parameters (speed: 2 mm/s, travel distance, motion type). **Step 3: Temperature control:** The laboratory oven is preheated to the target curing temperature (75 °C).

(b) Layer Fabrication Process:

The silicone layer fabrication follows a five-step sequence, beginning with precise weighing of the ELASTOSIL® M 4601 A/B components using a precision balance Fig. 4.2a. The mixture is mixed and degassed in a planetary mixer (THINKY ARE-250, INTERTRONICS, UK) according to the parameters specified in Table 4.1. Following mixture preparation, the material is deposited on the steel substrate and spread using LBCM at 2 mm/s (Fig. 4.1a). Thermal curing occurs in a preheated oven at 75 °C for 11 minutes, as determined by preliminary studies (Hu et al., 2018). After being cooled to room temperature 25 °C, DFT is measured using coating thickness gauge (Elcometer 456 Ferrous, Model S, UK) according to a standardised grid-based measurement protocol. This standardised process ensures consistent layer quality while allowing precise control over critical parameters that affect the final layer properties.

Experimental Stages for Layer Thickness Characterisation

Following the preparation of silicone layer samples, a four-stage experimental characterisation was developed to systematically investigate thickness formation across different fabrication conditions. These conditions reflect the various substrate configurations used in the fabrication of the PneuThin actuators, as described in Chapter 5. All experiments used Elastosil® 4601 A/B with processing parameters kept constant as specified in Table 4.1.

Table 4.1: Experimental parameters used for fabricating silicone layers using LBCM

Parameter name	Value's description
Mixture Weight	50 g of Elastosil 4601 A/B, at mix ratio 9:1 (A:B)
Mixing	2000 RPM for 1 minute
Degassing	2200 RPM 1 minute and 30 seconds
Coating speed	2 mm.s ⁻¹
Curing (force dry)	11 minutes at 75°C

The four experimental stages are summarised in Table 4.2 and illustrated schematically in Fig. 4.5.

Stage 1: Base Layer Formation on Steel Substrate, the initial Stage investigated DFT formation directly on a steel substrate. Steel was chosen because it is compatible with the magnetic coating thickness gauge used for measuring layer thickness. The $GH_{experiment}$ varied from 100 to 1000 μm in 100 μm increments. This investigation mapped the relationship between the GH settings and the resulting layer thickness DFT, when coating silicone on steel, providing baseline data for subsequent coating configurations (Fig. 4.1).

Stage 2: Layer-on-Layer silicone Formation, based on Stage 1, this stage studied the formation of a new silicone layer deposited onto a previously cured silicone surface. To maintain consistent coating conditions, a $GH_{practical}$ adjustment method introduced. For example, when targeting $GH_{experiment} = 200 \mu\text{m}$ and building on a base layer with DFT $\approx 130 \mu\text{m}$, $GH_{practical}$ is set to $GH_{experiment}$ plus the base layer DFT, which equals 330 μm . This adjustment ensures that the blade-to-surface gap accounts for the thickness of

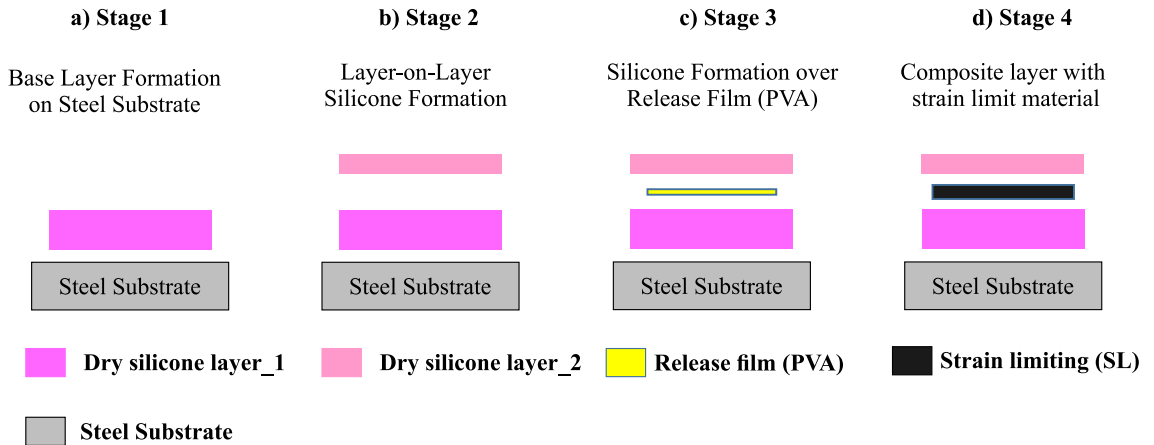


Figure 4.5: Schematic illustration of the four stages developed for layer thickness characterisation: (a) Base layer formation directly on steel substrate, (b) Layer-on-layer silicone formation for multilayer structures, (c) silicone formation over PVA release film for cavity creation, and (d) Composite layer formation incorporating strain-limiting (SL) material. The pink layers represent silicone, gray represents the steel substrate, and the patterned blue layer indicates either PVA or SL material.

Table 4.2: Experimental thickness characterisation of four fabrication stages

Stage	GH Range (μm)	Key Purpose
1. Base Layer Formation on Steel Substrate	100-1000 (100 μm steps)	Establish baseline DFT-GH relationship
2. Layer-on-Layer silicone Formation	200, 400, 600, 800	Study thickness formation on silicone substrate
3. silicone Formation over Release Film (PVA)	400	Verify thickness formation on release film
4. Composite Layer with Strain-Limiting Material	400	Study thickness formation in composite structures

the existing layer. The $GH_{\text{experiment}}$ values of 200, 400, 600, and 800 μm were tested using this compensation method.

Stage 3: silicone Formation over Release Film PVA, to validate the behaviour of layer formation with an intermediate release film PVA, $GH_{\text{experiment}} = 400 \mu\text{m}$ as a test case is selected. The calculation $GH_{\text{practical}}$ was modified to include the PVA thickness (100 μm): $GH_{\text{practical}} = GH_{\text{experiment}} + \text{base layer DFT} + \text{PVA thickness} = 400 + 130 + 100 = 630 \mu\text{m}$. Thickness measurements did not show significant differences in formation patterns compared to direct silicone-on-silicone coating (see Fig. 4.16a, which allows us to apply the findings of Stage 2 to silicone Formation over PVA).

Stage 4: Composite layer formation with strain limit material, the thickness formation with a SL is examined using $GH_{\text{experiment}} = 400 \mu\text{m}$. $GH_{\text{practical}}$ was adjusted to account for the thickness of the base layer and SL layer: $GH_{\text{practical}} = GH_{\text{experiment}} + \text{base layer DFT} + \text{SL thickness} = 730 \mu\text{m}$. This tests layer formation in multimaterial structures while maintaining consistent processing conditions. This Stage confirms the Validity of the model from Stage 2 for composite structures, provided that the total thickness of the stacked layers on the steel is known because the top surface remains silicone.

Test and Measurement Protocol

To evaluate the quality and uniformity of the fabricated layer structures, a measurement protocol was developed to quantify the thickness uniformity across the samples. The protocol divides the effective coating area approximately $180 \times 125 \text{ mm}$ (yellow region in Fig. 4.6a) into a 4×3 measurement grid, creating 12 distinct measurement nodes. The

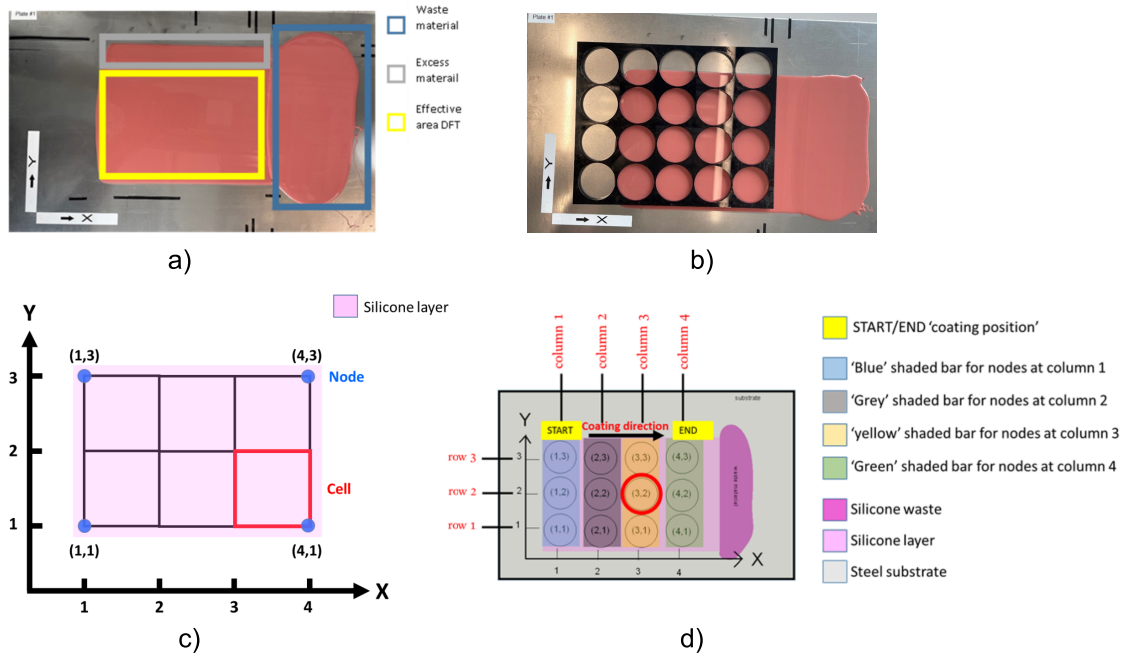


Figure 4.6: Protocol for mapping thickness uniformity of fabricated soft layers. (a) Effective coating area (yellow box) and waste material regions on steel substrate. (b) Circular template overlay enabling consistent probe placement for repeated measurements. (c) Grid system showing measurement nodes and cell divisions for thickness mapping. (d) Schematic showing four-column measurement zones with different shading, coating direction, and node coordinate system. For example, red circle node (3,2) represents measurement location in column 3, row 2.

location of each node is identified using a coordinate system with two subscripts: the first number indicates the column position (1-4), and the second indicates the row position (1-3); see Fig. 4.6 b. For example, as illustrated in Fig. 4.6d, node (3,2) represents the measurement point at column 3, row 2.

To ensure consistency of measurement and variation in track thickness in relation to the coating direction, the grid incorporates four distinct zones marked by different colours (Fig. 4.6d). The blue-shaded column 1 represents the initial coating region, followed by the grey-shaded column 2 for the early stabilisation zone. The yellow-shaded column 3 marks the mid-coating region, while the green-shaded column 4 indicates the end-coating region. This zonal Stage, combined with the grid system, enables tracking of DFT variations along both the coating direction (X-axis) and the transverse direction (Y-axis).

To achieve reliable and repeatable measurements, a circular template overlay (Fig. 4.6d) was laser cut to match the geometry of the magnetic hall probe tip (Elcometer 456 Separate Coating Thickness Gauge, model S). At each node, five thickness measurements are taken, with three samples tested per experimental condition to ensure statistical reliability. The coating direction is maintained consistent from the START position to the END

position, as indicated in Fig. 4.6d, allowing for direct comparison of thickness profiles across different coating configurations. This measurement protocol forms the basis for analysing the effectiveness of the FlexiLayer fabrication process, with detailed results presented in Section 4.5.1. The measurement methodology described here directly supports the broader goal of achieving precise layer thickness control, which Chapter 3 identified as critical for successful FlexiLayer fabrication. The results obtained through this protocol inform the controlling of processing parameters and validate the fabrication Stage’s capability to produce uniform, well-controlled layer thicknesses, essential for reliable soft actuator performance.

Primary analysis methods include visual and statistical approaches. Visual analysis uses scatter plots showing DFT versus position for each GH setting, along with box plots illustrating the thickness distribution along the X and Y axes. For statistical metrics, the mean thickness and standard deviation are calculated per measurement node. The Coefficient of variation (CV), calculated as the ratio of standard deviation to mean thickness (expressed as a percentage), allows a direct comparison between different settings of GH. The relationship between GH and DFT, for steel and silicone substrates, is modelled using a linear model. The detailed analysis of these relationships and their implications for coating quality control is presented in Section 4.5.1.

4.4.2 Method 2: Alignment Between Layers

Following the FlexiLayer fabrication protocol described in Section 4.3.1, where the vacuum chuck design was used for the handling of PVA mask layer. This investigation compares the alignment accuracy of two PVA mask placement methods: manual, where the mask was placed by hand on the template grid, and vacuum-assisted, which employed the vacuum chuck. The experimental setup used an iPhone camera mounted above the workspace to capture alignment images (Fig. 4.7a). The setup included a steel base plate with global fiducial markers⁴ and an A3 template that matched the grid pattern of the vacuum chuck introduced in Section 4.3.1. The alignment process used two matching grid systems. The first grid showed the target star shape with exact coordinates (Fig. 4.7b, top). The second grid, etched on the vacuum chuck surface (Fig. 4.7b, bottom), helped place the PVA mask in the correct position. Four global fiducial markers provided reference points for both placement and further alignment between layer orientation and laser cutting.

The alignment accuracy was quantified using ImageJ software (Schneider et al., 2012).

⁴Reference points fixed on the steel substrate that establish a consistent coordinate system for aligning multiple layers during fabrication.

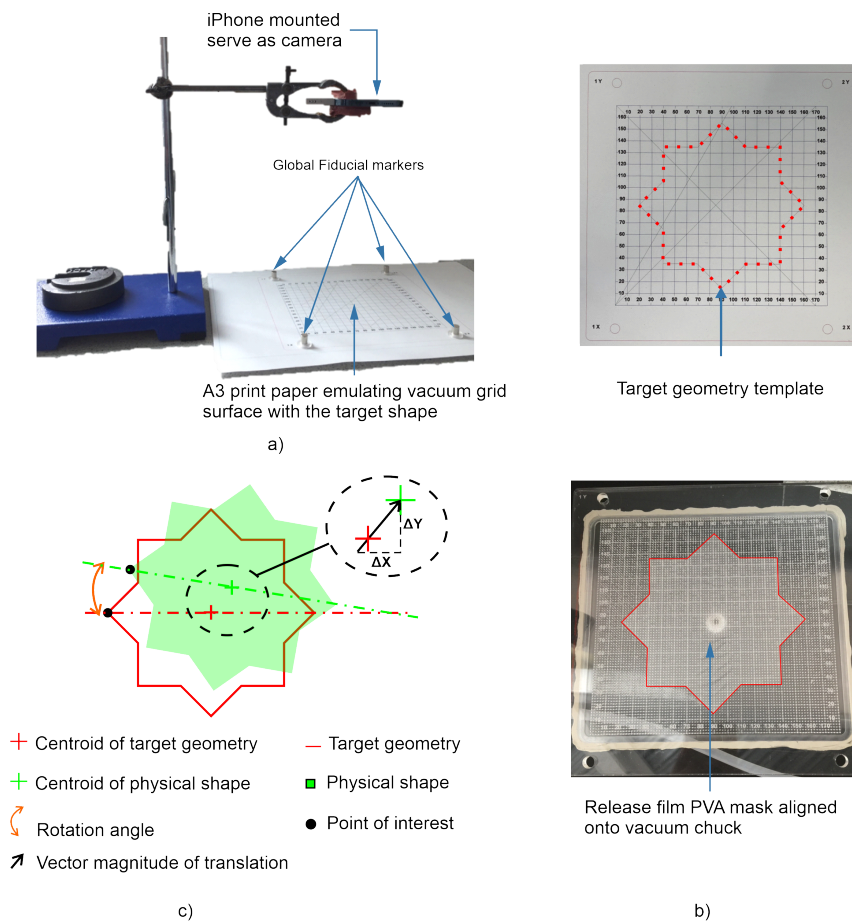


Figure 4.7: Experimental setup and methodology for PVA mask layer alignment: (a) Image acquisition setup showing iPhone camera mount above A3 print paper with vacuum grid surface and global fiducial markers for reference positioning; (b) Target geometry template displaying coordinate grid with star pattern outline (top) and PVA release film aligned onto vacuum chuck surface with visible grid pattern (bottom); (c) Schematic diagram illustrating alignment measurement parameters, where translational error (ΔX , ΔY) represents displacement between target geometry centroid (red cross) and actual position (green cross), whilst rotation error indicates angular deviation from intended orientation. The schematic demonstrates key geometric elements: target geometry (red outline), physical shape (green area), centroids (crosses), point of interest (black dot), rotation angle (curved orange arrow), and translation vector (straight black arrow).

As shown in Fig. 4.7c, translation error was measured as displacement (ΔX , ΔY) between the target centroid (red cross) and the actual position of the mask (green cross). The rotational error was determined by the angular deviation between the points of interest, indicated by the curved orange arrow. To ensure statistical significance, multiple trials were conducted for both methods. Section 4.5 presents the results, showing how vacuum-assisted alignment improved precision.

4.4.3 Method 3: Laser Cutting

Laser Cut Alignment to the Actuator Outline

This experiment verified the precision of laser cut actuator perimeters against their intended 2D design layout. The study examined an effective fabrication area of 180 x 120 mm (Fig. 4.8), corresponding to the region used for thickness measurements in Section 4.4.1. A printed A3 template simulated the actual layer stacking configuration used in PneuThin fabrication. This template incorporated the vacuum chuck grid pattern, fiducial markers, and target perimeter outlines marked in red, replicating the physical arrangement of layers on the steel substrate during fabrication (Fig. 4.8a). A corresponding template was created in 2D vector software (CorelDRAW, Corel Corporation, 2021) that matched the steel substrate dimensions and the vacuum chuck grid pattern. This digital template, positioned at coordinates (0,0) within a page size that corresponds to the dimensions of the laser cutting bed (Universal Laser System, VLS3.50), ensured accurate translation of the actuator design into the laser cutting system (Fig. 4.8b). The steel substrate with stacked layers was positioned similarly at coordinates (0,0) on the laser cutting bed, maintaining consistent alignment between design and fabrication (Fig. 4.8c). ImageJ software measured the maximum deviation between the actual laser-cut paths and the target perimeter outlines, quantifying the accuracy of the laser cutting process relative to the intended design.

Preliminary Investigation of Laser-Cutting Settings

This experiment aimed to explore viable laser cutting parameters for fabricating PneuThin using 1 mm thick Elastosil 4601 M sheets. The preliminary testing investigated parameter combinations that could achieve clean cuts with minimal thermal damage to the soft actuator structure. Parameter tests on effective power and speed were conducted using a laser cutter (Universal Laser System, VLS3.50). As shown in Fig. 4.8d, the experimental samples consisted of 10 mm × 10 mm square patterns cut from Elastosil 4601 M sheets (150 mm × 200 × 1 mm) prepared using the LBCM protocol (detailed in Section 4.4.1). All tests maintained a fixed pulse per inch setting of 1000, while power and speed settings were varied. Table 4.3 summarises the test coverage in different combinations of parameters.

The tests started with the initial screening examined broad ranges of parameters with power settings of 10%, 50%, 60%, and 100%, tested against speed settings of 25%, 50%, 75% and 100%. When increased speeds proved ineffective for cutting, subsequent tests focused on reduced speeds (1%, 5%, 10%, 15%) with power settings of 10% and 50%. These tests revealed that the combination of very low speeds with high power caused thermal

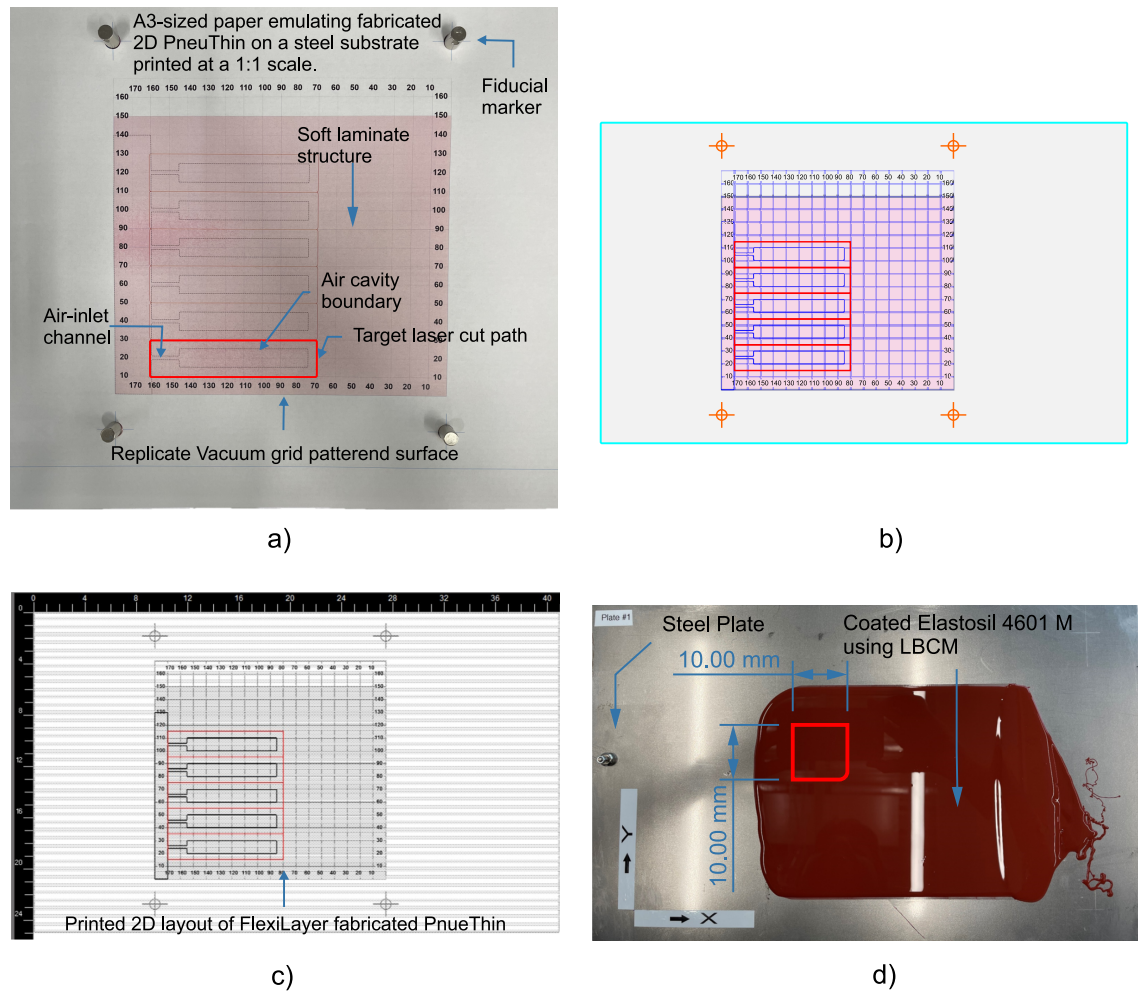


Figure 4.8: Template design and experimental setup for laser cutting characterisation: (a) A3-sized template emulating fabricated PneuThin on steel substrate, displaying vacuum grid pattern, fiducial markers and target laser cut paths at 1:1 scale; (b) 2D vector graphics software (CorelDraw) showing actuator layout (609.6×304.8 mm workspace) with origin point (0,0) positioned at top-left corner; (c) Laser cutting system interface (VLS3.50/60) displaying imported design with matching workspace dimensions and coordinate origin, ensuring precise alignment between design and cutting stages; (d) Test specimen on steel substrate showing 1 mm thick Elastosil M 4601 layer coated using LBCM with 10 mm \times 10 mm square test pattern (highlighted in red) for preliminary exploration of effective laser cutting settings.

damage. Based on these findings, the final test stage concentrated on moderate ranges of 5-50% power and 5-20% speed. The quality of the cut was evaluated through visual inspection of the smoothness of the edge, thermal damage, and the completeness of the cut. The testing identified workable parameter ranges that achieved successful cutting. The parameters that produced clean cuts are presented in Section 4.5.3.

Table 4.3: Parameter Testing Coverage for Laser Cutting Optimization

Speed (%)	Power Range (%)			
	1-25	26-50	51-75	76-100
5-20	■■■	■■	□	□
21-40	■■	□	□	□
41-60	■	■	□	□
> 60	□	□	■	■

Legend:
■■■ Primary testing region
■■ Secondary testing region
■ Limited testing
□ Not tested

4.4.4 Method 4: Investigation of Channel Layout Effects on PneuThin inflation

This study investigated how channel geometry influences air transfer in PneuThin. Unlike traditional soft pneumatic actuators that use open channels ($>1\text{mm}$) for air delivery, PneuThin employs an ultrathin zero-volume channel design ($<100\ \mu\text{m}$ thick). Fig. 4.9a illustrates the basic three-layer design concept of PneuThin, showing the stack arrangement of the elastomer and mask layers that creates the zero-volume channel structure. Understanding the effectiveness of these channels is crucial for developing complex multi-actuator systems, such as multigait soft robots.

The experimental design used the precision layer control achieved through LBCM in the FlexiLayer fabrication protocol; see Section 4.3. The basic PneuThin geometry, shown in Fig. 4.9b, maintained consistent overall dimensions ($110\ \text{mm}$ length \times $20\ \text{mm}$ width) with a cavity size of $50\ \text{mm} \times 10\ \text{mm}$. This base design served as the basis for two distinct studies that examined channel performance. The first study, depicted in Fig. 4.9c, investigated five different channel widths ranging from $1.0\ \text{mm}$ to $3.0\ \text{mm}$ while maintaining identical cavity dimensions. Based on these findings, the second study explored channel geometries with smooth and sharp curve configurations with a fixed channel width of $2\ \text{mm}$ Fig. 4.9d. Fig. 4.9e demonstrates the two-phase fabrication process following the FlexiLayer protocol. In phase 1, precise layer stacking was achieved using LBCM for elastomer deposition. The Elastosil M4601 was mixed in a 9:1 ratio (A:B) and deposited at $2\ \text{mm/s}$, with partial curing at $75\ ^\circ\text{C}$ for 3 minutes between layers. The PVA mask layer was laser-cut and precisely aligned using a custom vacuum chuck before applying the top elastomer layer, followed by final curing at $75\ ^\circ\text{C}$ for 11 minutes. Phase 2 involved laser cutting of the complete soft laminate structure to define the final perimeter of the actuator and the access points. Success was evaluated by visual confirmation of cavity inflation under a consistent pressure of 1 psi.

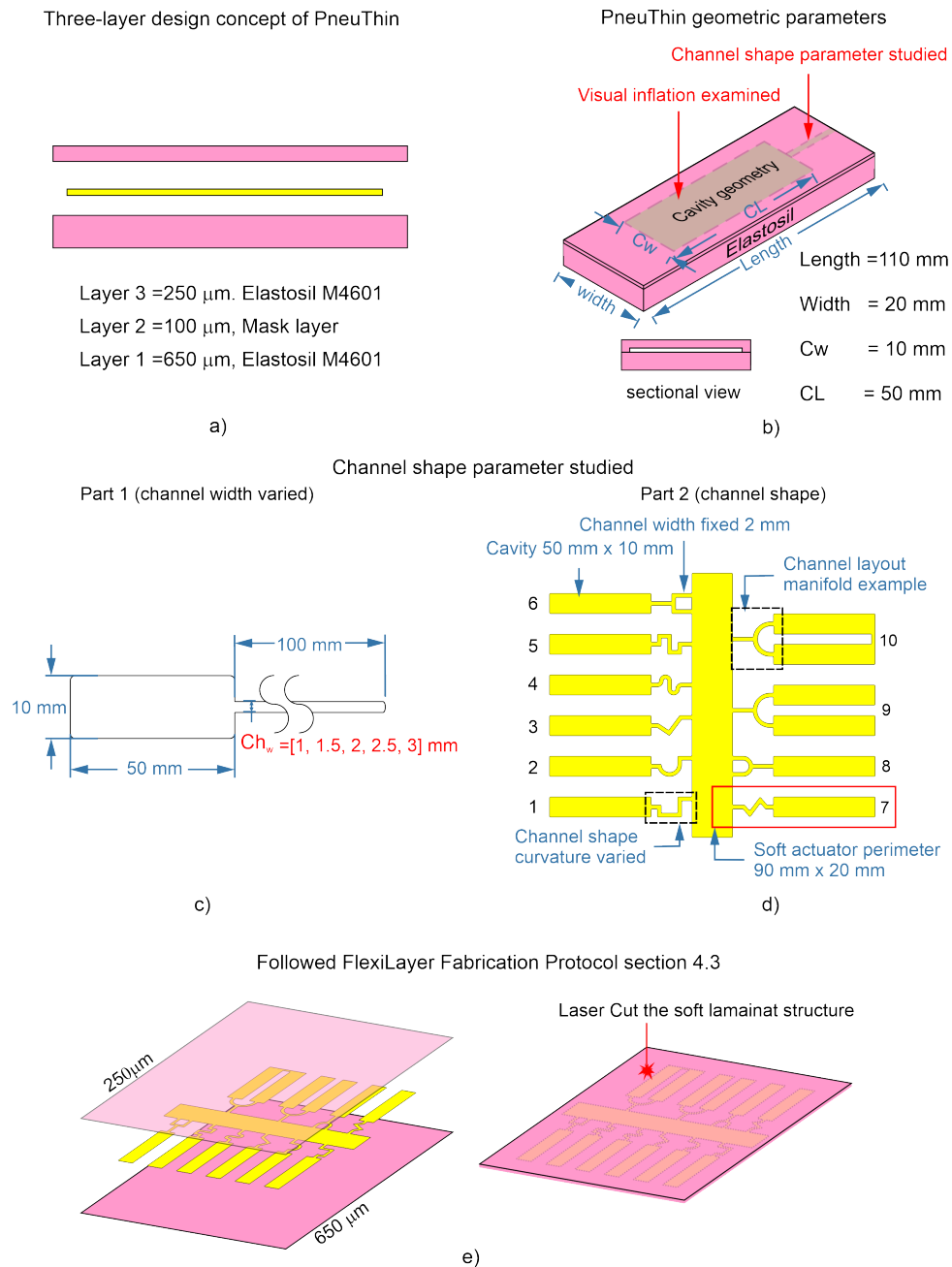


Figure 4.9: PneuThin design characterisation and fabrication analysis: (a) Three-layer structure comprising 650 μm bottom and 250 μm top Elastosil M4601 layers sandwiching a 100 μm mask layer; (b) Key geometric parameters showing cavity dimensions and sectional view with overall length 110 mm, width 20 mm, channel width (Cw) 10 mm, and cavity length (CL) 50 mm; (c) Part 1 of channel study investigating width variations (1-3 mm in 0.5 mm increments); (d) Part 2 examining channel path configurations with fixed 2 mm width, including curved routing and manifold distribution patterns (actuators 1-10); (e) Implementation of FlexiLayer fabrication protocol showing sequential layer formation (left) and laser cutting of the soft laminate structure (right). PneuThin layer stack concept showing three-layer design: 650 μm bottom Elastosil layer, 100 μm PVA mask layer, and 250 μm top Elastosil layer.

4.4.5 Method 5: Integration of Sacrificial Skeleton Features for Complex Cavity Shape Alignment

Building on the challenges identified in Method 4, this experiment investigated the effectiveness of sacrificial skeleton features⁵ in maintaining precise cavity alignment during the FlexiLayer fabrication process. The primary challenge addressed was the difficulty in handling and aligning the delicate 100 μm thick PVA mask layer, particularly for complex cavity layouts. The experimental design tested seven different channel widths ranging from 0.2 mm to 0.8 mm (in increments of 0.1 mm), each with a fixed length of 6 mm. These skeleton features connected to a main cavity (50 mm \times 10 mm) within the standard actuator perimeter of 90 mm \times 20 mm, as shown in Fig. 4.10. Each configuration maintained identical cavity dimensions and overall actuator shape. The fabrication process followed the established FlexiLayer protocol detailed in Section 4.4.4, with the key difference being the PVA mask pattern that incorporates the additional features of the sacrificial skeleton. This modified mask design layout was tested to identify which channel width could prevent leaks while providing support for handling and alignment of the cavity layer.

4.4.6 Method 6: Layer Bonding Strength Characterisation

Building on the stress analysis findings from Chapter 3 and initial fabrication attempts that revealed delamination problems⁶, this experiment quantified the bonding strength between silicone layers using standardised T-peel testing. The investigation was particularly motivated by the observations of Method 5 (channel width study) Section 4.4.4, where layer separation occurred during pneumatic actuation, indicating insufficient adhesion strength.

Following (ISO 11339:2010) standards, T-peel tests were performed using Elastosil M4601 silicone elastomer samples. As illustrated in Fig. 4.11(left), the test configuration consisted of two bonded strips with 25 mm width and 0.7 mm thickness. Fig. 4.11(right) provides the side-view schematic showing the 150 mm bonded length and 50 mm grip sections necessary for proper test alignment. The test specimens were mounted on a tensile testing machine (Instron 5940, Instron, Norwood, MA, USA), with one end separated to create the characteristic T shape for the peeling evaluation. The specimen fabrication

⁵Sacrificial skeleton features are temporary supporting structures integrated into the PVA mask layer during fabrication. These features are designed to dissolve along with the mask layer, leaving only the intended cavity structure in the final actuator.

⁶Delamination occurred during initial fabrication trials in Method 5, during the channel width study. The protocol involved fully curing the first layer for 15 minutes at 75 $^{\circ}\text{C}$ before adding the second layer. After fabrication and pressurisation, actuators failed due to delamination. This started at the edges of the channel, where the stress concentrates. The failure was possibly due to poor bonding due to inadequate curing parameters.

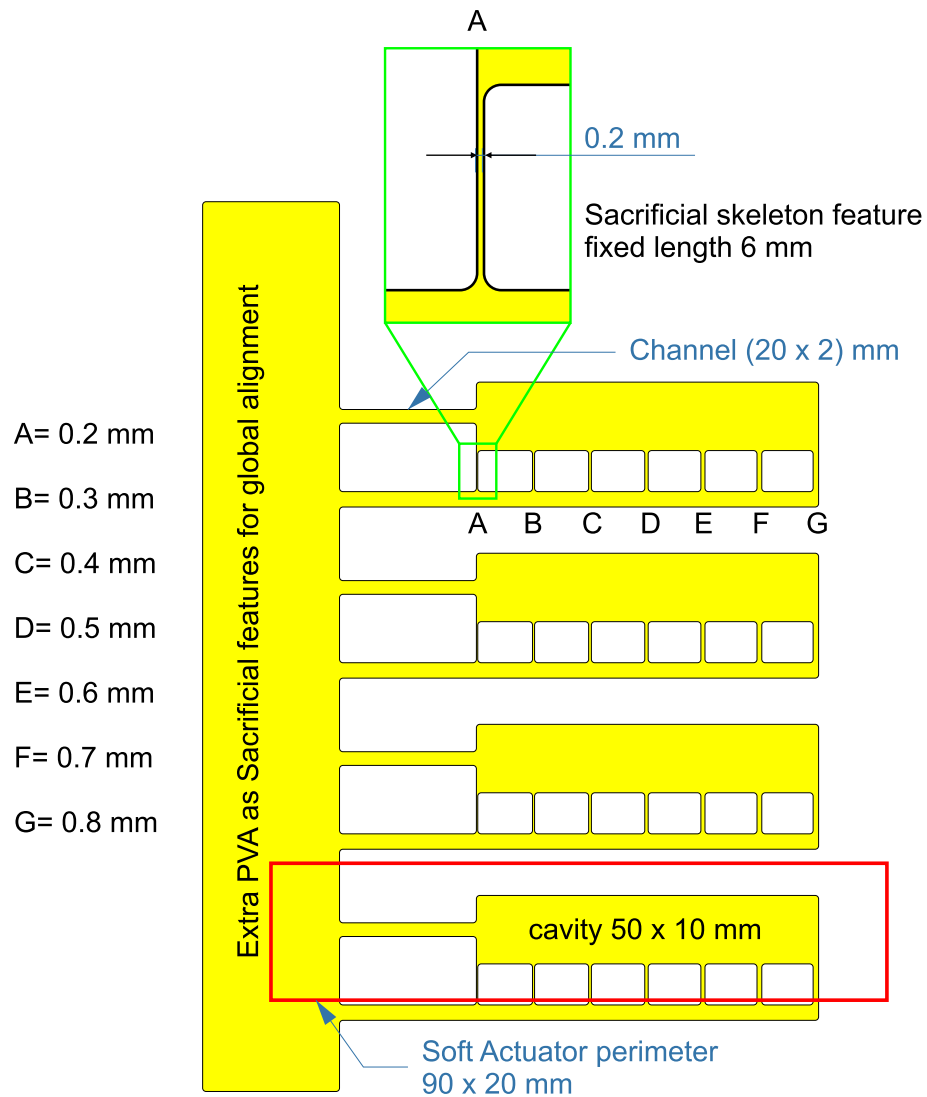


Figure 4.10: Schematic showing the layout of sacrificial skeleton features integrated with the cavity design. Inset A shows detailed dimensions of a single channel (width 0.2 mm). Yellow areas represent the PVA mask pattern to be laser-cut, with channel widths labeled A through G. Extra PVA features along the edge provide global alignment support during fabrication.

process followed the FlexiLayer protocol established in Section 4.4.1. The layered structure, beginning with a base silicone layer that underwent semi-curing at 75 °C for different durations (3, 7, and 15 minutes). A PVA spacer (Solvay, Sulky) was intentionally placed to create the unbonded region necessary for grip attachment, followed by the application of a second silicone layer. The complete assembly was final curing at 75 °C for 15 minutes. The samples were then laser cut according to the specified dimensions to achieve precise test geometries. The test proceeded with an initial preload of 0.5 N, followed by a controlled separation rate of 10 mm/min. The peeling force was recorded continuously until 80 mm of separation was achieved, ensuring consistent data collection throughout the bonded length. Five specimens were tested for each curing condition to ensure statistical reliability.

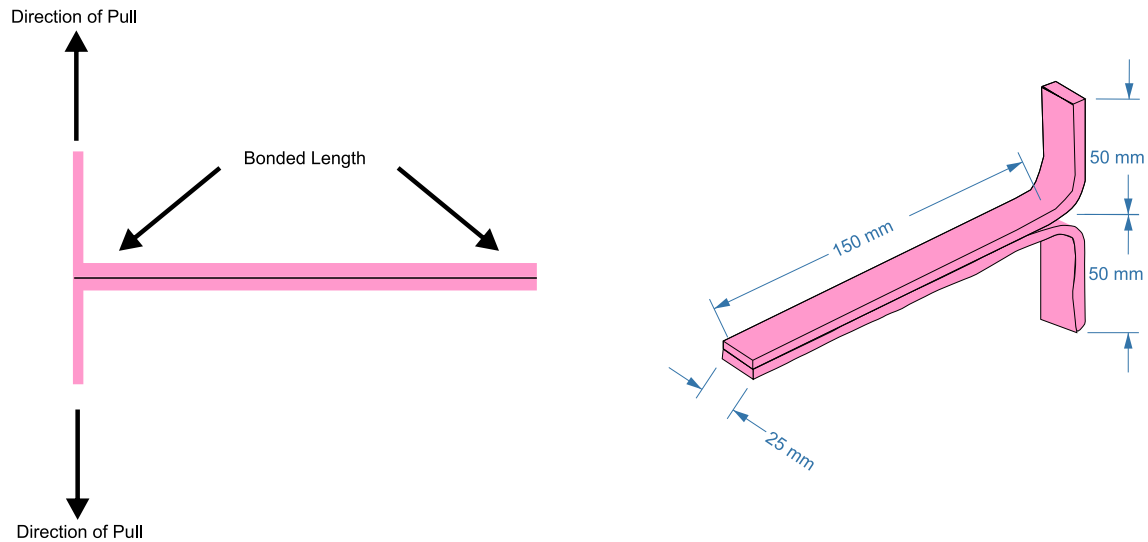


Figure 4.11: T-peel test configuration: (Left) Side-view showing bonded length and pull directions; (Right) Isometric-view schematic with key dimensional parameters for specimen preparation and testing.

The analysis focused on the average peeling force and peel resistance (measured in N/100 mm width), with particular attention to the maximum and minimum values to assess bonding consistency. The results from this investigation directly informed the optimal semi-curing parameters for the FlexiLayer fabrication protocol, addressing the delamination concerns observed in earlier fabrication attempts. Detailed analysis and implications of these findings are presented in Section 4.5.6.

4.5 Results

4.5.1 Results from Layer Thickness Control and Characterisation

Base Layer Formation on Steel Substrate

Fig. 4.12 shows how the DFT changes with different GH when coating silicone layers on steel. Ten different GH from 100 μm to 1000 μm tested, measuring three samples at each GH (60 measurements per sample). A 1:1 reference line (GH = DFT) is included in the figure to illustrate the idealised case where the dry film thickness equals the applied gap height, enabling clearer comparison with the experimental data. The results show that DFT increases predictably with GH, following the equation

$$\text{DFT} = 0.7604(\text{GH}) - 15 \quad (R^2 = 0.9969)$$

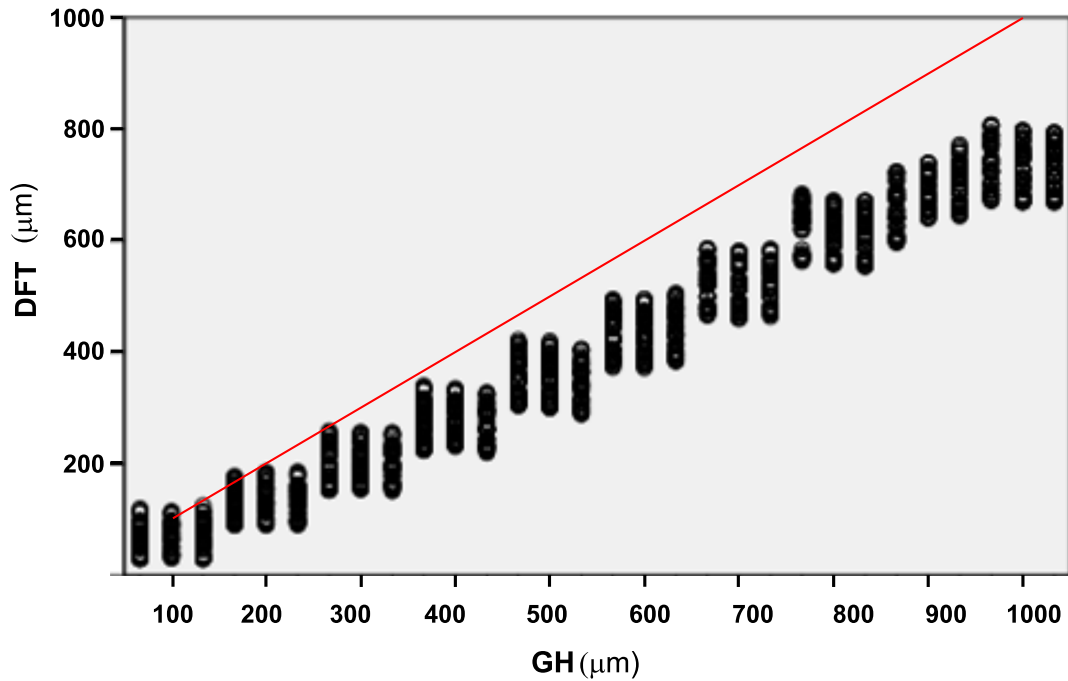


Figure 4.12: Relationship between GH and DFT for silicone layers coated on steel substrates. The graph shows measurements across ten GH settings from 100 to 1000 μm . At each GH setting, three samples were tested ($n=60$ per sample), with five measurements taken at each of the twelve nodes. Black dots represent individual measurements, demonstrating the distribution and variability of coating thickness at each GH value. A red 1:1 reference line is included to illustrate the idealised case where GH equals DFT.

This empirical equation was obtained by applying a linear regression fit to the entire data set in all the tested GH values for silicone coated over a steel substrate. This strong linear relationship means that the DFT based on the GH setting can reliably predicted.

Table 4.4 provides detailed measurements showing that as GH increases, the DFT also increases, while maintaining consistent measurement precision (SEM between 3-5 μm). The reduction ratio stayed fairly constant between 1.3 and 1.5, meaning that the final thickness is consistently about 70% of the initial GH. Table 4.4 shows how the uniformity of the coating improves with larger GH - the variation (CV%) drops significantly from 38.2% at GH = 100 μm to 5.6% at GH = 1000 μm . The thickness mapping profiles for key GH (200, 400, 600, and 800 μm) are shown in (Fig. 4.13a-d), and the remaining profiles are available in Appendix B. These maps help to visualise how thickness varies across the coating. For example, at GH = 200 μm , a thickness of 133 ± 27 μm achieved, while at GH = 800 μm , the thickness reached 620 ± 36 μm . Though the absolute variation in thickness increases at larger GH, the coating becomes uniform relative to its mean thickness.

Table 4.4: DFT measurements for different GH values of layer formation on steel substrate. Values represent mean thickness with standard deviation (n=60 per sample). CV: Coefficient of Variation (%).

GH (μm)	Sample 1 (μm)	Sample 2 (μm)	Sample 3 (μm)	Mean (μm)	Reduction Ratio	CV (%)
100	67 \pm 26	69 \pm 25	68 \pm 28	68 \pm 26	1.50	38.2
200	130 \pm 26	134 \pm 28	134 \pm 27	133 \pm 27	1.50	20.3
300	200 \pm 31	201 \pm 30	200 \pm 31	200 \pm 30	1.50	15.0
400	274 \pm 35	278 \pm 31	270 \pm 32	274 \pm 33	1.46	12.0
500	358 \pm 36	355 \pm 35	345 \pm 35	353 \pm 35	1.42	9.9
600	435 \pm 38	431 \pm 37	441 \pm 37	436 \pm 37	1.38	8.5
700	527 \pm 37	520 \pm 37	524 \pm 36	524 \pm 36	1.34	6.9
800	630 \pm 38	616 \pm 35	614 \pm 37	620 \pm 36	1.29	5.8
900	654 \pm 40	686 \pm 31	700 \pm 35	680 \pm 35	1.32	5.1
1000	736 \pm 42	726 \pm 41	726 \pm 40	729 \pm 41	1.37	5.6

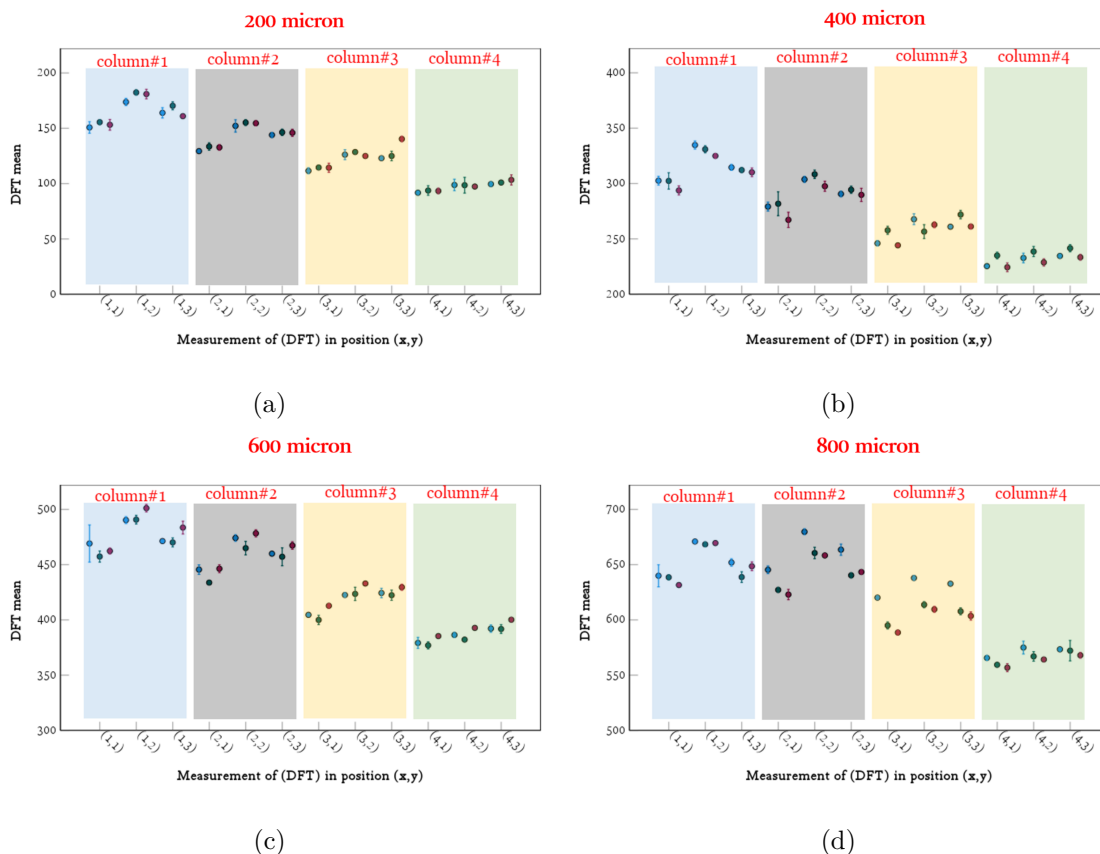


Figure 4.13: Thickness distribution maps showing the DFT measurements of the SL1 coated onto a steel substrate. The measurements demonstrate spatial variations across 12 nodes, with 5 measurements per node, yielding 60 measurements per sample. Three samples are presented in each plot (shown in blue, green, and magenta) for tested GH of 200, 400, 600, and 800 μm , with error bars indicating ± 1 standard deviation.

Table 4.5: Statistical analysis of dry film thickness measurements for second silicone layer (SL2)

Gap height (μm)	Sample DFT (μm)			Mean (μm)	SD (\pm)	CV (%)
	1	2	3			
200	141 \pm 14	140 \pm 13	138 \pm 16	140	13	9.3
400	291 \pm 15	279 \pm 17	282 \pm 15	284	14	4.9
600	432 \pm 19	442 \pm 16	443 \pm 13	439	15	3.4
800	610 \pm 19	600 \pm 18	611 \pm 17	607	17	2.8

The DFT of a Silicone Layer Coated onto a Dry Silicone Layer

A strong linear correlation is observed between GH and DFT when a silicone rubber layer (ELASTOSIL® M 4601 A/B) is applied on a pre-cured silicone surface, as described by the equation $\text{DFT} = 0.7565\text{GH} - 8.6$ and $R^2 = 0.9986$. This empirical equation was obtained by applying a linear regression fit to the entire dataset across all tested GH values for silicone coated over a previously cured silicone substrate. Three samples were tested at each GH (200, 400, 600, and 800 μm), showing consistent results in all measurements. Fig. 4.14a-d, display the thickness distribution patterns in different positions for each GH setting. The uniformity of the thickness improved significantly compared to the coating on steel, with CV values of 9.3% for 200 μm , 4.9% for 400 μm , 3.4% for 600 μm , and 2.8% for 800 μm , as summarised in Table 4.5. The mean DFT values achieved were $140 \pm 13 \mu\text{m}$, $284 \pm 14 \mu\text{m}$, $439 \pm 15 \mu\text{m}$, and $607 \pm 17 \mu\text{m}$ for the respective GHs. This indicates that coating silicone on silicone produces uniform layers than coating on steel, with thickness variations decreasing as GH increases.

The improved uniformity is attributed to the first silicone layer compensating for substrate flatness defects, creating a uniform surface for subsequent coating. Fig. 4.15a provides direct evidence for this conclusion by comparing the standard deviations (SD) of the thickness measurements at different reference points. The schematic shows that SD3, which represents the thickness variation of SL2 relative to SL1, is significantly smaller than both SD1 (variation of SL1 relative to steel) and SD2 (variation of SL2 relative to steel). Fig. 4.15b demonstrates this effect quantitatively through thickness distribution patterns for GH = 100 μm . When measured against the steel substrate, the direction of the coating matters significantly: the forward coating shows a decrease in thickness (blue points, 100 to 40 μm), while the reverse coating shows an increase in thickness (green points, 20 to 100 μm). However, when SL2 is measured relative to SL1, these directional variations diminish substantially. This reduction in variance ($\text{SD3} < \text{SD1}, \text{SD2}$) confirms that the first silicone layer effectively masks the surface irregularities of the substrate, providing a

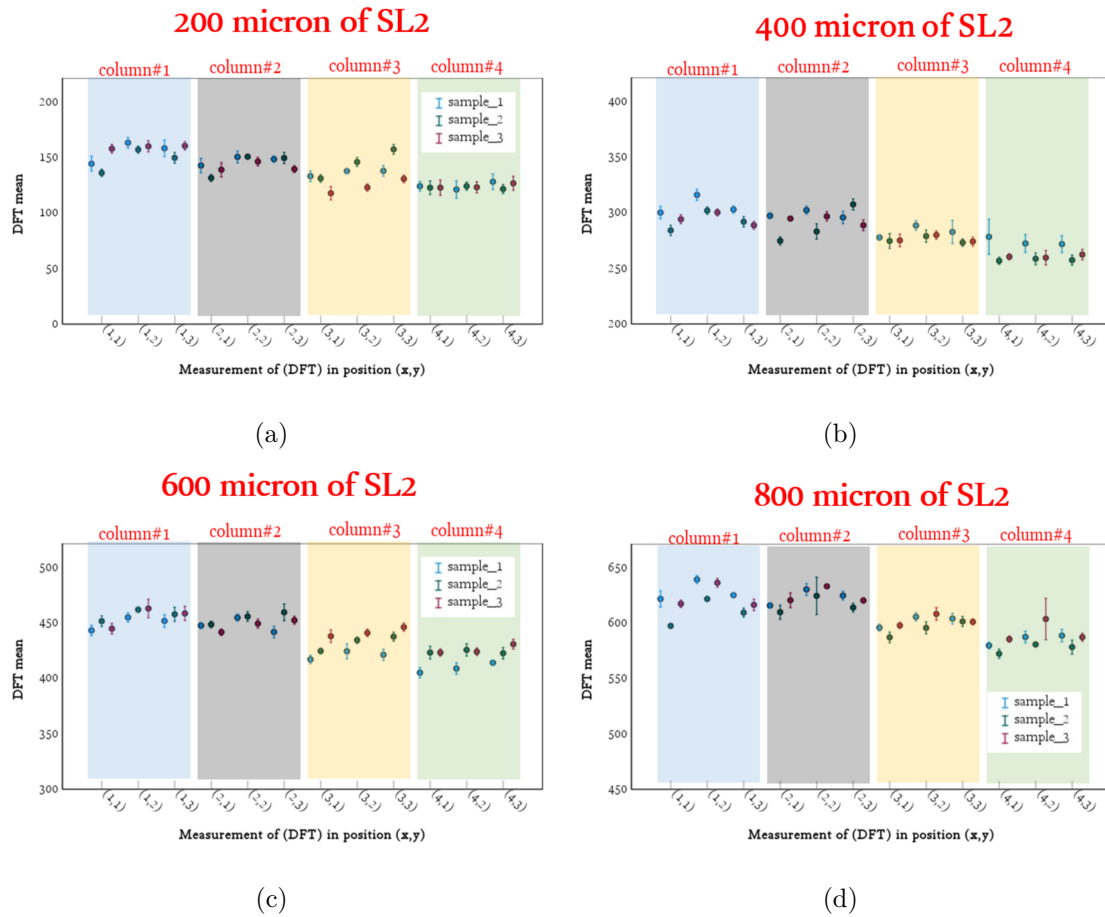


Figure 4.14: Thickness distribution maps showing the DFT measurements of the SL2 coated onto a previously cured silicone substrate. The measurements demonstrate spatial variations across 12 nodes, with 5 measurements per node, yielding 60 measurements per sample. Three samples are presented in each plot (shown in blue, green, and magenta) for GH of 200, 400, 600, and 800 μm , with error bars indicating ± 1 standard deviation.

uniform foundation for subsequent layer deposition.

silicone Formation Over Release Film (PVA)

The thickness measurements of the silicone layers coated on the PVA release film with $GH_{\text{experiment}} = 400 \mu\text{m}$ demonstrated a uniform formation behaviour. Fig. 4.16a shows the thickness distribution map in the measurement grid, achieving an average thickness of $275 \pm 11 \mu\text{m}$ with a coefficient of variation of 3.98%. The thickness measurements maintained consistency across all twelve measurement positions, indicating stable layer formation over the PVA substrate.

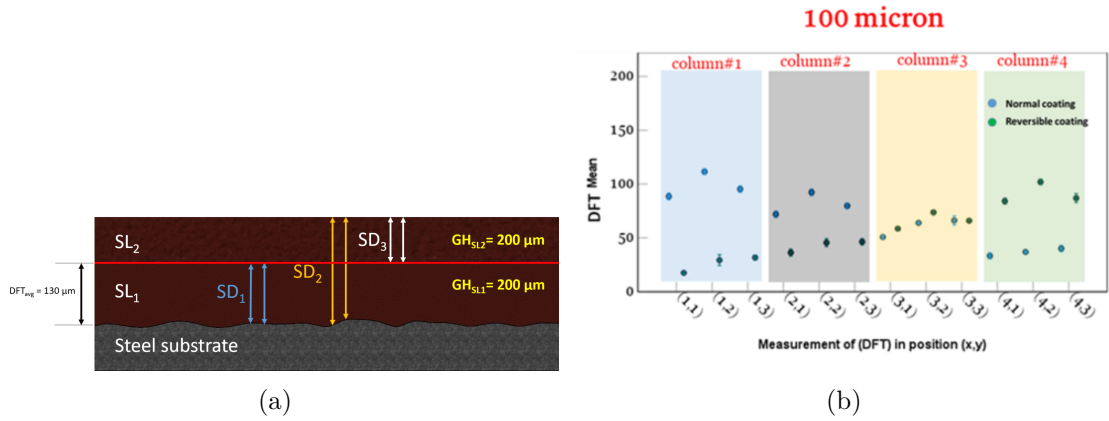


Figure 4.15: Analysis of layer thickness variation: (a) Schematic illustration of standard deviation (SD) measurements for silicone layers. SL1: first silicone layer; SL2: second silicone layer; SD1: standard deviation of SL1 thickness relative to steel substrate; SD2: standard deviation of SL2 thickness relative to steel substrate; SD3: standard deviation of SL2 thickness relative to SL1. Both layers fabricated with $GH = 200 \mu\text{m}$. Note that $SD3 < SD1$ and $SD2$, indicating improved thickness uniformity when measuring relative to the previous silicone layer rather than the steel substrate. (b) DFT distribution for $GH = 100 \mu\text{m}$ showing the effect of coating direction. Blue points represent normal (forward) coating direction, showing thickness decrease from 100 to $40 \mu\text{m}$ relative to steel substrate. Green points show reverse coating direction, with thickness increase from 20 to $100 \mu\text{m}$. Measurements taken at twelve positions (x,y) across four columns. The contrasting trends demonstrate the impact of substrate flatness on coating uniformity

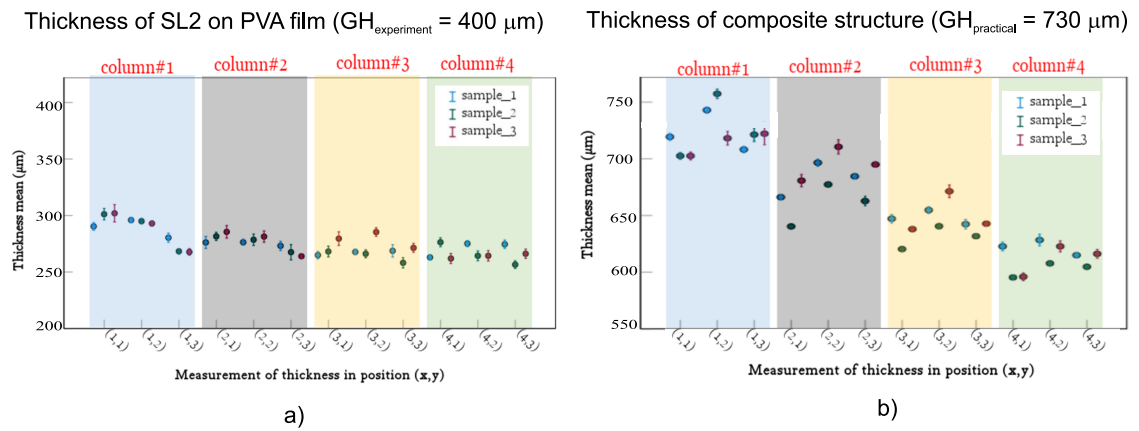


Figure 4.16: Thickness distribution analysis across measurement positions (x,y): (a) Second silicone layer coated on PVA release film with gap height $400 \mu\text{m}$, showing average thickness $276 \pm 11 \mu\text{m}$ ($CV = 3.98\%$); (b) Composite structure combining first silicone layer, strain-limiting layer and second silicone layer, demonstrating average thickness $664 \pm 44 \mu\text{m}$ ($CV = 6.63\%$). Measurements taken across four columns (shaded regions) with three independent samples.

Integration with Strain-Limiting Materials

Fig. 4.16b presents thickness measurements for a multilayer structure fabricated using approach 4 from Section 4.4.1. The structure combines a first silicone layer (SL1, $DFT = 130 \mu\text{m}$), strain limiting layer ($200 \mu\text{m}$) and a second silicone layer (SL2, $GH = 400 \mu\text{m}$).

Measurements in three samples yielded an average thickness of $664 \pm 44 \mu\text{m}$ with a CV of 6.63%. The red line at $730 \mu\text{m}$ represents the target thickness based on the cumulative layer measurements.

4.5.2 Results from PVA Mask Layer Alignment Analysis

Fig. 4.17a compares two methods for placing release films - manual placement and a vacuum chuck. The left image shows manual placement with visible misalignment, while the right image shows the vacuum chuck method that achieves precise alignment with the marked outline. Each method was tested five times to measure the distance the film shifted from its target position and the degree of rotation from its intended angle. Fig. 4.17b presents the results of the measurement of these tests. Manual placement showed large errors, up to 4 mm in position shift and 3 degrees in rotation. The vacuum chuck performed much better, keeping both position and rotation errors under 1 mm and 1 degree. This indicates that the vacuum chuck method achieves four times better accuracy than manual placement, making it reliable for creating consistent actuators.

4.5.3 Results from Laser Cutting Test

Results from Laser Cut Path Analysis

Fig. 4.18 shows the alignment accuracy between the designed perimeter outlines and actual laser cut paths for PneuThin fabrication. The left panel displays multiple actuator patterns with their corresponding cut paths, while the right inset provides a magnified view for detailed inspection. Measurements in multiple samples showed a maximum misalignment of less than 1 mm per cm between the designed outlines and the actual cut paths. The magnified inset (with 1 mm scale bar) demonstrates this precision, particularly visible in the comparison between the perimeter outline and the green laser cut path. This indicates that the FlexiLayer fabrication method can consistently achieve submillimeter precision in geometric accuracy for PneuThin production.

Results from Preliminary Laser Cutting Parameters Testing

Building on the test methodology described in Section 4.4.3, Fig. 4.19 shows the laser cut quality analysis of 1 mm thick Elastosil M4601 layers using different power and speed combinations. The top inset image demonstrates a clean cut achieved with 30% power and 5% speed settings. In contrast, the bottom inset shows thermal damage when using 50% power and 1% speed, showing significant melting and discolouration around the cut

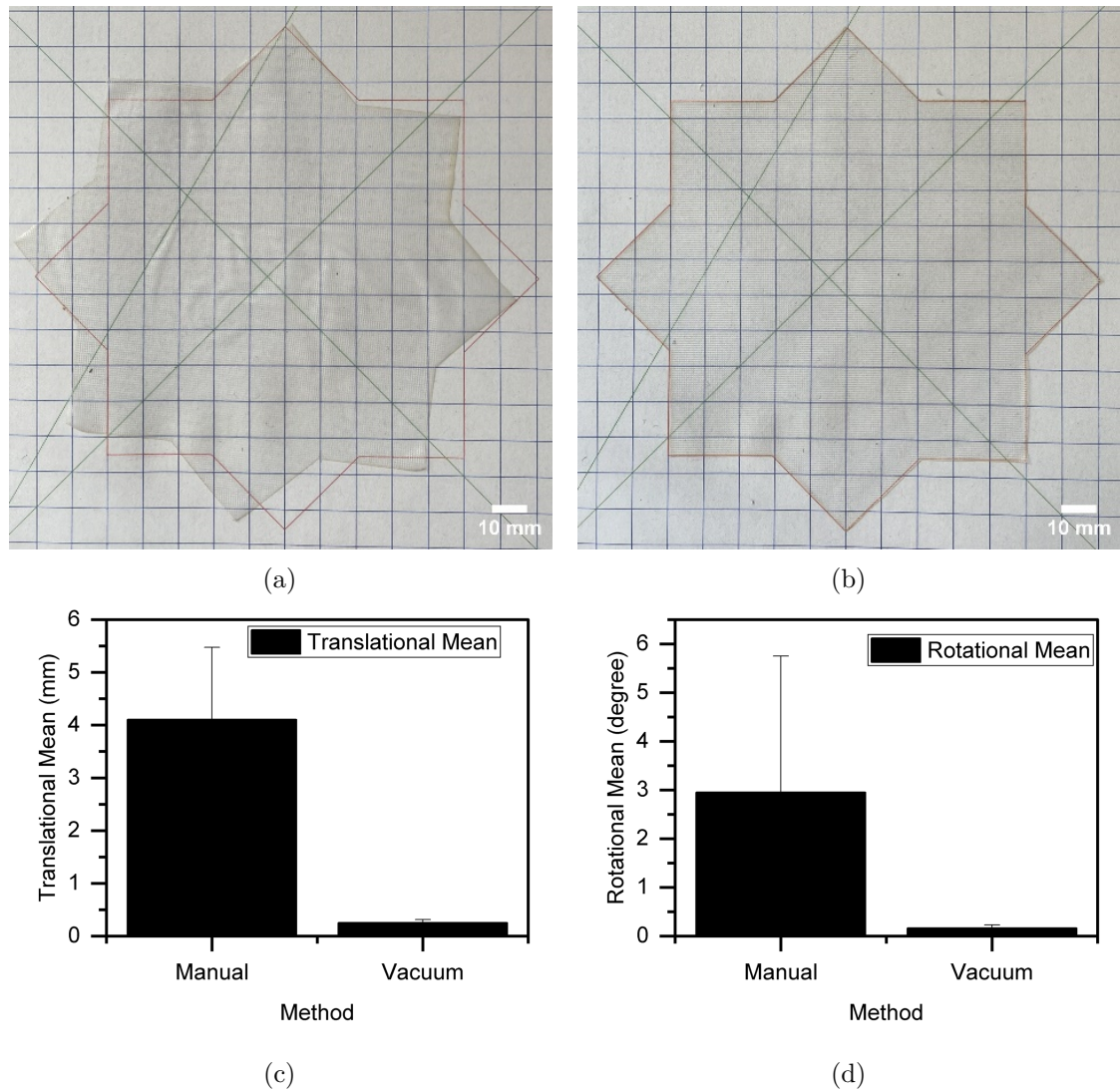


Figure 4.17: Comparison of alignment methods and quantitative analysis. (a,b) Visual comparison between manual alignment and vacuum chuck alignment, with red outline indicating target perimeter area. (c,d) Quantitative measurements showing mean values with error bars (± 1 standard deviation, $n=5$) for translation error in millimeters and rotation error in degrees, respectively.

edges. Based on the initial testing stages that identified 5-50% power and 5-20% speed as promising ranges, further testing refined these parameters. The results showed that effective cutting could be achieved using single or multiple pass methods, as summarised in Table 4.6. This indicates that controlled power and consistent speed settings produce cleaner cuts in Elastosil M4601 compared to high-power cutting methods.

4.5.4 Results from Channel Layout Study

The investigation of channel geometry yielded two key sets of findings related to PneuThin's air transfer capabilities. **Channel Width Study**; the five channel width variations (1.0,

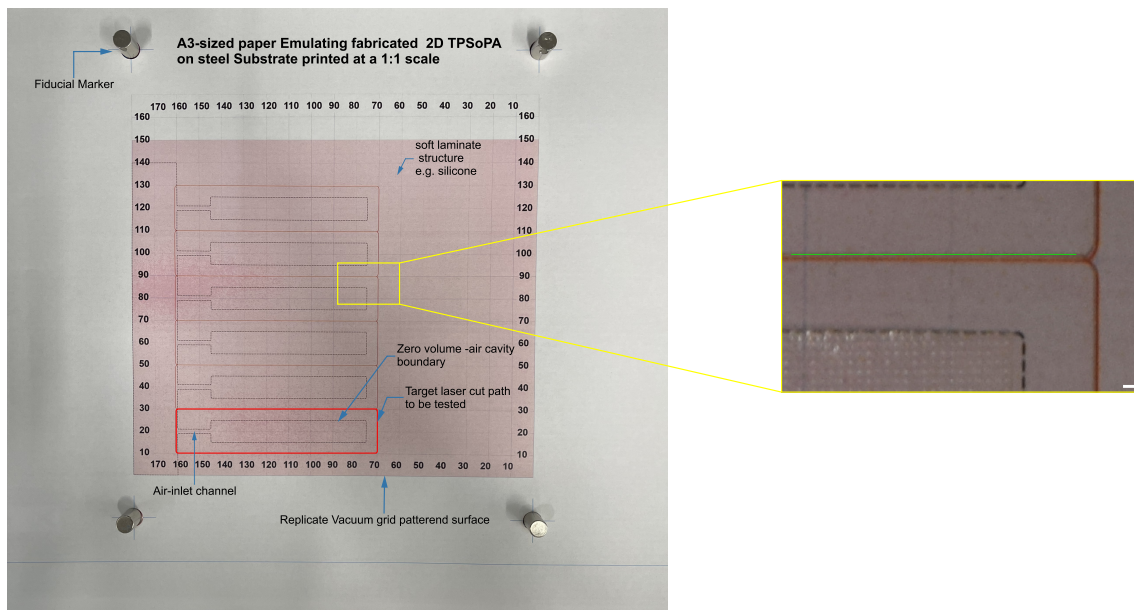


Figure 4.18: Laser cut path alignment analysis for PneuThin fabrication. Left: Multiple actuator patterns showing perimeter outlines (red) and corresponding laser cut paths (brown) on an A3-sized steel substrate with fiducial markers. Right inset: Magnified view comparing design outline to actual cut path (green), demonstrating alignment precision with 1 mm scale bar.

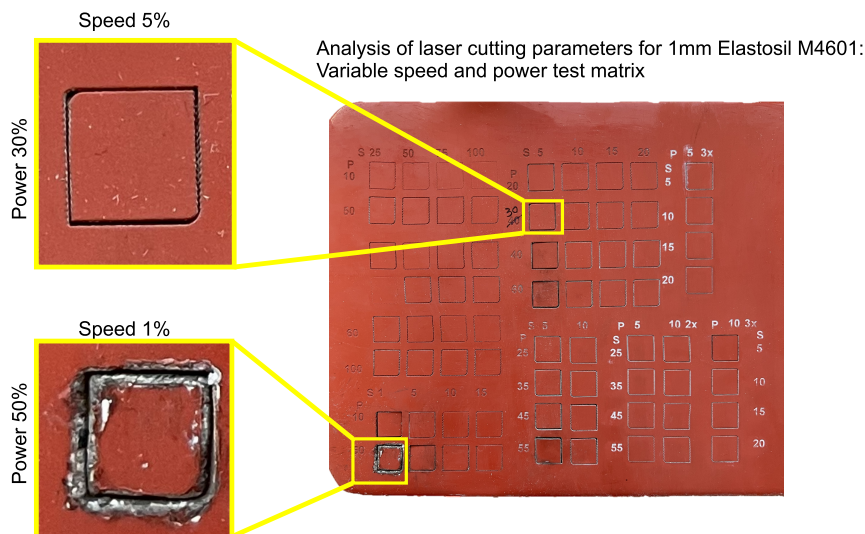


Figure 4.19: Laser cut quality analysis for 1 mm thick Elastosil M4601. Top inset shows a clean cut achieved with 30% power and 5% speed. Bottom inset demonstrates thermal damage using 50% power and 1% speed.

1.5, 2.0, 2.5, and 3.0 mm) successfully transferred air to their respective cavities at 1 psi pressure. Visual confirmation showed complete cavity inflation in each case. Each actuator demonstrated consistent inflation behaviour regardless of channel width. This indicates that even the narrowest channel (1.0 mm) provides sufficient air transfer for PneuThin operation. **Channel Configuration Study**; all tested channel designs successfully transferred air at 1 psi pressure, regardless of path complexity. The seven basic actuators demonstrated

Table 4.6: Effective laser cutting parameters for 1 mm thick Elastosil M4601

Method	Speed (%)	Power (%)
Single Pass	5	25
Single Pass	5	30
Single Pass	5	35
Single Pass	5	40
Multiple Pass (3x)	5	10

successful inflation with smooth and sharp curved channels. The branched manifold designs (actuators 8-10) achieved simultaneous inflation of multiple connected cavities. This indicates that PneuThin’s zero-volume channel architecture can effectively distribute air in both single and multi-actuator configurations, supporting the development of complex soft robotic systems.

4.5.5 Results from Sacrificial Skeleton Testing

Following the test procedure outlined in Section 4.4.5, the leak testing of each fabricated actuator was carried out underwater at three different pressure levels (4, 5, and 6 psi). Through submerged observation, the 0.2 mm channel width configuration demonstrated no air bubble formation at any pressure level, while actuators with wider channels showed various degrees of leakage. This indicates that the 0.2 mm channel width successfully maintains structural integrity while providing the necessary support for cavity alignment. These findings establish a key design parameter for the FlexiLayer fabrication technique that will guide the development of future actuator designs in Chapter 5.

4.5.6 Results from Layer Bonding Analysis

Fig. 4.20a illustrate the distinct failure modes observed at different semi-curing times. At 3 minutes of cure time, the specimens exhibited substrate failure⁷ with complete material rupture, while 7 and 15 minute cure times showed adhesive failure⁸ at the interface (Fig. 4.20a). These different failure modes directly influenced the measured peel strengths. Table 4.7 summarises the failure characteristics and bond strengths between curing times. The 15-minute cure specimens showed the lowest peel strength (0.51 ± 0.02 N/100 mm), with minimum and maximum values of 0.49 ± 0.04 N/100 mm and 0.59 ± 0.10 N/100 mm respectively, as detailed in Table 4.8. The 7-minute cure specimens demonstrated

⁷Substrate failure: Complete rupture/tearing of the base material itself before any separation at the bonded interface occurs, indicating that the bond strength exceeds the material strength.

⁸Adhesive failure: Smooth separation occurs at the interface between the bonded layers, where the two surfaces separate without material damage, allowing direct measurement of the bond strength

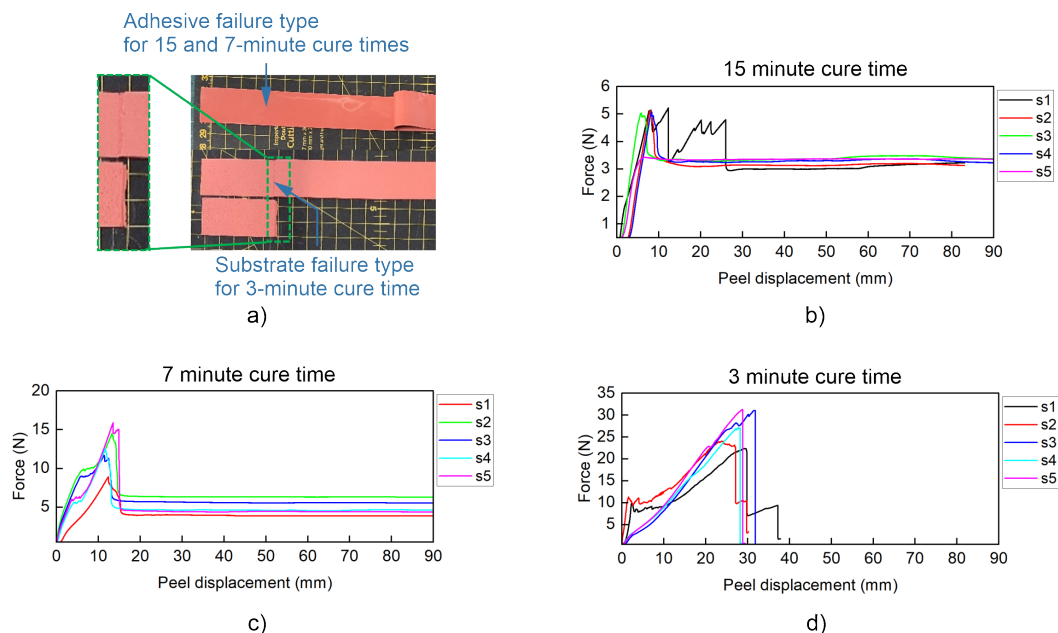


Figure 4.20: T-peel test analysis at different semi-cure times: (a) Representative specimens showing adhesive failure mode at 15 and 7 minutes versus substrate failure at 3 minutes; force-displacement response for (b) 15-minute, (c) 7-minute, and (d) 3-minute semi-cure times, demonstrating five specimens per condition (s1-s5).

Table 4.7: Summary of failure characteristics and bond strengths across semi-cure times

Semi-Cure Time (min)	Peel Strength (N/100mm)		Failure Mode
	Average \pm SD	Range (Min - Max)	
3	$>2.09^*$	N/A	Substrate
7	0.75 ± 0.17	$0.73 \pm 0.20 - 0.81 \pm 0.14$	Adhesive
15	0.51 ± 0.02	$0.49 \pm 0.04 - 0.59 \pm 0.10$	Adhesive

*Minimum threshold value, actual bond strength exceeds substrate strength

moderately higher values with an average peel strength of 0.75 ± 0.17 N/100 mm, ranging from 0.73 ± 0.20 N/100 mm to 0.81 ± 0.14 N/100 mm (Table 4.9). Both conditions exhibited consistent adhesive failure modes with complete interface separation.

For the 3-minute cure condition, all specimens experienced substrate failure at significantly higher forces (23.0 ± 5.8 N). Although complete peel strength measurement was not possible due to substrate failure, the maximum force before failure indicates that the bond strength exceeded 2.09 N/100 mm. The force-peel displacement curves for each curing condition are provided in Fig. 4.20b-d. The force-displacement behaviour varies significantly with curing time. For full curing (15 minutes at 75°C, Fig. 4.20b), the samples show consistent adhesive failure with force plateaus around 3-4 N and stable peeling until 100 mm displacement. Semi-curing for 7 minutes (Fig. 4.20c) produces higher initial peak forces (10-14 N) followed by stable adhesive failure with forces between 4-6 N. The shortest semi-cure time of 3 minutes (Fig. 4.20d) results in substrate failure, with specimens showing

Table 4.8: T-peel test results for fully cured specimens at 75 °C for 15 minutes

Specimen	Peel Force (N)			Peel Strength (N/100mm)			Type of Failure
	Average	Maximum	Minimum	Average	Maximum	Minimum	
1	3.05	4.80	2.94	0.49	0.77	0.47	Adhesive
2	3.13	3.17	3.12	0.50	0.51	0.50	Adhesive
3	3.40	3.48	3.29	0.54	0.56	0.53	Adhesive
4	3.28	3.37	3.21	0.52	0.54	0.51	Adhesive
5	3.11	3.50	2.68	0.50	0.56	0.43	Adhesive
Mean	3.19 ± 0.14	3.66 ± 0.64	3.05 ± 0.24	0.51 ± 0.02	0.59 ± 0.10	0.49 ± 0.04	

Table 4.9: T-peel test results for semi-cured specimens (7 minutes at 75°C)

Specimen	Peel Force (N)			Peel Strength (N/100mm)			Type of Failure
	Average	Maximum	Minimum	Average	Maximum	Minimum	
1	3.41	5.08	2.95	0.55	0.81	0.47	Adhesive
2	3.85	4.01	3.74	0.62	0.64	0.60	Adhesive
3	6.30	6.34	6.27	1.01	1.01	1.00	Adhesive
4	5.55	5.69	5.49	0.89	0.91	0.88	Adhesive
5	4.60	4.67	4.51	0.74	0.75	0.72	Adhesive
6	4.37	4.46	4.31	0.70	0.71	0.69	Adhesive
Mean	4.68 ± 1.08	5.04 ± 0.86	4.55 ± 1.24	0.75 ± 0.17	0.81 ± 0.14	0.73 ± 0.20	–

steep force increases up to 20-30 N before material tearing occurs at 30 peel displacement. This behaviour indicates that shorter semi-cure times promote stronger interfacial bonding, exceeding the material's bulk strength.

4.6 Discussion

The development of precise thickness control represents a fundamental advance in the fabrication of a controlled bending motion of PneuThin. The results demonstrate predictable and controllable layer formation, with final thickness consistently achieving approximately 76% of the initial GH setting ($DFT = 0.7604(GH) - 15$, $R^2 = 0.9969$). Published studies of doctor blade coating indicate that thickness reductions commonly occur during curing, with PDMS films shrinking between 40-78% from wet state to final cured thickness (Zhao et al., 2017). Although these findings confirm thickness reduction as an inherent aspect of the coating process, the FlexiLayer approach achieves consistent results, maintaining a predictable reduction 24% across different GHs.

The initial coating on steel exhibits thickness variations (CV) that improve from 20% at 400 μm to 5.8% at 800 μm GHs. The linear decrease in thickness observed from column 1 to column 4, as shown in Fig. 4.13a-d, is attributed to flatness defects in the steel substrate. This interpretation is further supported by the results shown in Fig. 4.15(b), where coating at a 100 μm GH in two opposite directions revealed a directional dependence: coating from left to right produced a decreasing thickness trend, while coating from right to left resulted

in an increasing trend. This behaviour confirms that the thickness variation originates from substrate flatness rather than the coating process itself. Significantly, coating silicone on previous silicone layers substantially improves uniformity - CV values decrease to 9.3% at 200 μm and 2.8% at 800 μm . This improvement enables reliable fabrication of multilayer structures, with the first silicone layer effectively mitigating substrate surface irregularities. This understanding directly influenced the fabrication protocol for the eight actuator designs presented in Chapter 5. The protocol specifies depositing the thick layer first, as this layer experiences minimal expansion during actuation, when bending motion desired. This approach addresses the higher coefficient of variation observed in silicon-on-steel deposition, which could otherwise lead to non-uniform expansion in the actively deforming thin layer. By positioning the thick layer against the steel substrate, the protocol ensures controlled and predictable bending behaviour in the final actuator. The investigation of silicone formation over PVA release film focused on $GH_{\text{experiment}} = 400 \mu\text{m}$ as a representative test case for several compelling reasons. First, this GH represents a median value within the working range established in Stage 2, making it suitable for validation purposes. Second, a direct comparison of the coating results at this GH revealed a minimal difference between the two Stages: silicone-on-silicone achieved $284 \pm 14 \mu\text{m}$ while silicone-on-PVA yielded $275 \pm 11 \mu\text{m}$, representing only a 3.2% difference in average thickness. This small variation, combined with similar coefficients of variation (4.9% for silicone-on-silicone versus 3.98% for silicone-on-PVA), provided strong evidence that the behaviour of layer formation remains consistent regardless of the underlying substrate. Third, this close correlation between the two Stages indicated that the model developed for silicone-on-silicone coating could reliably predict layer formation over PVA release film, eliminating the need for extensive testing across multiple GHs.

The T-peel test results reveal a fundamental change in the failure mechanism with curing time. For the 3-minute cure condition, the consistently high forces ($23.0 \pm 5.8 \text{ N}$) required to cause substrate failure rather than interface separation demonstrate that the bond strength exceeds the inherent strength of the material (Unger et al., 2000). This is visually evidenced by the tear in the base material shown in Fig. 4.20, where a complete substrate rupture occurred before any interface separation could begin. The dramatic difference in maximum forces between cures of 3 minutes (23.0 N) versus cures of 7 minutes (6.34 N) and 15 minutes (4.80 N) indicates that shorter cure times create significantly stronger interfacial bonds. This aligns with the theory of polymer chain mobility, where partially cured surfaces maintain higher molecular mobility for the formation of strong

intermolecular bonds (Unger et al., 2000). Visual evidence of substrate failure in all six 3-minute specimens provides compelling proof that this curing condition maximises bonding strength. These findings strongly support the adoption of a 3-minute semi-curing protocol for the FlexiLayer fabrication process. While this condition requires careful handling due to surface tackiness, it ensures that the interface bonding strength exceeds the material's cohesive strength - a crucial factor for actuator reliability under operational pressures. This characteristic directly addresses the stress concentration concerns identified in Chapter 3's FEM analysis Fig. 3.11. The fabrication process described in this chapter ensures a controlled and predictable bending behaviour in the final actuator, addressing key requirements identified during preliminary FEM analysis (Chapter 1) to achieve reliable actuation performance.

4.7 Chapter Summary

This chapter presents the development of the FlexiLayer fabrication technique, a new method that combines doctor blade coating and laser cutting to PneuThin. Building on Chapter 3's FEM analysis, The focus was placed on three main objectives: developing an automated blade coating platform, establishing a reliable layer-by-layer assembly process, and characterising critical fabrication parameters.

The LBCM was built as the main tool. This machine combines a commercial casting knife applicator with an automated motion system to precisely control the GH and coating speed. Characterisation revealed clear relationships between the GH and the final DFT. For the first layer on the steel substrate, the thickness of the dry film follows $DFT = 0.7604(GH) - 15$ ($R^2 = 0.9969$). The second layer, coated on cured silicone, shows a similar relationship: $DFT = 0.7565(GH) - 8.6$ ($R^2 = 0.9986$). Importantly, the second layer demonstrates better thickness uniformity than the first, with the coefficient of variation improving from approximately 38% to 3%. This improvement occurs because the first layer helps to level out the irregularities in the steel substrate.

Several key processes were developed to ensure precise fabrication. A custom vacuum chuck achieves cavity placement accuracy within 1mm, four times better than manual alignment. For layer bonding, It was found that a three-minute partial cure at 75 °C creates the strongest interface, demonstrated by substrate failure rather than delamination in peel tests. The laser cutting parameters (25-40% power at 5% speed) produce clean edges with alignment precision within 1 mm/cm.

Investigation of channel configurations confirmed successful air transfer through both

simple and complex channel designs. All channel widths tested effectively delivered air to their cavities at a pressure of 1 psi, enabling consistent actuation. Importantly, this success extended to branched manifold designs, demonstrating that our zero-volume channel architecture can distribute air effectively in multi-actuator systems. This capability is crucial for developing complex soft robotic structures (see details in Section 5.4). Chapter 5 will validate this fabrication process through experimental testing of PneuThin with different geometric configurations.

Chapter 5

Characterisation and Case Studies of PneuThin

5.1 Introduction

This chapter experimentally validates the FlexiLayer fabrication technique developed in Chapter 4. Based on the preliminary FEM analysis (Chapter 3) and the established fabrication protocol (Chapter 4), the design, fabrication and characterisation of PneuThin are presented. Through evaluation of fabricated actuators and demonstration of practical in a set of two case studies, both the reliability and flexibility of the FlexiLayer technique are validated.

Primary Objectives

The primary objectives of this chapter are:

1. Characterise PneuThin performance through evaluation of geometric parameters (cavity shapes, cavity widths, layer thicknesses) and their influence on the actuation behaviour.
2. Validate the reliability of fabrication through the quantitative analysis of actuator deformation profiles (e.g. bending angle) and force generation capabilities.
3. Demonstrate technique flexibility and scalability through fabrication of functional prototypes in case studies for (multi-gait robot and soft gripper).

The experimental results presented here provide the foundation for the refined FEM analysis in Chapter 6.

5.2 PneuThin Characterisation Methods

5.2.1 Actuator Design Configurations

The experimental testing examined eight distinct PneuThin configurations, varying key geometric parameters while maintaining consistent overall dimensions of 60 mm in length, 20 mm in width and 1 mm total thickness; see Fig. 5.1. The design concept follows the principles established in Section 3.3. Each configuration in Fig. 5.1 was fabricated following the FlexiLayer process described in Section 4.3.1 and Figs. 4.2 and 4.4. The configurations follow a consistent naming convention where the first letter indicates the cavity shape (R for rectangular, T for triangular, O for oval), followed by the cavity width in millimetres, and then 'd' with a number showing the thickness difference between layers in micrometres. For example, R10-d400 represents a rectangular cavity of 10 mm width with a 400 μm thickness difference between layers. When a strain-limiting layer is included, 'sl' is added as a suffix. The investigation examined four key parameters: layer thickness distribution ranging from 0 to 400 μm difference, three cavity shapes (rectangular, triangular, oval), three cavity widths (5, 10, 15 mm) and the integration of a strain limiting layer. Throughout all configurations, certain structural elements remained constant: a cavity length of 50 mm, a cavity thickness of 0.1 mm, total actuator thickness of 1 mm, and a basic three-layer structure consisting of a thick silicone layer, a cavity layer, and a thin silicone layer Fig. 3.2. This variation of the design parameters builds on the FEM analysis presented in Chapter 3, allowing validation of the flexibility of the FlexiLayer technique through detailed experimental characterisation in subsequent sections.

5.2.2 Bending Angle Measurement

An experimental setup was developed to characterise the bending response of the eight PneuThin configurations (detailed in Section 5.2.1, Fig. 5.1). The experimental setup consisted of a rigid holder that fixed one end of the actuator in a cantilever configuration, allowing free bending in the vertical plane parallel to gravity. A high-resolution camera, positioned perpendicular to the bending plane, captured images for subsequent analysis. Prior to formal bending angle measurements, a preliminary cyclic test was conducted on the R10-d400 actuator at 3.5 psi for ten cycles. This initial assessment revealed a noticeable increase in bending angle over the first several cycles, suggesting strain softening

Actuator configuration						
No.	Design Label	Cavity Shape	Cavity Width, cw (mm)	Thickness Difference (μm)	Strain-Limiting Layer	Figure/Diagram
1	R10-dzero	Rectangular	10	0 $t_1 = 450 \mu\text{m}$ $t_2 = 450 \mu\text{m}$	No	$t_2 - t_1 = 0 \mu\text{m}$
2	R10-d200	Rectangular	10	200 $t_1 = 550 \mu\text{m}$ $t_2 = 350 \mu\text{m}$	No	$t_2 - t_1 = 200 \mu\text{m}$
3	R10-d400	Rectangular	10	400 $t_1 = 650 \mu\text{m}$ $t_2 = 250 \mu\text{m}$	No	$t_2 - t_1 = 400 \mu\text{m}$
4	R5-d400	Rectangular	5	400 $t_1 = 650 \mu\text{m}$ $t_2 = 250 \mu\text{m}$	No	$t_2 - t_1 = 400 \mu\text{m}$
5	R15-d400	Rectangular	15	400 $t_1 = 650 \mu\text{m}$ $t_2 = 250 \mu\text{m}$	No	$t_2 - t_1 = 400 \mu\text{m}$
6	T10-d400	Triangular	10	400 $t_1 = 650 \mu\text{m}$ $t_2 = 250 \mu\text{m}$	No	$t_2 - t_1 = 400 \mu\text{m}$
7	O10-d400	Oval	10	400 $t_1 = 650 \mu\text{m}$ $t_2 = 250 \mu\text{m}$	No	$t_2 - t_1 = 400 \mu\text{m}$
8	R10-d400-SL	Rectangular	10	400 $t_1 = 650 \mu\text{m}$ $t_2 = 250 \mu\text{m}$	Yes	$t_2 - t_1 = 400 \mu\text{m}$

Thick layer (Elastosil 4601 M)
 Strain limiting layer
 Thin layer (Elastosil 4601 M)
 Zero-volume chamber

Figure 5.1: Actuator design configurations

behaviour¹, as shown in Fig. 5.2a. Based on this observation, a conditioning protocol was established, where each actuator was cycled ten times above its threshold pressure (0.5 psi higher) to stabilise the mechanical response before data collection. Fig. 5.2b illustrates the three key stages of actuator response: (A) pre-threshold where the actuator maintains its straight configuration, (B) threshold pressure where initial bending becomes visible,

¹Strain softening refers to a fundamental material behaviour where elastomers become more compliant after repeated deformation cycles (Villani and Lavallata, 2024). This results in a larger deformation under the same applied pressure in subsequent loading cycles

Table 5.1: Threshold activation pressures for mitigating strain softening in different actuator configurations

Design Label	Threshold Pressure (psi)
R10-d0	5.0
R10-d200	4.0
R10-d400	3.0
R5-d400	6.5
R15-d400	2.5
T10-d400	3.5
O10-d400	3.0
R10-d400-sl	4.0

and (C) exceed-threshold where profound bending deformation occurs. The 0.5 psi margin above the threshold pressure ensured sufficient deformation for effective conditioning. For example, an actuator with a 2.5 psi threshold was conditioned at 3.0 psi to ensure consistent results. This protocol aligns with established practices in soft robotics and material characterisation, where actuators are repeatedly inflated and deflated prior to data collection to account for stress softening effects. Similar procedures have been reported in the literature (Moseley et al., 2016; Wehner et al., 2016; Miller, 2025; Kim et al., 2011).

Actuation testing was performed using fluid dispensing device (Ultimus V, Nordson EFD, US) provide precise mechanical regulation of input air pressure. The testing sequence employed an incremental pressure load in 0.5 psi steps. At each pressure level, a 5-7 second hold period allowed the actuator to reach steady state, confirmed through visual observation of no further deformation. The images were captured in steady state before proceeding to the next pressure increment. The maximum pressure for each configuration was determined as the point at which undesirable ballooning effects became apparent, preventing potential actuator failure. The bending angles (θ) were measured through image analysis using a Matlab R2021a programme (The MathWorks, Inc., 2021) that implements the geometric construction method illustrated in Fig. 5.2c. This method, adapted from Thomson and Motani (2021), is based on the concept of measuring claw curvature by Feduccia (1993). Statistical analysis on three specimens per configuration provided mean values and standard deviations, allowing quantitative comparison between different PneuThin configurations. This experimental characterisation validated both the relationship between geometric parameters and bending performance and the repeatability of the FlexiLayer fabrication process. Detailed plots showing the measurements of the bending angle for each PneuThin configuration can be found in Appendix C (Figs. C.4 to C.11).

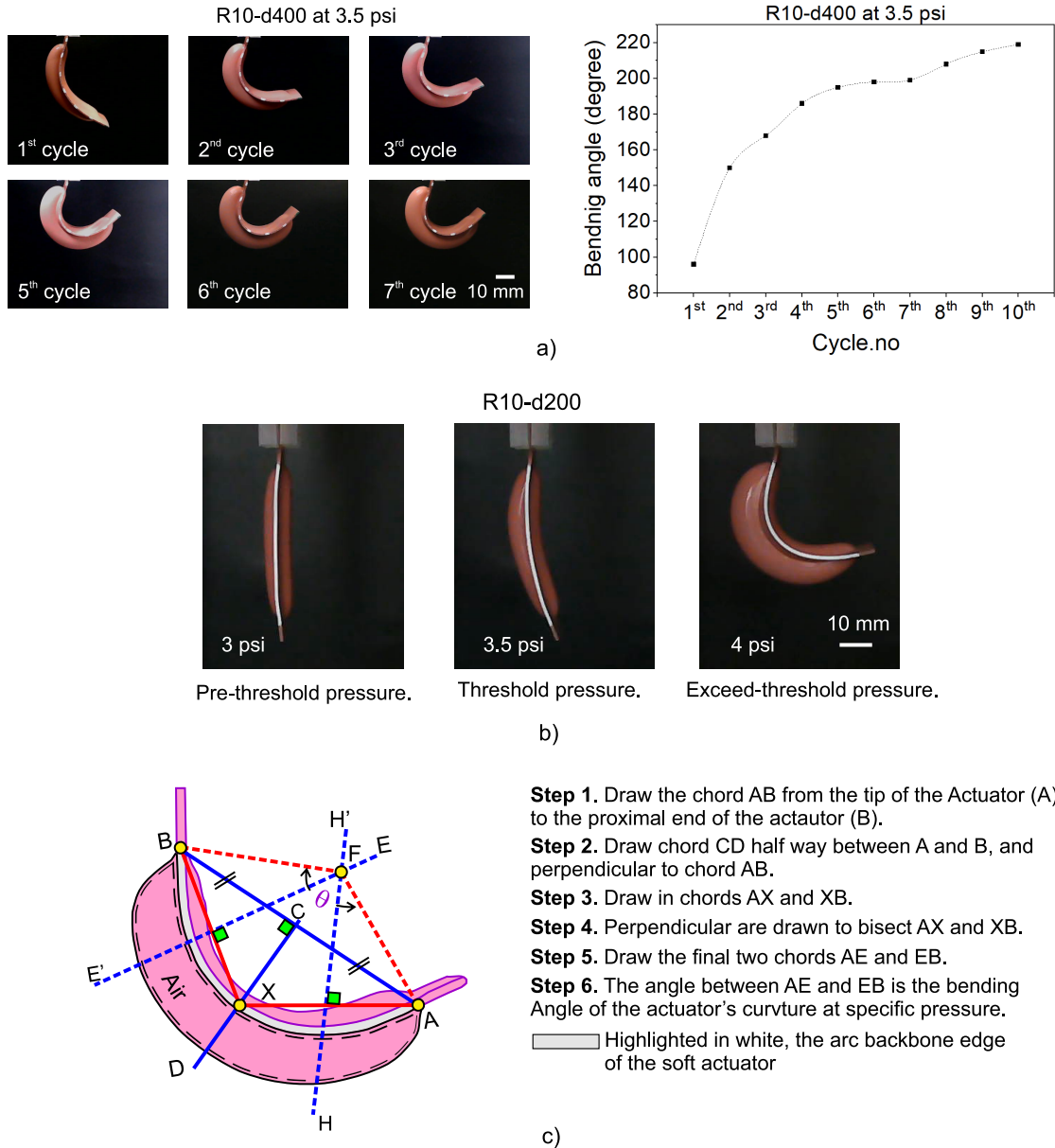


Figure 5.2: Characterisation of PneuThin bending behaviour: a) Evolution of bending response during conditioning at 3.5 psi, showing progressive deformation changes across seven pressurisation cycles (each cycle involves pressurisation from 0.5 to 5 psi in 0.5 psi increments). A quantitative plot is included to show bending angle versus cycle number for the R10-d400 configuration, highlighting the presence of strain-softening behaviour and response stabilisation after multiple cycles; b) Determination of actuation threshold pressure for configuration R10-d200: left shows pre-threshold state with no bending at 3 psi, middle demonstrates initial bending at threshold pressure of 3.5 psi, and right exhibits pronounced bending at exceed-threshold pressure of 4 psi; c) Geometric construction method for measuring bending angle (θ) along the actuator's backbone, adapted from Feduccia (1993).

5.2.3 Blocked-Force Measurement

After characterising the bending response, the blocking force output of each PneuThin configuration was evaluated using a modified experimental setup (Fig. 5.3a-b). The cantilever

configuration was maintained, but a strain gauge load cell (Model GSO-100, Transducer Techniques) with 100 g capacity was placed to contact the actuator tip perpendicular to its length. The proximal end was clamped using a custom laser cut acrylic clamp designed with extended sides to ensure a pure bending response and prevent hinging (Fig. 5.3a-b). This arrangement allowed the actuator tip to slide freely across the load cell surface while measuring the force generated throughout the pressure range. This force measurement method is similar to the experiment approach used in previous studies (Shintake et al., 2017).

Each actuator was tested by incrementally increasing the air pressure by 0.5 psi until failure occurred. To ensure repeatability, force measurements were taken at least five times at each pressure level. A custom-designed pneumatic control box², was used for precise pressure regulation and simultaneous data recording (see Fig. C.1). Detailed specifications and components of this control system are available in Appendix C. The pneumatic control system managed the air pressure, subjecting the actuators to pressurisation and depressurisation cycles with a 50% duty ratio and a frequency of 0.1 Hz over 60 seconds. The average peak force from these measurements was calculated using OriginPro 2023b (see Fig. 5.3c).

²The custom-designed pneumatic control box used for actuator characterisation in this study was developed by a PhD researcher in the healthcare mechatronics research lab.

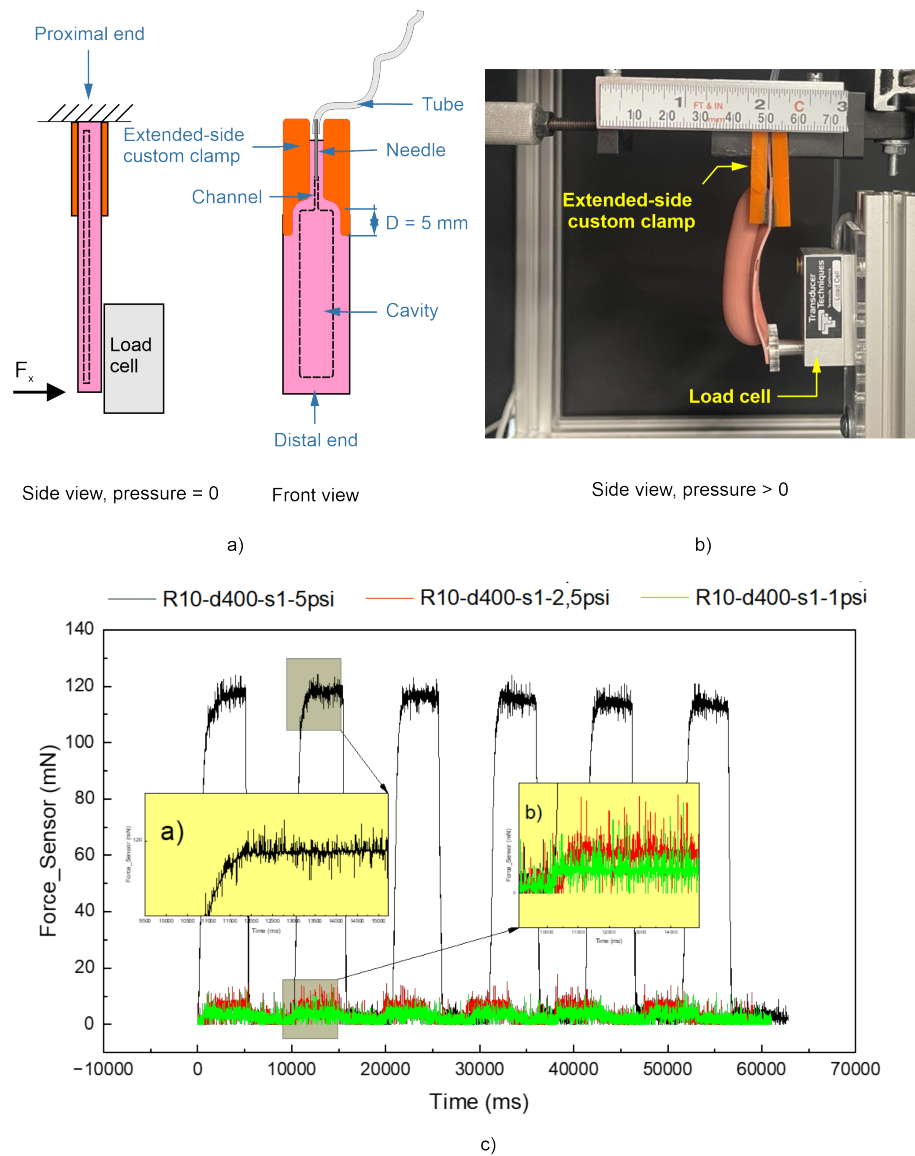


Figure 5.3: Experimental setup and force measurement characterisation of PneuThin: a) Schematic diagram showing the force measurement configuration in side and front views, illustrating key components including the extended-side custom clamp, load cell placement, and pneumatic connections with dimensions; b) Photograph of the actual experimental setup during actuation, showing the inflated actuator interacting with the load cell under the guidance of the extended-side custom clamp; c) Force output measurement for configuration R10-d400-sl at three pressure levels (1 psi, 2.5 psi, and 5 psi) over time, with magnified regions showing detailed signal responses, demonstrating consistent peak force generation across multiple actuation cycles.

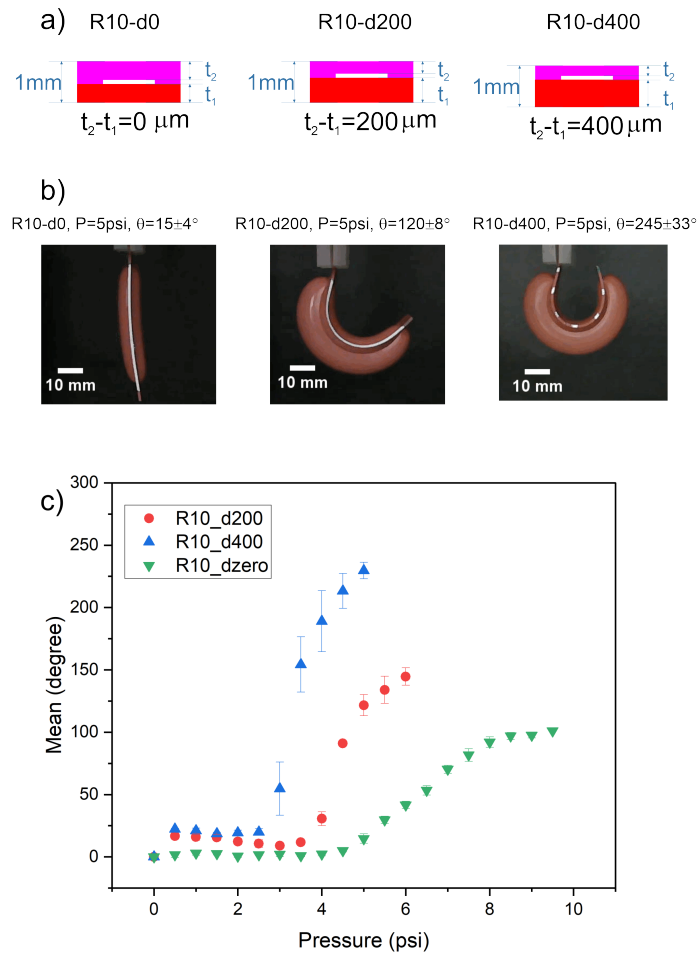


Figure 5.4: Effect of Thickness Distribution on Bending Angle. (a) Schematics depict three configurations (R10-dzero, R10-d200, R10-d400) with increasing thickness differences (t_2-t_1) of 0 μm , 200 μm , and 400 μm , respectively. (b) Photographs show the actuators at 5 psi, with corresponding bending angles of $15 \pm 4^\circ$, $120 \pm 8^\circ$, and $245 \pm 33^\circ$. (c) A graph plots bending angle vs. pressure, revealing a strong positive correlation between thickness difference and bending magnitude.

5.3 PneuThin Characterisation Results

5.3.1 Bending Angle Characterisation

Effect of Layer Thickness Distribution

Fig. 5.4 illustrates the relationship between the thickness distribution of the layer and the response of the bending angle for three PneuThin configurations with different thickness differences (t_2-t_1): 0 μm (R10-d0), 200 μm (R10-d200), and 400 μm (R10-d400). Under 5 psi pressure, R10-d400 achieved the largest bending angle of $245 \pm 33^\circ$, followed by R10-d200 at $120 \pm 8^\circ$, while R10-d0 showed a minimal bending of $15 \pm 4^\circ$ (Fig. 5.4b).

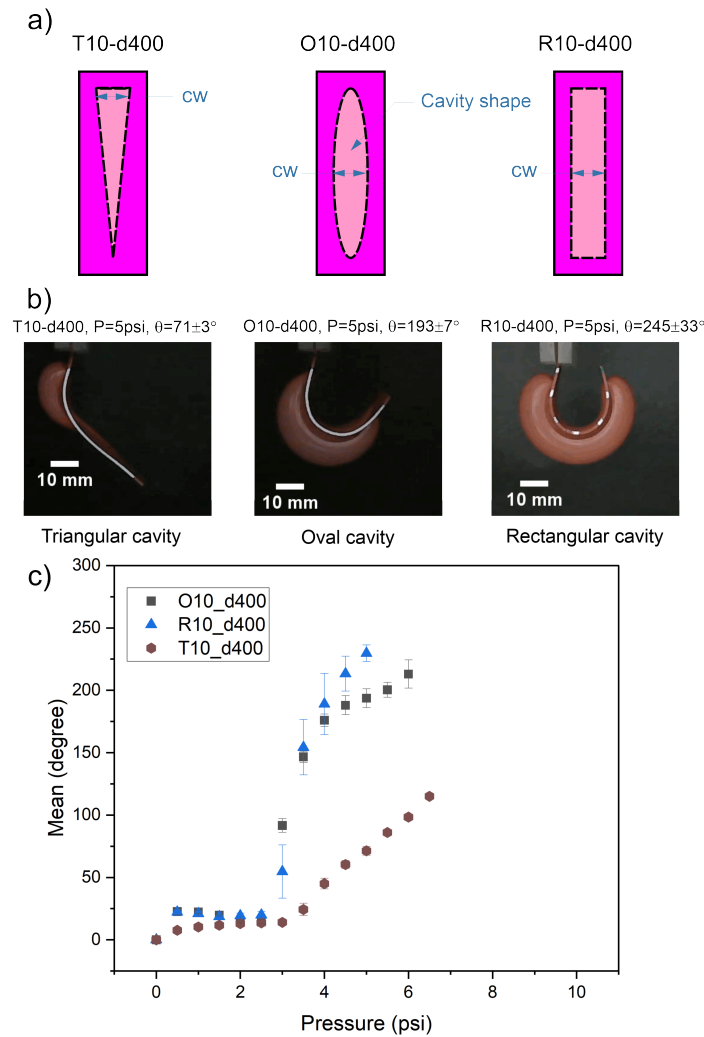


Figure 5.5: Effect of Cavity Shape on Bending Actuation. (a) Schematics of PneuThin with triangular, oval, and rectangular cavities and a thickness difference (t_2-t_1) of 400 μm . (b) Actuators at 5 psi with a 10 mm scale, showing varying bending angles. (c) Graph of bending angle vs. pressure, highlighting the influence of cavity shape on bending magnitude.

Effect of Cavity Shape

Fig. 5.5 compares the response to the bending angle of the PneuThin configurations with three different cavity shapes: triangular (T10-d400), oval (O10-d400) and rectangular (R10-d400), while maintaining a constant thickness difference (400 μm) and cavity width (10 mm). At 5 psi pressure, the rectangular cavity achieved the highest bending angle of $245 \pm 33^\circ$, followed by the oval cavity at $193 \pm 7^\circ$, while the triangular cavity showed the lowest at $71 \pm 3^\circ$ (Fig. 5.5b).

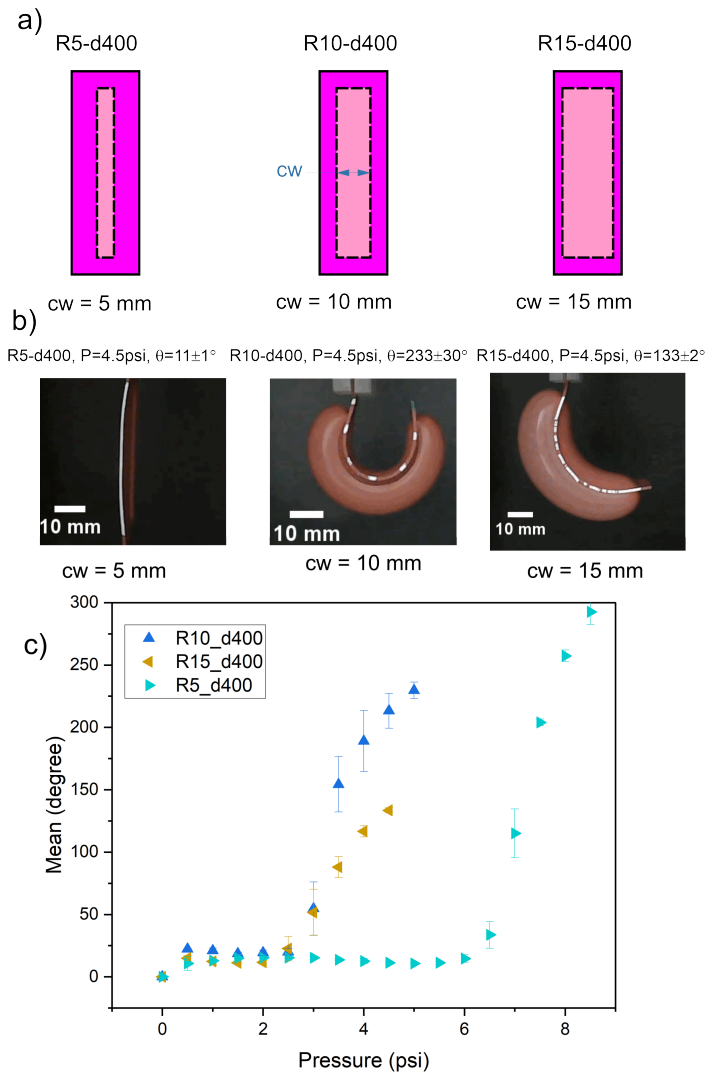


Figure 5.6: Influence of Cavity Width on Bending Actuation. (a) Schematic diagrams of three PneuThin configurations: R5-d400 (5 mm), R10-d400 (10 mm), and R15-d400 (15 mm). (b) Real-life photographs of the actuators at a pressure of 4.5 psi. (c) A graph plotting bending angles against pressure for each PneuThin configuration.

Effect of Cavity Width

Fig. 5.6 demonstrates the effect of cavity width on PneuThin bending performance, comparing three rectangular configurations with widths of 5 mm (R5-d400), 10 mm (R10-d400), and 15 mm (R15-d400) at a constant thickness difference (400 μm). At 4.5 psi, R10-d400 achieved the highest bending angle of $233 \pm 30^\circ$, followed by R15-d400 at $133 \pm 2^\circ$, while R5-d400 showed a minimal bending of $11 \pm 1^\circ$ (Fig. 5.6b).

Effect with/without Strain Limiting Layer Embedded in Elastosil 4601 M

Fig. 5.7 shows the bending angle response of two PneuThin configurations with and without the strain-limiting layer (R10-d400 and R10-d400-sl) under increasing pressure.

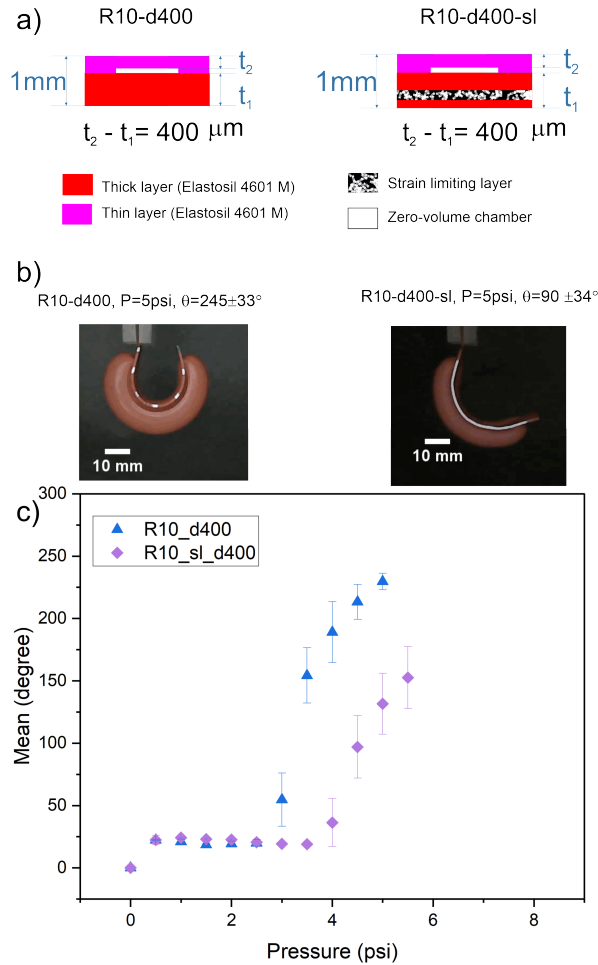


Figure 5.7: Impact of Strain-Limiting Layer on Bending Actuation. (a) Schematic diagrams of two PneuThin configurations: R10-d400 (without strain-limiting layer) and R10-d400-SL (with strain-limiting layer). (b) inflated actuator photographs at 5 psi. (C) A graph plotting bending angle versus pressure for each PneuThin configuration.

The unconstrained configuration (R10-d400) exhibits a non-linear increase in the bending angle beginning at 2.5 psi, reaching $245 \pm 33^\circ$ at 5 psi. In contrast, configuration (R10-d400-sl) begins a significant bending only after 4 psi, achieving $90 \pm 34^\circ$ at 5 psi (Fig. 5.7c). This observation suggests that the unconstrained PneuThin actuator demonstrates greater flexibility under applied pressure as opposed to the constrained variants, which exhibit increased stiffness and consequently a reduced bending angle.

5.3.2 Blocked-Force

Effect of Layer Thickness Distribution

Fig. 5.8 shows the force output versus pressure relationship for three PneuThin configurations with varying thickness distributions (t_2-t_1): R10-d0 ($0 \mu\text{m}$), R10-d200 ($200 \mu\text{m}$), and R10-d400 ($400 \mu\text{m}$). All three configurations exhibit minimal force generation (<5

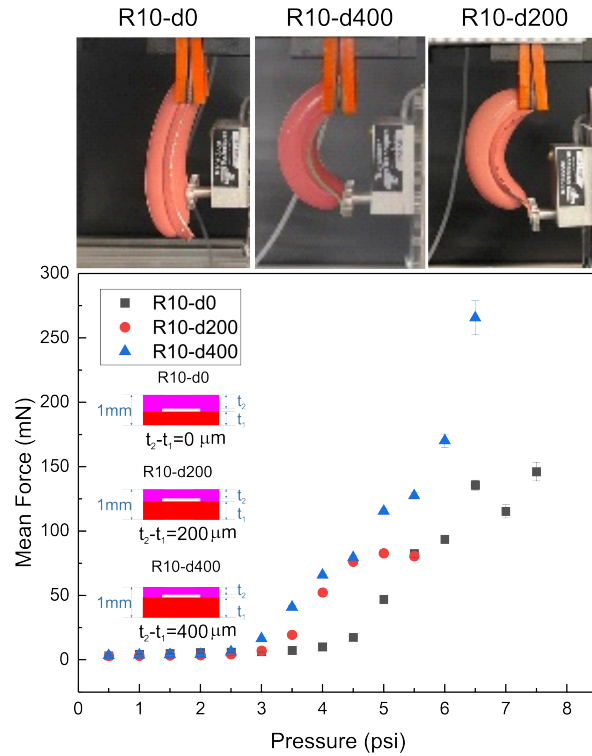


Figure 5.8: Peak force output versus actuation pressure for actuators with varied thickness distributions (R10-d0, R10-d200, R10-d400).

mN) below 2.5 psi. Beyond this threshold, R10-d400 demonstrates superior performance, achieving the highest maximum force of 265.6 ± 13.3 mN at 6.5 psi, followed by R10-d200 reaching 170.1 ± 5.2 mN, while R10-d0 produces 127.5 ± 2.3 mN.

Effect of Cavity Shape

Fig. 5.9 compares the force output characteristics of three shapes of the cavity: triangular (T10-d400), oval (O10-d400) and rectangular (R10-d400), all with identical thickness distributions ($400 \mu\text{m}$). The triangular cavity configuration shows minimal force generation, reaching only 40 ± 5 mN at 6.5 psi. A moderate performance was achieved by the oval cavity, achieving 65 ± 8 mN at 4.5 psi before failure. The rectangular cavity exhibits superior performance, generating forces up to 265 ± 10 mN at 6.5 psi with a consistent exponential increase.

Effect of Cavity Width

Fig. 5.10 investigates how the width of the cavity affects the generation of force in PneuThin configurations. Three rectangular cavities were tested: narrow (R5-d400, 5 mm), medium (R10-d400, 10 mm) and wide (R15-d400, 15 mm). The narrow cavity requires high activation pressure (>6 psi) and produces limited force (40 ± 5 mN maximum). The

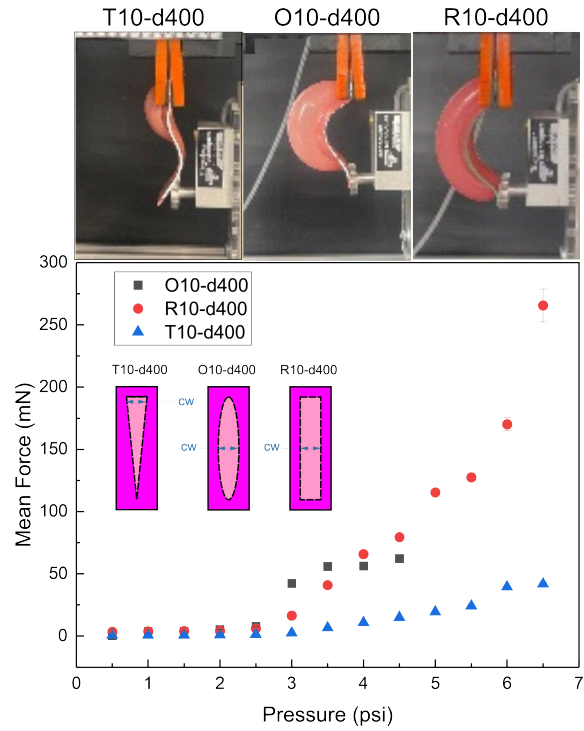


Figure 5.9: Peak force output versus actuation pressure for actuators with oval (O10-d400), rectangular (R10-d400), and triangular (T10-d400) cavity shapes.

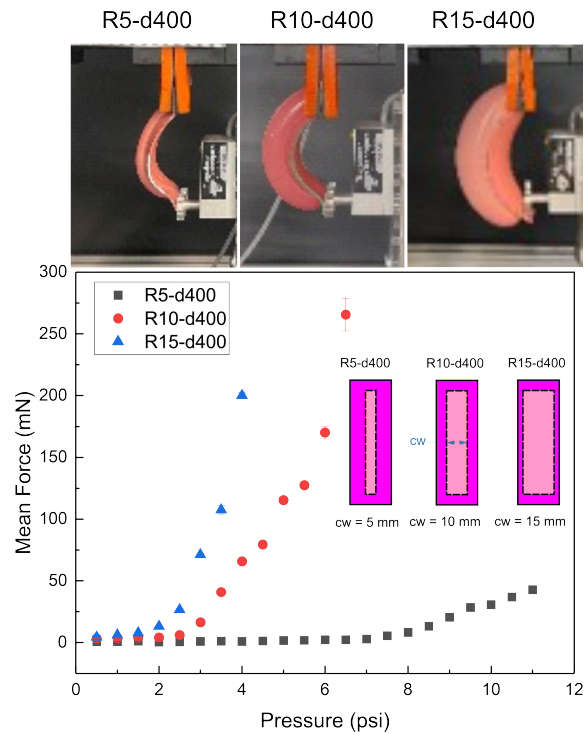


Figure 5.10: Peak force output versus actuation pressure for actuators with 5 mm (R5-d400), 10 mm (R10-d400), and 15 mm (R15-d400) cavity widths.

medium cavity starts generating force at 2.5 psi and achieves the highest output (265 ± 10 mN at 6.5 psi). The wide cavity activates earliest (2 psi) but reaches its maximum force limit of 200 ± 8 mN at 4 psi.

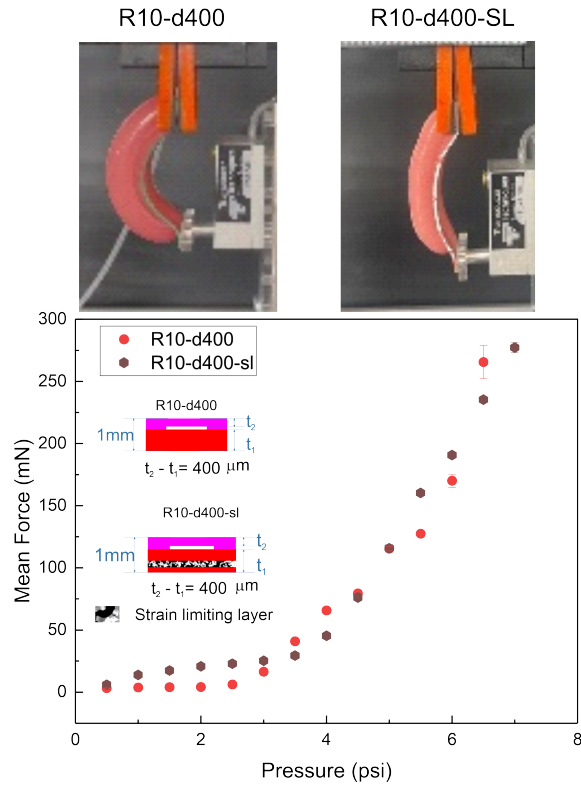


Figure 5.11: Force output versus actuation pressure for actuators with strain limiting layer (R10-d400-sl), and without strain limiting layer (R10-d400) configurations.

Effect with/without Strain Limiting Layer Embedded in Elastosil 4601 M

Fig. 5.11 compares force generation between two PneuThin configurations: R10-d400 (without strain-limiting layer) and R10-d400-SL (with embedded Soft'n Sheer Sulky layer). Both actuators share identical cavity geometry (10 mm in width) and thickness distribution (400 μm). The R10-d400-SL configuration begins force generation earlier (2 psi) compared to R10-d400 (2.5 psi). As pressure increases, both configurations show a consistent increase in force, with R10-d400-SL achieving 280 ± 10 mN at 7 psi while R10-d400 reaches 265 ± 10 mN at 6.5 psi.

5.4 Case Studies

Two case studies were developed to demonstrate the applicability of the FlexiLayer technique: a soft gripper for object handling and a quadrupedal robot to mimic locomotion. These studies validate how the layer-by-layer stacking approach, 'FlexiLayer', enables the creation of functional thin soft robots.

5.4.1 Case Study 1: Soft Gripper

This case study examined using two PneuThin constraint actuators (R10-d400-sl configuration), selected for its enhanced force output and controlled bending characteristics demonstrated in Section 5.3. The two PneuThins integrated into a form of two-finger gripper (1.5 g each) mounted on a custom-built clamp to create a grip configuration. The complete assembly weighs only 3 g and has a total thickness of 1 mm, demonstrating the lightweight and thin structure capabilities that can be achieved using the FlexiLayer fabrication technique Fig. 5.12. Operating pressures ranged from 6-8 psi during the testing to evaluate the gripper’s capabilities across various objects. The assessment included 11 test objects ranging from delicate produce to rigid items (5-194 g). The gripper demonstrated precise force control with delicate items, including a blackberry (5 g), a cherry tomato (9 g), and a cherry (10 g). For irregular shapes, it was effectively adapted to grasp a date (13 g), a battery (44 g) and a plastic tube cutter (31 g). A series of broccoli pieces (8-32 g) validated the adaptability of the size, while manipulation of a deformable doh square frame (194 g) established the maximum payload capacity Fig. 5.12a-k. The following section examines another effectiveness of using FlexiLayer through the development of a Quadrupedal Soft Robot, further demonstrating the technique’s versatility in creating complex robotic structures.

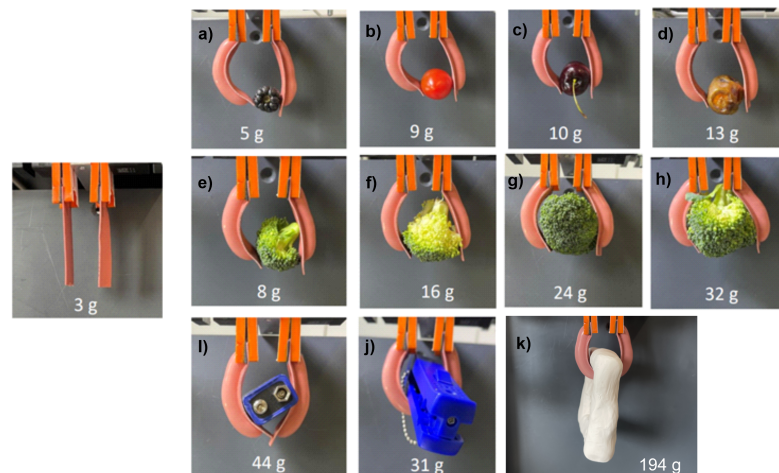


Figure 5.12: Demonstration of the FlexiLayer-fabricated soft gripper’s capability. The gripper (total weight 3 g, shown in relaxed state) successfully holds various objects ranging from 5 g to 194g within a working pressure range of 6-8 psi. Objects include: (a) blackberry (5 g), (b) cherry tomato (9 g), (c) cherry (10 g), (d) date (13 g), (e-h) broccoli pieces of varying sizes (8 g, 16 g, 24 g, 32 g), (i) battery (44 g), (j) plastic tube cutter (31 g), and (k-l) play-doh dumbbell (194 g) shown from two angles. This showcases the gripper’s ability to adapt to different shapes, sizes, and delicate objects while maintaining a high grasping-to-weight ratio.

Table 5.2: Operating parameters for quadrupedal robot locomotion

Parameter (unit)	Value
Inlet pressure (psi)	6.5 ± 0.15 (45 ± 1 kPa)
Actuation frequency (Hz)	0.33
Actuation time (s)	1.5
Inter-actuation delay (ms)	500
Total weight (g)	4

5.4.2 Case Study 2: Soft Quadrupedal Robot Locomotion

The quadrupedal robot, inspired by multigait robot design (Shepherd et al., 2011), demonstrated the ability of the FlexiLayer technique to create complex robotic structures. The robot construction (dimensions of the design, see Appendix C and Fig. C.2) used a five-layer stacking approach using the FlexiLayer protocol Section 4.3, incorporating PneuThin (R10-d400-sl configuration) to achieve stable and controlled motion. Layer thicknesses were precisely controlled through established GH-DFT relationships (Section 4.5.1), , with PVA mask layers positioned using the vacuum chuck alignment system (Fig. 4.3). The design incorporated six PneuThin actuators: two in the v-shaped configuration (back legs), two in the parallel configuration (middle section), and two in the v-shape configuration (front legs). The semi-curing protocol (Section 4.5.6) enabled strong layer bonding, resulting in a 4 g robot. Under the operating parameters of 6.5 ± 0.15 psi (45 ± 1 kPa) inlet pressure, 0.33 Hz actuation frequency, 1.5 s actuation time, and 500 ms interactuation delay, summarised in Table 5.2, the robot achieved forward motion by sequential activation of its actuators using the custom-designed pneumatic control box Fig. C.1. As shown in Fig. 5.13(A-H), each 3-second locomotion cycle begins with the back actuators inflating, followed by the middle actuators, and then the front actuators in a coordinated sequence. This timed activation pattern creates a wavelike motion from back to front, similar to the undulating locomotion seen in biological systems. Under the operating parameters in Table 5.2 the robot achieved an average velocity of 1.7 ± 0.2 mm/s. The sequential activation pattern produces controlled undulation in a 3-second cycle, resulting in a cumulative forward displacement of 72 mm after multiple cycles (at $t = 42.0$ s) Fig. 5.13k.

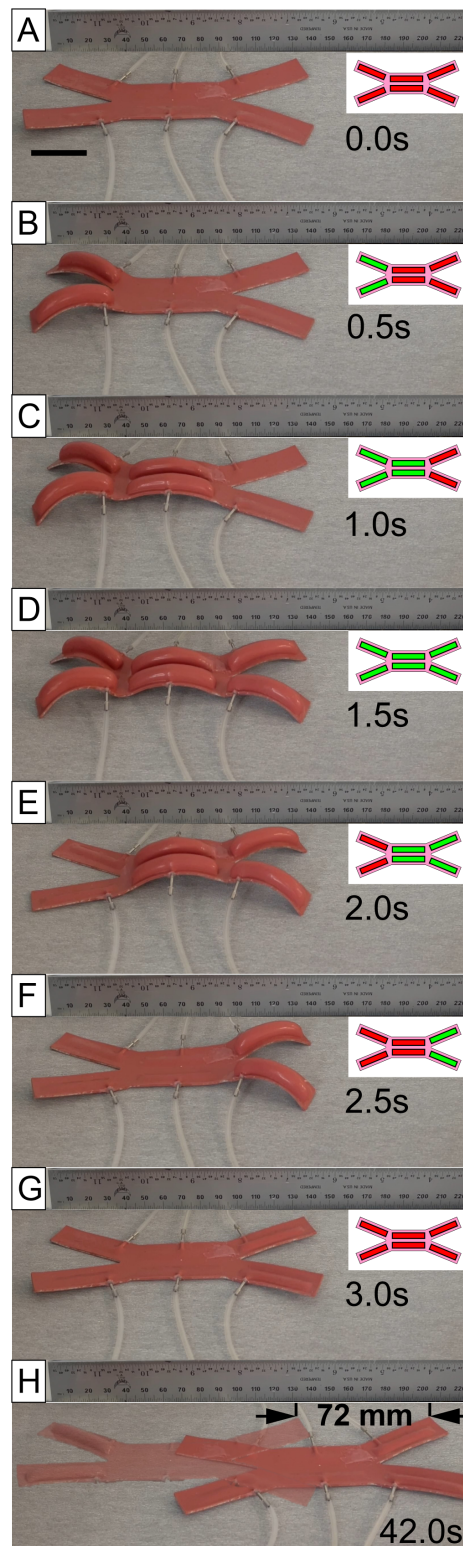


Figure 5.13: Sequential actuation of a quadrupedal soft robot showing undulating locomotion over 3 seconds (A-G) and resulting displacement after multiple cycles (H). The scale bar in A represents 30 mm.

5.5 Discussion

The experimental results demonstrate both the capabilities and limitations of PneuThin fabricated using the FlexiLayer technique described in Chapter 4. This investigation of eight actuator configurations revealed distinct relationships between geometric parameters and performance metrics. The thickness difference between layers emerged as the primary factor controlling the actuation behaviour. For the R10-d400 configuration with a 400 μm thickness difference, a bending angle of 245° was achieved at 5 psi, while the symmetric R10-d0 showed a minimal bending of 15° at the same air pressure. This aligns with the findings of Gorissen et al. (2013) that the built-in structural asymmetry directly enhances bending deformation in soft pneumatic actuators. The limited bending angle observed in the R10-d0 configuration can be explained by the almost identical thicknesses of the top and bottom layers ($t_1 \approx t_2 \approx 450 \mu\text{m}$), which produced an isotropic cavity expansion under pressure, resulting in balloon-like inflation rather than generating anisotropic strain between the two layers that drives the bending motion in the PneuThin soft actuator. However, at pressures exceeding 5 psi, a small increase in the bending angle was observed, likely due to a minor fabrication error introducing an unintended anisotropic strain, resulting in a bending motion. This highlights the sensitivity of actuator performance to even slight deviations in layer thickness, emphasising the importance of precise control of layer thickness during fabrication. In particular, it suggests that further refinement of the empirical layer thickness model, derived from linear regression fitting of GH to DFT measurements for both silicone-on-steel and silicone-on-silicone deposition cases, could improve manufacturing consistency, see Section 4.5.1. In addition, the shape of the cavity also significantly influenced actuator performance. The rectangular cavity consistently provided better bending performance compared to oval and triangular configurations. An optimal cavity width-to-actuator width ratio of 50% (10 mm cavity in 20 mm actuator) was found to achieve 233° bending at 4.5 psi. Wider cavities reduced actuator performance due to ballooning effects, whereas narrower cavities required higher activation pressures. This observation supports Zhu et al. (2022b) work showing how radial expansion in soft bending actuators consumes strain potential energy, reducing the bending angle, and potentially leading to actuator failure. The trend of non-linearity in the relationship between pressure and bending angle (Figs. 5.4 to 5.7) is attributed to the inflated cavity area that increases non-linearly with applied pressure (Sinatra et al., 2018).

In addition to geometric non-linearity influences of the soft actuator, the mechanical response of the elastomer also changes with repeated cycling due to the Mullins effect. A

preliminary cyclic test on the R10-d400 actuator at 3.5 psi showed a significant increase in bending angle from 96° in the first cycle to 198° by the sixth—a 106% rise, see Section 5.2.2 and Fig. 5.2a. From the sixth to the tenth cycle, the angle increased only slightly to 219° , only an additional 10.6%, indicating that the actuator response stabilised after repeated use. This softening behaviour, commonly observed in elastomers such as silicone rubber, arises from internal rearrangements of the polymer network, such as the slipping of chains and breakage of weak internal links (Diani et al., 2009). Diani et al. (2009) reviewed these mechanisms, noting that although multiple theories exist, they all describe a softening related to the history of deformation. To minimise this effect, all actuators were pre-conditioned with ten pressurisation cycles above their activation threshold prior to measurement. This step ensured mechanical stability and improved repeatability of the results.

The integration of strain-limiting layers introduced an interesting performance trade-off in the constrained PneuThin actuator (R10-d400-sl configuration). The modification increased the activation threshold pressure and reduced the maximum bending by 63%. This indicates that the addition of the SL layer reduces the sensitivity of the constrained configuration (R10-d400-SL) to variations in bending motion with increasing applied air pressure, leading to a closer-to-linear relationship between the applied pressure and the resulting bending angle compared to the unconstrained configuration (R10-d400) without the SL layer. This behaviour can be interpreted as a consequence of the increased structural stiffness introduced by the SL layer. This finding is consistent with previous studies. Zhu et al. (2022b) demonstrated that strain-limiting layers in soft pneumatic actuators restrict deformation while improving control precision. Similarly, Sinatra et al. (2018) found that the nanofibre-reinforced actuators increased the maximum pressure tolerance by 25.8% compared to the pure PDMS configuration. Their subsequent work (Sinatra et al., 2019) further confirmed this trend, reporting a 33% higher burst pressure in soft reinforced actuators based on a lower shore hardness elastomer (Shore 20A, Dragon Skin 20, Smooth-On), attributed to the increase in the stiffness of the soft structure. This modification proves particularly valuable for applications that require accurate position or force control, such as the soft gripper demonstrated in these case studies. The results of this observational study suggest that the addition of a patterned fibre sheet with different orientations selectively in the elastomer matrix may provide hybrid (e.g., bend and twist) or various modes of motion during actuation (Sinatra et al., 2019). Future work will expand on this concept to test the possibility of creating various motions (e.g., elongation, contraction, and twisting)

within the PneuThin actuator by altering the orientation of a patterned fabric sheet (Luo et al., 2021).

These experimental findings align well with the prediction pattern from the preliminary FEM analysis Section 3.5.1 and Fig. 3.7, particularly regarding the effects of the thickness distribution and shape of the cavity on deformation patterns. The established relationships provide design guidelines for optimising PneuThin performance: the thickness difference controls the activation threshold and the range of motion, the shape of the cavity determines the deformation patterns and the width of the cavity must be carefully balanced to avoid instability. The successful development of functional prototypes demonstrates the versatility of the FlexiLayer technique beyond individual actuators. The multi-gait soft robot achieved controlled undulating locomotion at 1.7 ± 0.2 mm/s through the coordinated activation of six bending actuators. In comparison to the previous work by Futran et al. (2018), which demonstrated the locomotion of a travelling soft robot (≈ 1.1 mm/s) using the moulding method. This demonstrating the technique’s capability to create complex integrated systems. The soft gripper showcased the practical utility of strain-limited actuators, handling objects from delicate berries (5 g) to heavier items (194 g) with a gripping-weight ratio of $\simeq 65$. These case studies validate both the scalability of the fabrication process and its ability to produce functional thin-planar soft robots for real-world applications. In addition, it emphasises the parallel and series fabrication capability of PneuThin, which is a key advantage of the FlexiLayer technique as demonstrated in Chapter 4, Section 4.4.4 and Fig. 4.9e, where the effective fabrication area enables the production of multiple actuators in a single process cycle. This batch fabrication capability contrasts with traditional single-unit moulding methods.

5.6 Chapter Summary

This chapter validated the FlexiLayer fabrication technique developed in Chapter 4 through the design, fabrication and characterisation of PneuThin, focussing on two key metrics: bending angle and blocking force. The experimental investigation examined eight PneuThin configurations to understand how geometric parameters influence these performance metrics.

The characterisation of the bending angle revealed that actuators with 400 μ m thickness difference achieved maximum bending ($245 \pm 33^\circ$ at 5 psi), while rectangular cavities demonstrated superior performance compared to oval and triangular shapes. A cavity width of 10 mm provided optimal bending characteristics and the integration of strain-limiting layers offered more controlled but reduced bending ($90 \pm 34^\circ$ at 5 psi). In parallel, force

measurements showed the highest output (265.6 ± 13.3 mN at 6.5 psi) from the 400 μm thickness difference configuration, with rectangular cavities consistently generating higher forces than other shapes. The strain limiting layer improved the maximum force generation, reaching 280 ± 10 mN at 7 psi.

Based on these findings, the R10-d400-sl configuration was selected for practical demonstrations due to its enhanced force output and controlled bending characteristics. Two case studies validated both the scalability and practical utility of the FlexiLayer technique. The first demonstrated a soft gripper, weighing only 3g, that used two R10-d400-sl actuators to successfully handle objects ranging from delicate berries (5g) to heavier items (194g), achieving a gripping-to-weight ratio of 64.7. The second case study showcased a quadrupedal soft robot that achieved controlled locomotion at 1.7 ± 0.2 mm/s through coordinated activation of six bending actuators, demonstrating the technique's capability to create complex integrated systems. These results validate both the reliability of the FlexiLayer technique and its potential in creating functional thin planar soft robotic systems. The experimental data provide a quantitative foundation for the refined FEM analysis presented in Chapter 6.

Chapter 6

Developing of FEM as a Design Tool for PneuThin

6.1 Introduction

Chapter 6 evaluates FEM as a design tool for PneuThin by comparing computational predictions with experimental results. Two representative PneuThin configurations: the unconstrained rectangular cavity (R10-d400) and the constrained with embedded fabric (R10-d400-SL). These configurations, previously characterised in Chapter 5, provide a suitable platform to evaluate FEM's predictive capabilities across different material configurations. It should be noted that the FEM analysis in Chapter 3 proved the conceptual feasibility of FlexiLayer for the design of PneuThin using material models based on published data. This current evaluation defines material models based on the actual fabrication process to improve prediction accuracy. The aim is to demonstrate how FEM can effectively guide design decisions for similar PneuThin configurations.

Primary Objectives

The primary objectives of this chapter are:

1. **Determine the performance of FEM:** To confirm the ability of FEM to accurately predict activation threshold pressures, progressive deformation patterns and force generation capabilities.
2. **Establish the efficacy of using FEM as a Design Tool:** To demonstrate FEM's utility as a reliable tool for optimising PneuThin designs, reducing prototype iterations, and minimising material waste.

The evaluation tests the FEM as part of the design process for future PneuThin configurations by examining bending profiles and force generation under pressure loading.

6.2 Methods

This section establishes a framework to assess the predictive capabilities of FEM for PneuThin design. The methodology, illustrated in Figs. 6.1 and 6.2, consists of three main phases: material characterisation, FEM development, and performance comparison with experimental data. The material characterisation phase involved the testing of two PneuThin configurations: unconstrained actuator (Design R10-d400) and constrained actuator (Design R10-d400-sl), as detailed in Section 5.2.1. The unconstrained actuator used bulk ELASTOSIL® M 4601 silicone elastomer, while the constrained design integrated ELASTOSIL® M 4601 with nonwoven fabric (Soft'n Sheer, Sulky, USA) as a strain-limiting layer. Based on the rationale for material selection presented in Section 3.2.2 and the experimental characterisation in Section 5.3, these configurations represent the fundamental design variants examined in this study. Testing protocols were developed to measure the tensile and compression responses of these materials under controlled loading conditions, providing essential data for accurate FEM simulation of the PneuThin performance such as bending and force generation observed in Section 5.3.

6.2.1 Material Characterisation for Modelling

Material Characterisation for Unconstrained Actuator

For the unconstrained actuator (Design R10-d400), the characterisation involved tensile and compression tests to capture the complete nonlinear response. Tensile test samples were prepared using the doctor blade coating process established in Section 4.4.1, maintaining consistency with the actuator fabrication methodology. The testing followed ISO 37:2017 (Type 2) (International Organization for Standardization, 2017b) specifications using a uniaxial machine (Autograph AG-X plus Universal Tester), with specimens of 20 ± 0.5 mm gauge length tested at 300 mm/min crosshead speed. The sample thickness was 1.109 ± 0.20 mm measured using the coating thickness gauge (Elcometer 456). The compression samples were prepared using CNC milling aluminium moulds, according to the specifications of ISO 7743: 2017 (Method C, Type B) (International Organization for Standardization, 2017a). Cylindrical specimens of 17.8 ± 0.5 mm diameter and 25 ± 0.25 mm length underwent four consecutive compression-release cycles at 10 mm / min, reaching maximum strain

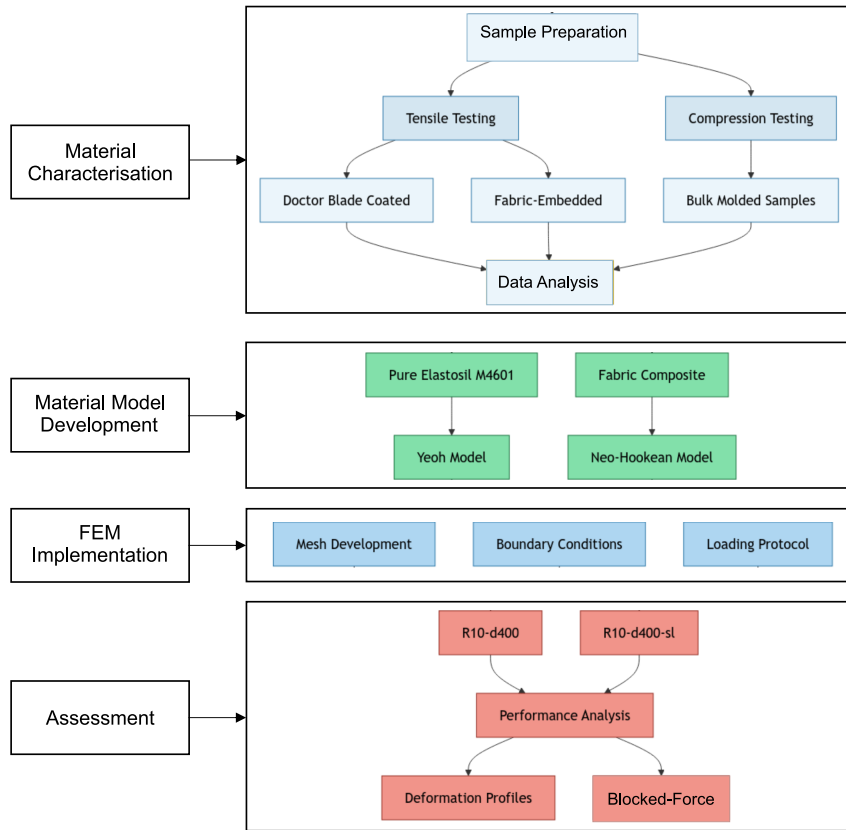


Figure 6.1: Methodology flowchart for FEM assessment of PneuThin, showing the progression from material characterization through testing, model development, and assessment across two representative actuator design configurations (R10-d400 and R10-d400-sl).

25%. The combined tensile compression data allowed the determination of parameters for the Yeoh hyperelastic model (Yeoh, 1993a), chosen for its effectiveness in modelling large deformations typical in pneumatic actuators.

Material Characterisation for Constrained Actuator

For the Constrained Actuator (Configuration R10-d400-sl), the characterisation focused on the composite behaviour of the fabric-reinforced structure. The test samples were fabricated following the FlexiLayer process detailed in Section 4.4.1 and Fig. 4.5, to ensure that the samples accurately represented the material configuration in the actual actuator. Tensile testing followed the ISO 1421-2016 protocol (International Organization for Standardization, 2016) with a gauge length of 100 mm and a jaw separation of 150 mm at a strain rate of 100 mm / min. Four specimens were tested to ensure statistical reliability. Tensile test data informed the parameters for the Neo-Hookean model, selected for its ability to characterise elastomeric behaviour within the limited deformation range (under 50% strain) (Dezaki et al., 2022a) imposed by the fabric reinforcement.

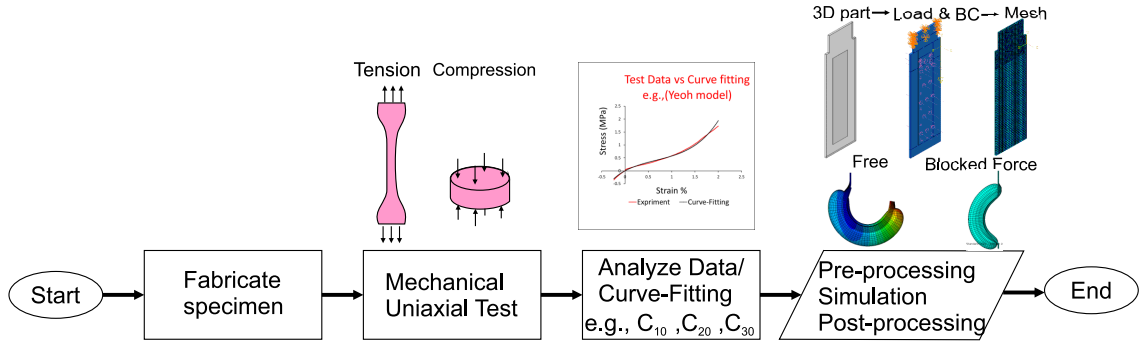


Figure 6.2: Experimental workflow for material model development and FEM simulation, illustrating the sequence from specimen fabrication through mechanical testing, data analysis, and computational simulation.

6.2.2 Finite Element Model Development

The FEM software (Abaqus 2024) was used to construct models for unconstrained (R10-d400) and constrained (R10-d400-sl) actuator configurations. Both models shared external dimensions of 60 mm long, 20 mm width and 1 mm total thickness, with an internal cavity of 50 mm \times 10 mm. The 3D geometry was created as a single part with a cavity defined by cut extrusion, as shown Fig. 6.3. Purple arrows indicate the application of the pressure load, whereas orange arrows show the boundary conditions. The gravitational force was included to match the experimental conditions. For the constrained design, an additional cell partition step allowed material property assignment based on experimentally determined values in Table 6.1.

The geometry was meshed using quadratic hexahedral elements with hybrid formulation (C3D20RH)¹ (Moseley et al., 2016). Two analysis configurations replicated the experimental setup from Chapter 5. For bending analysis, the nodes at one end of the actuator were constrained while the other end remained free to deform under pressure loading (Polygerinos et al., 2013). The blocked force analysis maintained the same end constraints, with the distal end sliding friction-free across a displacement support that mimicked the load cell contact, allowing the force measurement Fig. 6.3. The modelling procedures were conducted according to previously published research (Moseley et al., 2016; Dezaki et al., 2022a; Tiboni and Loda, 2023). The simulation results and their correlation with the experimental data are presented in the following section.

¹C3D20H denotes a 20-node quadratic hexahedral element with hybrid formulation in ABAQUS.

Table 6.1: Material properties and FEM parameters for R10-d400 and R10-d400-sl configurations

Design Type	Layer	Thickness (mm)	Test Data Utilized	Material Constants (MPa)
R10-d400	L1	0.650	Pure ELASTOSIL [®] M4601	$C_{10} = 0.152, C_{20} = 1.88 \times 10^{-3}, C_{30} = 1.10 \times 10^{-3}$
	L2	0.250	Pure ELASTOSIL [®] M4601	$C_{10} = 0.152, C_{20} = 1.88 \times 10^{-3}, C_{30} = 1.10 \times 10^{-3}$
R10-d400-sl	L1	0.650	ELASTOSIL [®] M4601 with Strain-Limiting	$D_1 = 0, C_{10} = 3.862, C_{01} = 0$
	L2	0.250	Pure ELASTOSIL [®] M4601	$C_{10} = 0.152, C_{20} = 1.88 \times 10^{-3}, C_{30} = 1.10 \times 10^{-3}$

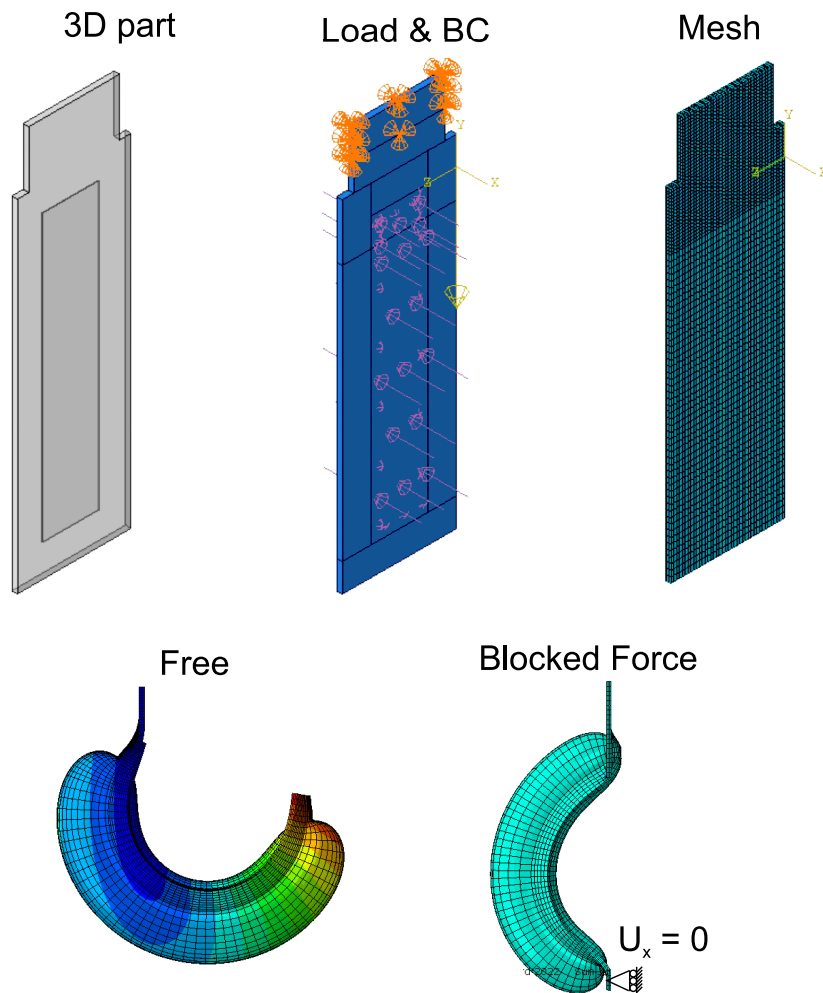


Figure 6.3: FEM workflow and results for PneuThin simulation. Top row shows model development stages: 3D part geometry creation, application of boundary conditions and pressure loads with fixed end constraints and meshed model using C3D20H hexahedral elements. Bottom row demonstrates simulation outcomes under 5 psi pressure for R10-d400 design: (left) free bending deformation with displacement contours, and (right) blocked force configuration showing constrained tip displacement in x-direction.

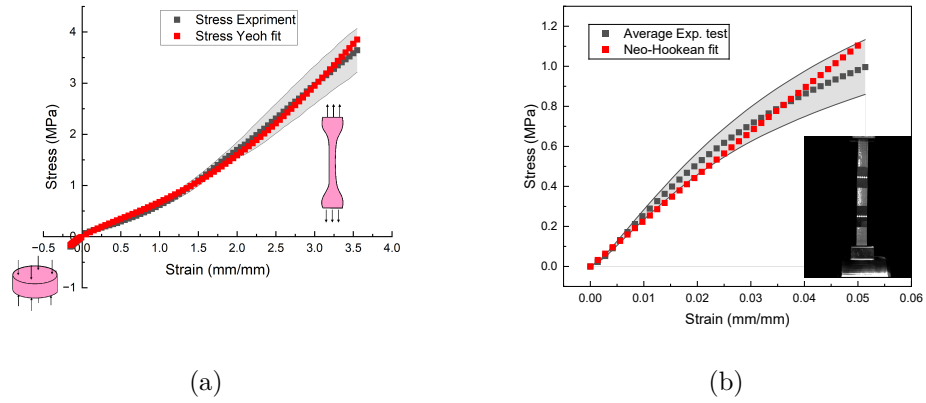


Figure 6.4: Material characterisation results showing stress-strain responses: (a) Pure Elastosil M 4601 under tension-compression loading, with Yeoh model fit up to 350% strain. (b) Fabric-reinforced Elastosil M 4601 under tension, with Neo-Hookean model fit up to 5% strain. Grey squares represent experimental data, red squares show model predictions, and shaded regions indicate experimental variation ($n = 3$ for pure elastomer, $n = 4$ for composite).

6.3 Results

6.3.1 Experimental Stress-Strain and Model Fitting

For the configuration of the unconstrained actuator (R10-d400), the tensile compression test of ELASTOSIL® M 4601 (Fig. 6.4a) showed that the Yeoh hyperelastic model accurately captured the nonlinear response up to 350% strain. This choice of model is supported by the work of (Mosadegh et al., 2014), who used the same silicone material (Elastosil M4601) and fitted its experimental data using the Yeoh model. Polygerinos et al. (2013) also highlighted that the Yeoh model is well suited to simulate the behaviour of soft elastomers. For the constrained configuration (R10-d400-sl), where silicone embedded with fabric represents an inextensible structure that bends but does not stretch, the material exhibited low strain during actuation (Wienzek and Seibel, 2019). This characteristic led to the selection of the Neo-Hookean model (Xavier et al., 2020), which showed good agreement with the experimental data up to 5% strain (Fig. 6.4b). The material constants derived from these tests, presented in Table 6.1, were implemented directly in the FEM simulations to predict actuator performance.

6.3.2 Assessment of FEM Predictions for Bending response

The predictions of the bending performance were evaluated for both the unconstrained (R10-d400) and constrained (R10-d400-sl) actuator configurations. The unconstrained design was tested to 5 psi, beyond which the ballooning effects became significant. The constrained

design, stabilised by the fabric reinforcement that prevented excessive radial expansion, enabled testing up to 5.5 psi. The evaluation of the model used three comparative methods: experimental photographs, FEM simulation images, and quantitative profile plots, allowing the evaluation of computational predictions against physical behaviour.

Unconstrained Actuator (Design configuration R10-d400)

Figs. 6.6 and 6.7 document the deformation sequence at incremental pressures of 0.5 to 5 psi. The actuator behaviour exhibited three distinct phases. In the initial phase at 0.5 psi, the actuator showed slight deflection toward the thinner layer (left). A transition phase occurred between 2.5-3.0 psi, where the actuator reoriented from left to right deflection. During the progressive phase (3.5-5 psi), rightward bending increased steadily with pressure. The FEM predictions demonstrated good fidelity in capturing these characteristic phases, particularly the bidirectional motion sequence typical of eccentric void actuators. Quantitative comparison between FEM predictions and experimental results showed varying agreement across these phases. Fig. 6.5a shows the comparison between FEM and experimental bending angles for R10-d400, revealing a maximum percentage discrepancy of 48.5% at 3.5 psi and a minimum of 1.26% at 2.5 psi. The overall correlation between FEM and experimental data is strong, with an R^2 value of 0.857, see Fig. 6.5a. At 3.5 psi, experimental bending exceeded FEM predictions significantly. This discrepancy decreased at 4.0 psi and became minimal at 5 psi. The profile plots demonstrated consistent behaviour in all the experimental trials (s1, s2, s3), with FEM capturing the general deformation pattern despite the deviation at 3.5 psi.

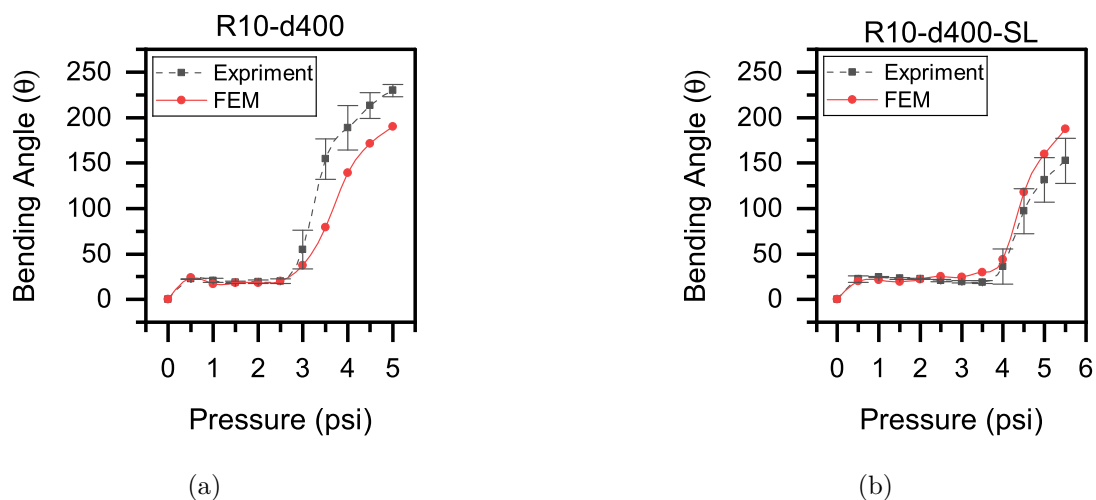
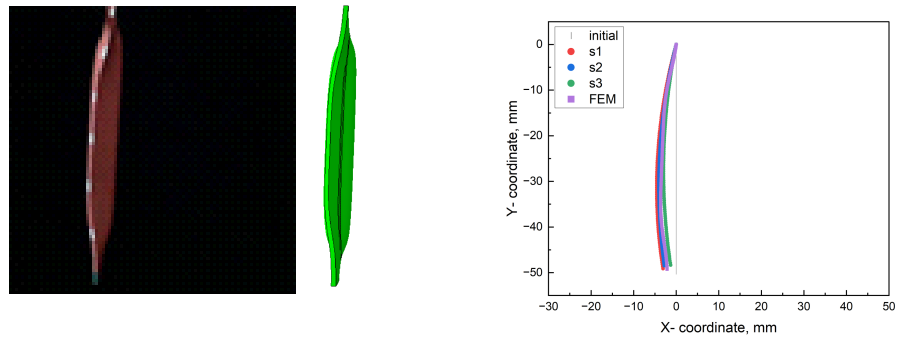
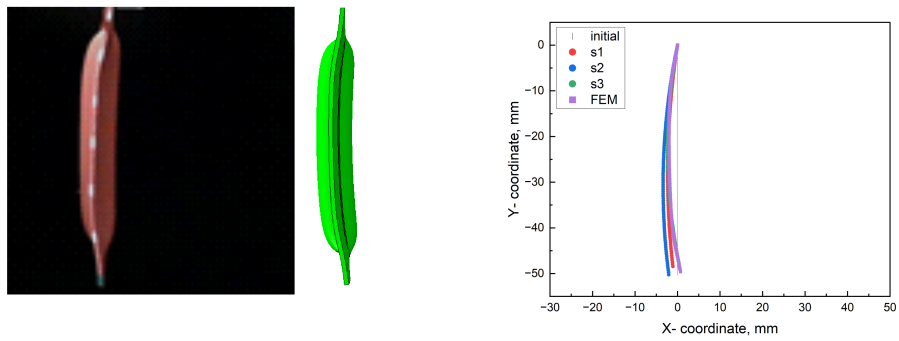


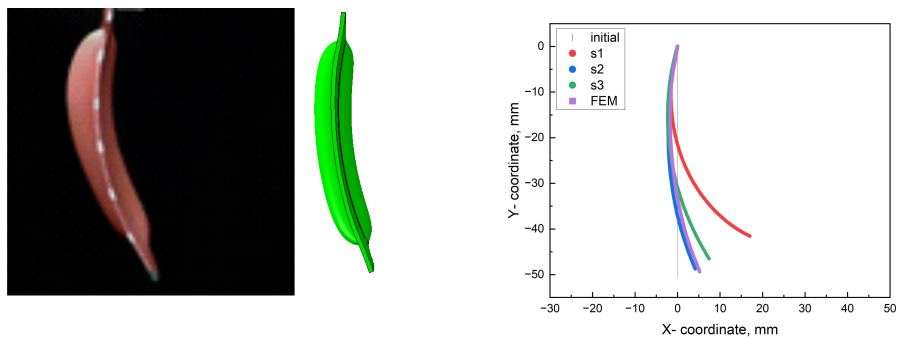
Figure 6.5: FEM vs. experimental bending angles for PneuThin actuators: (a) unconstrained and (b) constrained



(a) 0.5 psi

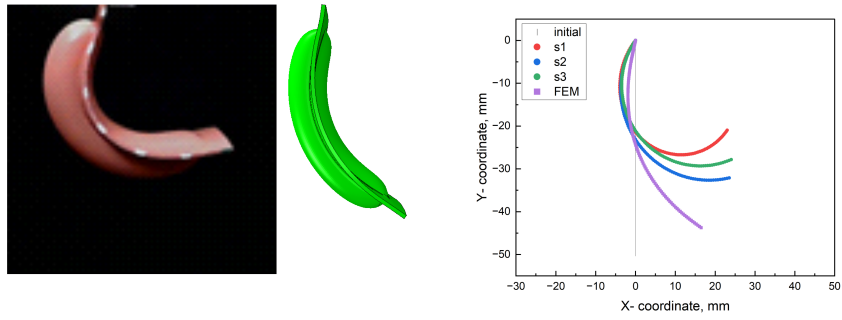


(b) 2.5 psi

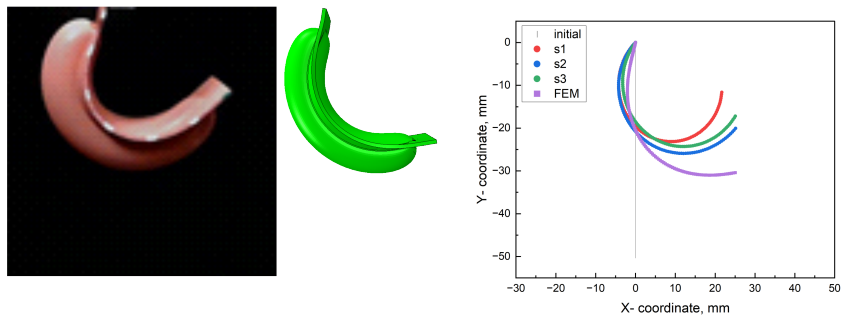


(c) 3 psi

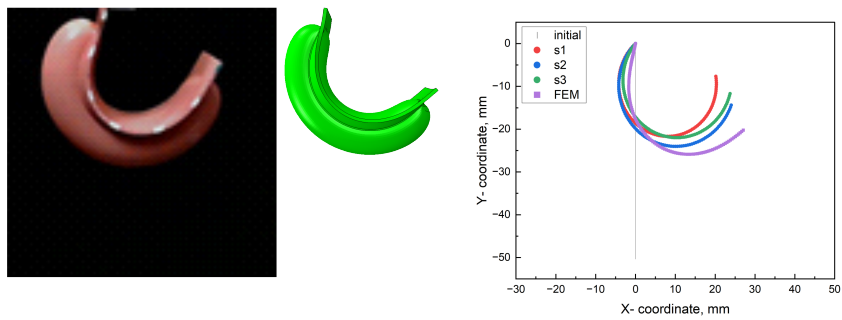
Figure 6.6: Inflation sequence of the R10-d400 actuator from 0.5 to 3 psi through experimental images, FEM simulations, and profile plots



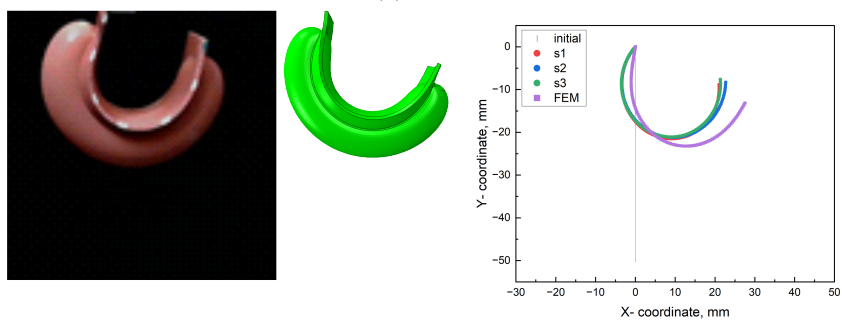
(a) 3.5 psi



(b) 4 psi



(c) 4.5 psi



(d) 5 psi

Figure 6.7: deformation sequence of the R10-d400 actuator from 3.5 to 5 psi through experimental images, FEM simulations, and profile plots

Constrained Actuator (Design configuration R10-D400-SL)

Figs. 6.8 and 6.9 document the deformation sequence at incremental pressures from 0.5 to 5.5 psi. The actuator exhibited two distinct phases. In the initial phase (0.5-3.0 psi), the actuator maintained a consistent leftward deflection toward its thinner layer. The transition phase began at 3.5 psi, characterised by a shift to rightward bending that progressively increased to 5.5 psi. Fabric reinforcement effectively regulated the deformation pattern, resulting in more predictable bending behaviour compared to the unconstrained design. FEM predictions demonstrated excellent agreement with the experimental results during the initial phase (0.5-3.5 psi), accurately capturing both the magnitude and the direction of deflection. Fig. 6.5b presents a comparison between experimental and FEM bending responses for the R10-d400-SL configuration, showing a maximum percentage discrepancy of 57.9% at 3.5 psi and a minimum of 1.90% at 2.0 psi. The overall correlation between FEM and experiment is strong, with an R^2 value of 0.903, see Fig. 6.5b. Profile plots confirmed consistent behaviour across experimental trials. However, at higher pressures (5.0-5.5 psi), FEM simulations slightly overestimated the magnitude of bending compared to the experimental observations. This discrepancy can be attributed to dimensional variations in the fabrication process.

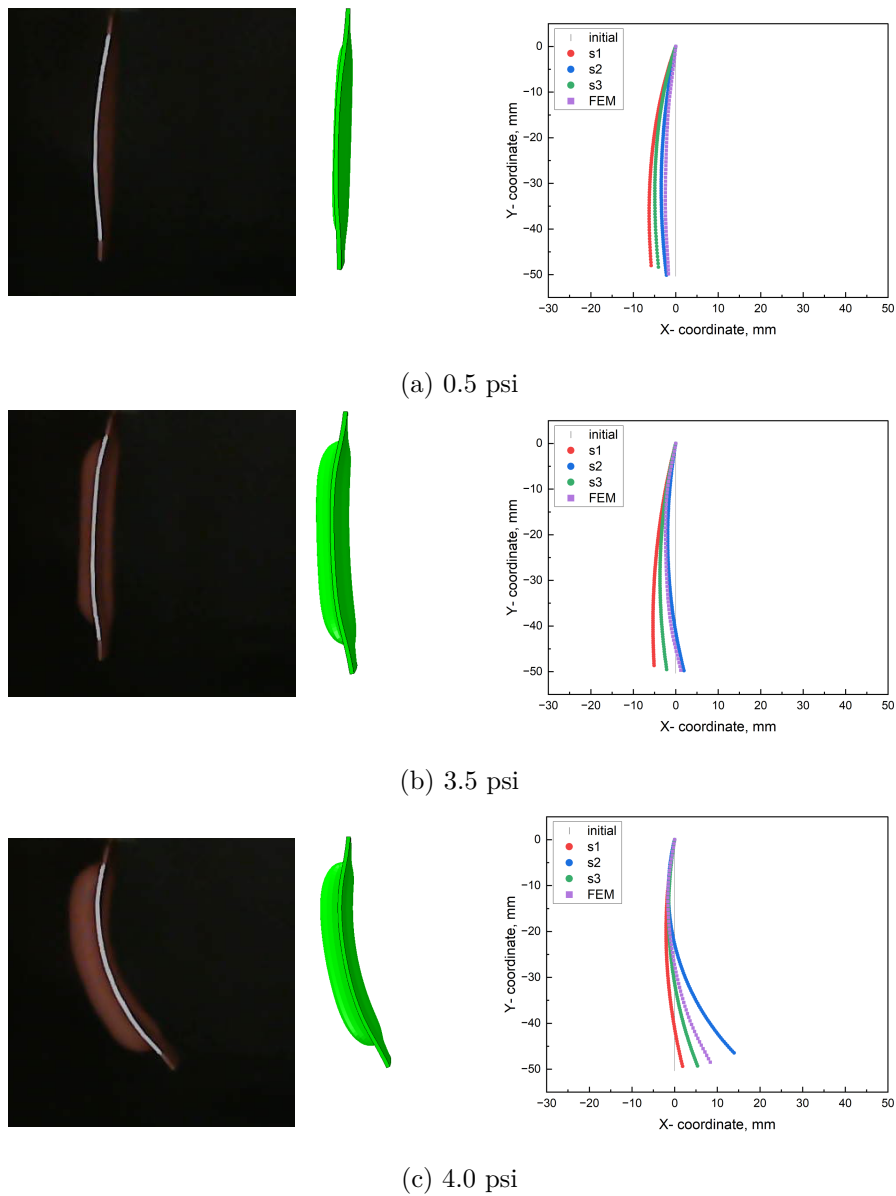
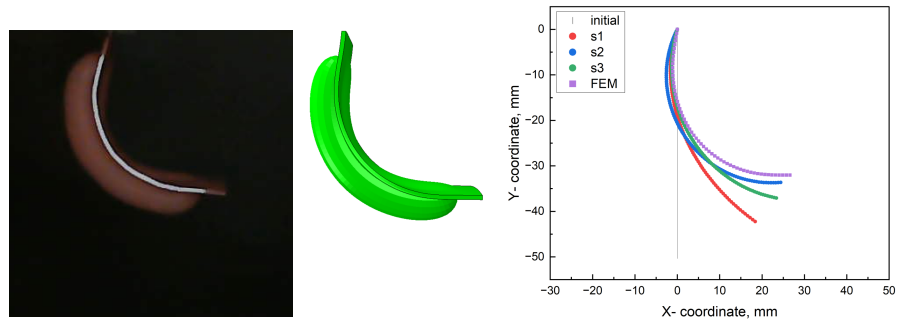
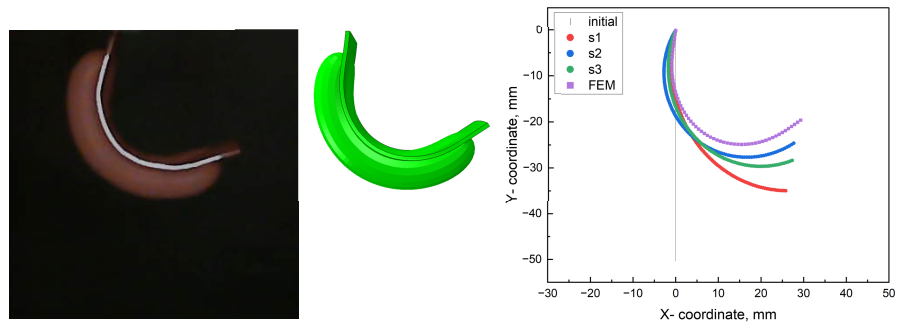


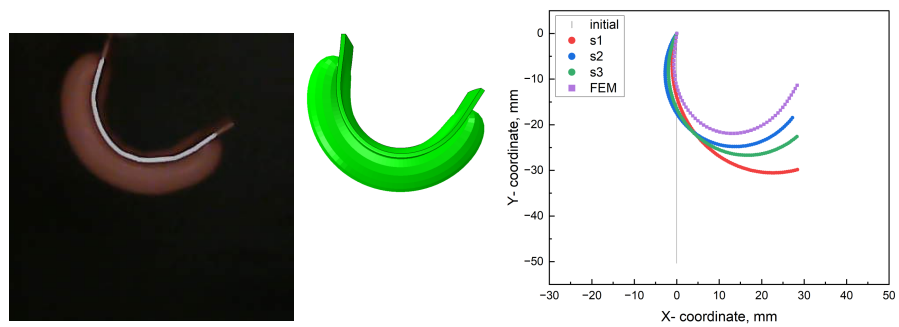
Figure 6.8: Deformation sequence of the R10-d400-SL actuator from 0.5 to 4 psi through experimental images, FEM simulations, and profile plots



(a) 4.5 psi



(b) 5.0 psi



(c) 5.5 psi

Figure 6.9: Deformation sequence of the R10-d400-SL actuator from 4.5 to 5.5 psi through experimental images, FEM simulations, and profile plots

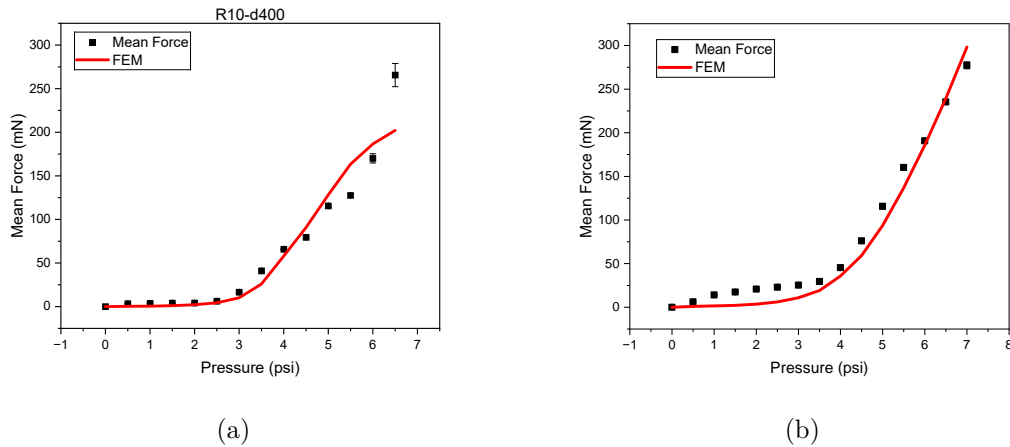


Figure 6.10: Comparison between experimental measurements and FEM predictions of force output: (a) R10-d400 configuration without strain-limiting layer, and (b) R10-d400-sl configuration with embedded strain-limiting layer.

6.3.3 Assessment of FEM Blocked-Force Predictions

Blocked force characteristics were evaluated for the configurations of the unconstrained actuator (R10-d400) and the constrained actuator (R10-d400-sl). The analysis examined the relationship between applied pressure and blocked force output, comparing experimental measurements with FEM predictions. The results are presented through force-pressure curves and quantitative error analysis to evaluate the predictive accuracy of the model across the operating pressure range of each design.

Unconstrained Actuator (Design configuration R10-d400)

Fig. 6.10a shows the blocked force response with increasing pressure, comparing the experimental measurements with FEM predictions ($R^2 = 0.9647$). The force-pressure relationship exhibited three distinct regions. At low pressures (below 2 psi), the actuator produced minimal forces (< 5 mN), and FEM accurately tracked this initial response. Force generation became pronounced beyond 3 psi, showing a gradual increase to 4.5 psi followed by a steeper growth. At higher pressures (5-6.5 psi), the actuator reached 265.6 ± 13.3 mN, though the predictions of the FEM underestimated these values. The simulation curve resembles the exponential growth shown in the experiment, particularly in capturing the transition from minimal to significant force generation. A similar trend of force-pressure was observed in previous research by (Moseley et al., 2016; Ko et al., 2022). Table 6.2 presents detailed force values and error analysis in the full pressure range.

Table 6.2: Experimental vs. FEM Predicted Forces for PneuThin configurations

Pressure (psi)	Unconstrained Configuration (R10-d400)			Constrained Configuration (R10-d400-sl)		
	Mean \pm SD (mN)	FEM (mN)	Absolute Error (mN)	Mean \pm SD (mN)	FEM (mN)	Absolute Error (mN)
0.5	3.320 \pm 0.186	0.322	2.998	6.032 \pm 0.325	0.969	5.062
1.0	3.775 \pm 0.152	0.500	3.275	13.925 \pm 0.579	1.538	12.387
1.5	4.031 \pm 0.184	1.008	3.023	17.446 \pm 0.393	2.156	15.290
2.0	4.162 \pm 0.209	2.177	1.985	20.827 \pm 0.311	3.491	17.335
2.5	6.226 \pm 0.235	4.346	1.881	22.898 \pm 0.313	6.091	16.807
3.0	16.500 \pm 0.848	10.038	6.462	25.286 \pm 0.333	10.809	14.477
3.5	40.954 \pm 1.306	25.882	15.072	29.436 \pm 0.404	19.110	10.326
4.0	65.786 \pm 0.563	58.018	7.768	45.408 \pm 1.118	35.739	9.669
4.5	79.404 \pm 1.419	90.687	11.283	76.064 \pm 1.747	59.273	16.792
5.0	115.503 \pm 1.751	128.131	12.628	115.725 \pm 3.047	93.613	22.112
5.5	127.563 \pm 2.295	163.418	35.855	160.295 \pm 1.655	136.770	23.524
6.0	170.101 \pm 5.247	186.526	16.425	190.692 \pm 1.325	185.675	5.018
6.5	265.618 \pm 13.323	202.157	63.461	235.367 \pm 2.209	239.462	4.095
7.0	-	-	-	277.199 \pm 3.994	298.216	21.017

Constrained Actuator (Design configuration R10-D400-SL)

Fig. 6.10b shows the response of the blocked force with increasing pressure, demonstrating a strong correlation between the experimental measurements and the predictions of FEM ($R^2 = 0.989$). The force-pressure relationship showed three distinct regions. At low pressures (below 2 psi), the actuator produced minimal forces (< 20 mN), and FEM slightly underestimated these values. Force generation became significant beyond 3.5 psi, consistent with the actuation threshold identified in Section 5.3.1. At higher pressures (5-7 psi), the actuator reached 280 ± 10 mN at 7 psi, and the FEM predictions showed excellent agreement (relative errors $< 8\%$). Similarly to the unconstrained design, the simulation curve captured the exponential growth pattern observed experimentally. Table 6.2 presents detailed force values and error analysis in the full pressure range.

6.4 Discussion

FEM demonstrated strong predictive capabilities for the behaviour of both unconstrained and constrained PneuThin configurations, particularly at low to moderate pressures; however, some limitations were evident at higher pressures. This section examines the strengths and limitations of the FEM approach and analyses its effectiveness as a design tool for FlexiLayer-fabricated actuators.

The computational models showed a strong correlation with the experimental measurements of the blocked force, achieving R^2 values of 0.98. This high accuracy confirms that FEM can reliably predict force generation capabilities during the design process. The models accurately captured key behavior characteristics, the activation threshold

pressures (approximately 3 psi for standard designs and 4 psi for fabric-embedded variants) and the subsequent force development patterns. Notably, FEM successfully captured the bidirectional motion characteristic of eccentric void actuators. This behaviour, where actuators initially bend toward the low stiffness side at low pressures before transitioning to the opposite direction at higher pressures, aligns with previous findings of Gorissen et al. (2017), Gorissen et al. (2011), Konishi et al. (2006) and Konishi et al. (2005). The observed bidirectional response provides support for the modelling approach; however, models consistently underestimated bending angles at higher pressures (above 3.5 psi), particularly for the unconstrained design configuration.

A possible explanation for this bidirectional bending phenomenon is the presence of anisotropic elasticity introduced through differences in bending stiffness (EI) between the layers above and below the cavity, where E is the Young's modulus and I is the second moment of area. At low pressures, the actuator bends toward the thin layer due to its lower resistance to deformation. As the internal pressure increases, the strain in the thin layer increases significantly more than in the thick layer, generating an imbalance in internal tensile forces that causes the actuator to reverse direction and bend toward the thicker side. This behaviour is observed in both R10-d400 and R10-d400-SL configurations. In the former, the difference in stiffness arises from geometric asymmetry (i.e., difference in I), while in the latter it results from material property differences (i.e., difference in E due to the strain-limiting layer). A similar explanation was reported by Konishi et al. (2006), who attributed the reversal in the bending direction to changes in the dominant pulling forces between thin and thick diaphragms as pressure increases. The accurate reproduction of this pressure-dependent behaviour by the FEM model provides further confidence in its predictive capability.

A key limitation of the current FEM implementation is its reliance on the properties of the initial tensile or first stretch material, which neglects the effects of stress softening (Moseley et al., 2016). During experimental testing, PneuThin samples undergo repeated inflation cycles, leading to the Mullins effect (Mullins, 1969), a characteristic stress softening phenomenon of elastomers during cyclic loading, where the stress at a given stretch decreases during reloading compared to the initial loading path (Guo et al., 2017). This behaviour, arising from the deformation-dependent contributions of chain entanglements within the rubber network (Villani and Lavallata, 2024), explains the slightly higher bending angles observed in our experimental samples compared to the predictions of FEM at higher pressures. This finding aligns with Libby et al. (2022), showing that repetitive high-

deformation tests lead to fatigue in soft actuator pneu-nets, causing deviations in the FEM model predictions. Initially, their FEM model predicts the bending angle with an error of 4% compared to the experimental data of trial 1, but this increases to an error of 20% after ten cycles of bending actuation (Libby et al., 2022).

A good agreement at high pressure between FEM and experimental results is observed in the constrained configuration (R10-d400-SL), as shown in Fig. 6.10b. This improved correlation is hypothesised to be due to the incorporation of the strain-limiting layer, which increases stiffness and modulates curvature compared to the actuator structure without it (Sinatra et al., 2018). This effect may reduce ballooning and excessive deformation of the thin layer (Lekakou et al., 2015), thus minimising the influence of neglecting the Mullins effect in the hyperelastic material model and enhancing FEM predictions at high pressures in constrained configurations compared to unconstrained ones. Despite this strong correlation in constrained designs, the current study recommends FEM primarily for optimisation within low to moderate pressure ranges (below 4 psi), particularly for unconstrained configurations where larger deformations and stress softening effects are not well captured. Hence, for PneuThin designs operating at high pressure without strain-limiting layers, experimental testing becomes crucial. Although current hyperelastic material models derived from doctor blade-coated samples provided adequate results, refining these models by characterising the mechanical properties of conditioned tensile samples after multiple loading cycles may enhance prediction accuracy. Future research should prioritise developing hyperelastic material models that incorporate cyclic softening behaviour, as suggested by (Guo et al., 2017), to improve the predictive capabilities of FEM.

Although the Mullins effect provides one plausible explanation for the underestimation of bending angles in FEM at higher pressures, it may not fully account for the observed discrepancies. A further limitation lies in the current material model's reliance on uniaxial tensile and compressive tests, which may not sufficiently capture the complex deformation behaviour of the thin silicone layer during inflation. In soft actuators such as PneuThin, inflation of the internal cavity causes the thin silicone layer to stretch in two directions at the same time, along the length of the actuator and across its width, creating a biaxial strain state. This multiaxial deformation cannot be fully described by uniaxial data alone. To improve model fidelity, future FEM development should incorporate biaxial material characterisation, such as biaxial tensile testing or bulge inflation tests, to obtain more representative data for fitting hyperelastic material models. This would allow for a more

accurate simulation of highly stretched regions, especially in the thin layer, and reduce prediction errors at high pressures (Xavier et al., 2020).

Despite these limitations, the evaluated FEM approach provides a valuable tool for initial design optimisation of FlexiLayer-fabricated actuators. It performs well, particularly in predicting activation thresholds and force-generation capabilities. When used within its established reliable range, FEM can significantly reduce the need for physical prototyping while providing information on actuator behaviour. This computational approach, combined with targeted experimental testing, offers an efficient pathway for developing new PneuThin designs.

6.5 Chapter Summary

Chapter 6 evaluates the efficacy of FEM as a design evaluation tool for PneuThin fabricated using the FlexiLayer technique. The study examines the configurations of the unconstrained actuators (R10-d400) and the constrained (R10-d400-SL), building on the preliminary analysis of Chapter 3 and the experimental results of Chapter 5. The methodology encompasses three phases: material characterisation, FEM implementation, and experimental comparison. Material characterisation involved testing both configurations to develop appropriate hyperelastic models. FEM implementation created detailed 3D models in finite element software (Abaqus 2024) for free-bending and blocked force analyses. The comparative phase assessed computational predictions against experimental measurements.

The results demonstrate an accurate prediction of key performance metrics: actuation threshold pressures (3 psi for unconstrained design, 4.5 psi for constrained design) and blocked force generation ($R^2 > 0.96$). The models demonstrated strong agreement on the bending profiles at low pressures, with some deviation at higher pressures. The constrained design exhibited a more predictable linear force response compared to the unconstrained configuration. This focused assessment establishes FEM as an effective tool for initial PneuThin design optimisation, enabling efficient development through accurate prediction of performance variations across different material configurations and geometric parameters.

Chapter 7

Discussion, Future Work and Conclusion

Chapter 7 synthesises the key findings of the thesis and evaluates them within the broader context of soft robotics fabrication. First, the chapter presents a comprehensive discussion of the experimental and computational results, examining the strengths and limitations of the FlexiLayer technique. Next, potential directions for future research are outlined, highlighting opportunities to expand the technique's capabilities and applications. Finally, the conclusion section summarises the key findings and outcomes of the research.

7.1 Overall Discussion

This research aimed to develop and validate a novel fabrication technique for pneumatic thin planar soft actuators through systematic phases. The objectives outlined in Chapter 1 were successfully met. The preliminary analysis of the FEM provided an understanding of how geometric parameters influence actuator bending deformation. This analysis identified critical relationships between layer thickness, cavity dimensions, and bending performance. The FlexiLayer fabrication protocol was subsequently developed to achieve precise control over the design parameters of the PneuThin fabrication. The doctor blade coating demonstrated high uniformity in the thickness of the coated layer. Precision was achieved using a coating thickness gauge (Elcometer 456, UK) fitted with a specialised soft coating probe, ensuring accurate measurements without compressing the soft material (Lee and Langdon, 1996). A reliable predictive model was established between GH and DFT, following the equation ($DFT = 0.7604(GH) - 15$). This linear relationship achieved a determination coefficient of $R^2 = 0.9969$, demonstrating strong predictive accuracy.

The model enabled repeatable production of soft actuators and robots with precise layer thickness control.

The validation of this developed fabrication protocol steps, successfully achieved by experimental fabrication and characterisation through eight PneuThin configurations fabricated to demonstrate the versatility of the FlexiLayer technique (see Chapter 5). The results showed a consistent nonlinear relationship between pressure and bending angle (Figs. 5.4 to 5.7). The trend of non-linearity in the relationship between pressure and bending angle is attributed to the inflated cavity area that increases non-linearly with applied pressure (Sinatra et al., 2018). Among these configurations, the constrained PneuThin configuration (R10-d400-sl) which contains a strain-limiting layer, produces the highest blocked force of 280 mN at 7 psi. This outcome is consistent with previous research, which showed that the integration of nanofiber sheets in silicone-based elastomer actuators made them tougher and stronger than the pure unconstrained silicone actuator (Sinatra et al., 2018; Sinatra et al., 2019). The average maximum force displayed in this research exhibited comparable performance to existing soft bending actuators fabricated using moulding (500 mN at ≈ 7.5 -8 psi) (Mosadegh et al., 2014; Wang et al., 2019), soft lithography (500 mN at ≈ 6.5 psi) (Moseley et al., 2016), and 3D printing (200 mN at ≈ 9 psi) (Peele et al., 2015). Based on these findings, it appears that the FlexiLayer method represents a promising alternative to existing fabrication methods for pneumatic soft actuators. Based on these findings, it appears that the FlexiLayer method represents a promising alternative to existing fabrication methods for pneumatic soft actuators.

Impact of the FlexiLayer Method

The proposed FlexiLayer approach demonstrated several practical and design-related advantages over existing soft actuator fabrication methods, as evidenced by experimental findings presented in Chapters 4 and 5:

- **Fabrication similarity of simple and complicated shapes:**

Uniform fabrication steps, regardless of the number of layers and different geometries, provide an advantage in the development of complicated robotic structures (see Section 5.4.2).

- **Batch fabrication:**

Having a well-defined fabrication step enables the large-scale production of soft robotic systems with less variability in dimensions, helping to fabricate uniform items in large quantities (see Fig. 4.9e).

- **Rapid fabrication:**

The limited number of well-defined steps allows a rapid fabrication process. This streamlined process supports iterative prototyping and accelerates design exploration in a manner similar to 3D printing, where fast failures facilitate fast convergence toward successful designs.

- **Material compatibility:**

The FlexiLayer fabrication method supports the development of robot/actuator systems with different capabilities by changing individual materials (see Fig. 5.7).

- **Ability to fabricate thin planar devices:** The ability to fabricate submillimeter thicknesses enables the creation of actuators as thin as approximately 1 mm. This thinness allows lightweight and compact actuators, which makes them potentially suitable for assistive soft wearable devices and rehabilitation systems (Park et al., 2014b; Wirekoh and Park, 2017).

- **Physical parameter variation to achieve the necessary motion and forces:**

The output force and bending angle can be drastically changed by modifying physical parameters. Section 5.3 shows that parameters such as the thickness of the layer material, the shape and width of the cavity are critical to adjusting the performance. These are key attributes in the development of actuators and complete systems.

These advantages demonstrate how FlexiLayer improves fabrication efficiency and flexibility for soft robotics. The following discussion highlights some of the current limitations and technical challenges identified during experimental implementation, before moving on to other key observations and implications drawn from the study.

The demonstrated FlexiLayer method is a versatile method for developing simple and complicated shapes and actuator designs for soft robotics. However, this method has a few shortcomings, such as delamination of layers if the curing process has not been performed well. It also has difficulty in keeping the inserted needles and the cavity channel sealed. Additionally, misalignment between the PVA mask layer and the laser cut can lead to unexpected motion due to distortion of the cavity orientation, particularly in asymmetric designs. Minor wrinkles in the PVA mask layer during fabrication can also induce uneven thickness in the top layer along the cavity edge, leading to stress concentration, rupture, or leaks upon pressurisation. Furthermore, the actuation mechanism in the presented research is based on the swelling of the cavity (see Fig. 3.2). This may result in ballooning effects (e.g., significant radial expansion) at high pressure (Fig. 5.6), which are regarded

as a drawback (Lekakou et al., 2015; Elsayed et al., 2014; Gariya et al., 2023). However, these problems will be addressed in future research.

To maximize the effectiveness of this fabrication method, the FEM was utilized in Chapter 6 to assess it as a design tool in the design process. The FEM demonstrated strong predictive capabilities for PneuThin. The predictions of the numerical simulation aligned well with the experimental results, achieving R^2 values greater than 0.96 for force measurements in an unconstrained configuration (R10-d400) and constrained fabric embedded configuration (R10-d400-sl). The models accurately predicted activation threshold pressures of 3 psi for standard designs and 4 psi for fabric-embedded variants. FEM successfully captured the bidirectional motion characteristic of eccentric void actuators, where initial bending occurs toward the thinner wall at low pressures before transitioning to the opposite direction at higher pressures. In addition, the predicted (XY) deformation profile is in fairly good agreement with the quantified observed profile across the applied air pressure. As a consequence, this verified the simulation modelling approach for predicting these discrete deformation patterns of the PneuThin actuator during inflation. Similarly, this finding supports studies linking bidirectional bending motion to pneumatic balloon soft actuator designs (Gorissen et al., 2011; Jeong et al., 2005). However, the FEM model of the unconstrained configuration underestimated the bending angles at pressures greater than 3.5 psi. This limitation may be associated with the current material model, which relies on initial tensile properties and does not account for the Mullins effect, the characteristic stress softening observed in elastomers during cyclic loading (see Section 6.4). The verification focused on two configurations from a larger set of eight configurations, providing proof-of-concept while highlighting areas for future refinement. These improvements should incorporate material models that account for cyclic softening behaviour, direct mechanical property characterisation of doctor-blade coated samples, and extended verification across diverse cavity geometries. Nevertheless, the current FEM model developed in Chapter 6 still provides useful insights for the design of the PneuThin, for instance regarding the force output prediction.

The FlexiLayer technique has the potential to be compatible with a wider range of soft materials, but this research is limited by the specific properties of Elastosil 4601M. The focus of Elastosil 4601M in this investigation as the primary soft material was due to the selection criteria provided in Section 3.2.2. In particular, its viscosity, which falls within the recommended range for doctor blade coating (around $10,000 \text{ Pa} \cdot \text{s}$), allows for effective application and spread of the silicone material. This focus on a single

suitable material serves to validate the technique and establish a robust characterisation methodology, demonstrating the feasibility of fabricating and evaluating PneuThin with the FlexiLayer approach. Therefore, factors may affect the generalisability of certain results. For example, the model formulation derived from the DFT characterisation against different blade GH may not be directly applicable to other silicones, such as Dragon Skin or Ecoflex (SmoothOn Inc., USA). However, the overall methodology and fabrication protocol developed in Chapter 4 can be generalised to other materials with appropriate adjustments. This can be achieved by exploring viscosity modifications through thinning (Silicone Thinner Smooth-On Inc., USA) or thickening (THI-VEX Smooth-On Inc., USA) agents. This adaptation would enable material selection based on application requirements rather than processing constraints, thereby broadening the utility of the technique across soft robotics applications.

The experimental validation using laboratory-scale prototypes provides a proof-of-concept, although it represents only a subset of potential applications. In particular, the FlexiLayer method holds promise for industrial feasibility. The current laboratory-scale validation provides a foundation for exploring automated manufacturing processes. Roll-to-Roll manufacturing presents a promising approach to scale-up the FlexiLayer technique, as this method adapts well to continuous doctor blade coating processes (Ou et al., 2016). This manufacturing approach enables high-volume production while maintaining cost-effectiveness (Krebs, 2009; Goodship et al., 2016). Therefore, exploring continuous coating methods, automated alignment, thickness measurement systems, and rapid curing protocols in future research is highly recommended. These advancements could improve the production efficiency of the soft robot device, thereby broadening its use.

7.2 Future Research Directions for FlexiLayer Fabrication

The showcase effectiveness of FlexiLayer fabrication in this research focused on bending actuators, although the technique has potential for broader applications (see Fig. 3.1). Future studies should explore the development of twisting actuators (Sinatra et al., 2018) bending and twisting actuators (Futran et al., 2018) and linear contraction actuators (Martinez et al., 2012) using the FlexiLayer approach. The creation of biomimetic 3D deformation patterns requires further investigation through controlled elastic moduli within the soft laminate structure, as demonstrated by Pikul et al. (2017). This control could be achieved through the strategic placement of patterned nonwoven fabric (Sulky soft'n sheer, USA) within the elastomer silicone layers during fabrication. To implement these

advancements, modifications to the vacuum chuck device described in Chapter 4 would be necessary to accommodate the assist in aligning porous materials (see Fig. 4.3).

Further exploration of PneuThin configurations could enable advanced actuation modes through strategic placement of the PVA mask layer (Sulky solvy, USA). The implementation of overlapping mask layers, separated by elastomer silicone, could facilitate independent bidirectional bending motions. The integration of discrete cavities, which are similar to the PneuNets actuator configuration, presents opportunities for achieving controlled twisting motions. This can obtain when these cavities are orientated at different angles relative to the central axis of the actuator and connected through air-transfer channels, they enable motions similar to those demonstrated by Gorissen et al. (2014) and Liang et al. (2017). These geometric and layout variations of the PVA layer could expand the capability of FlexiLayer-fabricated actuators beyond the validated bending configurations. Hence, multiple motion modes can be obtained, thus improving its adaptability to an unstructured environment.

The integration of sensing capabilities into the PneuThin actuator represents another critical direction for future research. The incorporation of an electrically functional layer could enhance the intelligence of PneuThin actuators. Several approaches need to be explored for this integration. A mixture of silicone elastomer and conductive nanoparticles could be applied to the soft layered laminates following the FlexiLayer protocol, using a capacitive-based soft sensor similar to that published by Tsouti et al. (2016). Direct alignment of conductive fabric sheets offers another viable approach, as demonstrated by Atalay et al. (2017). Selective deposition of conductive networks via precision fluid dispensing (EFD Nordson, USA) presents a third option, similar to the multi-material direct ink writing approach presented by Wang et al. (2022b). The implementation of these sensing elements would enable real-time feedback mechanisms within the soft robotic structure.

Planned Publications

As part of the anticipated publication of this research, two manuscripts are currently in preparation. The first paper, which is under internal review, introduces the FlexiLayer fabrication method and presents a systematic evaluation of its capabilities. This includes experimental validation through parameter variation studies and preliminary FEM simulations to demonstrate its effectiveness as a design tool. The paper then applies this method to the development of a complex robotic structure composed of multiple PneuThin

actuators with several degrees of freedom, all fabricated in a single integrated process. This showcases the versatility and broader applicability of the FlexiLayer technique in manufacturing intricate soft robotic systems. A second manuscript is planned as a collaborative work focussing on a case study involving the development and characterisation of a soft rolling polyhedral robot known as the 'Rolly Poly'. This spherical robot integrates twelve pneumatically driven soft actuators, each fabricated using the FlexiLayer protocol. The layer-by-layer deposition approach enabled the production of actuators with consistent quality and allowed them to easily integrate into the robot's shell design. This paper, co-authored with undergraduate students James McKay, Max O'Dare, and Victor Mwendia, will describe the architecture of the system, including chassis design, electronic control, and pneumatic circuitry, and will assess how effectively the robot can follow a planned route using discrete rolling motion. The study highlights the broader utility of FlexiLayer for producing multiple coordinated actuators within complex soft robotic systems.

7.3 Conclusion

This research has established the FlexiLayer fabrication technique as an effective method to create PneuThin. Through development and validation, the technique demonstrates precise control over critical fabrication parameters. The doctor blade coating process achieves exceptional layer uniformity, with coefficient of variation below 4% for GH ranging from 200 to 800 μm . The implementation of a vacuum-assisted alignment system significantly improves the precision of the fabrication, reducing the position error to less than 1mm and the rotational error to less than 1 degree, marking a substantial improvement over the manual alignment method. Investigation of fabrication process parameters proved crucial for actuator performance. The laser cutting parameters were refined to 25-40% power at 5% speed, allowing clean cuts through 1 mm thick Elastosil M4601 without thermal damage. Experimental testing determined that 3 minutes of semicuring time at 75 $^{\circ}\text{C}$ provides optimal bonding strength between layers, essential for structural integrity during actuation. These parameters ensure reliable and reproducible fabrication results.

Experimental validation through eight distinct PneuThin configurations demonstrated the adaptability of the FlexiLayer technique. The PneuThin configuration (R10-d400) achieved remarkable bending performance, reaching $245 \pm 33^{\circ}$ at 5 psi, while its fabric-reinforced configuration (R10-d400-sl) exhibited more controlled motion with $90 \pm 34^{\circ}$ at the same pressure. Force generation capabilities proved substantial, with the R10-d400 configuration producing 265.6 ± 13.3 mN at 6.5 psi and the R10-d400-sl configuration

achieving 280 ± 10 mN at 7 psi. These results confirm the technique's capability to produce actuators with specific, predictable performance characteristics such as bending angle and force generation.

The practical utility of the FlexiLayer technique was demonstrated through the use of two functional case studies. A soft gripper successfully handled objects ranging from 5g to 194g, demonstrating precise force control and adaptability. The soft quadrupedal robot achieved consistent locomotion at 1.7 ± 0.2 mm/s, demonstrating the technique's ability to fabricate a multiactuator device incorporating five independently PneuThin. These applications validate the practical viability of FlexiLayer-fabricated actuators. FEM analysis provided strong validation of the fabrication technique, achieving R^2 values exceeding 0.96 for force prediction. The models accurately predicted activation threshold pressures of 3 psi for the unconstrained (R10-d400) and constrained (R10-d400-sl) configurations, with the mean absolute error in force prediction remaining below 14 mN. This correlation between computational and experimental results establishes FEM as a reliable tool for design process optimisation prior to fabrication.

Bibliography

3580/5, E. 2025. *Elcometer 3580/5 Casting Knife Film Applicator*.

AG, W. C. 2024. *ELASTOSIL® M 4601 A/B: Room Temperature Curing Silicone Rubber (RTV-2)*. Accessed: 2024. Wacker Chemie AG. URL: <https://www.wacker.com/h/en-us/silicone-rubber/room-temperature-curing-silicone-rubber-rtv-2/elastosil-m-4601-a-b/p/000007879>.

Alici, G., Canty, T., Mutlu, R., Hu, W. and Sencadas, V. 2018. Modeling and Experimental Evaluation of Bending Behavior of Soft Pneumatic Actuators Made of Discrete Actuation Chambers. *Soft Robot*. **5**(1), pp. 24–35. DOI: 10.1089/soro.2016.0052. URL: <https://www.ncbi.nlm.nih.gov/pubmed/29412079>.

Allen, E. A. and Swensen, J. P. 2019. Versatile Layering Approach to Pneumatic Soft Actuator Manufacturing. *ASME 2019 Conference on Smart Materials, Adaptive Structures and Intelligent Systems*. URL: <https://api.semanticscholar.org/CorpusID:214291341>.

Amiri Moghadam, A. A., Alaie, S., Deb Nath, S., Aghasizade Shaarbaf, M., Min, J. K., Dunham, S. and Mosadegh, B. 2018. Laser Cutting as a Rapid Method for Fabricating Thin Soft Pneumatic Actuators and Robots. *Soft Robot*. **5**(4), pp. 443–451. DOI: 10.1089/soro.2017.0069. URL: <https://www.ncbi.nlm.nih.gov/pubmed/29924697>.

Ang, B. W. K. and Yeow, R. C. H. 2017. A Novel Fold-Based Design Approach toward Printable Soft Robotics Using Flexible 3D Printing Materials. *Advanced Materials Technologies*. **3**(2), p. 1700172. DOI: 10.1002/admt.201700172.

Atalay, A. T., Sanchez, V., Atalay, O., Vogt, D. M., Haufe, F. L., Wood, R. J. and Walsh, C. J. 2017. Batch Fabrication of Customizable Silicone-Textile Composite Capacitive Strain Sensors for Human Motion Tracking. *Advanced Materials Technologies*. **2**. URL: <https://api.semanticscholar.org/CorpusID:34374670>.

- Auysakul, J., Vittayaphadung, N., Gonsrang, S. and Smithmaitrie, P. 2020. ‘Bending Angle Effect of the Cross-Section Ratio for a Soft Pneumatic Actuator’. *Proceedings of the 2020 IEEE International Conference on Robotics and Automation (ICRA)*. URL: <https://api.semanticscholar.org/CorpusID:219631075>.
- B.Gorissen, Donose, R., Reynaerts, D. and De Volder, M. 2011. Flexible pneumatic micro-actuators: analysis and production. *Procedia Engineering*. **25**, pp. 681–684. DOI: 10.1016/j.proeng.2011.12.168. URL: <https://dx.doi.org/10.1016/j.proeng.2011.12.168>.
- Blanco, K., Navas, E., Emmi, L. and Fernández, R. 2024. Manufacturing of 3D Printed Soft Grippers: A Review. *IEEE Access*. **12**, pp. 30434–30451. URL: <https://api.semanticscholar.org/CorpusID:268013352>.
- Bower, A. F. 2009. ‘Applied Mechanics of Solids’. 1st. Accessed 26 April 2025. CRC Press, p. 75. URL: <https://www.perlego.com/book/1509820>.
- Case, J. C., White, E. L. and Kramer, R. K. 2015. Soft Material Characterization for Robotic Applications. *Soft robotics*. **2**, pp. 80–87. URL: <https://api.semanticscholar.org/CorpusID:137498339>.
- Chernov, N. 2025. *Circle Fit (Taubin method)*. MATLAB Central File Exchange. Retrieved February 2, 2025. URL: <https://www.mathworks.com/matlabcentral/fileexchange/22678-circle-fit-taubin-method>.
- Choi, J., Ahn, S. H. and Cho, K. J. 2020. ‘Design of Fully Soft Actuator with Double-Helix Tendon Routing Path for Twisting Motion’. *2020 IEEE/RSJ International Conference on Intelligent Robots and Systems (IROS)*, pp. 8661–8666. DOI: 10.1109/IROS45743.2020.9341363.
- Chubb, K., Berry, D. A. and Burke, T. 2019. Towards an ontology for soft robots: what is soft? *Bioinspiration & Biomimetics*. **14**. URL: <https://api.semanticscholar.org/CorpusID:203568839>.
- Cianchetti, M., Ranzani, T., Gerboni, G., Falco, I. D., Laschi, C. and Menciassi, A. 2013. ‘STIFF-FLOP surgical manipulator: Mechanical design and experimental characterization of the single module’. *2013 IEEE/RSJ International Conference on Intelligent Robots and Systems*, pp. 3576–3581. DOI: 10.1109/IROS.2013.6696866.

- Cohrs, N. H., Petrou, A., Loepfe, M., Yliruka, M., Schumacher, C. M., Kohll, A. X., Starck, C. T., Schmid Daners, M., Meboldt, M., Falk, V. and Stark, W. J. 2017. A Soft Total Artificial Heart-First Concept Evaluation on a Hybrid Mock Circulation. *Artif Organs*. **41**(10), pp. 948–958. DOI: 10.1111/aor.12956. URL: <https://www.ncbi.nlm.nih.gov/pubmed/28691283>.
- Connolly, F., Polygerinos, P., Walsh, C. J. and Bertoldi, K. 2015. Mechanical Programming of Soft Actuators by Varying Fiber Angle. *Soft Robotics*. **2**(1), pp. 26–32. DOI: 10.1089/soro.2015.0001. URL: <https://doi.org/10.1089/soro.2015.0001>.
- Dämmer, G., Gablenz, S., Hildebrandt, A. and Major, Z. 2019. PolyJet-Printed Bellows Actuators: Design, Structural Optimization, and Experimental Investigation. *Frontiers in Robotics and AI*. **6**. URL: <https://api.semanticscholar.org/CorpusID:153310799>.
- De Greef, A., Lambert, P. and Delchambre, A. 2009. Towards flexible medical instruments: Review of flexible fluidic actuators. *Precision Engineering*. **33**(4), pp. 311–321. DOI: 10.1016/j.precisioneng.2008.10.004. URL: <https://dx.doi.org/10.1016/j.precisioneng.2008.10.004>.
- De Pascali, C., Naselli, G. A., Palagi, S., Scharff, R. B. N. and Mazzolai, B. 2022. 3D-printed biomimetic artificial muscles using soft actuators that contract and elongate. *Sci Robot*. **7**(68), eabn4155. DOI: 10.1126/scirobotics.abn4155. URL: <https://www.ncbi.nlm.nih.gov/pubmed/35895921>.
- Delgado, J. M. D., Oyedele, L., Ajayi, A., Akanbi, L., Akinade, O., Bilal, M. and Owolabi, H. 2019. Robotics and automated systems in construction: Understanding industry-specific challenges for adoption. *Journal of Building Engineering*. **26**, p. 100868.
- Dezaki, M. L., Bodaghi, M., Serjouei, A., Afazov, S. and Zolfagharian, A. 2022a. Soft Pneumatic Actuators with Controllable Stiffness by Bio-Inspired Lattice Chambers and Fused Deposition Modeling 3D Printing. *Advanced Engineering Materials*. **24**(12), p. 2200797. DOI: 10.1002/adem.202200797.
- Dezaki, M. L., Bodaghi, M., Serjouei, A., Afazov, S. M. and Zolfagharian, A. 2022b. Soft Pneumatic Actuators with Controllable Stiffness by Bio-Inspired Lattice Chambers and Fused Deposition Modeling 3D Printing. *Advanced Engineering Materials*. **25**. URL: <https://api.semanticscholar.org/CorpusID:255037688>.

- Diani, J., Fayolle, B. and Gilormini, P. 2009. A review on the Mullins effect. *European Polymer Journal*. **45**(3), pp. 601–612. DOI: <https://doi.org/10.1016/j.eurpolymj.2008.11.017>. URL: <https://www.sciencedirect.com/science/article/pii/S0014305708006332>.
- Elango, N. and Faudzi, A. A. M. 2015. A review article: investigations on soft materials for soft robot manipulations. *The International Journal of Advanced Manufacturing Technology*. **80**(5-8), pp. 1027–1037. DOI: 10.1007/s00170-015-7085-3.
- Elsayed, Y., Vincensi, A., Lekakou, C., Geng, T., Saaj, C. M., Ranzani, T., Cianchetti, M. and Menciassi, A. 2014. Finite Element Analysis and Design Optimization of a Pneumatically Actuating Silicone Module for Robotic Surgery Applications. *Soft Robotics*. **1**(4), pp. 185–198. DOI: 10.1089/soro.2014.0016.
- Feduccia, A. 1993. Evidence from Claw Geometry Indicating Arboreal Habits of Archaeopteryx. *Science*. **259**, pp. 790–793. URL: <https://api.semanticscholar.org/CorpusID:27475082>.
- Feng, M., Yang, D. and Gu, G. 2021. High-Force Fabric-Based Pneumatic Actuators With Asymmetric Chambers and Interference-Reinforced Structure for Soft Wearable Assistive Gloves. *IEEE Robotics and Automation Letters*. **6**(2), pp. 3105–3111. DOI: 10.1109/lra.2021.3062588.
- Festo Ltd. 2025. *Bionic Handling Assistant*. Accessed: 2025-05-04. URL: https://www.festo.com/gb/en/e/about-festo/research-and-development/bionic-learning-network/bionic-grippers-and-soft-robots/bionic-handling-assistant-id_33759/?siteName=Festo+GB.
- Fras, J. and Althoefer, K. 2019. ‘Soft Fiber-Reinforced Pneumatic Actuator Design and Fabrication: Towards Robust, Soft Robotic Systems’. *Towards Autonomous Robotic Systems*. URL: <https://api.semanticscholar.org/CorpusID:195755405>.
- Fujiwara, N., Sawano, S. and Konishi, S. 2009. Linear Expansion and Contraction of Paired Pneumatic Balloon Bending Actuators Toward Telescopic Motion. *2009 IEEE 22nd International Conference on Micro Electro Mechanical Systems*, pp. 435–438. URL: <https://api.semanticscholar.org/CorpusID:8921823>.
- Futran, C. C., Ceron, S., Mac Murray, B. C., Shepherd, R. F. and Petersen, K. H. 2018. ‘Leveraging fluid resistance in soft robots’. *2018 IEEE International Conference on Soft*

- Robotics (RoboSoft)*. IEEE. Livorno, Italy: IEEE, pp. 24–28. DOI: 10.1109/ROBOSOFT.2018.8405371.
- Galloway, K. C., Polygerinos, P., Walsh, C. J. and Wood, R. J. 2013. Mechanically programmable bend radius for fiber-reinforced soft actuators. *2013 16th International Conference on Advanced Robotics (ICAR)*, pp. 1–6. URL: <https://api.semanticscholar.org/CorpusID:2652379>.
- Gariya, N., Kumar, P. and Singh, T. 2023. Experimental study on a bending type soft pneumatic actuator for minimizing the ballooning using chamber-reinforcement. *Heliyon*. **9**(4), e14898. DOI: 10.1016/j.heliyon.2023.e14898. URL: <https://www.ncbi.nlm.nih.gov/pubmed/37025851>.
- Ge, L., Chen, F., Wang, D., Zhang, Y., Han, D., Wang, T. and Gu, G. 2020. Design, Modeling, and Evaluation of Fabric-Based Pneumatic Actuators for Soft Wearable Assistive Gloves. *Soft Robot*. **7**(5), pp. 583–596. DOI: 10.1089/soro.2019.0105. URL: <https://www.ncbi.nlm.nih.gov/pubmed/31995436>.
- Ge, L., Dong, L., Wang, D., Ge, Q. and Gu, G. 2018. A digital light processing 3D printer for fast and high-precision fabrication of soft pneumatic actuators. *Sensors and Actuators A-physical*. **273**, pp. 285–292. URL: <https://api.semanticscholar.org/CorpusID:116463117>.
- Georgopoulou, A., Vanderborght, B. and Clemens, F. 2021. Fabrication of a Soft Robotic Gripper With Integrated Strain Sensing Elements Using Multi-Material Additive Manufacturing. *Frontiers in Robotics and AI*. **8**. URL: <https://api.semanticscholar.org/CorpusID:244967520>.
- Gonzalez, D., Garcia, J., Voyles, R. M., Nawrocki, R. A. and Newell, B. 2022. Characterization of 3D Printed Pneumatic Soft Actuator. *Sensors and Actuators: A. Physical*. **334**, p. 113337. DOI: 10.1016/j.sna.2021.113337.
- Gonzalez, D. C., García, J. M. H. and Newell, B. A. 2019. Electromechanical characterization of a 3D printed dielectric material for dielectric electroactive polymer actuators. *Sensors and Actuators A: Physical*. URL: <https://api.semanticscholar.org/CorpusID:202102823>.
- Goodship, V., Middleton, B. and Cherrington, R. 2016. ‘2.2.4 Doctor Blading’. *Design and Manufacture of Plastic Components for Multifunctionality - Structural Composites*,

- Injection Molding, and 3D Printing*. Elsevier. URL: <https://app.knovel.com/hotlink/khtml/id:kt010SM0Z1/design-manufacture-plastic/doctor-blading>.
- Gorissen, B., Reynaerts, D., Konishi, S., Yoshida, K., Kim, J. W. and De Volder, M. 2017. Elastic Inflatable Actuators for Soft Robotic Applications. *Adv Mater.* **29**(43), p. 1604977. DOI: 10.1002/adma.201604977. URL: <https://www.ncbi.nlm.nih.gov/pubmed/28949425>.
- Gorissen, B., Chishiro, T., Shimomura, S., Reynaerts, D., De Volder, M. and Konishi, S. 2014. Flexible pneumatic twisting actuators and their application to tilting micromirrors. *Sensors and Actuators A: Physical.* **216**, pp. 426–431. DOI: 10.1016/j.sna.2014.01.015. URL: <https://www.sciencedirect.com/science/article/pii/S092442471400017X>.
- Gorissen, B., De Volder, M., De Greef, A. and Reynaerts, D. 2011. Theoretical and experimental analysis of pneumatic balloon microactuators. *Sensors and Actuators A: Physical.* **168**(1), pp. 58–65. DOI: 10.1016/j.sna.2011.03.057. URL: <https://dx.doi.org/10.1016/j.sna.2011.03.057>.
- Gorissen, B., Vincentie, W., Al-Bender, F., Reynaerts, D. and De Volder, M. 2013. Modeling and bonding-free fabrication of flexible fluidic microactuators with a bending motion. *Journal of Micromechanics and Microengineering.* **23**(4), p. 045012. DOI: 10.1088/0960-1317/23/4/045012. URL: <http://dx.doi.org/10.1088/0960-1317/23/4/045012>.
- Gu, G. Y., Zhu, J., Zhu, L. M. and Zhu, X. 2017. A survey on dielectric elastomer actuators for soft robots. *Bioinspir Biomim.* **12**(1), p. 011003. DOI: 10.1088/1748-3190/12/1/011003. URL: <https://www.ncbi.nlm.nih.gov/pubmed/28114111>.
- Gubbels, F. 2024. An overview of the chemistry of condensation curing silicone sealants and adhesives. *International Journal of Adhesion and Adhesives*. URL: <https://api.semanticscholar.org/CorpusID:269784293>.
- Guo, J., Li, Z. and Zhang, X. 2017. Effect of curing systems on vulcanization, mechanical properties, and stress softening of hydrogenated nitrile butadiene rubber vulcanizates. *Journal of Elastomers & Plastics.* **49**, pp. 243–257. URL: <https://api.semanticscholar.org/CorpusID:138258575>.
- Hao, Y., Zhang, S., Fang, B., Sun, F., Liu, H. and Li, H. 2022. A Review of Smart Materials for the Boost of Soft Actuators, Soft Sensors, and Robotics Applications. *Chinese*

- Journal of Mechanical Engineering*. **35**(1), p. 37. DOI: 10.1186/s10033-022-00707-2. URL: <https://doi.org/10.1186/s10033-022-00707-2>.
- AL-Hasni, S. and Santori, G. 2020. 3D printing of vacuum and pressure tight polymer vessels for thermally driven chillers and heat pumps. *Vacuum*. URL: <https://api.semanticscholar.org/CorpusID:208701927>.
- Herianto, Irawan, W., Ritonga, A. S. and Prastowo, A. 2019. Design and fabrication in the loop of soft pneumatic actuators using fused deposition modelling. *Sensors and Actuators A: Physical*. URL: <https://api.semanticscholar.org/CorpusID:202092846>.
- Herianto, Mastrisiswadi, H., Atsani, S. I., Sari, W. P. and Tontowi, A. E. 2024. Characterization of 3D printed multi-material soft pneumatic actuator. *International Journal of Intelligent Robotics and Applications*. URL: <https://api.semanticscholar.org/CorpusID:273497219>.
- Howard, I. A., Abzieher, T., Hossain, I. M., Eggers, H., Schackmar, F., Ternes, S., Richards, B. S., Lemmer, U. and Paetzold, U. W. 2019. Coated and Printed Perovskites for Photovoltaic Applications. *Adv Mater*. **31**(26), e1806702. DOI: 10.1002/adma.201806702. URL: <https://www.ncbi.nlm.nih.gov/pubmed/30932255>.
- Hu, W., Mutlu, R., Li, W. and Alici, G. 2018. A structural optimisation method for a soft pneumatic actuator. *robotics*. **7**(2), p. 24.
- International Organization for Standardization. *Adhesives — T-peel test for flexible-to-flexible bonded assemblies*. 2010. ISO 11339:2010. URL: <https://www.iso.org/standard/52890.html>.
- International Organization for Standardization. *Rubber- or plastics-coated fabrics – Determination of tensile strength and elongation at break*. 2016. ISO 1421:2016. URL: <https://www.iso.org/standard/65588.html>. Accessed: 2024-12-12.
- International Organization for Standardization. *Rubber, vulcanized or thermoplastic – Determination of compression stress-strain properties*. 2017. ISO 7743:2017. URL: <https://www.iso.org/standard/72784.html>. Accessed: 2024-12-12.
- International Organization for Standardization. *Rubber, vulcanized or thermoplastic – Determination of tensile stress-strain properties*. 2017. ISO 37:2017. URL: <https://www.iso.org/standard/68116.html>. Accessed: 2024-12-12.

- Jeong, O. C. and Konishi, S. 2006. All PDMS Pneumatic Microfinger With Bidirectional Motion and Its Application. *Journal of Microelectromechanical Systems*. **15**(4), pp. 896–903. DOI: 10.1109/jmems.2006.879377.
- Jeong, O. C., Kusuda, S. and Konishi, S. 2005. ‘All PDMS pneumatic balloon actuators for bidirectional motion of micro finger’. *18th IEEE International Conference on Micro Electro Mechanical Systems, 2005. MEMS 2005*, pp. 407–410. DOI: 10.1109/MEMSYS.2005.1453953.
- Jin, B., Song, H., Jiang, R., Song, J., Zhao, Q. and Xie, T. 2018. Programming a crystalline shape memory polymer network with thermo- and photo-reversible bonds toward a single-component soft robot. *Sci Adv.* **4**(1), eaao3865. DOI: 10.1126/sciadv.aao3865. URL: <https://www.ncbi.nlm.nih.gov/pubmed/29387791>.
- Johnston, I. D., McCluskey, D. K., Tan, C. K. L. and Tracey, M. C. 2014. Mechanical characterization of bulk Sylgard 184 for microfluidics and microengineering. *Journal of Micromechanics and Microengineering*. **24**. URL: <https://api.semanticscholar.org/CorpusID:3401788>.
- Kastor, N., Vikas, V., Cohen, E. and White, R. D. 2017. A Definition of Soft Materials for Use in the Design of Robots. *Soft robotics*. **4** **3**, pp. 181–182. URL: <https://api.semanticscholar.org/CorpusID:38927197>.
- Keong, B. A. W. and Hua, R. Y. C. 2018. A Novel Fold-Based Design Approach toward Printable Soft Robotics Using Flexible 3D Printing Materials. *Advanced Materials Technologies*. **3**. URL: <https://api.semanticscholar.org/CorpusID:139830208>.
- Khanafer, K., Duprey, A., Schlicht, M. and Berguer, R. 2009. Effects of strain rate, mixing ratio, and stress–strain definition on the mechanical behavior of the polydimethylsiloxane (PDMS) material as related to its biological applications. *Biomedical Microdevices*. **11**, pp. 503–508. URL: <https://api.semanticscholar.org/CorpusID:19073796>.
- Kim, T. K., Kim, J. K. and Jeong, O. C. 2011. Measurement of nonlinear mechanical properties of PDMS elastomer. *Microelectronic Engineering*. **88**(8), pp. 1982–1985. DOI: 10.1016/j.mee.2010.12.108.
- Ko, U., Kumar, V., Rosen, B. L. and Varghese, S. 2022. Characterization of bending balloon actuators. *Frontiers in Robotics and AI*. **9**. URL: <https://api.semanticscholar.org/CorpusID:252357218>.

- Konishi, S., Nokata, M., Ok Chan, J., Kusuda, S., Sakakibara, T., Kuwayama, M. and Tsutsumi, H. 2006. 'Pneumatic micro hand and miniaturized parallel link robot for micro manipulation robot system'. *Proceedings 2006 IEEE International Conference on Robotics and Automation, 2006. ICRA 2006*. Pp. 1036–1041. DOI: 10.1109/ROBOT.2006.1641846.
- Konishi, S. 2015. 'Small, soft and safe micro-machines for biomedical applications'. *2015 Transducers - 2015 18th International Conference on Solid-State Sensors, Actuators and Microsystems (TRANSDUCERS)*. IEEE, pp. 21–25. DOI: 10.1109/TRANSDUCERS.2015.7181060.
- Konishi, S., Kawai, F. and Cusin, P. 2001. Thin flexible end-effector using pneumatic balloon actuator. *Sensors and Actuators A: Physical*. **89**(1-2), pp. 28–35. DOI: 10.1016/S0924-4247(00)00533-1. URL: [https://dx.doi.org/10.1016/S0924-4247\(00\)00533-1](https://dx.doi.org/10.1016/S0924-4247(00)00533-1).
- Konishi, S., Nokata, M., Jeong, O. C., Sakakibara, T., Kusuda, S., Kuwayama, M. and Tsutsumi, H. 2005. 'Merging micro and macro robotics toward micro manipulation for biomedical operation'. *Proceedings of the IEEE International Conference on Robotics and Automation (ICRA)*. URL: <https://api.semanticscholar.org/CorpusID:55502412>.
- Kozuki, H., Yoshida, K., Yasuga, H. and Kurashina, Y. 2024. 'Hybrid Soft Actuator Driven by Temperature-Responsive Hydrogel and Soft Grid Skeleton with Residual Stress'. *2024 IEEE 37th International Conference on Micro Electro Mechanical Systems (MEMS)*, pp. 206–208. DOI: 10.1109/MEMS58180.2024.10439341.
- Krebs, F. C. 2009. Fabrication and processing of polymer solar cells: A review of printing and coating techniques. *Solar Energy Materials and Solar Cells*. **93**, pp. 394–412. URL: <https://api.semanticscholar.org/CorpusID:264208037>.
- Kulasekera, A. L., Arumathanthri, R. B., Chathuranga, D. S., Gopura, R. A. R. C. and Lalitharatne, T. D. 2021. A Low-Profile Vacuum Actuator (LPVAc) With Integrated Inductive Displacement Sensing for a Novel Sit-to-Stand Assist Exosuit. *IEEE Access*. **9**, pp. 117067–117079.
- Kusuda, S., Sawano, S. and Konishi, S. 2007. 'Fluid-Resistive Bending Sensor Having Perfect Compatibility with Flexible Pneumatic Balloon Actuator'. *Proceedings of the IEEE International Conference on Micro Electro Mechanical Systems (MEMS)*. IEEE, pp. 615–618.

- Lalegani Dezaki, M. and Bodaghi, M. 2023. A Review of Recent Manufacturing Technologies for Sustainable Soft Actuators. *International Journal of Precision Engineering and Manufacturing-Green Technology*. **10**(6), pp. 1661–1710. DOI: 10.1007/s40684-023-00533-4. URL: <https://doi.org/10.1007/s40684-023-00533-4>.
- Laschi, C., Mazzolai, B. and Cianchetti, M. 2016. Soft robotics: Technologies and systems pushing the boundaries of robot abilities. *Sci Robot*. **1**(1). DOI: 10.1126/scirobotics.aah3690. URL: <https://www.ncbi.nlm.nih.gov/pubmed/33157856>.
- Lee, C., Kim, M., Kim, Y. J., Hong, N., Ryu, S., Kim, H. J. and Kim, S. 2017. Soft robot review. *International Journal of Control, Automation and Systems*. **15**(1), pp. 3–15. DOI: 10.1007/s12555-016-0462-3.
- Lee, J. M. and Langdon, S. E. 1996. Thickness measurement of soft tissue biomaterials: A comparison of five methods. *Journal of Biomechanics*. **29**(6), pp. 829–832. DOI: 10.1016/0021-9290(95)00121-2.
- Lekakou, C., Elsayed, Y., Geng, T. and Saaj, C. M. 2015. Skins and Sleeves for Soft Robotics: Inspiration from Nature and Architecture. *Advanced Engineering Materials*. **17**(8), pp. 1180–1188. DOI: 10.1002/adem.201400406. URL: <https://doi.org/10.1002/adem.201400406>.
- Liang, X., Sun, Y. and Ren, H. 2017. A Flexible Fabrication Approach Toward the Shape Engineering of Microscale Soft Pneumatic Actuators. *IEEE Robotics and Automation Letters*. **2**(1), pp. 165–170. DOI: 10.1109/LRA.2016.2585298.
- Liao, Z., Yang, J., Hossain, M., Chagnon, G., Jing, L. and Yao, X. 2021. On the stress recovery behaviour of Ecoflex silicone rubbers. *International Journal of Mechanical Sciences*. **206**, p. 106624. URL: <https://api.semanticscholar.org/CorpusID:237685051>.
- Libby, J., Somwanshi, A. A., Stancati, F., Tyagi, G., Patel, A., Bhatt, N., Rizzo, J. and Atashzar, S. F. 2022. What Happens When Pneu-Net Soft Robotic Actuators Get Fatigued? *2023 International Symposium on Medical Robotics (ISMR)*, pp. 1–6. URL: <https://api.semanticscholar.org/CorpusID:254366510>.
- Limited, W. R. 2022. *Measuring Rubber Hardness*. URL: <https://www.walker-rubber.co.uk/measuring-rubber-hardness>.

- Liu, Q., Zuo, J., Zhu, C. and Xie, S. Q. 2020. Design and control of soft rehabilitation robots actuated by pneumatic muscles: State of the art. *Future Generation Computer Systems*. **113**, pp. 620–634. DOI: 10.1016/j.future.2020.06.046.
- Luo, Y., Zou, J. and Gu, G. 2021. Multimaterial Pneumatic Soft Actuators and Robots through a Planar Laser Cutting and Stacking Approach. *Advanced Intelligent Systems*, p. 2000257.
- Majidi, C. 2013. Soft Robotics: A Perspective—Current Trends and Prospects for the Future. *Soft Robotics*. **1**(1), pp. 5–11. DOI: 10.1089/soro.2013.0001.
- Manns, M., Morales, J. and Frohn, P. 2018. Additive manufacturing of silicon based PneuNets as soft robotic actuators. *Procedia CIRP*. **72**, pp. 328–333. URL: <https://api.semanticscholar.org/CorpusID:67120775>.
- Marchese, A. D., Katzschmann, R. K. and Rus, D. 2015a. A Recipe for Soft Fluidic Elastomer Robots. *Soft Robotics*. **2**(1), pp. 7–25. DOI: 10.1089/soro.2014.0022.
- Marchese, A. D., Katzschmann, R. K. and Rus, D. 2015b. A Recipe for Soft Fluidic Elastomer Robots. *Soft Robotics*. **2**, pp. 7–25. URL: <https://api.semanticscholar.org/CorpusID:6622844>.
- Marechal, L., Balland, P., Lindenroth, L., Petrou, F., Kontovounisios, C. and Bello, F. 2021. Toward a Common Framework and Database of Materials for Soft Robotics. *Soft Robot*. **8**(3), pp. 284–297. DOI: 10.1089/soro.2019.0115. URL: <https://www.ncbi.nlm.nih.gov/pubmed/32589507>.
- Martinez, R. V., Fish, C. R., Chen, X. and Whitesides, G. M. 2012. Elastomeric Origami: Programmable Paper-Elastomer Composites as Pneumatic Actuators. *Advanced Functional Materials*. **22**(7), pp. 1376–1384. DOI: 10.1002/adfm.201102978.
- McCracken, J. M., Donovan, B. R. and White, T. J. 2020. Materials as Machines. *Advanced Materials*. **32**. URL: <https://api.semanticscholar.org/CorpusID:212418001>.
- Miller, K. 2025. Testing Elastomers for Hyperelastic Material Models in Finite Element Analysis. *Axel Products, Inc.* URL: <https://www.axelproducts.com>.
- Miriyev, A., Stack, K. and Lipson, H. 2017. Soft material for soft actuators. *Nat Commun*. **8**(1), p. 596. DOI: 10.1038/s41467-017-00685-3. URL: <https://www.ncbi.nlm.nih.gov/pubmed/28928384>.

- Mosadegh, B., Polygerinos, P., Keplinger, C., Wennstedt, S., Shepherd, R. F., Gupta, U., Shim, J., Bertoldi, K., Walsh, C. J. and Whitesides, G. M. 2014. Pneumatic Networks for Soft Robotics that Actuate Rapidly. *Advanced Functional Materials*. **24**(15), pp. 2163–2170. DOI: 10.1002/adfm.201303288. URL: <https://onlinelibrary.wiley.com/doi/abs/10.1002/adfm.201303288>.
- Moseley, P., Florez, J. M., Sonar, H. A., Agarwal, G., Curtin, W. A. and Paik, J. K. 2016. Modeling, Design, and Development of Soft Pneumatic Actuators with Finite Element Method. *Advanced Engineering Materials*. **18**. URL: <https://api.semanticscholar.org/CorpusID:110448324>.
- Mullins, L. 1969. Softening of Rubber by Deformation. *Rubber Chemistry and Technology*. **42**, pp. 339–362. URL: <https://api.semanticscholar.org/CorpusID:138712485>.
- Ou, J., Skouras, M., Vlavianos, N., Heibeck, F., Cheng, C.-Y., Peters, J. and Ishii, H. 2016. aeroMorph - Heat-sealing Inflatable Shape-change Materials for Interaction Design. *Proceedings of the 29th Annual Symposium on User Interface Software and Technology*. URL: <https://api.semanticscholar.org/CorpusID:14073534>.
- Park, Y. L., Santos, J., Galloway, K. G., Goldfield, E. C. and Wood, R. J. 2014a. ‘A Soft Wearable Robotic Device for Active Knee Motions Using Flat Pneumatic Artificial Muscles’. *Proceedings of the 2014 IEEE International Conference on Robotics and Automation (ICRA)*, pp. 4805–4810. DOI: 10.1109/ICRA.2014.6907562.
- Park, Y.-L., Santos, J., Galloway, K. C., Goldfield, E. C. and Wood, R. J. 2014b. A soft wearable robotic device for active knee motions using flat pneumatic artificial muscles. *2014 IEEE International Conference on Robotics and Automation (ICRA)*, pp. 4805–4810. URL: <https://api.semanticscholar.org/CorpusID:10291511>.
- Partridge, A. J., Chen, H.-Y., Le, N. H., Xu, C., Eichorn, H. and Pulvirenti, E. 2022. ‘ReRobot: Recycled Materials for Trustworthy Soft Robots’. *2022 IEEE 5th International Conference on Soft Robotics (RoboSoft)*. IEEE. Edinburgh, United Kingdom, pp. 1–6. DOI: 10.1109/RoboSoft54090.2022.9762170.
- Patel, D. K., Sakhaei, A. H., Layani, M., Zhang, B., Ge, Q. and Magdassi, S. 2017. Highly Stretchable and UV Curable Elastomers for Digital Light Processing Based 3D Printing. *Advanced Materials*. **29**. URL: <https://api.semanticscholar.org/CorpusID:33987153>.

- Peele, B. N., Wallin, T. J., Zhao, H. and Shepherd, R. F. 2015. 3D printing antagonistic systems of artificial muscle using projection stereolithography. *Bioinspiration & Biomimetics*. **10**(5), p. 055003. DOI: 10.1088/1748-3190/10/5/055003.
- Petersen, K. H. and Shepherd, R. F. 2019. '4 - Fluid-driven intrinsically soft robots'. *Robotic Systems and Autonomous Platforms*. Ed. by S. M. Walsh and M. S. Strano. Woodhead Publishing in Materials. Woodhead Publishing, pp. 61–84. DOI: <https://doi.org/10.1016/B978-0-08-102260-3.00004-4>. URL: <https://www.sciencedirect.com/science/article/pii/B9780081022603000044>.
- Pikul, J. H., Li, S., Bai, H., Hanlon, R. T., Cohen, I. and Shepherd, R. F. 2017. Stretchable surfaces with programmable 3D texture morphing for synthetic camouflaging skins. *Science*. **358**(6360), pp. 210–214. DOI: 10.1126/science.aan5627.
- Pittiglio, G., Lloyd, P., da Veiga, T., Onaizah, O., Pompili, C., Chandler, J. H. and Valdastri, P. 2022. Patient-Specific Magnetic Catheters for Atraumatic Autonomous Endoscopy. *Soft Robot*. **9**(6), pp. 1120–1133. DOI: 10.1089/soro.2021.0090. URL: <https://www.ncbi.nlm.nih.gov/pubmed/35312350>.
- Polygerinos, P., Lyne, S., Wang, Z., Nicolini, L. F., Mosadegh, B., Whitesides, G. M. and Walsh, C. J. 2013. 'Towards a soft pneumatic glove for hand rehabilitation'. *2013 IEEE/RSJ International Conference on Intelligent Robots and Systems*, pp. 1512–1517. DOI: 10.1109/IRoS.2013.6696549.
- Polygerinos, P., Wang, Z., Overvelde, J. T. B., Galloway, K. C., Wood, R. J., Bertoldi, K. and Walsh, C. J. 2015. Modeling of Soft Fiber-Reinforced Bending Actuators. *IEEE Transactions on Robotics*. **31**(3), pp. 778–789. DOI: 10.1109/tro.2015.2428504.
- Pu, Y., Zheng, S., Hu, X., Tang, S. and An, N. 2024. Robotic skins inspired by auxetic metamaterials for programmable bending of soft actuators. *Materials & Design*. URL: <https://api.semanticscholar.org/CorpusID:272942776>.
- Rad, C.-R., Hancu, O. and Lapusan, C. 2022. Aspects Regarding the Modelling and Design of 3D-printed Bending Soft Pneumatic Actuators. *IOP Conference Series: Materials Science and Engineering*. **1268**. URL: <https://api.semanticscholar.org/CorpusID:253878542>.
- Ranzani, T., Russo, S., Bartlett, N. W., Wehner, M. and Wood, R. J. 2018. Increasing the Dimensionality of Soft Microstructures through Injection-Induced Self-Folding. *Adv*

- Mater.* **30**(38), e1802739. DOI: 10.1002/adma.201802739. URL: <https://www.ncbi.nlm.nih.gov/pubmed/30079470>.
- Rehman, T., Faudzi, A. A. M., Dewi, D. E. O. and Ali, M. S. M. 2017. Design, characterization, and manufacturing of circular bellows pneumatic soft actuator. *The International Journal of Advanced Manufacturing Technology*. **93**, pp. 4295–4304. URL: <https://api.semanticscholar.org/CorpusID:115416897>.
- Rehman, T., Faudzi, A. A. M., Dewi, D. E. O., Suzumori, K., Razif, M. R. M. and Nordin, I. N. A. M. 2016. ‘DESIGN AND ANALYSIS OF BENDING MOTION IN SINGLE AND DUAL CHAMBER BELLOWS STRUCTURED SOFT ACTUATORS’. URL: <https://api.semanticscholar.org/CorpusID:56168185>.
- Roche, E. T., Horvath, M. A., Wamala, I., Alazmani, A., Song, S.-E., Whyte, W., Machaidze, Z., Payne, C. J., Weaver, J. C., Fishbein, G., Kuebler, J. D., Vasilyev, N. V., Mooney, D. J., Pigula, F. A. and Walsh, C. J. 2017. Soft robotic sleeve supports heart function. *Science Translational Medicine*. **9**. URL: <https://api.semanticscholar.org/CorpusID:22531089>.
- Rukhlenko, I. D., Farajikhah, S., Lilley, C., Georgis, A., Large, M. and Fleming, S. 2020. Performance Optimization of Polymer Fibre Actuators for Soft Robotics. *Polymers (Basel)*. **12**(2), p. 454. DOI: 10.3390/polym12020454. URL: <https://www.ncbi.nlm.nih.gov/pubmed/32075203>.
- Rus, D. and Tolley, M. T. 2015. Design, fabrication and control of soft robots. *Nature*. **521**(7553), pp. 467–75. DOI: 10.1038/nature14543. URL: <https://www.ncbi.nlm.nih.gov/pubmed/26017446>.
- Russo, S., Ranzani, T., Walsh, C. J. and Wood, R. J. 2017. An Additive Millimeter-Scale Fabrication Method for Soft Biocompatible Actuators and Sensors. *Advanced Materials Technologies*. **2**(10), p. 1700135. DOI: 10.1002/admt.201700135. URL: <https://doi.org/10.1002/admt.201700135>.
- Sanan, S., Lynn, P. S. and Griffith, S. T. 2014. Pneumatic Torsional Actuators for Inflatable Robots. *Journal of Mechanisms and Robotics*. **6**, p. 031003. URL: <https://api.semanticscholar.org/CorpusID:122367081>.
- Schmalz UK Inc. 2025. *mGrip - Hygienic gripping, safe holding*. Accessed: 2025-05-04. URL: <https://www.schmalz.com/en-gb/solutions/media-center/mgrip---hygienic-gripping--safe-holding/>.

- Schmitt, F., Piccin, O., Barbe, L. and Bayle, B. 2018. Soft Robots Manufacturing: A Review. *Front Robot AI*. **5**(84), p. 84. DOI: 10.3389/frobt.2018.00084. URL: <https://www.ncbi.nlm.nih.gov/pubmed/33500963>.
- Schneider, C. A., Rasband, W. S. and Eliceiri, K. W. 2012. *NIH Image to ImageJ: 25 years of image analysis*. URL: <https://imagej.nih.gov/ij/>.
- Shapiro, Y., Wolf, A. and Gábor, K. 2011. Bi-bellows: Pneumatic bending actuator. *Sensors and Actuators A-physical*. **167**, pp. 484–494. URL: <https://api.semanticscholar.org/CorpusID:51739217>.
- Shepherd, R. F., Ilievski, F., Choi, W., Morin, S. A., Stokes, A. A., Mazzeo, A. D., Chen, X., Wang, M. and Whitesides, G. M. 2011. Multigait soft robot. *Proc Natl Acad Sci U S A*. **108**(51), pp. 20400–3. DOI: 10.1073/pnas.1116564108. URL: <https://www.ncbi.nlm.nih.gov/pubmed/22123978>.
- Shintake, J., Schubert, B., Rosset, S., Shea, H. and Floreano, D. 2015. ‘Variable stiffness actuator for soft robotics using dielectric elastomer and low-melting-point alloy’. *2015 IEEE/RSJ International Conference on Intelligent Robots and Systems (IROS)*, pp. 1097–1102. DOI: 10.1109/IROS.2015.7353507.
- Shintake, J., Sonar, H. A., Piskarev, E., Paik, J. K. and Floreano, D. 2017. Soft pneumatic gelatin actuator for edible robotics. *2017 IEEE/RSJ International Conference on Intelligent Robots and Systems (IROS)*, pp. 6221–6226. URL: <https://api.semanticscholar.org/CorpusID:15607499>.
- Shit, S. C. and Shah, P. 2013. A Review on Silicone Rubber. *National Academy Science Letters*. **36**, pp. 355–365. URL: <https://api.semanticscholar.org/CorpusID:256331885>.
- Sinatra, N. R., Ranzani, T., Vlassak, J. J., Parker, K. K. and Wood, R. J. 2018. Nanofiber-reinforced soft fluidic micro-actuators. *Journal of Micromechanics and Microengineering*. **28**. URL: <https://api.semanticscholar.org/CorpusID:50885949>.
- Sinatra, N. R., Teeple, C. B., Vogt, D. M., Parker, K. K., Gruber, D. F. and Wood, R. J. 2019. Ultragentle manipulation of delicate structures using a soft robotic gripper. *Science Robotics*. **4**. URL: <https://api.semanticscholar.org/CorpusID:201672301>.
- Smooth-On Inc. 2024a. *Dragon Skin™ 30 Product Information*. Accessed: 2024. Smooth-On Inc. URL: <https://www.smooth-on.com/products/dragon-skin-30/>.

- Smooth-On Inc. 2024b. *Ecoflex™ 00-10 Product Information*. Accessed: 2024. Smooth-On Inc. URL: <https://www.smooth-on.com/products/ecoflex-00-10/>.
- Smooth-On Inc. 2024c. *Ecoflex™ 00-30 Product Information*. Accessed: 2024. Smooth-On Inc. URL: <https://www.smooth-on.com/products/ecoflex-00-30/>.
- Smooth-On Inc. 2024d. *Ecoflex™ 00-50 Product Information*. Accessed: 2024. Smooth-On Inc. URL: <https://www.smooth-on.com/products/ecoflex-00-50/>.
- Smooth-On Inc. 2024e. *Mold Star™ 30 Product Information*. Accessed: 2024. Smooth-On Inc. URL: <https://www.smooth-on.com/products/mold-star-30/>.
- Stella, F. and Hughes, J. 2023. The science of soft robot design: A review of motivations, methods and enabling technologies. *Frontiers in Robotics and AI*. **9**. URL: <https://api.semanticscholar.org/CorpusID:255943837>.
- Sun, Y. C., Effati, M., Naguib, H. E. and Nejat, G. 2022. SoftSAR: The New Softer Side of Socially Assistive Robots-Soft Robotics with Social Human-Robot Interaction Skills. *Sensors (Basel)*. **23**(1). DOI: 10.3390/s23010432. URL: <https://www.ncbi.nlm.nih.gov/pubmed/36617030>.
- Suzumori, K., Iikura, S. and Tanaka, H. 1991a. 'Flexible microactuator for miniature robots'. *Proceedings. IEEE Micro Electro Mechanical Systems*, pp. 204–209. DOI: 10.1109/MEMSYS.1991.114797.
- Suzumori, K., Iikura, S. and Tanaka, H. 1992. Applying a flexible microactuator to robotic mechanisms. *IEEE Control Systems*. **12**(1), pp. 21–27. DOI: 10.1109/37.120448.
- Suzumori, K., Maeda, T., Wantabe, H. and Hisada, T. 1997. Fiberless flexible microactuator designed by finite-element method. *IEEE/ASME Transactions on Mechatronics*. **2**(4), pp. 281–286. DOI: 10.1109/3516.653052.
- Suzumori, K., Endo, S., Kanda, T., Kato, N. and Suzuki, H. 2007. A Bending Pneumatic Rubber Actuator Realizing Soft-bodied Manta Swimming Robot. *Proceedings 2007 IEEE International Conference on Robotics and Automation*, pp. 4975–4980. URL: <https://api.semanticscholar.org/CorpusID:16713769>.
- Suzumori, K., Iikura, S. and Tanaka, H. 1991b. Flexible microactuator for miniature robots. [1991] *Proceedings. IEEE Micro Electro Mechanical Systems*, pp. 204–209. URL: <https://api.semanticscholar.org/CorpusID:114776079>.

- Suzumori, K., Iikura, S. and Tanaka, H. 1991c. Development of flexible microactuator and its applications to robotic mechanisms. *Proceedings. 1991 IEEE International Conference on Robotics and Automation*, 1622–1627 vol.2. URL: <https://api.semanticscholar.org/CorpusID:18329100>.
- Tang, X., Li, H., Ma, T., Yang, Y., Luo, J., Wang, H. and Jiang, P. 2022. A Review of Soft Actuator Motion: Actuation, Design, Manufacturing and Applications. *Actuators*. URL: <https://api.semanticscholar.org/CorpusID:253564336>.
- Taubin, G. 1991. Estimation of Planar Curves, Surfaces, and Nonplanar Space Curves Defined by Implicit Equations with Applications to Edge and Range Image Segmentation. *IEEE Trans. Pattern Anal. Mach. Intell.* **13**, pp. 1115–1138. URL: <https://api.semanticscholar.org/CorpusID:16553641>.
- Tawk, C. and Alici, G. 2020a. Finite Element Modeling in the Design Process of 3D Printed Pneumatic Soft Actuators and Sensors. *Robotics*. **9**, p. 52. URL: <https://api.semanticscholar.org/CorpusID:224818427>.
- Tawk, C. and Alici, G. 2020b. Finite element modeling in the design process of 3D printed pneumatic soft actuators and sensors. *Robotics*. **9**(3), p. 52.
- The MathWorks, Inc. 2021. *MATLAB R2021a*. The MathWorks, Inc. Natick, Massachusetts. URL: https://www.mathworks.com/products/new_products/release2021a.html.
- Thomson, T. J. and Motani, R. 2021. Functional morphology of vertebrate claws investigated using functionally based categories and multiple morphological metrics. *Journal of Morphology*. **282**, pp. 449–471. URL: <https://api.semanticscholar.org/CorpusID:230486405>.
- Tiboni, M. and Loda, D. 2023. Monolithic PneuNets Soft Actuators for Robotic Rehabilitation: Methodologies for Design, Production and Characterization. *Actuators*. URL: <https://api.semanticscholar.org/CorpusID:260181123>.
- Tinsley, L. J. and Harris, R. A. 2020. A Novel Computer-Controlled Maskless Fabrication Process for Pneumatic Soft Actuators. *Actuators*. URL: <https://api.semanticscholar.org/CorpusID:230570464>.
- Tolley, M. T., Shepherd, R. F., Mosadegh, B., Galloway, K. C., Wehner, M., Karpelson, M., Wood, R. J. and Whitesides, G. M. 2014. A Resilient, Untethered Soft Robot.

- Soft Robotics*. **1**(3), pp. 213–223. DOI: 10.1089/soro.2014.0008. URL: <https://www.liebertpub.com/doi/abs/10.1089/soro.2014.0008>.
- Tsouti, V., Mitrakos, V., Broutas, P. and Chatzandroulis, S. 2016. Modeling and Development of a Flexible Carbon Black-Based Capacitive Strain Sensor. *IEEE Sensors Journal*. **16**(9), pp. 3059–3067. DOI: 10.1109/JSEN.2016.2524508.
- Unger, M. A., Chou, H.-p., Thorsen, T., Scherer, A. and Quake, S. R. 2000. Monolithic microfabricated valves and pumps by multilayer soft lithography. *Science*. **288** 5463, pp. 113–6. URL: <https://api.semanticscholar.org/CorpusID:14028193>.
- Van Vlerken, C., Ballén-Moreno, F., Roels, E., Ferrentino, P., Langlois, K., Vanderborght, B. and Verstraten, T. 2023. Development of an Active Physical Interface for Physical Human-Robot Interaction: Investigation of Soft Pneumatic Actuator Straps for Automatic Enclosure System. *Actuators*. URL: <https://api.semanticscholar.org/CorpusID:259133540>.
- Veale, A. J., Xie, S. Q. and Anderson, I. A. 2016. Modeling the Peano fluidic muscle and the effects of its material properties on its static and dynamic behavior. *Smart Materials and Structures*. **25**. URL: <https://api.semanticscholar.org/CorpusID:137911148>.
- Villani, V. and Lavallata, V. 2024. The Theories of Rubber Elasticity and the Goodness of Their Constitutive Stress–Strain Equations. *Physchem*. URL: <https://api.semanticscholar.org/CorpusID:272033315>.
- Wacker Chemie AG. 2024. *ELASTOSIL® M 4601 A/B: Room Temperature Curing Silicone Rubber (RTV-2)*.
- Wakimoto, S., Ogura, K., Suzumori, K. and Nishioka, Y. 2009. Miniature soft hand with curling rubber pneumatic actuators. *2009 IEEE International Conference on Robotics and Automation*, pp. 556–561. URL: <https://api.semanticscholar.org/CorpusID:10986011>.
- Wang, J., Fei, Y. and Pang, W. 2019. Design, Modeling, and Testing of a Soft Pneumatic Glove With Segmented PneuNets Bending Actuators. *IEEE/ASME Transactions on Mechatronics*. **24**(3), pp. 990–1001. DOI: 10.1109/TMECH.2019.2911992.
- Wang, Z., Zhang, B., Cui, W. and Zhou, N. 2022a. Freeform Fabrication of Pneumatic Soft Robots via Multi-Material Jointed Direct Ink Writing. *Macromolecular Materials and Engineering*. URL: <https://api.semanticscholar.org/CorpusID:246562105>.

- Wang, Z., Zhang, B., Cui, W. and Zhou, N. 2022b. Freeform Fabrication of Pneumatic Soft Robots via Multi-Material Jointed Direct Ink Writing. *Macromolecular Materials and Engineering*. **307**(4), p. 2100813. DOI: 10.1002/mame.202100813.
- Watanabe, Y., Maeda, M., Yaji, N., Nakamura, R., Iseki, H., Yamato, M., Okano, T., Hori, S. and Konishi, S. 2007. ‘Small, soft, and safe microactuator for retinal pigment epithelium transplantation’. *2007 IEEE 20th International Conference on Micro Electro Mechanical Systems (MEMS)*, pp. 659–662. DOI: 10.1109/MEMSYS.2007.4433083.
- Wehner, M., Tolley, M. T., Mengüç, Y., Park, Y.-L., Mozeika, A., Ding, Y., Onal, C., Shepherd, R. F., Whitesides, G. M. and Wood, R. J. 2014. Pneumatic Energy Sources for Autonomous and Wearable Soft Robotics. *Soft Robotics*. **1**(4), pp. 263–274. DOI: 10.1089/soro.2014.0018. URL: <https://doi.org/10.1089/soro.2014.0018>.
- Wehner, M. F., Truby, R. L., Fitzgerald, D. J., Mosadegh, B., Whitesides, G. M., Lewis, J. A. and Wood, R. J. 2016. An integrated design and fabrication strategy for entirely soft, autonomous robots. *Nature*. **536**, pp. 451–455. URL: <https://api.semanticscholar.org/CorpusID:205250180>.
- Wei, S. and Ghosh, T. K. 2022. Bioinspired Structures for Soft Actuators. *Advanced Materials Technologies*. **7**(10), p. 2101521. DOI: 10.1002/admt.202101521. URL: <https://doi.org/10.1002/admt.202101521>.
- Whitesides, G. M. 2018. Soft Robotics. *Angewandte Chemie International Edition*. **57**(16), pp. 4258–4273. DOI: 10.1002/anie.201800907.
- Wienzek, T. and Seibel, A. 2019. Elastomeric Prepregs for Soft Robotics Applications. *Advanced Engineering Materials*. **21**. URL: <https://api.semanticscholar.org/CorpusID:139960681>.
- Wirekoh, J. and Park, Y.-L. 2017. Design of flat pneumatic artificial muscles. *Smart Materials and Structures*. **26**(3), p. 035009. DOI: 10.1088/1361-665X/aa5496. URL: <http://dx.doi.org/10.1088/1361-665X/aa5496>.
- Xavier, M. S., Fleming, A. J. and Yong, Y. K. 2020. Finite Element Modeling of Soft Fluidic Actuators: Overview and Recent Developments. *Advanced Intelligent Systems*. **3**(2), p. 2000187. DOI: 10.1002/aisy.202000187. URL: <https://onlinelibrary.wiley.com/doi/abs/10.1002/aisy.202000187>.

- Xavier, M. S., Tawk, C. D., Yong, Y. and Fleming, A. J. 2021. 3D-Printed Omnidirectional Soft Pneumatic Actuators: Design, Modeling and Characterization. *Sensors and Actuators A: Physical*. URL: <https://api.semanticscholar.org/CorpusID:243465050>.
- Xavier, M. S., Tawk, C. D., Zolfagharian, A., Pinskiar, J., Howard, D., Young, T., Lai, J., Harrison, S. M., Yong, Y. K., Bodaghi, M. and Fleming, A. J. 2022. Soft Pneumatic Actuators: A Review of Design, Fabrication, Modeling, Sensing, Control and Applications. *IEEE Access*. **10**, pp. 59442–59485. DOI: 10.1109/ACCESS.2022.3179589.
- Xin, Y., Zhou, X., Bark, H. and Lee, P. S. 2023. The Role of 3D Printing Technologies in Soft Grippers. *Advanced materials*, e2307963. URL: <https://api.semanticscholar.org/CorpusID:265275519>.
- Yang, G. Z., Bellingham, J., Dupont, P. E., Fischer, P., Floridi, L., Full, R., Jacobstein, N., Kumar, V., McNutt, M., Merrifield, R., Nelson, B. J., Scassellati, B., Taddeo, M., Taylor, R., Veloso, M., Wang, Z. L. and Wood, R. 2018. The grand challenges of Science Robotics. *Sci Robot*. **3**(14), eaar7650. DOI: 10.1126/scirobotics.aar7650. URL: <https://www.ncbi.nlm.nih.gov/pubmed/33141701>.
- Yap, Y. L., Sing, S. L. and Yeong, W. Y. 2020. A review of 3D printing processes and materials for soft robotics. *Rapid Prototyping Journal*. URL: <https://api.semanticscholar.org/CorpusID:225667357>.
- Yeoh, O. H. 1993a. Some Forms of the Strain Energy Function for Rubber. *Rubber Chemistry and Technology*. **66**(5). Accessed: 2024-12-12, pp. 754–771. DOI: 10.5254/1.3538343.
- Yeoh, O. H. 1993b. Some Forms of the Strain Energy Function for Rubber. *Rubber Chemistry and Technology*. **66**, pp. 754–771. URL: <https://api.semanticscholar.org/CorpusID:139019730>.
- Yin, J., Lu, C. T., Fu, J., Huang, Y. and Zheng, Y. 2018. Interfacial bonding during multi-material fused deposition modeling (FDM) process due to inter-molecular diffusion. *Materials & Design*. URL: <https://api.semanticscholar.org/CorpusID:139150430>.
- Yin, S., Yao, D. R., Song, Y., Heng, W., Ma, X., Han, H. and Gao, W. 2024. Wearable and Implantable Soft Robots. *Chemical reviews*. URL: <https://api.semanticscholar.org/CorpusID:273288663>.

- You, Y., Dai, C., Goldschmidt, E. and Fearing, R. S. 2024. Multi-Layer LDPE Pouch Robots Enabled by Inkjet-Printed Masking Layers. *Advanced Materials Technologies*. URL: <https://api.semanticscholar.org/CorpusID:273321415>.
- Zhang, Q., Weng, S., Zhao, Z., Qi, H. J. and Fang, D. 2021. Soft pneumatic actuators by digital light processing combined with injection-assisted post-curing. *Applied Mathematics and Mechanics*. **42**, pp. 159–172. URL: <https://api.semanticscholar.org/CorpusID:234213758>.
- Zhang, Y., Li, P., Quan, J., Li, L., Zhang, G. Y. and Zhou, D. 2022. Progress, Challenges, and Prospects of Soft Robotics for Space Applications. *Advanced Intelligent Systems*. **5**. URL: <https://api.semanticscholar.org/CorpusID:250199268>.
- Zhang, Y.-F., Ng, C. J.-X., Chen, Z., Zhang, W., Panjwani, S., Kowsari, K., Yang, H. Y. and Ge, Q. 2019. Miniature Pneumatic Actuators for Soft Robots by High-Resolution Multimaterial 3D Printing. *Advanced Materials Technologies*. **4**. URL: <https://api.semanticscholar.org/CorpusID:201906983>.
- Zhang, Z., Long, Y., Chen, G., Wu, Q., Wang, H. and Jiang, H. 2023. Soft and lightweight fabric enables powerful and high-range pneumatic actuation. *Science Advances*. **9**. URL: <https://api.semanticscholar.org/CorpusID:258108745>.
- Zhao, X., Wang, Y. and Liu, J. 2017. A New Model for Predicting the Thickness of Dry Film in Blade Coating of Non-Evaporative Newtonian Fluids. *Journal of Coating Technology and Research*. **14**, pp. 123–134. DOI: 10.1007/s11998-017-9954-3. URL: <https://pdfs.semanticscholar.org/9c34/b0cce5afad3fc0c9cfbde5b81ab1ec04f2c9.pdf>.
- Zhu, M., Biswas, S., Dinulescu, S. I., Kastor, N., Hawkes, E. W. and Visell, Y. 2022a. Soft, Wearable Robotics and Haptics: Technologies, Trends, and Emerging Applications. *Proceedings of the IEEE*. **110**(2), pp. 246–272. DOI: 10.1109/jproc.2021.3140049. URL: <https://doi.org/10.1109/jproc.2021.3140049>.
- Zhu, Y., Feng, K., Hua, C., Wang, X., Hu, Z., Wang, H. and Su, H. 2022b. Model Analysis and Experimental Investigation of Soft Pneumatic Manipulator for Fruit Grasping. *Sensors (Basel, Switzerland)*. **22**. URL: <https://api.semanticscholar.org/CorpusID:249810545>.
- Zolfagharian, A., Mahmud, M. A. P., Gharaie, S., Bodaghi, M., Kouzani, A. Z. and Kaynak, A. B. 2020. 3D/4D-printed bending-type soft pneumatic actuators: fabrication,

modelling, and control. *Virtual and Physical Prototyping*. **15**, pp. 373–402. URL: <https://api.semanticscholar.org/CorpusID:222136939>.

Appendix A

Appendix 1

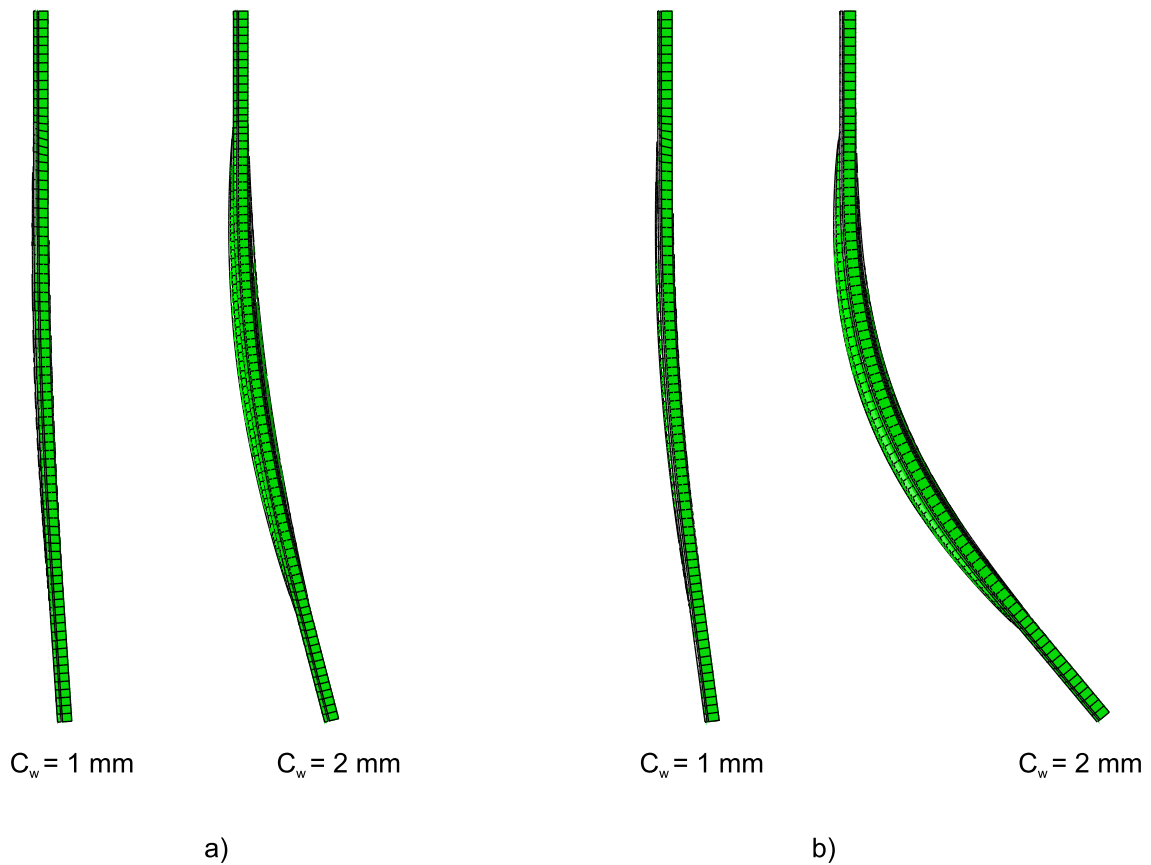


Figure A.1: Deformation patterns of PneuThin with oval cavity at smaller cavity widths. Panel (a) shows configurations with thickness ratio $L_r=0.38$, and panel (b) shows configurations with $L_r=0.20$. Both panels display cavity widths of $C_w=1$ mm and $C_w=2$ mm, demonstrating minimal bending deformation under 6 psi pressure.

Appendix B

Appendix 1

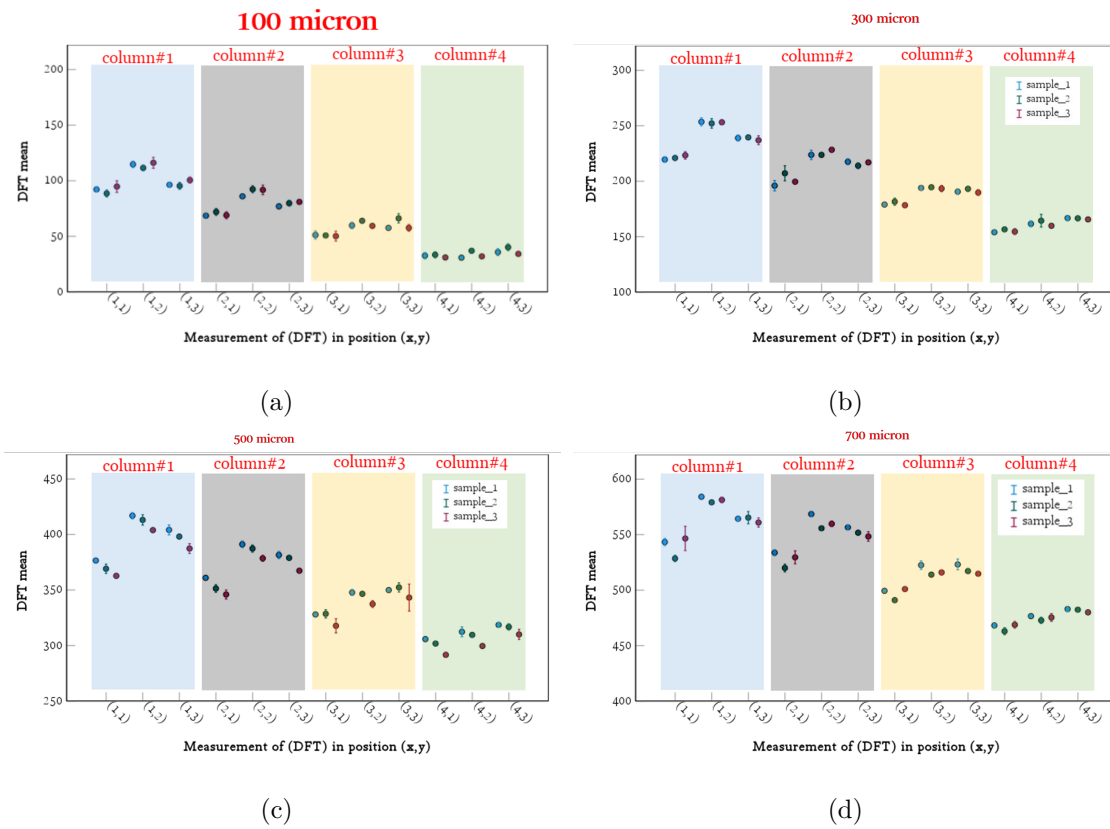


Figure B.1: Thickness mapping profiles for key GH, a) 100 μm , b) 300 μm , c) 500 μm and d) 700 μm

Appendix C

Appendix 1

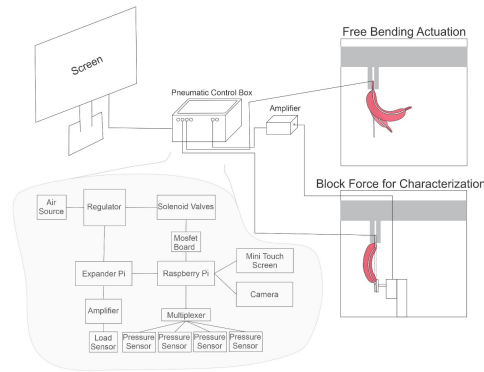


Figure C.1: shows a schematic of the custom-designed pneumatic control box. It features a high-precision pressure regulator (SMC: ITV 1030-21F2BL-) that ensures consistent air pressure delivery from 0 to 100 kPa (0 to 14.5 psi) to actuate the soft bending actuator. Integrated within the setup is a sensitive pressure transducer (Honeywell Digital Pressure Sensor: SSC-D-AN-N-015PG-2-A-3) capable of measuring pressures from 0 to 103 kPa (0 to 15 psi). For controlled actuation, the system incorporates solenoid valves (SMC: V114A-5MUBM5) that allow precise modulation of airflow to the soft pneumatic actuators. An external pressure reservoir ensures a stable and continuous air supply, while pneumatic fittings and flexible tubes connect the components, ensuring leak-proof operations and efficient energy transmission. The core of the control system runs on a Raspberry Pi 4B board, providing essential computational capabilities for control and data processing.

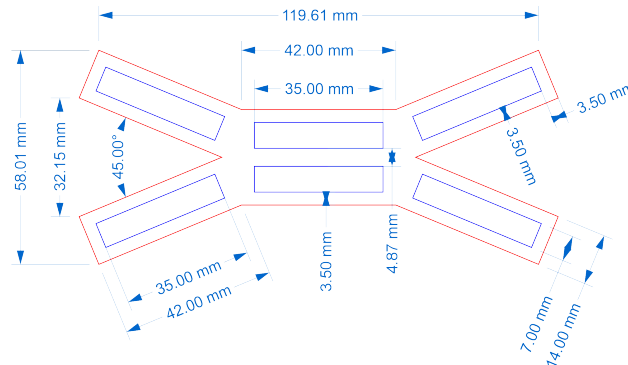


Figure C.2: Technical drawing of the quadrupedal soft robot showing key dimensions. The design integrates six bending actuators arranged symmetrically

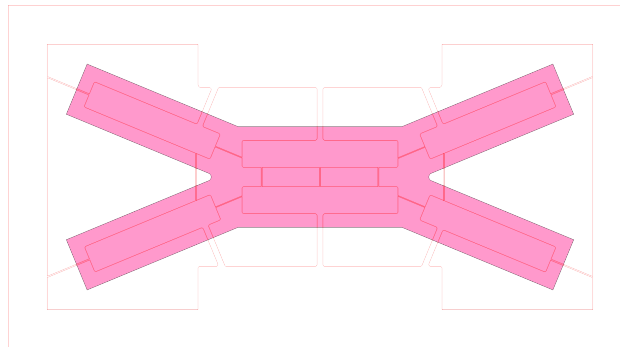


Figure C.3: 2D layout of the quadrupedal soft robot showing integrated chambers. Pink regions denote six pneumatic cavities interconnected by channels for sequential limb actuation. Thin connecting features serve as sacrificial skeletons to enhance alignment accuracy during fabrication.

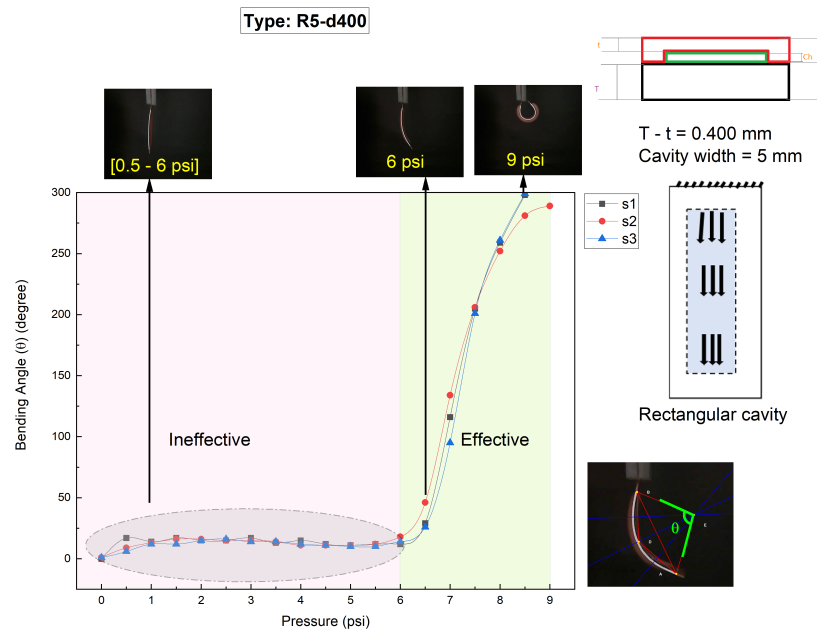


Figure C.4: Bending angle response of PneuThin design R5-d400 (5 mm cavity width) under increasing pressure. The plot shows an ineffective range (0.5 to 6 psi) with minimal bending, followed by an effective range (above 6 psi) with rapid angle increase. Top images show actuator deformation at key pressures. Side diagrams illustrate actuator cross-section and cavity geometry. Bottom right shows angle measurement method

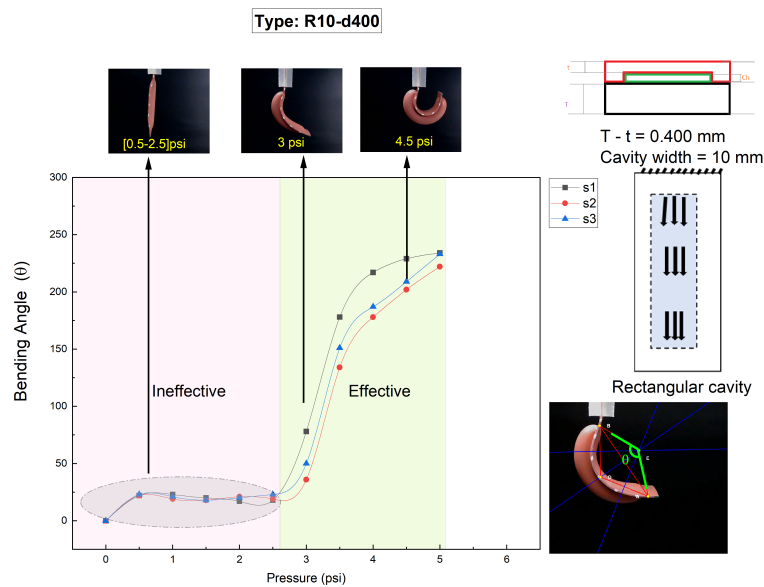


Figure C.5: Bending angle response of PneuThin design R10-d400 (10 mm cavity width) under increasing pressure. The plot shows an ineffective range (0.5 to 2.5 psi) with minimal bending, followed by an effective range (above 2.5 psi) with rapid angle increase. Top images show actuator deformation at key pressures. Side diagrams illustrate actuator cross-section and cavity geometry. Bottom right shows angle measurement method

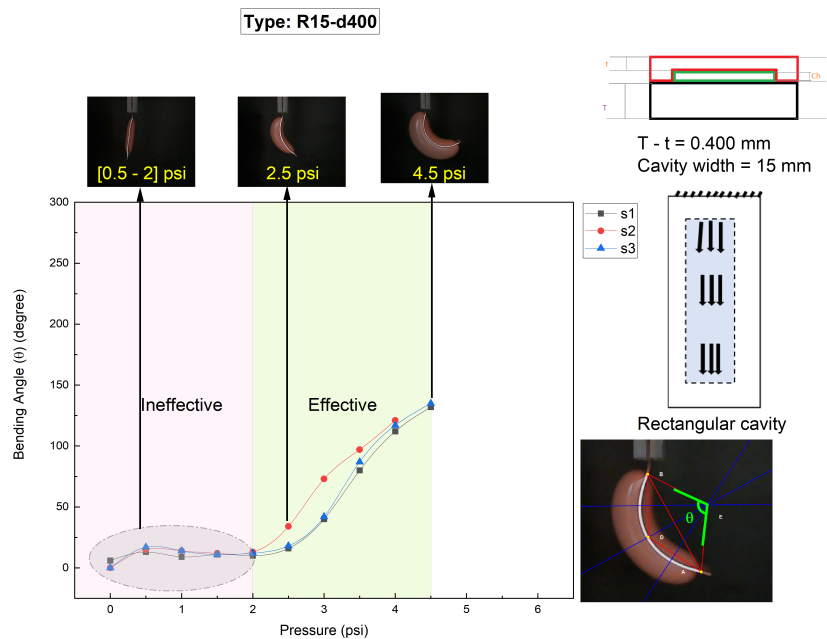


Figure C.6: Bending angle response of PneuThin design R15-d400 (15 mm cavity width) under increasing pressure. The plot shows an ineffective range (0.5 to 2 psi) with minimal bending, followed by an effective range (above 2 psi) with rapid angle increase. Top images show actuator deformation at key pressures. Side diagrams illustrate actuator cross-section and cavity geometry. Bottom right shows angle measurement method

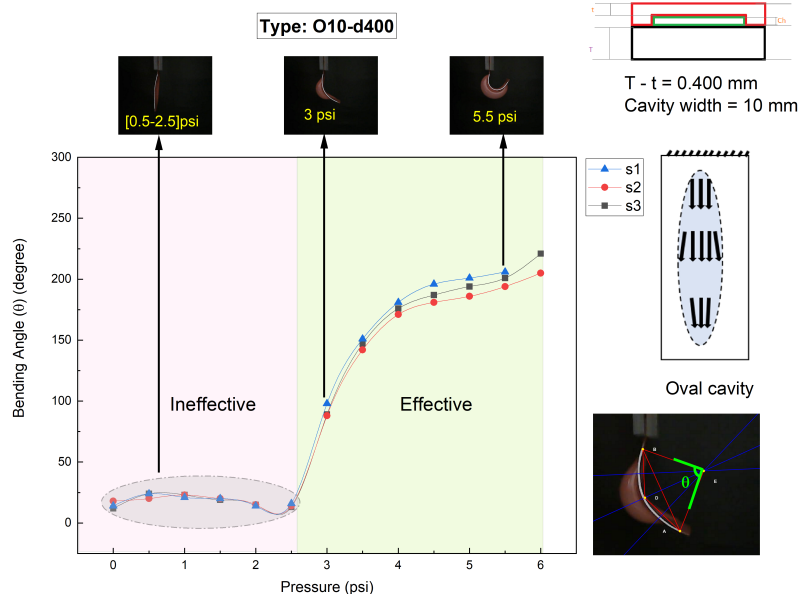


Figure C.7: Bending angle response of PneuThin design O10-d400 (10 mm cavity width) under increasing pressure. The plot shows an ineffective range (0.5 to 2.5 psi) with minimal bending, followed by an effective range (above 2.5 psi) with rapid angle increase. Top images show actuator deformation at key pressures. Side diagrams illustrate actuator cross-section and cavity geometry. Bottom right shows angle measurement method

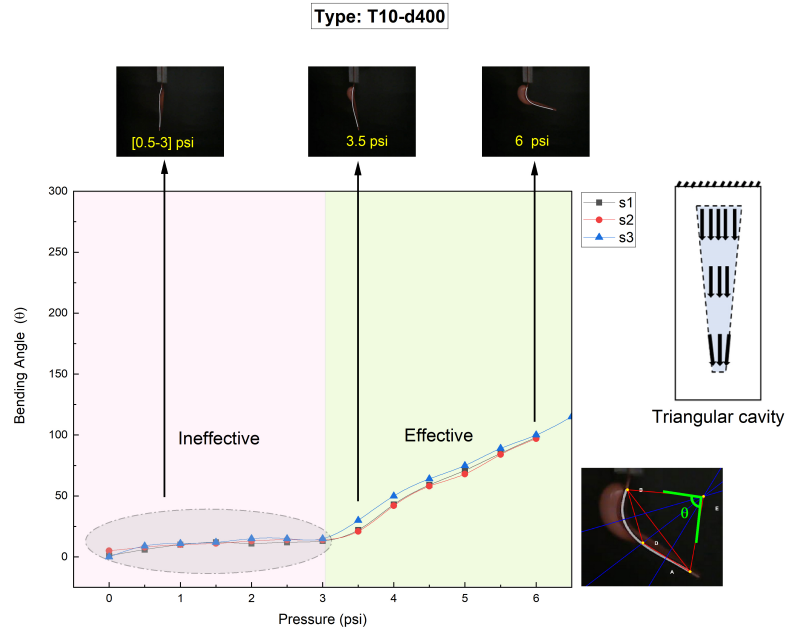


Figure C.8: Bending angle response of PneuThin design T10-d400 (10 mm cavity width) under increasing pressure. The plot shows an ineffective range (0.5 to 3 psi) with minimal bending, followed by an effective range (above 3 psi) with rapid angle increase. Top images show actuator deformation at key pressures. Side diagrams illustrate actuator cross-section and cavity geometry. Bottom right shows angle measurement method

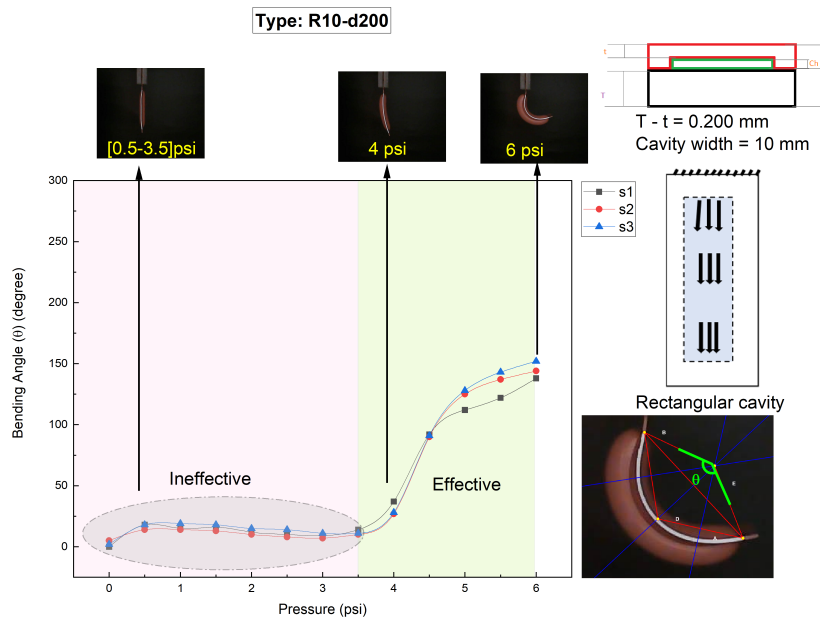


Figure C.9: Bending angle response of PneuThin design R10-d200 (10 mm cavity width) under increasing pressure. The plot shows an ineffective range (0.5 to 3.5 psi) with minimal bending, followed by an effective range (above 3.5 psi) with rapid angle increase. Top images show actuator deformation at key pressures. Side diagrams illustrate actuator cross-section and cavity geometry. Bottom right shows angle measurement method

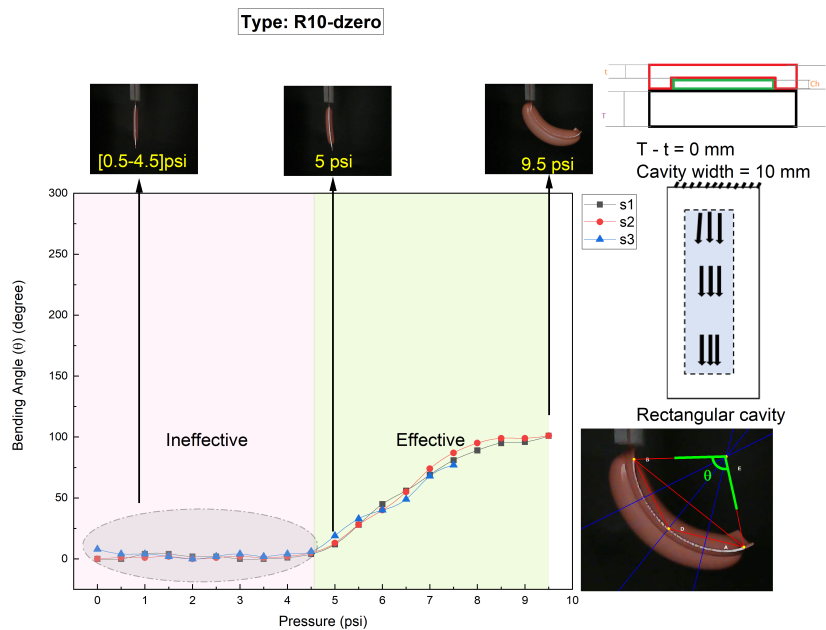


Figure C.10: Bending angle response of PneuThin design R10-d0 (10 mm cavity width) under increasing pressure. The plot shows an ineffective range (0.5 to 5 psi) with minimal bending, followed by an effective range (above 5 psi) with rapid angle increase. Top images show actuator deformation at key pressures. Side diagrams illustrate actuator cross-section and cavity geometry. Bottom right shows angle measurement method

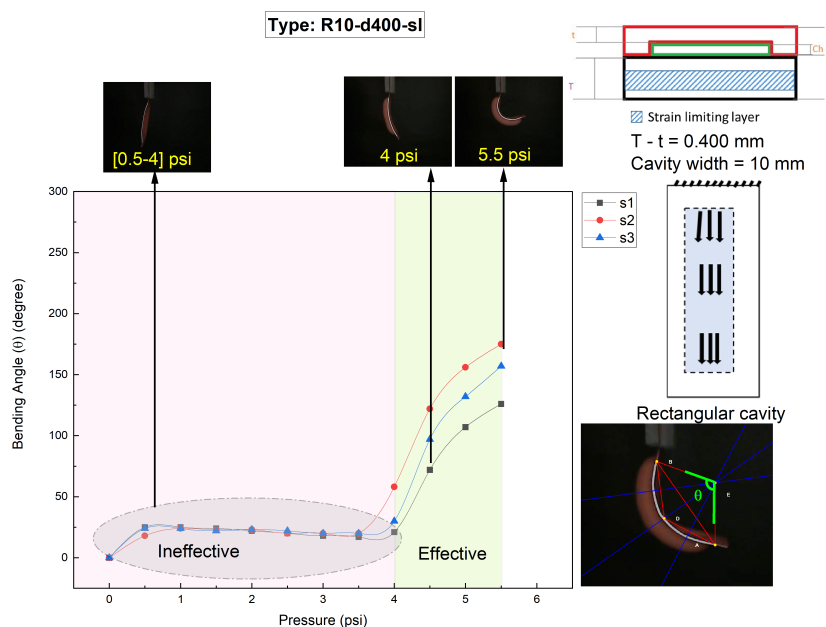


Figure C.11: Bending angle response of PneuThin design R10-d400-sl (10 mm cavity width) under increasing pressure. The plot shows an ineffective range (0.5 to 3.5 psi) with minimal bending, followed by an effective range (above 3.5 psi) with rapid angle increase. Top images show actuator deformation at key pressures. Side diagrams illustrate actuator cross-section and cavity geometry. Bottom right shows angle measurement method